

Department of Mechanical and
Industrial Engineering
University of Illinois at
Urbana-Champaign
Urbana, IL 61801

DTIC
ELECTE
JUL 22 1992
S C D

AEOSR-TR-

0668



AD-A253 389

UILU ENG 92-4016



Final Technical Report

NON-LOCAL THERMODYNAMIC EQUILIBRIUM IN LASER SUSTAINED PLASMAS

David K. Zerkle and Herman Krier

Approved for public release; distribution unlimited.

Final Report Submitted to

Air Force Office of Scientific Research
Dr. Mitat Birkan, Program Manager
for research conducted during the period
16 March 1991 to 16 June 1992

under
Grant No. AFOSR-89-0274

June 1992

Approved for Public Release;
Distribution Unlimited

92

1-12

92-19260

ST P

REPORT DOCUMENTATION PAGE

1a. REPORT SECURITY CLASSIFICATION Unclassified		1b. RESTRICTIVE MARKINGS None	
2a. SECURITY CLASSIFICATION AUTHORITY		3. DISTRIBUTION/AVAILABILITY OF REPORT Approved for public release; distribution is unlimited	
2b. DECLASSIFICATION/DOWNGRADING SCHEDULE			
4. PERFORMING ORGANIZATION REPORT NUMBER(S) UILU ENG 92-4016		5. MONITORING ORGANIZATION REPORT NUMBER(S) AFOSR-TR	
6a. NAME OF PERFORMING ORGANIZATION University of Illinois at Urbana-Champaign	6b. OFFICE SYMBOL (If applicable) UIUC	7a. NAME OF MONITORING ORGANIZATION AFOSR/NA	
6c. ADDRESS (City, State, and ZIP Code) Department of Mechanical & Industrial Eng. 140 MEB; 1206 W. Green St.; MC-244 Urbana, IL 61801		7b. ADDRESS (City, State, and ZIP Code) Building 410, Bolling AFB DC 20332-6448	
8a. NAME OF FUNDING/SPONSORING ORGANIZATION AFOSR/NA	8b. OFFICE SYMBOL (If applicable) AFOSR	9. PROCUREMENT INSTRUMENT IDENTIFICATION NUMBER AFOSR Grant No. 89-0274	
8c. ADDRESS (City, State, and ZIP Code) Building 410, Bolling AFB DC 20332-6448		10. SOURCE OF FUNDING NUMBERS PROGRAM ELEMENT NO. 1011024 PROJECT NO. 23X8 TASK NO. PS WORK UNIT ACCESSION NO.	

11. TITLE (Include Security Classification) Non-Local Thermodynamic Equilibrium in Laser Sustained Plasmas (u)			
---	--	--	--

12. PERSONAL AUTHOR(S) D. Zerkle, H. Krier		13a. TYPE OF REPORT Final Report		13b. TIME COVERED FROM 3/16/91 TO 6/16/92	14. DATE OF REPORT (Year, Month, Day) June 16, 1992	15. PAGE COUNT 198
16. SUPPLEMENTARY NOTATION						

17. COSATI CODES			18. SUBJECT TERMS (Continue on reverse if necessary and identify by block number) Beamed Energy Propulsion; Laser Plasma Formation; Non-Local Thermodynamic Equilibrium			
FIELD	GROUP	SUB-GROUP				

19. ABSTRACT (Continue on reverse if necessary and identify by block number)						
--	--	--	--	--	--	--

An argon laser sustained plasma (LSP) at atmospheric pressure has been studied spectroscopically and the existence of a non-local thermodynamic state has been determined. The spectroscopic data consist of several argon neutral and ion line emissions used to spatially resolve electronic energy level population densities in each plasma species. A hydrogen seed is added to the argon flow for the purpose of determining electron number density by Stark broadening analysis of the Balmer series alpha line. Neutral and ionic argon electronic excitation temperatures are calculated from the spectroscopic data. Electron and heavy particle kinetic temperatures are calculated through the use of an appropriate nonequilibrium model which includes multitemperature gas state, and ionization equations. The dominant nonequilibrium effect in this plasma is kinetic nonequilibrium where the electron kinetic temperature can be more than twice the heavy particle kinetic temperature in high laser power flux regions. Typical electron and heavy particle kinetic temperatures are 14000 K and 8000 K, respectively. Electron number density ranges from $6 \times 10^{22} \text{ m}^{-3}$ to $2.1 \times 10^{23} \text{ m}^{-3}$.

(continued)

20. DISTRIBUTION/AVAILABILITY OF ABSTRACT <input checked="" type="checkbox"/> UNCLASSIFIED/UNLIMITED <input checked="" type="checkbox"/> SAME AS RPT. <input checked="" type="checkbox"/> DTIC USERS		21. ABSTRACT SECURITY CLASSIFICATION Unclassified
22a. NAME OF RESPONSIBLE INDIVIDUAL Dr. Mitat Birkin		22b. TELEPHONE (Include Area Code) (202) 767-4937
		22c. OFFICE SYMBOL AFOSR/NA

19. Abstract (continued)

It is found that a local thermodynamic equilibrium (LTE) analysis of an ion upper energy level population density leads to an excellent prediction of ion number density. This is determined by comparison of the ion number density to the electron number density calculated through the hydrogen Stark broadening analysis, and assuming low temperature quasi-neutrality. Boltzmann equilibrium in the ionic argon system is indicated. LTE analysis of a neutral argon upper energy level population density leads to a very poor prediction of electron number density, but a fairly accurate prediction of neutral particle number density.

The results of the non-LTE spectroscopic analysis are compared to the results of a single temperature (LTE) numerical LSP model. It is found that the numerical model poorly predicts the plasma location with respect to the laser focus. Peak electron number density is comparable in both analyses, as is the overall plasma length, thus the prediction of total laser power absorbed by the plasma is approximately the same for both analyses.

FINAL TECHNICAL REPORT

No. UILU ENG 92-4016

For research supported by
AFOSR Grant No. 89-0274

for period 03/16/91 to 06/16/92

NON-LOCAL THERMODYNAMIC EQUILIBRIUM
IN LASER SUSTAINED PLASMAS

prepared by

David K. Zerkle⁽²⁾ and Herman Krier⁽¹⁾

Department of Mechanical and Industrial Engineering
University of Illinois at Urbana-Champaign
1206 West Green Street
Urbana, IL 61801

Work supported by

Air Force Office of Scientific Research
Dr. Mitat Birkan is Program Manager

(1) Co-Principal Investigator
(2) Graduate Research Assistant

Accession For	
NTIS	GRANT
DTIC TAB	<input checked="" type="checkbox"/>
Unannounced	<input type="checkbox"/>
Justification	
By	
Distribution/	
Availability Codes	
Dist	Avail and/or Special
R-1	

APPROVED FOR PUBLIC RELEASE; DISTRIBUTION UNLIMITED

ACKNOWLEDGEMENTS

The authors would like to acknowledge the contributions of several people who have been invaluable to the completion of this investigation. First we would like to thank Professor Jyotirmoy Mazumder for his advice and insight concerning laser-gas interactions. In addition Professor Lee Sentman of the Aeronautical and Astronautical Engineering Department, and Professor Alexander Scheeline of the Chemistry Department are acknowledged for their helpful suggestions throughout the course of this work.

There are several other people who must also be acknowledged. The previous work performed in the field of non-LTE plasma diagnostics by Dr. Thomas Eddy of the Idaho National Engineering Laboratory has been most enlightening. Without his efforts and personal advice, this research would not have been as successful as it has been. Graduate student Ayhan Mertogul and Materials Engineering Research Laboratory staff member Justin Koch have also been of great help in this investigation.

Dr. Mitat Birkan of the Air Force Office of Scientific Research has been the program manager for this work. We thank him for his support and many inquiries concerning the direction and scientific approach taken in this investigation.x

TABLE OF CONTENTS

NOMENCLATURE	vi
1. INTRODUCTION	1
1.1. RESEARCH OBJECTIVES	2
1.2. LASER PROPULSION	4
1.3. PLASMA THERMODYNAMIC MODELS	15
1.4. LITERATURE REVIEW	30
2. LSP EMISSION SPECTROSCOPY	34
2.1. EXPERIMENTAL FACILITY	34
2.2. EMISSION LINES	50
3. DATA ANALYSIS	54
3.1. DATA REDUCTION	55
3.2. ABEL INVERSION	63
3.3. PRELIMINARY DATA ANALYSIS	68
3.4. NON-LTE DATA ANALYSIS	79
4. RESULTS AND DISCUSSION	91
4.1. PRELIMINARY RESULTS	91
4.2. NON-LTE RESULTS	109
5. CONCLUSIONS AND RECOMMENDATIONS	142
5.1. CONCLUSIONS	142
5.2. RECOMMENDATIONS	145
APPENDICES	147
A. COMPUTER CODE LISTINGS	147
A.1. Raw Spectroscopic Data Reduction	147
A.2. Abel Inversion by Inverse Hankel Transform	158
A.3. Electron Number Density by Stark Broadening	162
A.4. Hydrogen Profile Conversion	176
A.5. LTE Temperature and Composition	178
A.6. Non-LTE Analysis	183
B. ERROR ANALYSIS	189
C. EXCITATION ENERGY DENSITY	194
REFERENCES	195

NOMENCLATURE

ENGLISH

A_{mn} Einstein's coefficient of spontaneous emission for levels m and n

a_0 first Bohr radius

c speed of light

C_p specific heat

E electronic energy level

e electron charge

E_H hydrogen ionization potential

E_{Ia} lowered neutral particle ionization potential

E_{Ii} lowered ion ionization potential

$E_{\lambda,b}$ blackbody spectral emissive power

$E_{0,j}$ zero-point energy of species j

E_0^2 amplitude of electric field

f.l. optical focal length

f/# optical f-number

f_{12} oscillator strength for resonance transition

F_{exp} experimental pixel count

FFT Fast Fourier Transform

F_{imp} calibration lamp pixel count

fsc fine structure constant

g electronic energy level degeneracy

g_{ff} free-free gaunt factor

g_I degeneracy of the highest effective electronic energy level

g_0 acceleration due to gravity at sea level

h Planck's constant

H_{α} hydrogen Balmer series alpha line
 H_{β} hydrogen Balmer series beta line
 I laser power flux
 IB inverse bremsstrahlung
 I_{exp} experimental absolute radiance
 I_{sp} specific impulse
 k_b Boltzmann's constant
 LSP Laser Sustained Plasma
 LTE Local Thermodynamic Equilibrium
 \dot{m} mass flow rate
 M overall optical magnification, or particle mass
 m particle mass
 M_1 first intermediate optical magnification
 M_2 second intermediate optical magnification
 m_e electron mass
 MW molecular weight
 n particle number density
 n_a neutral particle number density
 ND neutral density
 n_e electron number density
 n_e^* critical electron number density
 n_e^{\prime} iterated electron number density
 n_l population number density of the highest effective electronic energy level
 P system pressure
 P_c^{DH} Debye-Huckel pressure correction
 P_e rocket nozzle exit pressure
 P_o stagnation pressure

q	discrete Fourier index
\tilde{R}	universal gas constant
R	under-relaxation factor
r	radial position
S_{imp}	standard lamp spectral radiance
T	temperature
T_e	electron kinetic temperature
$T_{e\text{`}}$	iterated electron kinetic temperature
T_{exa}	neutral particle total excitation temperature
$T_{\text{ex}\beta,\text{a}}$	neutral particle upper electronic level excitation temperature
T_{exi}	ion total excitation temperature
$T_{\text{ex}\beta,\text{i}}$	ion upper electronic level excitation temperature
T_g	heavy particle kinetic temperature
T_{jt}	kinetic temperature of species j
u	axial velocity component
v	radial velocity component
v_e	electron thermal velocity
v_o	peak electron velocity in an oscillating electric field
x	lateral position
x_i	optical image distance
x_o	optical object distance
y	lateral position
Z	partition function; or ionic charge
Z_a	neutral particle partition function based on T
Z_i	ion partition function based on T
Z_{exa}	neutral particle partition function based on T_{exa}
Z_{exi}	ion partition function based on T_{exi}

GREEK

α chemical affinity; or global absorption
 α_{IB} inverse bremsstrahlung laser absorption coefficient
 X_{pq} critical electron number density parameter
 $\epsilon(r)$ radial emission coefficient
 Φ_j critical electron number density parameter
 γ ratio of specific heats
 η rocket conversion efficiency
 η_{th} plasma thermal conversion efficiency
 λ wavelength
 λ_e electron thermal conductivity
 λ_h heavy particle thermal conductivity
 λ_{mn} wavelength of transition from level m to level n
 μ dynamic viscosity
 v_j stoichiometric coefficient of species j
 π mathematical pi
 ρ bulk mass density
 ρ_D plasma Debye length
 ΔE_{∞} lowering of ionization potential
 $\Delta \lambda$ wavelength increment
 ΔT bulk temperature change

1. INTRODUCTION

Laser sustained plasmas (LSP's) have been proposed as the mechanism by which laser energy is converted into thermal energy of a propellant for use in space propulsion applications [Kantrowitz, 1971,1972]. In this so-called laser propulsion system the optically thick plasma gas absorbs laser radiation and transports that energy via the various primary mechanisms of radiation, conduction, and convection. For this system to be successful for space propulsion, it is important to absorb all or nearly all of the incident laser energy and to retain as much of that as possible in the form of thermal energy of the plasma exhaust gas.

To this end a detailed understanding of the absorption and subsequent conversion processes is of utmost importance. The character and relative importance of all the above mentioned conversion and transport mechanisms depends directly on the thermodynamic state of the plasma propellant gas. Plasma constituent particle temperatures and densities are key elements in the thermodynamic description of the LSP, and are the focus of this investigation.

In a plasma environment it is often assumed that local thermodynamic equilibrium (LTE) exists. This assumes that all the energy modes in the plasma gas, both electronic and kinetic, are governed by a single equilibrium temperature. Due to the large external radiation field applied by the laser and strong temperature and density gradients within the plasma, this LTE assumption is not valid all the time. Under conditions important to laser propulsion and other applications, laser sustained plasmas may exhibit differences in electron and heavy particle kinetic temperatures, which may be different from temperatures describing the populations of excited electronic levels. In this non-LTE state the constituent particle number densities cannot be determined in the straightforward manner familiar to LTE plasma analyses.

The coefficients of plasma energy conversion and transport, namely laser absorption, total radiation loss, thermal conductivity, viscosity, and diffusion can be expressed as functions of temperature and particle number densities. In an LTE plasma analysis there exists a one to one correspondence between temperature and composition at a given pressure. From a single

measurement of plasma emission the temperature, and thus all particle number densities, can be deduced directly. In an LTE analysis of a non-LTE plasma these quantities are calculated from oversimplified expressions and are inaccurate. To get a more meaningful analysis the expressions for these quantities must include non-LTE temperature parameters and corresponding particle number densities. A complete non-LTE LSP analysis results in a better picture of where and how much laser energy is absorbed in the plasma, how much of this energy is immediately radiated away, and how much and in what proportions energy is retained by the gas and transported by conduction, convection, and diffusion.

1.1. RESEARCH OBJECTIVES

The main objective of this research is to determine the existence and extent of various non-LTE effects in laser sustained plasmas. The investigation is chiefly experimental, with extensive manipulation of the resulting data. The weaknesses of LTE spectroscopic analysis are pointed out, as are some possible advantages when applied to this plasma. A comparison is made to the results of an LTE numerical model [Eguiguren, 1989] employed to simulate this plasma. The numerical model is known to predict LSP performance parameters, for example total laser power absorption, with satisfactory accuracy. However, the important comparisons between the non-LTE experimental analysis and the LTE numerical model involve local plasma behavior. The weaknesses of the model which result in its poor prediction of the local plasma thermodynamic state are discussed.

As laser sustained plasma applications such as laser propulsion become more mature, it will be all the more important to know how the LSP performs in terms of total laser power absorption and thermal conversion efficiency, as laser power is increased into the megawatt range. Total laser power absorption, or global absorption, is defined as the total laser power absorbed by the plasma divided by the total incident laser power. If transmitted laser power is measured calorimetrically, the expression for global absorption is:

$$\alpha = \frac{P_{\text{laser}} - P_{\text{trans}}}{P_{\text{laser}}} = \frac{P_{\text{abs}}}{P_{\text{laser}}} \quad (1.1)$$

Thermal conversion efficiency is defined as the net thermal power increase of the propellant flow divided by the input laser power:

$$\eta_{\text{th}} = \frac{\dot{m} C_p \Delta T}{P_{\text{laser}}} \quad (1.2)$$

where ΔT is the net rise in mass averaged propellant temperature.

Without a dependable numerical simulation, one which accurately predicts behavior on a local level, successful full scale laser thruster design would be very difficult and expensive. It is for this reason that critique of the current state-of-the-art model is so important, and that proper direction be given for future modeling efforts.

In order to undertake a non-LTE plasma investigation some plasma emission measurements must be made and used in conjunction with an appropriate thermodynamic model. In this investigation an atmospheric pressure argon plasma with a trace of hydrogen is sustained by a 5 kW of CO₂ laser power. Spectroscopic measurements of several argon neutral and ion emission lines are made in both the axial and lateral dimensions. A similar measurement is made of the hydrogen Balmer series alpha line profile for the purpose of electron number density determination through Stark broadening theory.

A thermodynamic model based on the Generalized Multithermal Equilibrium (GMTE) [Cho, 1988] model is used. It assumes no equivalence between electron and heavy species kinetic temperatures, nor does it constrain the electronic excitation temperatures to be equivalent to the electron kinetic temperature. A chief difference between Cho's model and the model used here is that ion electronic distributions are considered separately from the neutral.

The important quantities resulting from this non-LTE argon LSP investigation are the electron and heavy particle kinetic temperatures, T_e and T_g (all heavy particles are assumed to be in kinetic equilibrium due to their nearly equivalent atomic masses), the electron number

density, n_e , the neutral argon number density, n_a , and the neutral and first ionic argon upper level electronic excitation temperatures, $T_{ex\beta,a}$ and $T_{ex\beta,i}$. Secondary calculations result in the local laser beam power absorption at each LSP measurement volume. From this the total beam power absorption, or global absorption, is calculated. Finally the local energy densities associated with various LSP energy modes are calculated. The modes of interest are the electron kinetic energy, heavy particle kinetic energy, and ionization energy. Total LSP radiation loss, conduction, convection, and diffusion cannot be determined with this experimental analysis for reasons to be discussed in the data analysis chapter.

1.2. LASER PROPULSION

This section proceeds considering laser propulsion to be the primary application for laser sustained plasmas. An overview of laser propulsion technology and the potential advantages it provides over competing space propulsion technologies will be followed by a general discussion of LSP characteristics and behavior.

1.2.1. Technology Overview

As laser and laser optics technologies become more advanced and megawatt range continuous wave laser power becomes available, laser propulsion promises to be an important means of space propulsion. A schematic of one possible system configuration is shown in Figure 1.1. Remotely beamed laser energy, in this case from a space-based laser, is collected by an appropriate optical system and focused into the laser thruster's absorption chamber. The LSP stabilized in this chamber absorbs the laser energy and converts a substantial portion into thermal energy of the propellant gas. Many rockets could be powered by a single laser for station keeping or orbital transfer missions.

All rocket propulsion systems heat a propellant which is then expanded through a nozzle to produce thrust. Different propulsion technologies represent variations of the method used to heat the propellant. Many relations between performance parameters are valid independent of

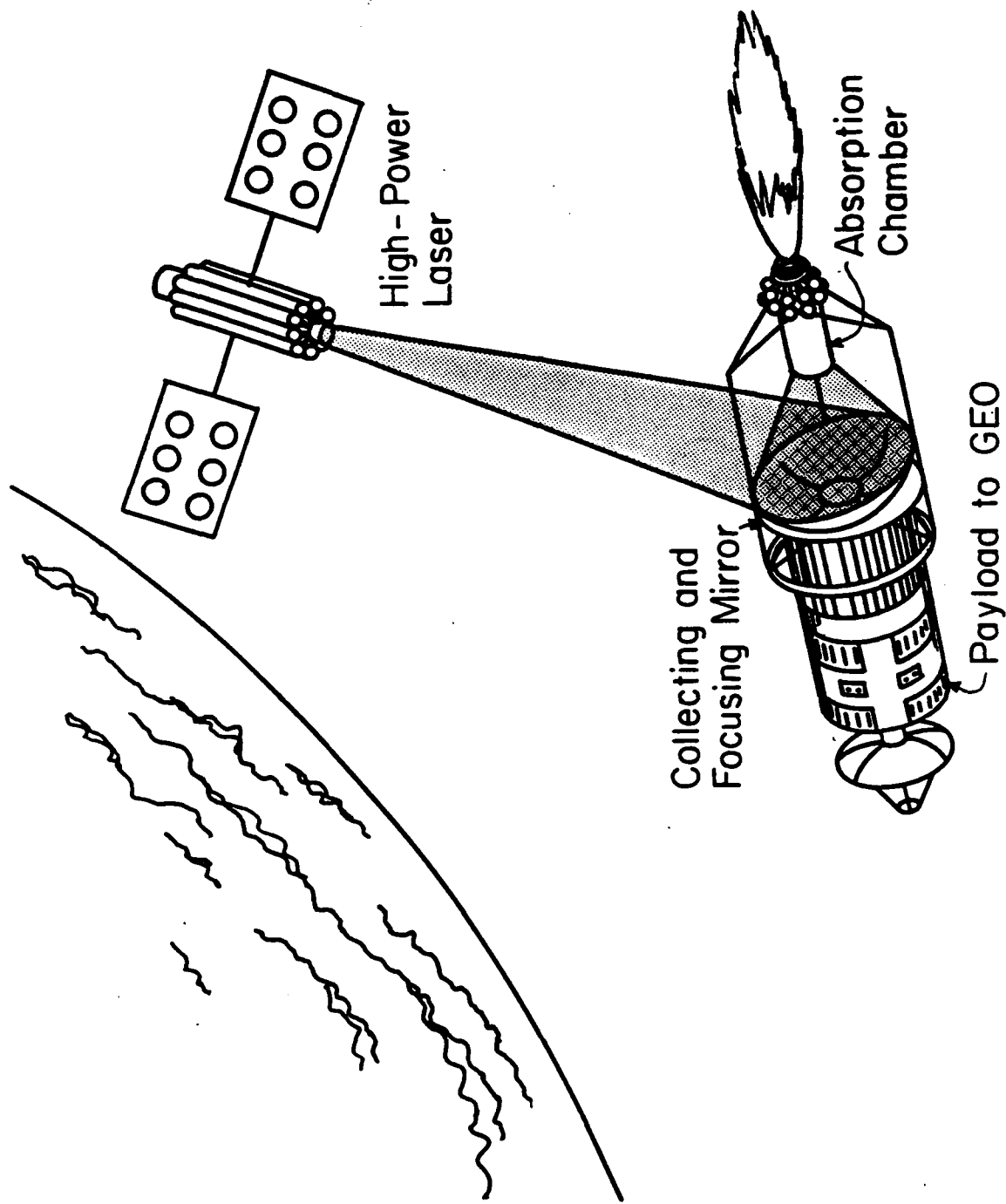


Figure 1.1 Schematic of a possible laser propulsion system configuration. Taken from Glumb [1986] with permission.

the type of rocket being considered, and the relative advantages and disadvantages of differing rocket systems can be compared considering these relations.

Rocket thrust can be written in terms of the propellant mass flow rate, \dot{m} , the specific impulse, I_{sp} , and the acceleration due to gravity at sea level, g_0 :

$$\text{Thrust} = \dot{m} g_0 I_{sp} \quad (1.3)$$

Specific impulse can be thought of as the efficiency of the thrust produced (thrust force per unit weight propellant flow) and is directly related to the spacecraft payload fraction. Specific impulse is a function of a number of thruster flow parameters [Sutton, 1986]:

$$I_{sp} = \frac{1}{g_0} \sqrt{\frac{2\gamma \bar{R} T_0 \left(1 - \left(\frac{P_e}{P_0}\right)^{(\gamma-1)/\gamma}\right)}{(\gamma-1) MW}} \quad (1.4)$$

where γ is the ratio of specific heats, \bar{R} is the universal gas constant, T_0 is the chamber stagnation temperature, P_e is the nozzle exit pressure, P_0 is the chamber stagnation pressure, and MW is the propellant molecular weight. Clearly a high chamber propellant temperature and a low propellant molecular weight are desirable for high specific impulse.

Defining rocket conversion efficiency, η , as the ratio of the kinetic energy of the exhaust propellant to the input power (whether from chemical combustion or an external power source), it can be shown [Glumb and Krier, 1988] that the relation between thrust, specific impulse and input power is:

$$\text{Thrust} = \frac{2 \eta P_{\text{input}}}{g_0 I_{sp}} \quad (1.5)$$

Laser propulsion is expected to compete with both chemical and electric propulsion technologies. Chemical rockets burn either a solid or liquid fuel, the products of which are then used as propellant. Chemical systems can produce very high levels of thrust, limited only by the amount of propellant that can be passed through the system. However, they typically

produce low specific impulses with an upper limit of approximately 500 seconds. The chamber temperature in a chemical rocket can be as high as 4400 K, and the molecular weight of the propellant ranges between 8.9 and 29.3 kg/kg-mole depending on the fuel [Sutton, 1986]. Despite specific impulse limitations, high thrust chemical rockets are the system of choice for raising payloads from the earth's surface.

A typical electric thruster utilizes the energy of an external electromagnetic field to heat a propellant. Low molecular weight propellants can be used to achieve high specific impulse, but electric propulsion systems are thrust limited. The power source for an electric rocket, be it a nuclear reactor, solar collector/converter, or batteries is relatively heavy and inefficient [Sutton, 1986]. The source would be limited in the amount of power it could produce due to size and mass constraints, thus electric propulsion systems are thrust limited.

The motivation for developing laser propulsion technology is to fill the performance gap left by chemical and electric rocket systems. The power input to the propellant is not limited to the output of a given class of generator because the power source is not carried onboard the spacecraft. In addition, a low molecular weight propellant (such as hydrogen) can be chosen to maximize specific impulse. With the combination of these two factors, laser propulsion systems are theoretically capable of producing moderate thrusts (> 1 kN) with specific impulses in excess of 1000 s for 10 MW input power. A comparison of typical performance limits for chemical, electric, and laser propulsion systems is shown in Figure 1.2.

If an overall rocket thermal conversion efficiency of 75% is assumed, then 7.5 MW of laser power are required for 1000 seconds of specific impulse and 2 kN of thrust. These are the target performance parameters for orbital transfer vehicles in low earth orbit, where extremely high thrust is not important and high Isp is a necessity. Laser propulsion is not as well suited as chemical propulsion for launch vehicle missions because of the very high thrust required. Many gigawatts of laser power would be needed for that application. Because of the earth or earth-orbit based laser power source, laser propulsion is not practical for long-range

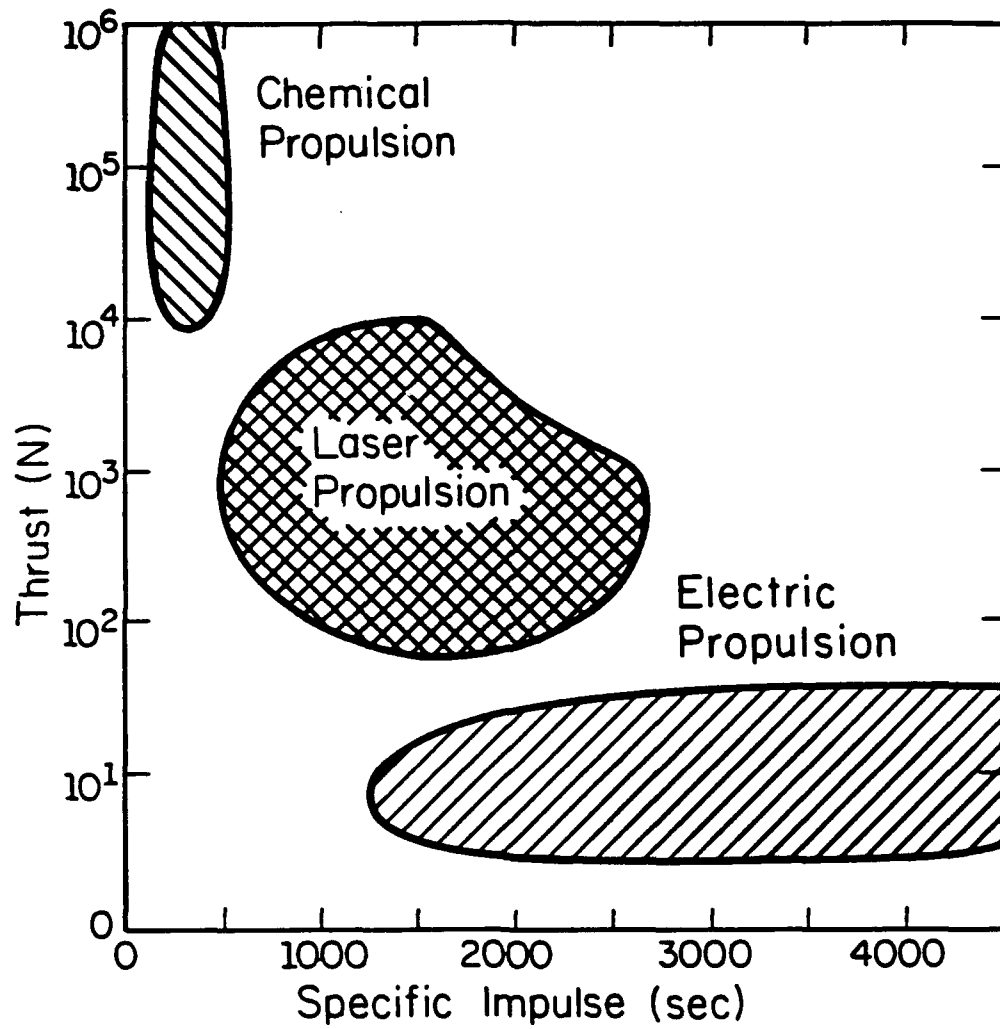


Figure 1.2 Laser Propulsion promises to fill the performance gap between high thrust - low specific impulse chemical propulsion, and low thrust - high specific impulse electric propulsion; Taken from Glumb [1986] with permission.

missions. These missions require the highest possible specific impulse and a nuclear reactor powered electric propulsion rocket might be the best choice.

A further discussion of laser propulsion techniques including repetitively pulsed (RP) and direct laser heating can be found in Ronald Glumb's Ph.D. Thesis [1986]. More general information on laser propulsion is also referenced [Glumb and Krier, 1984; Caveny, 1984; Legner and Douglas-Hamilton, 1978]. Discussion of rocket propulsion concepts such as specific impulse and thrust are also readily available [Sutton, 1986].

1.2.2. LSP Characteristics and Behavior

1.2.2.1. Laser Power Absorption

Argon gas is transparent to 10.6 μm CO_2 laser radiation with a power flux less than approximately 10^9 W/cm^2 [Rockstroh, 1986]. Without such extremely high power flux an external source of electrons is required to initiate an ionization cascade in cold argon (as in this investigation). Once the gas has been ionized and a LSP is formed, the power density required to sustain it is much lower and depends on other variables such as gas pressure, incident mass flux, and laser beam focusing geometry. The study of LSP maintenance power requirements has been included in much of the past research related to this investigation [McMillin, 1987; Zerkle, 1990; Schwartz, 1989].

The primary mechanism whereby laser radiation is absorbed by the plasma is called inverse bremsstrahlung (IB). The laser absorption coefficient of Wheeler and Fielding [1970] is used in this investigation. In the IB process free electrons in the presence of atoms or ions absorb laser photons and gain kinetic energy. Through collisional processes with the heavy particles the entire gas becomes heated. If the input power flux is great enough to overcome electron recombination and other electron energy losses, the heating and subsequent ionization will continue until the LSP stabilizes in the vicinity of the laser focus. A schematic representation of laser absorption and plasma stabilization is shown in Figure 1.3. The

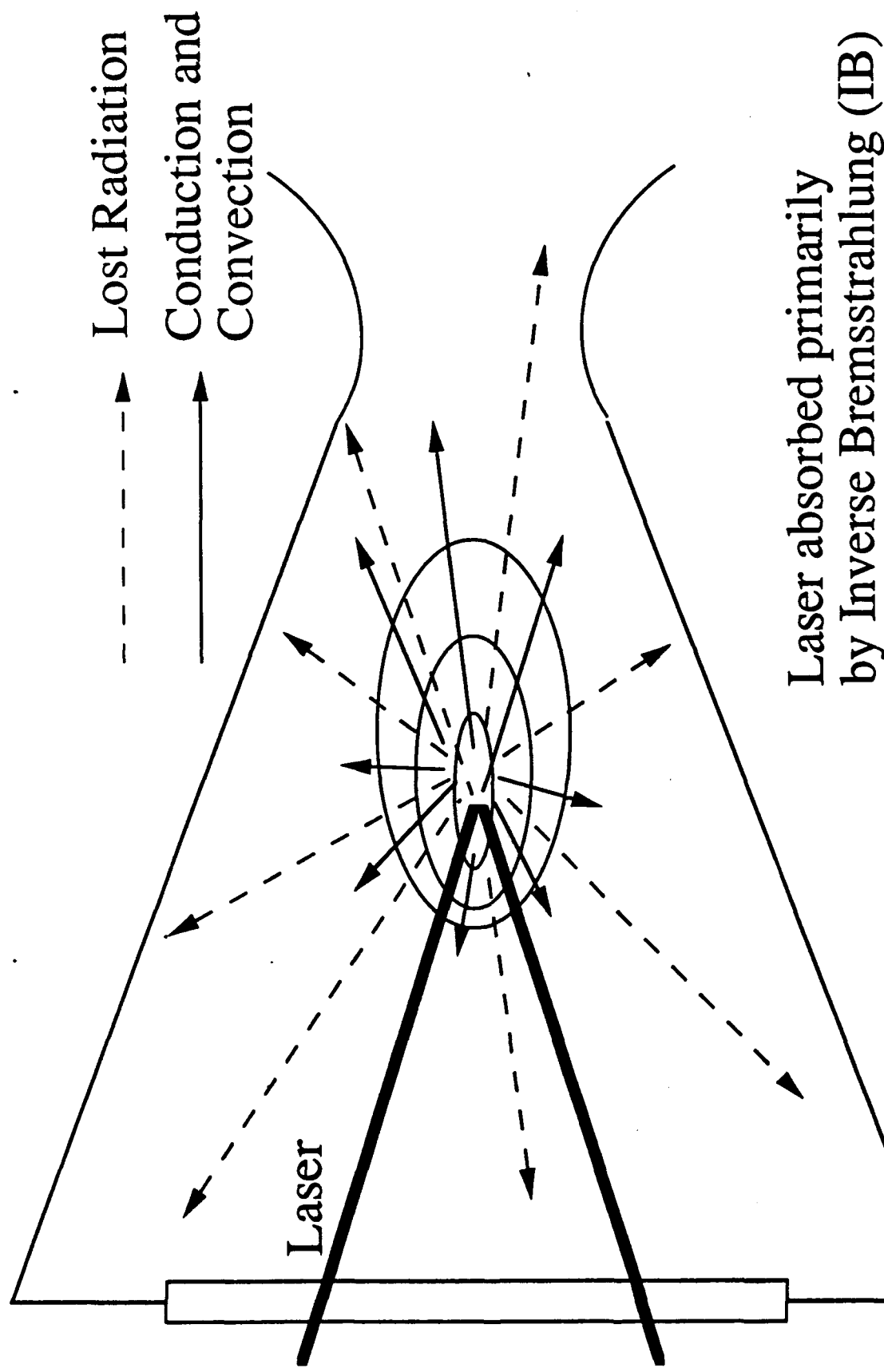


Figure 1.3 Schematic representation of LSP

Plasma stabilizes when processes are balanced

radiation, conduction, and convection sketched in the figure are examples of plasma loss mechanisms.

1.2.2.2. LSP Losses

As mentioned above, the LSP is stable if the total plasma losses do not exceed the input power. The primary LSP loss mechanisms are radiation, conduction, and convection to the surroundings, the latter two usually being desirable since they serve to heat the bulk argon gas flow. Radiation from the plasma can be reabsorbed by the plasma or transmitted to the absorption chamber walls. Optically thick radiative transport is often cast as a diffusion process similar to conduction, and is treated as such by adding an effective 'radiative conductivity' to the thermal conductivity of the heavy species. Optically thin radiation is assumed to be completely lost for the purposes of this discussion, although regenerative techniques may be used to recover most of that energy in a full scale laser thruster.

The plasma radiation consists of both spectral line radiation and continuum radiation. The line radiation is due to bound-bound electron transitions within bound states in atoms. The continuum radiation is due to free-bound transitions of free electrons to bound states within atoms or ions and free-free transitions of free electrons in the presence of atoms or ions. The free-free radiation is related to IB absorption and is called bremsstrahlung radiation. Continuum radiation and line radiation in argon have been studied by Oettinger and Bershader [1967] and Kozlov [1974] respectively. Both analyses rely on approximate corrections, known as gaunt factors, to the classical radiation expressions for quantum mechanical effects.

1.2.2.3. LSP Position Stabilization

A laser sustained plasma stabilizes in a gas flow stream at a location where the absorbed laser power exactly balances energy losses due to radiation, conduction, and convection. Gas upstream of the plasma is heated by conduction and plasma radiation at a rate determined by the laser input power flux and incident gas velocity. For a given input power flux and gas

pressure, a LSP will have a plasma wave velocity such that the LSP will remain stationary only if this velocity matches the input gas velocity [Glumb, 1986].

The stabilization process can be explained with the help of Figure 1.4. If the gas velocity is too low, the LSP will propagate in an upstream direction because the plasma wave velocity exceeds that of the incoming gas. If the gas velocity is too high it exceeds that of the plasma wave, and the LSP will propagate downstream or become unstable (extinguishes) because total losses have exceeded power input. For a parallel laser beam this means that the slightest variation in gas velocity or laser power could cause the LSP to shift position drastically or become unstable. This problem is dealt with in most LSP systems by focusing the laser beam to a small spot.

When a focused beam is used the LSP tends to fill the incoming beam upstream of the focus. In this position the LSP is dynamically stable and can adjust to fluctuations in laser input power or gas velocity. Figure 1.5 will help to understand the LSP stabilization process in a focused laser beam. Consider a plasma at position (1) in the focusing beam corresponding to an input power flux I_1 . At this point the input power absorbed matches the losses and thus the gas velocity matches the LSP wave velocity. Consider a momentary surge of laser power causing the power flux at position (1) to increase. The LSP moves upstream to a position of lower power flux (2) which results in a LSP wave velocity the same as at position (1) before the surge. If the disturbance ends and the laser again operates at the original power, the LSP wave velocity will be less than the incoming gas velocity at position (2) and it will be pushed back to position (1). Similarly, a sudden momentary decrease in laser power may displace the LSP to position (3), but as soon as the laser power returns to the original level the LSP will move back to position (1). Variations in gas velocity at constant laser power have a similar effect on LSP position.

A LSP cannot be stabilized in the diverging portion of the beam because it will either extinguish or move through the focus and stabilize in the converging section. This can be seen by referring again to Figure 1.5. Consider a LSP at position (4) with the gas velocity exactly

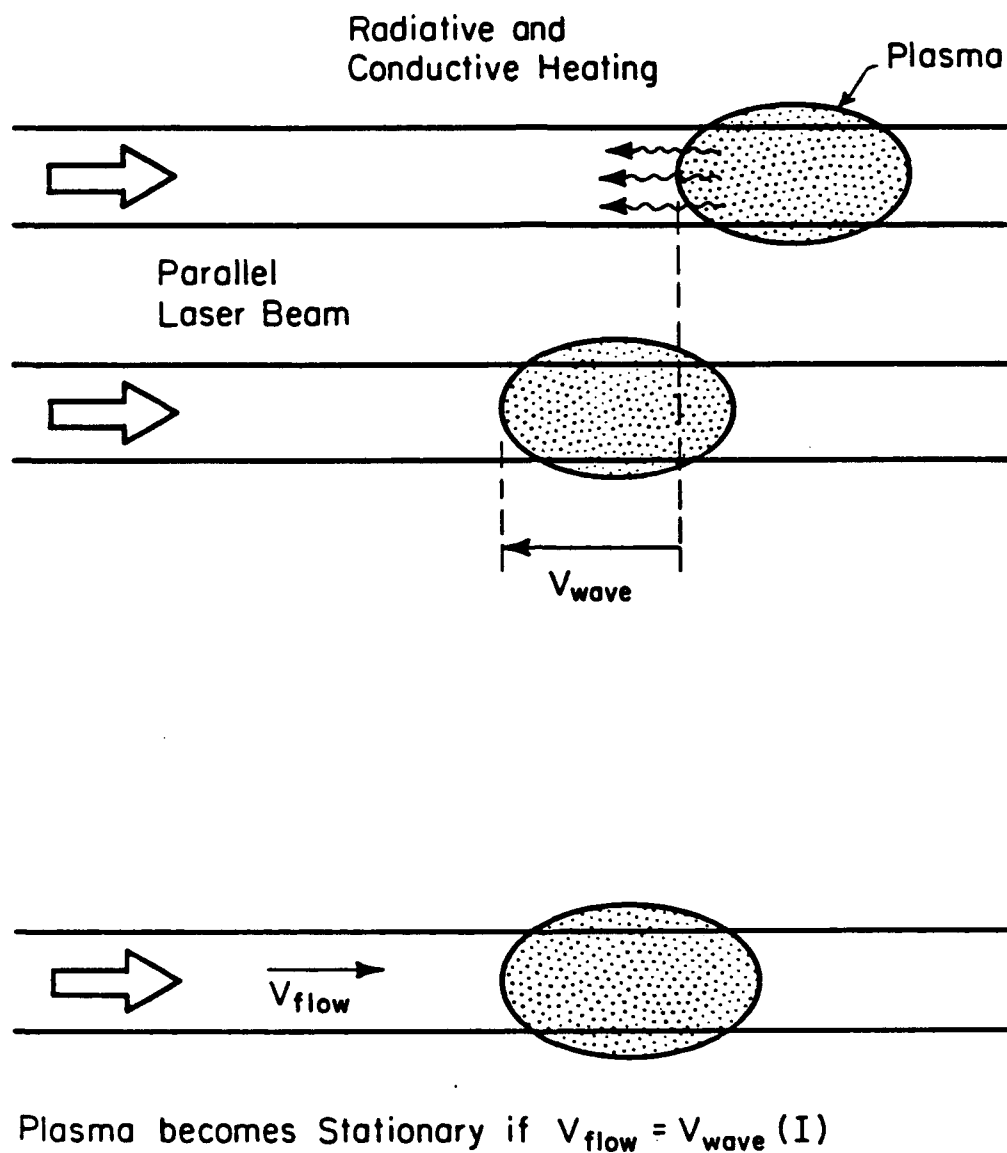


Figure 1.4 Schematic of a dynamically unstable LSP in a parallel laser beam.

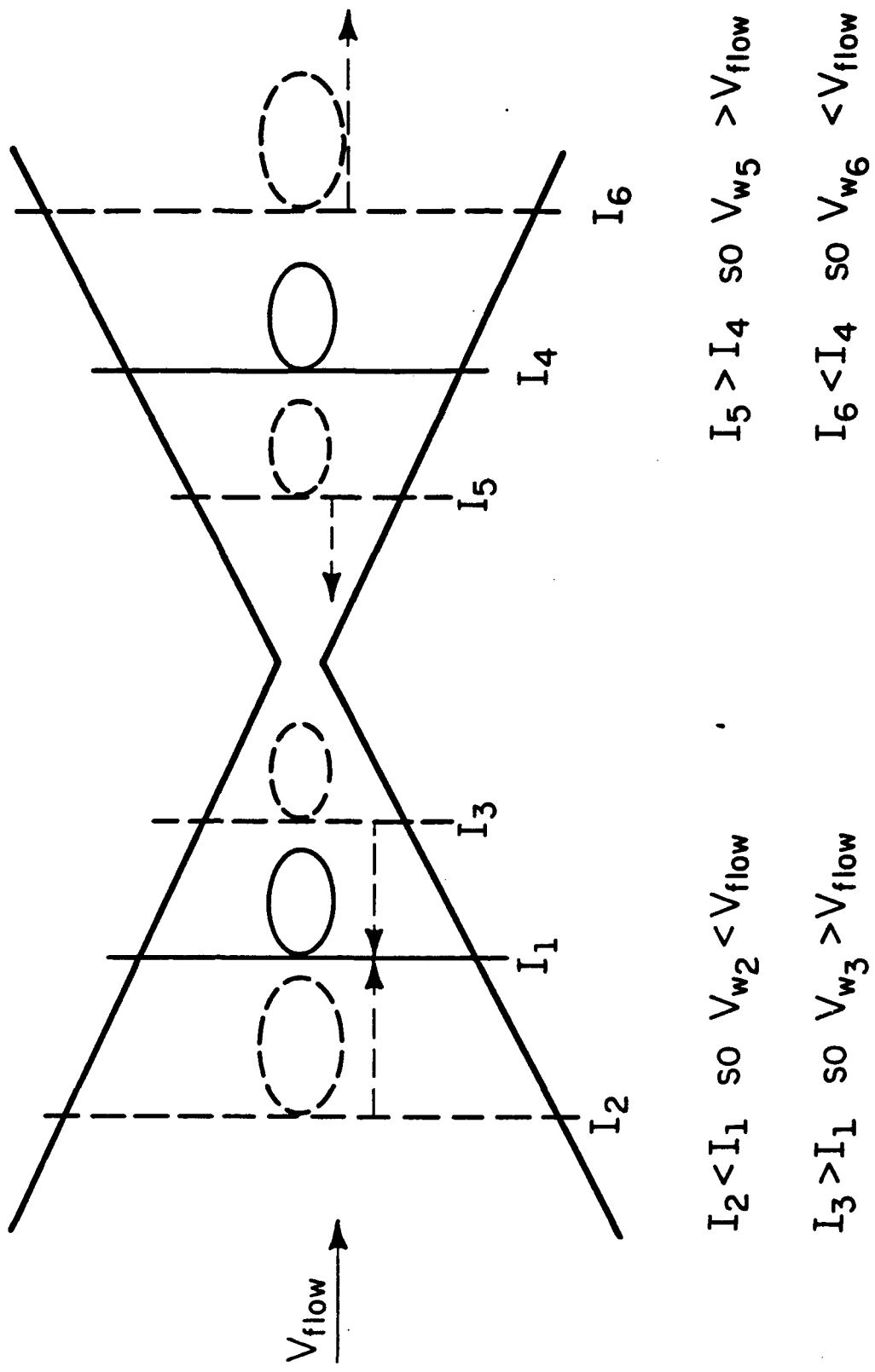


Figure 1.5 Schematic of a dynamically stable LSP in the converging portion of the laser beam, and a dynamically unstable LSP in the diverging portion of the laser beam.

balancing the LSP wave velocity. Either a laser power increase or a gas velocity decrease shifts the LSP toward position (5). At this point the power flux is even greater and the LSP wave speed increases and continues to increase until the LSP stabilizes at some position in the converging beam upstream of the focus. Alternatively, a decrease in laser power or an increase in flow velocity causes the LSP to shift toward position (6). Here the power flux is lower and the wave velocity decreases and continues to decrease until the LSP has blown completely downstream and extinguishes.

1.3. PLASMA THERMODYNAMIC MODELS

1.3.1. Thermodynamic Equilibrium

In order to achieve thermodynamic equilibrium in a laser sustained plasma a number of constraints must be met. A discussion of these constraints is helpful so that subsequent discussions of nonequilibrium plasmas are more meaningful.

Complete thermodynamic equilibrium is quite uncommon in laboratory plasmas. For this state to prevail the plasma must be homogeneous and have all processes, properties, mechanisms, and degrees of freedom governed by a single temperature. There are four basic functional relationships which must hold so that complete thermodynamic equilibrium exists. The laws of Maxwell, Boltzmann, Saha, and Planck determine the distribution of particle velocities, the excited level populations, the degree of ionization, and the spectral distribution of radiation, respectively [Venugopalan, 1971, p. 373].

- 1) A Maxwellian distribution of particle velocities exists if the density dn of particles with velocities between v and $v+dv$ may be expressed as:

$$dn = n f(v) dv \quad (1.6)$$

where n is the particle density of a given plasma constituent and $f(v)$ is the Maxwellian velocity distribution function given by [Venugopalan, 1971, p.374]:

$$f(v) = \frac{4\pi v^2}{2\pi k_b T} \left(\frac{m}{2\pi k_b T}\right)^{3/2} \exp\left(\frac{-mv^2}{2k_b T}\right) \quad (1.7)$$

For complete thermodynamic equilibrium, all plasma species must obey this law with the same kinetic temperature governing the distribution for each. This is to say that kinetic equilibrium is necessary for complete thermodynamic equilibrium.

2) A Boltzmann distribution exists on the electronic energy levels of a given particle if the number densities of particles on these levels can be related by:

$$\frac{n_m}{n_n} = \frac{g_m}{g_n} \exp\left(\frac{-(E_m - E_n)}{k_b T}\right) \quad (1.8)$$

where n_m and n_n are the number densities of particles on any two arbitrarily chosen excited levels m and n , E_m and E_n are the electronic excitation energies of those levels, and g_m and g_n are the degeneracies of those levels.

If n is the sum of all particles n_m over all energy levels m of a given particle, then another useful Boltzmann relation is:

$$\frac{n_m}{n} = \frac{g_m}{Z(T)} \exp\left(\frac{-E_m}{k_b T}\right) \quad (1.9)$$

where $Z(T)$ is the particle partition function:

$$Z(T) = \sum_m g_m \exp\left(\frac{-E_m}{k_b T}\right) \quad (1.10)$$

and the all energies are non-negative, starting with the ground state energy $E_1=0$.

3) Chemical equilibrium is necessary for complete thermodynamic equilibrium. Saha's equation arises from the law of mass action for an ionization reaction in chemical equilibrium [Potapov, 1966]. The functional form of Saha's equation is:

$$\frac{n_e n_i}{n_a} = 2 \frac{Z_i(T)}{Z_a(T)} \left(\frac{2\pi m_e k_b T}{h^2} \right)^{3/2} \exp\left(\frac{-E_{Ia}}{k_b T}\right) \quad (1.11)$$

where $Z_i(T)$ and $Z_a(T)$ are the electronic partition functions of the ions and neutrals, respectively, and E_{Ia} is the lowered ionization potential of the neutral particles. The lowering is due to Coulomb interactions within the plasma. Similar and equally valid equations can be written for higher order ionization reactions in chemical equilibrium.

- 4) The most distinctive aspect of a plasma in complete thermodynamic equilibrium is its isotropic blackbody radiation field described by Planck's law. This law gives the spectral emissive power (power radiated through normal unit surface per unit wavelength and unit solid angle) as a function of temperature and wavelength (in microns) [Incropera and DeWitt, 1981]:

$$E_{\lambda,b}(\lambda, T) = \frac{C_1}{\lambda^5 [\exp(C_2/\lambda T) - 1]} \quad (1.12)$$

where $C_1 = 2\pi h c^2 = 3.740 \times 10^8$ (W $\mu\text{m}^4/\text{m}^2$), and $C_2 = hc/k = 1.438 \times 10^4$ ($\mu\text{m K}$).

This constraint on a plasma's radiation field is extremely difficult to meet in the laboratory. Planck's distribution of radiated power is much more likely to be realized in stellar masses where huge plasma volumes at nearly uniform temperature exist. The radiation from a laboratory plasma is usually much weaker because of optically thin radiation loss over much of the emitted spectrum. This not only violates the blackbody radiation constraint, but tends to break down agreement with the others as well.

A simplifying concept can be used for the study of laboratory plasmas under certain conditions. Local thermodynamic equilibrium (LTE) implies that electron collisions wholly determine the state of matter within the plasma. This allows the laws of Maxwell, Boltzmann, and Saha to be used to determine the plasma composition with a temperature equal to the electron translational temperature, T_e . Planck's law is not valid for a plasma only in local

thermodynamic equilibrium. A more detailed description of LTE follows, along with some of the basic criteria for the establishment of LTE in a laboratory plasma.

1.3.2. Local Thermodynamic Equilibrium

Strictly speaking, there can be no gradients of temperature or density in order for complete thermodynamic equilibrium to hold. Because gradients practically always exist in laboratory plasmas, complete thermodynamic equilibrium is almost never observed. Radiation escaping from the plasma and diffusion of charged particles toward its boundaries are two of the causes for the breakdown of equilibrium. However, if the processes which tend to maintain equilibrium (collisions between plasma particles) are intense enough, then thermodynamic equilibrium can be maintained locally. Thus temperature and density are dependent upon location in the plasma, but the laws of thermodynamic equilibrium governing the state of matter hold at the local temperature. This situation is known as local thermodynamic equilibrium (LTE).

In all plasmas in which complete thermodynamic equilibrium does not exist, the opposing collisional processes which tend to maintain equilibrium (ionization and recombination, excitation and deactivation) do not exactly counterbalance each other [Biberman, et al., p.10]. However, LTE holds if at each point in the plasma these processes far outweigh the processes which lead to a departure from equilibrium. For example the collisional excitation and deactivation of a particular electronic level should compensate for the depletion of that level by the escape of radiation from the local plasma volume. Similarly the collisional rate of ionization should be many times higher than the rate of electron diffusion out of the local plasma volume.

Each of these collisional processes has associated with it a collision cross section, and the inelastic processes also have corresponding transition probabilities. These transition probabilities are functions of the density and energy of the electrons and are very important for evaluating the dominant plasma processes. The collisional transitions which are the most probable are the ones between adjacent energy levels [Biberman, et al., p.31], and the

ionization transitions which are the most probable are those originating in a highly excited level [Biberman, et al., p.45].

Loss of plasma energy due to spontaneous emission can have a strong impact on the plasma energy balance. For a fixed upper level, the most probable transition is to the ground state. Transitions to the adjacent lower level and to the first excited level in the atom are about 1/2 as likely to occur spontaneously. All other transitions are even less likely. For a fixed lower level a transition from the adjacent higher level is the most probable, and all other transitions are much less likely to occur spontaneously [Biberman, et al., p.70].

As a rule radiative transition probabilities decrease and collisional transition probabilities increase as the energy level in question increases [Biberman, et al., p.119]. It is then reasonable to expect that there will be a group of excited levels adjacent to the continuum that are in Boltzmann equilibrium amongst themselves. In addition, radiative processes in plasmas become more important with decreasing plasma electron density and collision frequency. A higher density, and therefore higher collision frequency, means that electronic transitions within the atomic system will be collision dominated in lower lying energy levels as well, and the Boltzmann distribution may include the ground level if the electron number density is high enough.

A process which tends to break down equilibrium in inhomogeneous plasmas is the radiative transport of atomic excitation energy from one point in a plasma to another. This kind of energy transport is a sequence consisting of absorption of radiation and its reradiation by the excited atoms resulting in excited atoms that seem to move in space. Although considered an optically thick radiative process, excitation transport can have a nonequilibrium influence because the density and spatial distribution of excited atoms is altered and thus can effect the plasma properties and processes such as ionization and recombination.

In many cases the average distance between the sites of photon emission and absorption is much larger than the mean free paths of the plasma particles. This means that radiative excitation transport couples regions of the plasma which otherwise would not strongly interact.

Due to the variation of absorption coefficient across a broadened line spectrum, the radiation emitted in these lines is attenuated more slowly than the familiar exponential decay of a pure frequency (Beer's law). As a result, excitation can be transported into a given plasma volume from remote regions of the plasma [Biberman, et al., p.88]. If this process is significant, then there is the possibility that even at high electron number density the distribution of excited states will not follow a Boltzmann distribution, or that the distribution is not in equilibrium with the local free electrons.

The electron density at which the plasma state is determined solely by electron collisions is not known precisely for all cases, and care must be taken before LTE is assumed. It is best to undertake a study of laboratory plasmas without assuming LTE and then later determine if such an assumption might be valid for similar cases. Many criteria have been proposed for the establishment of LTE in plasmas, and several of these will be examined in the next section.

1.3.3. Basic LTE Criteria

In general, external electromagnetic fields, the escape of radiation outside the plasma, gradients of physical quantities, and the finite rate of physical and chemical processes all work to destroy equilibrium in a plasma. Collisional processes, which lead to a redistribution of energy and momentum of the plasma particles, work to restore equilibrium. The criteria for determining if a plasma volume is in equilibrium requires comparing the efficiency of the processes working to destroy and restore equilibrium.

1.3.3.1. Kinetic Equilibrium

In this kind of nonequilibrium the electron kinetic temperature is not the same as the heavy particle kinetic temperature. It arises when an external field is applied to the plasma. The mobility of the electrons is much higher than that of the heavy particles, and so the bulk of the energy is transferred to the electrons. In other words the inverse bremsstrahlung (IB) laser

absorption process increases the kinetic energy of the electrons much more than it does the heavy particles in the electron-photon-heavy particle three body collision.

Laser irradiance (W/m^2) can be expressed in terms of the amplitude of its electric field vector (V/m) by the following:

$$I = \frac{c \epsilon_0}{2} E_0^2 \quad (1.13)$$

For a laser power of 5 kW giving a modest irradiance estimate of 10^8 W/m^2 the electric field amplitude is $2.7 \times 10^5 \text{ V/m}$. Griem [1964] gives a criterion for kinetic equilibrium based on the amount of energy absorbed by the electrons and the amount transferred to the heavy particles through elastic collisions. The expression is given in terms of the external electric field strength:

$$E^2 \ll \left[5.5 \times 10^{-12} n_e \frac{E_H}{k_b T_e} \right]^2 \frac{m_e}{M} \quad (1.14)$$

where E_H is the ionization potential of hydrogen (eV), n_e is the electron number density (cm^{-3}), $k_b T_e$ is the average plasma electron kinetic energy (eV), m_e is the mass of the electron, and M is the mass of the heavy particle in question. For an equilibrium composition of argon at one atmosphere the maximum electron density at 16700 K is $\sim 2 \times 10^{17}$. The right hand side of this inequality is 1.5×10^9 for these conditions and the criterion is failed by at least two orders of magnitude. Therefore it is reasonable to expect kinetic nonequilibrium in laser sustained argon plasmas.

At higher temperatures inelastic collisions play a role in the steady state energy balance as will other electron energy loss mechanisms such as thermal conduction, radiation, and diffusion out of the plasma volume. These processes ease the strictness of the above criterion, as does the presence of a molecular component in the plasma. With a molecular component the inelastic losses due to excitation of vibrational and rotational degrees of freedom become important and the effective energy transfer fraction becomes larger than m_e/M , thus enhancing

the electron energy loss. This has been shown to be true even when molecules constitute only a small fraction of the total number of particles [Biberman, et al., p.115]. Even with these additional considerations, the magnitude by which the above criterion is failed for the laboratory LSP leads to the expectation of kinetic nonequilibrium.

1.3.3.2. Boltzmann and Saha Equilibrium

For plasma diagnostics it is important to determine whether the atoms are distributed over the excited energy levels in accordance with a Boltzmann distribution at the electron kinetic temperature, and whether the electron density is given by the Saha equation at that same temperature. If these two situations hold, then the state of the plasma is greatly simplified and standard plasma diagnostic methods can be used.

LTE can be disturbed in a number of ways, the most important of which are, the escape of optically thin radiation, the diffusion of charged particles, and the optically thick transport of excitation energy. In general the breakdown of ionization equilibrium and the equilibrium excited state distribution are closely related.

A criterion given by Drawin [1969] gives the electron number density required for a Boltzmann distribution to extend to the ground state of an atom. If this criterion is met, it is implied that the distribution of excited states and the extent of ionization are controlled by the electron kinetic temperature. The expression for critical electron number density is:

$$n_e^* \geq 6.5 \times 10^{10} \frac{g_p}{g_q} (E_p - E_q)^3 \sqrt{T_e} \Phi_j (X_{pq}) \quad [\text{cm}^{-3}] \quad (1.15)$$

where levels p and q are the furthest separated in energy in the atom, g and E are the degeneracy and energy of a level, X_{pq} is a parameter defined as $(E_p - E_q)/k_b T_e$, and Φ_j is given as a function of X_{pq} by Drawin. The neutral species corresponds to $j = 1$, and $j = 2$ indicates singly charged ions. The energies must be given in eV and the temperature in Kelvin. For a typical argon electron kinetic temperature found in the LSP studied here, say $T_e = 14000$ K,

and using the ground ($q=1$) and first excited ($p=2$) levels of argon neutral and first ion, the quantities in Table 1.1 are determined from Drawin and the above criterion.

Table 1.1 Critical electron number densities, n_e^*

	Neutral	Ion
g_1	1	4
g_2	3	2
E_1	0	0
E_2	11.623	13.480
X_{pq}	9.634	11.173
Φ_i	10.601	3.031
n_e^*	$3.84 \times 10^{17} \text{ cm}^{-3}$	$2.85 \times 10^{16} \text{ cm}^{-3}$

As will be shown in the results of this work, the lowest measured electron number density in the LSP is approximately $6 \times 10^{16} \text{ cm}^{-3}$, and the highest approximately $2 \times 10^{17} \text{ cm}^{-3}$. So it seems that the ions should be in Boltzmann and Saha equilibrium, but the neutrals should not. However, the above criterion assumes that there are no factors at work to destroy equilibrium other than the escape of optically thin line radiation, and that collisions between plasma particles are the only means of maintaining equilibrium. The situation is actually quite complex due to the entrapment of resonance radiation which tends to enhance equilibrium, and the presence of an external radiation field which tends to destroy equilibrium. Trapped resonance radiation reduces the overpopulation of the ground state, while external radiation produces kinetic non-equilibrium which may influence the electronic energy modes.

The effect trapping of resonance radiation has on critical electron number density is treated by Griem [1964]. He states that the critical density may be reduced by a factor of ten if the following condition is met:

$$n_1 d > 8 \times 10^{10} \left[\frac{E_2 - E_1}{f_{12}} \right] \left[\frac{T_e}{M} \right]^{\frac{1}{2}} \quad (1.16)$$

where n_1 is the population of the ground level, d is the thickness of the plasma in cm, f_{12} is the oscillator strength of the resonance transition, and M is the atomic mass number of the particle considered. For argon neutral the resonance oscillator strength is $f_{12} = 0.061$, and the ion resonance oscillator strength is $f_{12} = 0.0089$ [Wiese, et al., 1969]. Taking the plasma thickness to be 1 cm, which approximates the LSP diameter, and the argon atomic mass number to be 40, the ground state population of neutrals must be $2.8 \times 10^{16} \text{ cm}^{-3}$, and that of the ions $2.3 \times 10^{15} \text{ cm}^{-3}$ for the criterion to be satisfied. These populations are easily met in the LSP studied in this investigation.

The above discussion indicates that the resonance radiation trapped by the argon neutral particles may reduce the critical electron number density to as low as $3.84 \times 10^{16} \text{ cm}^{-3}$, which is achieved in this LSP. It may then be expected that both the ionic and neutral argon electronic systems be in Boltzmann and Saha equilibrium. This would probably be true if line radiation loss and complete trapping of resonance radiation were the only considerations, however this is rarely the case, and the above criteria will be used with caution in future discussions of Boltzmann and Saha equilibrium.

Another important nonequilibrium factor is the diffusion of charged particles to the boundaries of the plasma volume. This process directly influences the ionization equilibrium by lowering the density of charged particles. In order to compensate for the resultant influx of neutral particles, ionization must exceed recombination. Saha equilibrium can also be disturbed as a result of the escape of recombinational radiation. In this case there is a depletion in the number of free electrons which must be made up for by more intense collisional ionization. Line radiation also has an indirect effect on ionizational equilibrium. Since it is mainly excited atoms which are ionized, a decrease in the density of these atoms due to line radiation will decrease the number of ionization events and hence the density of charged particles. Similarly the diffusion of charged particles has an indirect effect on Boltzmann equilibrium. In this case

(in the absence of radiation effects) ionization outweighs recombination, thus upward collisional transitions happen more often than downward collisional transitions.

The end result of the complex interaction of equilibrating and nonequilibrating processes is that it is not reasonable to rely on analytical expressions for the critical electron number density at which LTE will hold absolutely. Furthermore, doubt is cast on the reliability of LTE diagnostic techniques, and on the values of plasma properties calculated based on an LTE plasma composition. For these reasons non-LTE diagnostic techniques are called for in laser sustained plasmas, with the outcome of the interacting plasma processes being determined directly.

1.3.3.3. Maxwellian Electron Velocity Distribution

All of the above analysis hinges on the assumption that the electron velocity distribution is Maxwellian. This can be shown to be the case in LSP's by applying a criterion given by Langdon [1980]:

$$\frac{Zv_0^2}{v_e^2} \geq 1 \quad (1.17)$$

When this inequality is satisfied, inverse bremsstrahlung absorption of laser radiation results in a non-Maxwellian velocity distribution. In this inequality Z is the ionic charge, v_0 is the peak velocity of oscillation of the electrons in the high frequency electric field, and v_e is the electron thermal velocity. The above ratio may be expressed as:

$$\frac{Zv_0^2}{v_e^2} = (4 \times 10^{-16}) \frac{ZI\lambda^2}{T_e} \quad (1.18)$$

where I is the laser irradiance in W/cm^2 , λ is the laser wavelength in microns, and T_e is the electron temperature in keV. For a singly ionized gas at 1 eV, laser irradiance of 10^6 W/cm^2 , and a wavelength of 10.6 microns, this parameter has a very small value. Therefore it can safely be concluded that the electron velocity distribution in laboratory LSP's is Maxwellian.

1.3.4. Non-Local Thermodynamic Equilibrium

The existence of LTE in the plasma greatly simplifies the analysis required to fully describe the thermodynamic state. It is for this reason that the LTE assumption has been made in most LSP investigations. Among these are the absolute continuum emission study of Welle, et al. [1987], the quasi-two dimensional model of Glumb and Krier [1986], the fully two dimensional models of Jeng and Keefer [1986] and Eguiguren [1989], and the relative line-to-continuum emission studies of Rockstroh [1986] and Chen [1988].

There has been somewhat loose justification for the LTE assumption based on electron number density considerations, but the existence of temperature and density gradients, optically thin radiation losses, diffusion of charged particles, and an intense external electric field (laser beam) lead to the current belief that LTE does not exist in laboratory LSP's, in general.

Eddy [1976] gives an excellent review of the various LTE plasma diagnostic techniques and the problems which may arise in their application to a non-LTE situation. Without an assumption of LTE, plasma diagnostics must be used which are not based on assuming the usual partitioning of energy in the plasma system.

In this study diagnostic techniques will be applied which are independent of the LTE assumption. These techniques follow those of Eddy, et al. [1988, 1989] and Cho [1988] who work mainly with electric arc driven plasmas and plasma jets, and will incorporate terminology found in their work as it has proved quite applicable to LSP diagnostics. The terminology referred to concerns the names and definitions of certain plasma temperature parameters such as upper level excitation temperature and total excitation temperature, and will be discussed later in this section.

This study incorporates both direct spectroscopic measurements and analytic solution techniques. Electron number density is determined with a hydrogen spectral line broadening measurement. The upper electronic level populations are determined from measurements of argon neutral and ion spectral line emissivities. Other relevant parameters such as electron and

heavy particle kinetic temperatures, neutral atomic number density, and the aforementioned electronic excitation temperatures, are calculated with the use of appropriate analytical expressions.

It is these analytic expressions that characterize the non-local thermodynamic equilibrium model. Common to most non-LTE thermodynamic models are the use of Boltzmann factors, an equation of state, some type of ionization equation, and possibly some additional equations such as mass, momentum and energy conservation expressions. It is the form of the ionization equation which separates one model from the next, and it is the physical system to which the model is applied that determines the appropriate form of this equation.

The ionization equation is an expression of the law of mass action for an ionization reaction. It is known as the Saha equation when there is a single temperature appearing in the expression, which implies equilibrium in the system. When various non-equilibrium effects are present, such as non-equivalence of the electron and heavy particle kinetic temperatures, or non-equivalence of the electronic excitation temperatures and the electron kinetic temperature, then the ionization equation takes on different forms depending on the types of non-equilibrium to be considered. The most general form of the law of mass action describing the relationship among plasma particle number densities for an ionization reaction is due to Potapov [1966], and is written as:

$$\prod_j n_j^{v_j k_b T_{jt}} = e^{-\alpha} e^{-\sum_j v_j E_{0j}} \prod_j \left[\left(\frac{2\pi m_j k_b T_{jt}}{h^2} \right)^{v_j (3/2) k_b T_{jt}} \prod_{k>1} Z_{jk}^{v_j k_b T_{jk}} \right] \quad (1.19)$$

where v_j is the stoichiometric coefficient of species j in the ionization reaction, T_{jt} is the kinetic temperature of species j , E_{0j} is the zero-point energy of species j , T_{jk} is the temperature used in the calculation of Z_{jk} , the partition function for mode k of species j , and α is the chemical affinity. The chemical affinity is zero for a system in chemical equilibrium.

For the ionization of a monatomic gas in chemical equilibrium, (1.19) reduces to:

$$n_e \left(\frac{n_i}{n_a} \right) \frac{T_g}{T_e} = 2 \frac{Z_{\text{exi}} \left(\frac{T_{\text{exi}}}{T_e} \right)}{Z_{\text{exa}} \left(\frac{T_{\text{exa}}}{T_e} \right)} \left(\frac{2\pi m_e k_b T_e}{h^2} \right)^{(3/2)} \exp \left(\frac{-E_{\text{la}}}{k_b T_e} \right) \quad (1.20)$$

where the kinetic temperatures of the neutral atoms and ions are assumed equal to a gas temperature, T_g , and the total electronic excitation temperatures, T_{exa} for the neutrals and T_{exi} for the ions, are used in the calculation the electronic partition functions Z_{exa} and Z_{exi} , respectively. E_{la} is the lowered ionization potential of the neutral atoms.

The above ionization equation is the one used throughout this investigation. Its main features are that it allows for: (1) kinetic non-equilibrium between the electron and the heavy particles, $T_e \neq T_g$, (2) electronic excitation non-equilibrium between the electrons and the neutral atoms, $T_e \neq T_{\text{exa}}$, and (3) between the electrons and the ions, $T_e \neq T_{\text{exi}}$. In addition, the thermodynamic model employed allows for non-equilibrium within the electronic excitation modes of the neutrals and ions. Upper level excitation temperatures, $T_{\text{ex}\beta,a}$ and $T_{\text{ex}\beta,i}$ for the neutrals and ions, respectively, are permitted to differ from the total excitation temperatures used in the partition function calculations.

On the abscissa of a Boltzmann plot is the energy of the excited levels of an atomic system, usually scaled by Boltzmann's constant to arrive at units of temperature (Kelvin). On the ordinate is the natural logarithm of the population of an excited level scaled by the degeneracy of that level. The natural logarithm results in a linear plot extending from the ground level to the ionization limit if the system considered is in Boltzmann equilibrium. The slope of the linear plot is then equal to the negative inverse of the Boltzmann temperature describing the distribution of level populations.

Not all atomic systems are in complete Boltzmann equilibrium, but it is still quite useful to define some non-equilibrium temperatures in the context of a Boltzmann plot. The Boltzmann plot in Figure 1.6 helps in understanding the meaning of these temperatures, and their

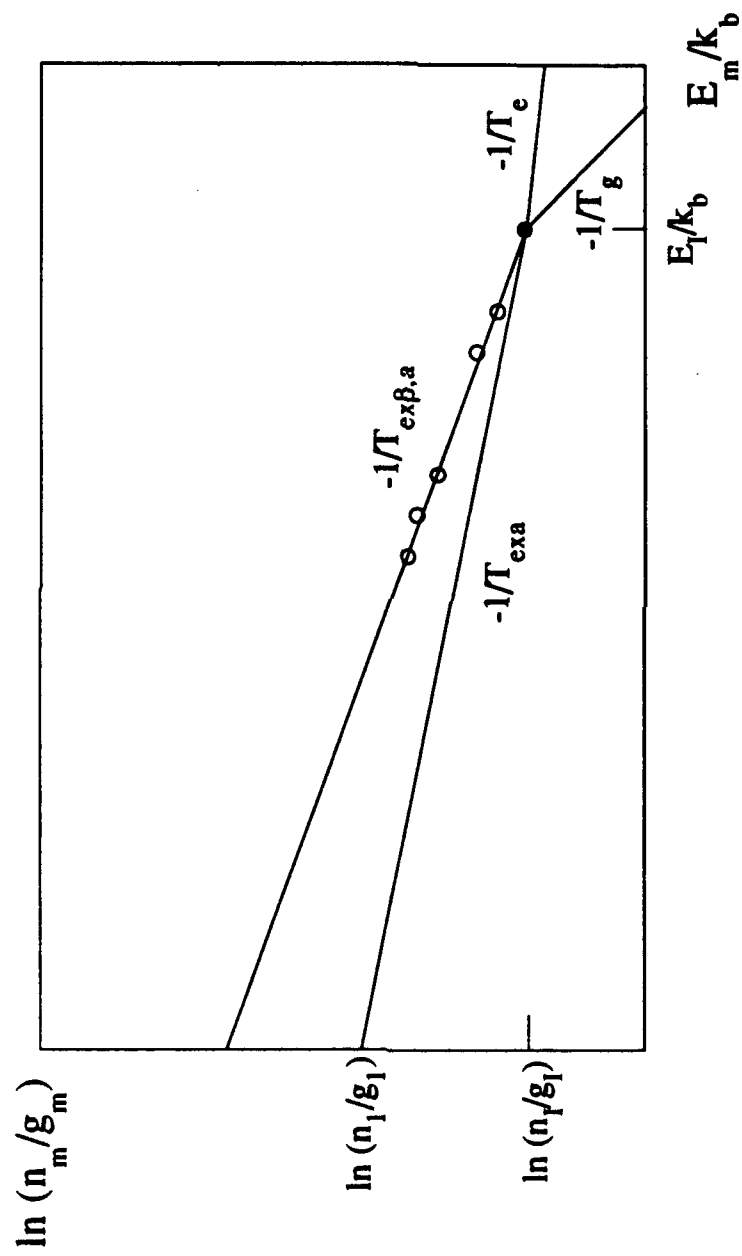


Figure 1.6 Example Boltzmann plot showing the relationship between the various non-LTE temperatures.

relationships to each other. There are four temperatures shown in the figure, $T_{\text{ex}\beta,a}$, $T_{\text{ex}a}$, T_e , and T_g . There are called the upper level excitation temperature, total excitation temperature, electron kinetic temperature, and heavy particle kinetic temperature, respectively. This figure corresponds to the neutral particle system, but a very similar plot can be drawn for the ion system with $T_{\text{ex}\beta,i}$ and $T_{\text{ex}i}$ appearing instead of $T_{\text{ex}\beta,a}$ and $T_{\text{ex}a}$.

The upper level excitation temperature only applies to the populations of energy levels above some cutoff level at which collisional transitions between levels become dominant over radiative transitions. Several points are drawn in Figure 1.6 to represent the measured populations of some of the upper levels used to determine $T_{\text{ex}\beta,a}$. If the slope corresponding to $T_{\text{ex}\beta,a}$ is extrapolated to the lowered ionization limit, the population of the effective highest excited level can be found. The total excitation temperature relates this population to the population of the ground state. The ground state shown in the figure is underpopulated with respect to the upper excited levels, resulting in $T_{\text{ex}a} > T_{\text{ex}\beta,a}$ for this example. The slopes corresponding to the kinetic temperatures are shown on the plot as well, although the endpoint locations are somewhat arbitrary.

1.4. LITERATURE REVIEW

To date we have found no record in the literature of non-LTE diagnostics performed on continuously maintained laser produced plasmas. However, there are several reports of LSP diagnostics performed which make claims concerning LTE.

Generalov et al. [1972] used Stark broadening of the $\text{H}\beta$ line to calculate electron number density in argon and xenon LSP's, and the Saha equation was used to calculate temperature assuming equilibrium. An approximate calculation of the maximum deviation of the electron temperature from the heavy particle temperature resulted in only a 6% deviation for argon based on 100 W input laser power. The conclusion was that the LSP is in LTE to a first approximation. In that experiment, however, no attempt was made to determine the excitation temperature or to resolve the electron number density and temperature spatially. In addition,

100 W is not much laser power and might not have produced a high enough flux to generate a significant kinetic temperature deviation.

In another study of air LSP's Keefer et al. [1975] used the Fowler-Milne and absolute line intensity techniques to measure plasma temperature. Both of these techniques require that LTE exist to be accurate, and although the results are in agreement internally, LTE cannot be concluded from this experiment. Keefer does state that the presence of anomalous excited rotational structures in the molecular nitrogen ion found near the plasma boundaries may be due to non-LTE processes.

In a study of xenon LSP's Cremers et al. [1985] measured electron number density via Stark broadening and temperature via the Saha equation (assuming equilibrium). A Boltzmann plot was made after adding 66% krypton and using the krypton relative line intensities. The Boltzmann temperature agreed well with the Saha temperature, but as stated by the authors, "The quality is not sufficient to indicate positively that the (Boltzmann) plot is linear." This along with no Abel inversion of the data, the comparison of two differently composed plasmas, and the assumption of equilibrium in the use of the Saha equation prevent a confirmation of LTE in these LSP's.

There are numerous reported investigations, both theoretical and experimental, of pulsed laser produced plasmas, and several of these are reviewed in what follows. The enormous power of most laser pulses and the transient nature of the plasmas in these articles reduce the applicability of their results to this investigation. The most recent work done on pulsed laser sustained pure argon plasmas for laser propulsion was done by Keefer, et al. [1990]. They used several techniques to calculate temperature, including ion-neutral ratios, ion Boltzmann factors, and absolute ion line emission. The results indicated that the various means of calculating temperature typically agreed to within the experimental uncertainty. However, the lines used in the 370 nm - 420 nm range were severely overlapping, and plasma homogeneity was assumed so no Abel inversion was performed. The assumption of homogeneity is probably not valid in this extremely high power, highly transient LSP, and the smoothing

effect of using line-of-sight rather than spatially resolved emission intensity probably aided the agreement among the temperature determination methods. No determination of kinetic temperatures was performed either. In general it is thought that LTE does not exist in high power pulsed plasmas, except at super high pressure [Rachman and Bassani, 1969].

Tonon, et al. [1971] concluded that electron and ion kinetic temperatures are the same in a plasma produced by a giant laser pulse on a solid target. This conclusion is based on a best fit of experimental data to theoretical analysis. It would be interesting to know what effect the ablated solid had on the results of their work. Vorob'ev and Khomkin [1984] performed a theoretical analysis of a continuous laser produced plasma near a metal surface. It was found that ionizational nonequilibrium existed for surface fluxes on the order of 10^6 W/cm^2 . Again, the presence of a solid ablate poses an interesting question concerning LSP thermodynamics.

A much larger amount of research has been done on plasmas produced in an electric arc. There is general agreement that complete LTE does not exist in electric arc plasmas at pressures less than or equal to one atmosphere. Above one atmosphere conclusions vary as to the pressure at which LTE can be expected. Farmer and Haddad [1984] state that above 1.4 atm. LTE existed in an argon arc based on evidence of a constant off-axis maximum in the emission coefficient. Bober and Tankin [1970] suggest that an argon arc will not be in LTE until a pressure of 3 atm. This conclusion comes from an extrapolation of measured transition probabilities of an ArI line to a pressure at which the probability becomes constant, indicating LTE. Eddy and Sedghinasab [1988] show that in an argon arc with 1 % hydrogen the electron and heavy particle temperatures converge above 5 bar, but the upper level excitation temperature of argon atoms is still well above the electron temperature even at 10 bar. This excitation nonequilibrium at high pressure was attributed to inaccurate spontaneous emission coefficient data, and corrections were calculated for numerous argon lines.

Other investigations of electric arc plasmas with similar conclusions relating to LTE can be found in the literature. Included are a study of LTE in an argon plasma jet [Freeman, 1984], nonequilibrium in an argon arc [Giannaris and Incropera, 1971], non-equilibrium in a confined

arc [Kruger, 1970], and diffusion and non-equilibrium populations in noble gas arcs [Uhlenbusch and Fischer, 1971].

2. LSP EMISSION SPECTROSCOPY

This chapter proceeds with a description of the laser sustained plasma experimental facility including the laser, laser absorption chamber, and some of the significant support equipment. Also included is a description of the spectroscopic data collection optics and equipment, and a discussion of the argon and hydrogen lines chosen for study.

2.1. EXPERIMENTAL FACILITY

2.1.1. Laser and LSP Flow Facility

2.1.1.1. Laser and Support Equipment

A 10 kW Avco-Everett HPL-10 continuous wave CO₂ laser with an output wavelength of 10.6 microns is used in this investigation. The unstable resonator output profile resembles a TEM 01* modeshape. This so-called donut mode produces an annular beam with a 74 mm o.d. and a 50 mm i.d. The optics are adjusted so that the power distribution is uniform around the annulus, and near Gaussian across the annulus. The laser is operated and maintained by Justin Koch, a staff member of the University's Materials Engineering Research Laboratory.

The laser absorption chamber is mounted on a test stand across the laboratory from the laser. Figure 2.1 is a schematic of the laser lab layout, showing the relative locations of the laser, laser control room, absorption chamber test stand, and spectroscopic experiment room. The beam propagates freely across the lab to the test stand, with the metal working optics and equipment moved out of the beam path during LSP experiments.

Figure 2.2 is a schematic of the absorption chamber test stand. It is constructed mainly of Unistrut components and is mobile when the wheels are lowered to the floor. During experiments the test stand is accurately positioned using two steel rods threaded into guide holes set into the concrete floor. The stand supports the laser absorption chamber, all of the beam steering optics, and much auxiliary diagnostic equipment. The original test stand and absorption chamber design was a major part of the early work on this project [Bender, 1985],

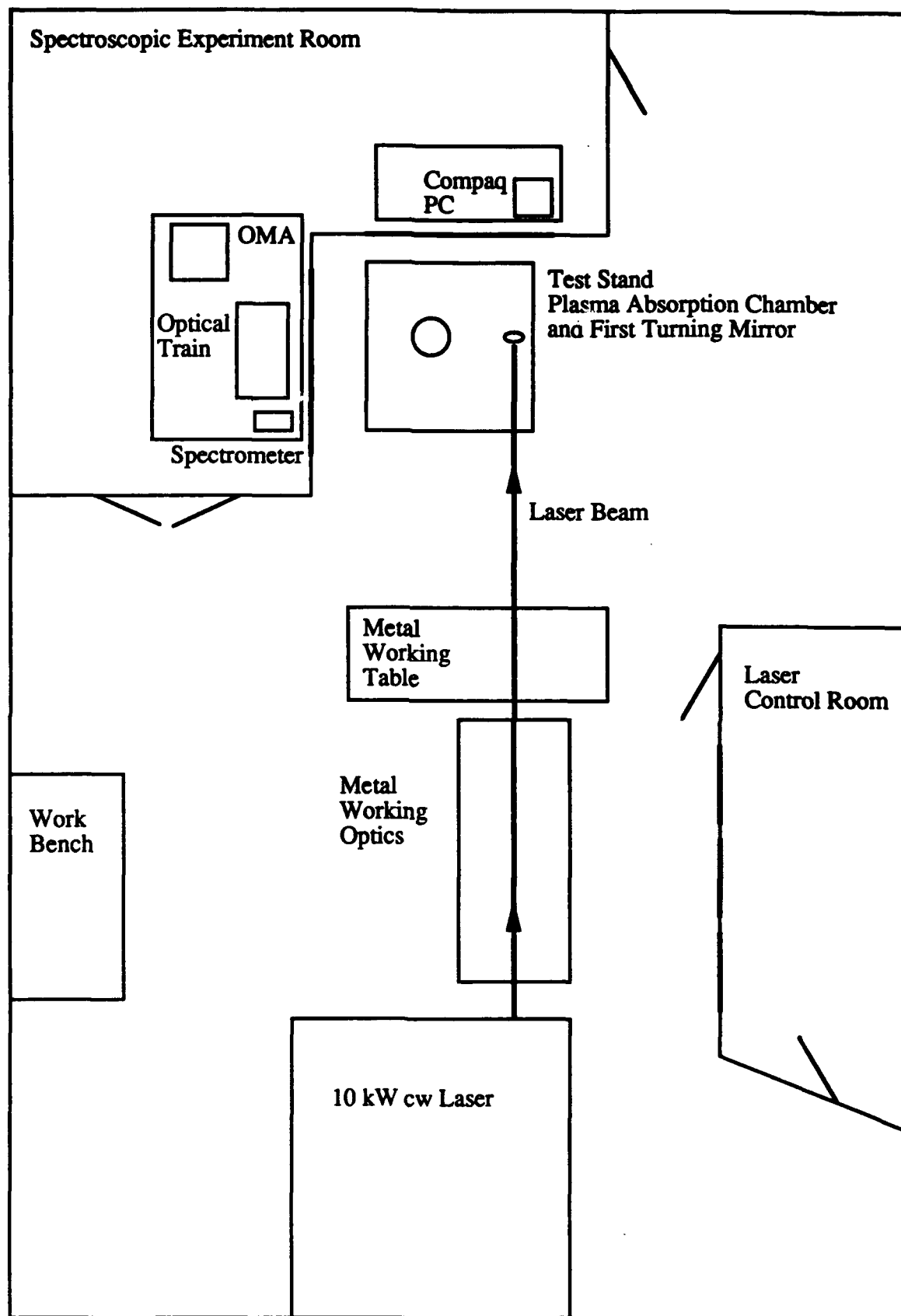


Figure 2.1 Schematic of the Laser Sustained Plasma Experimental Facility

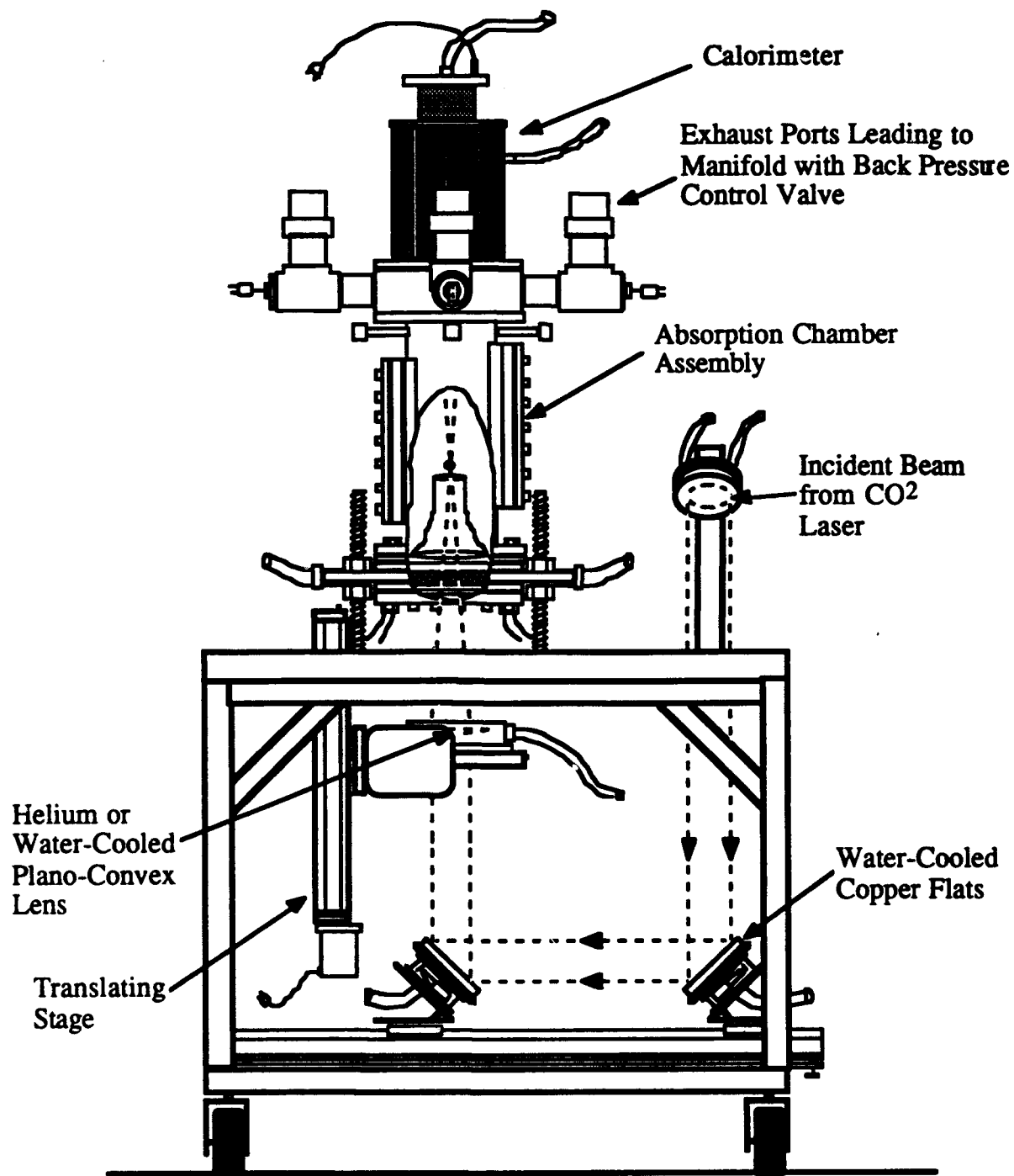


Figure 2.2 Schematic of the test stand highlighting positions of turning mirrors, lens, absorption chamber, exhaust ports, and calorimeter [Schwartz, 1989].

with subsequent improvements implemented as needed: on-axis focusing optics (NaCl lens) and exhaust port thermocouple measurements [McMillin, 1987], inlet flow straightening and quartz tube accelerator [Zerkle, 1988], zinc selenide optics and high flowrate exhaust system [Mertogul, 1989], precision dual plasma optical mounts and hydrogen safety features [Schwartz, 1989].

The direction of beam propagation is into the page in Figure 2.2. The beam steering optics consist of three water cooled flat copper turning mirrors, and a zinc selenide (ZnSe) focusing lens. There is also a ZnSe inlet window mounted at the bottom of the absorption chamber. ZnSe optics are used because they exhibit low absorption of infrared radiation, are very durable, have a high thermal conductivity and rupture modulus, and are easily cleaned with acetone. The lens has a focal length of 305 mm, resulting in an f/4.1 beam focusing geometry. All the ZnSe optics are anti-reflection coated for 10.6 μm radiation at normal incidence. Reflection losses are quoted at less than 1 % total for both surfaces.

The lens holder is also water cooled and is mounted in a two-axis gimbal on a vertically traversing stage. The stage is actuated by a stepper motor operated under remote control. By adjusting the turning mirrors, lens attitude, and lens vertical position the beam focus point can be precisely located within the absorption chamber for reliable plasma initiation.

A schematic of the gas delivery system is shown in Figure 2.3. The gas is brought in from high pressure tanks stored outside the lab via long flexible hose. There are two separate flow lines, one for argon and one for hydrogen. Each gas supply has its own flowmeter within the spectroscopic experiment room so that varying mixtures can be easily obtained. The argon flowmeter is a Brooks model 1020 capable of providing 25 g/s at a back pressure of 110 psig. The hydrogen flowmeter is a Brooks model 1355 capable of providing 120 mg/s at a back pressure of 15 psig. The gases are mixed in a plenum out on the test stand before entering the laser absorption chamber. A sintered steel filter is used to straighten the highly turbulent inlet flow before it enters the converging quartz tube used to accelerate the flow to the required mass fluxes. The filter and quartz tube can be seen in Figure 2.2.

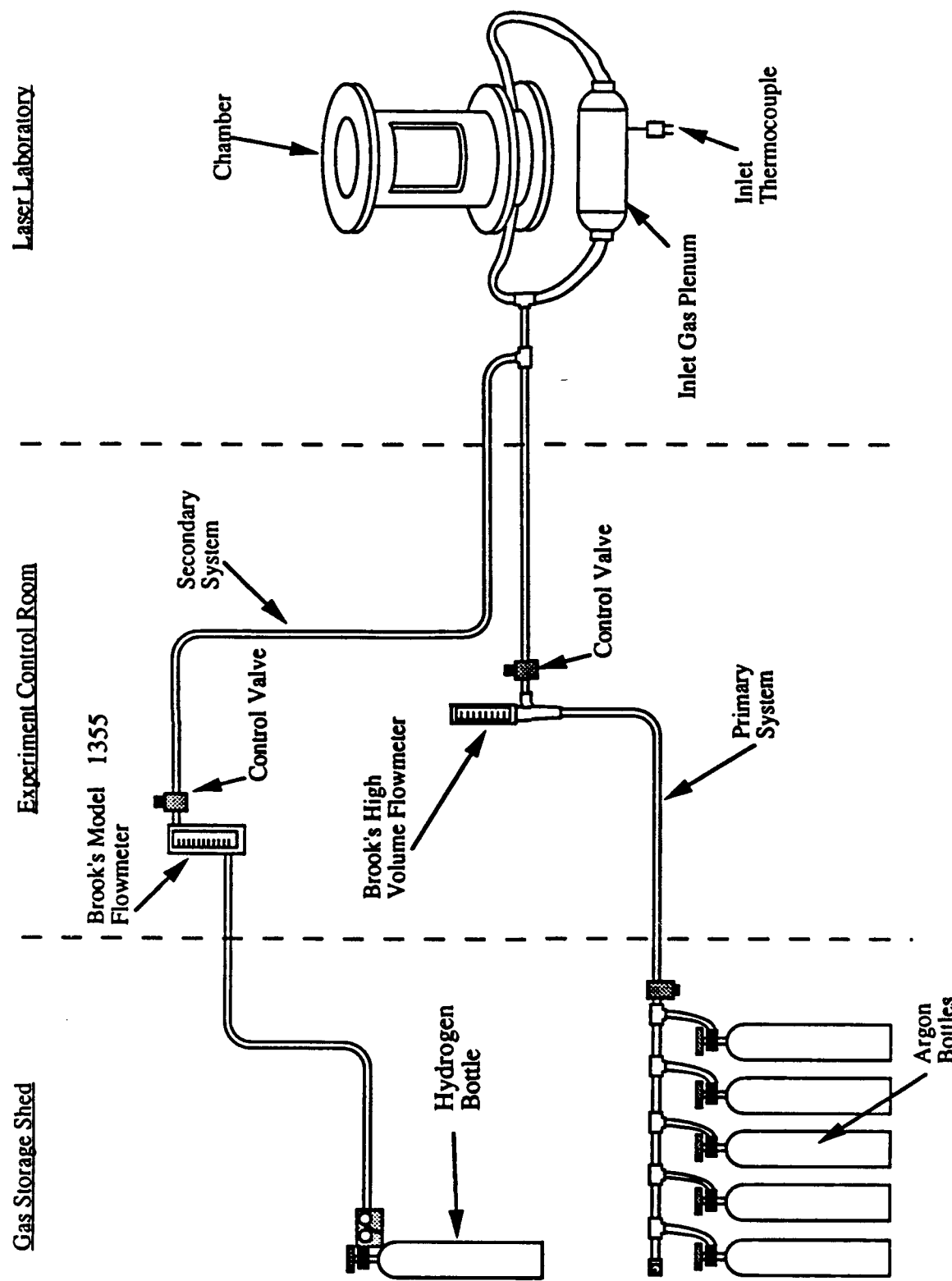


Figure 2.3 Schematic of the gas supply system used to mix trace hydrogen with the primary argon flow.

After the gas has passed through the absorption chamber it is exhausted through four chamber exit ports. These are then manifolded into a main exhaust pipe which can be constricted to produce elevated chamber pressures. However, all experiments in this investigation are performed at one atmosphere chamber pressure. In each of the four exhaust ports is a thermocouple used to measure the mass averaged temperature of the exhaust gas. There is also a thermocouple located near the inlet plenum so that the bulk temperature rise of the gas through the absorption chamber can be determined.

An important component to the gas flow system is the safety system required to handle hydrogen flows. It consists mainly of hydrogen detectors placed strategically around the laboratory and pressure transducers at a number of points in the flow system. If a detector or transducer should produce an alarm signal, a series of system shutdown events takes place including the shutdown of the laser and the hydrogen gas supply valve. An inert argon gas flow is also initiated in order to purge the entire gas flow system. A more detailed description of this safety system including schematic drawings can be found elsewhere [Schwartz, 1989; Mertogul, 1992].

2.1.1.2. Laser Absorption Chamber

The central component of the test stand is the laser absorption chamber. It consists of an 18 inch long, 5 inch i.d., 1/4 inch thick stainless steel tube with numerous flanges and ports bolted or welded to it. The large diameter limits the flow velocity for the range of mass flow rates producible with this facility. The placement of the converging quartz tube inside the absorption chamber accelerates the inlet flow, allowing for higher incident flow velocities for the same range of mass flow rates.

Referring to Figure 2.4, the important features of the laser absorption chamber assembly are the laser inlet window flange and retainer, the gas inlet assembly which holds the sintered steel filter and is located just above the inlet window, the side window flanges and retainer, the exhaust port flange and assembly, and the copper cone calorimeter. The laser inlet window

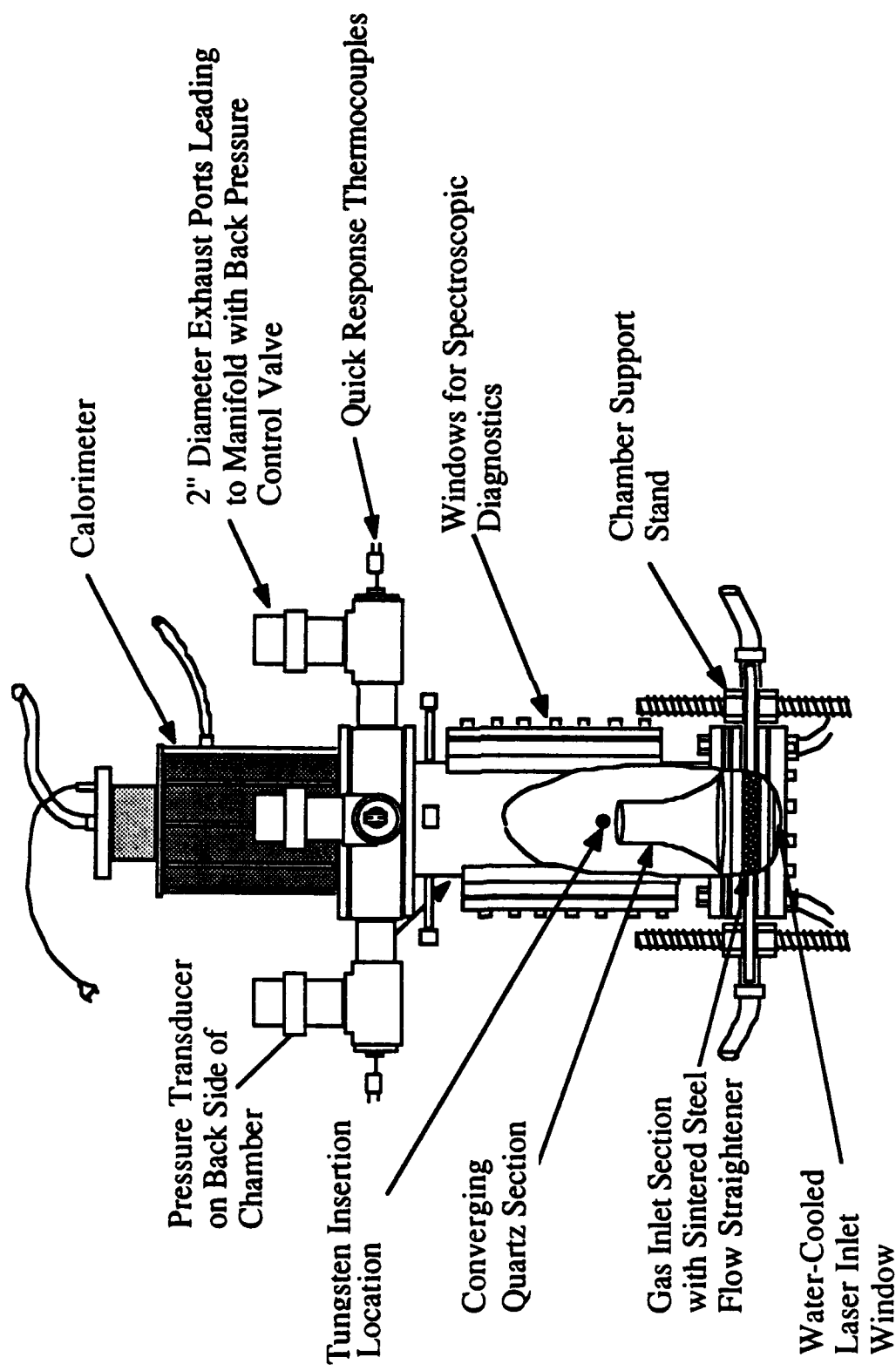


Figure 2.4 Detailed schematic of the laser absorption chamber including a cutaway view of the sintered steel flow straightener and quartz tube [Schwartz, 1989].

is water cooled so that the ZnSe window undergoes very little thermal stress. The side window mounts can hold quartz windows for spectroscopic access, Pyrex windows for general plasma viewing, or aluminum blanks to block out all plasma emission. The exhaust port assembly is insulated so that little heat is lost from the exhaust gas while on its way to the thermocouples. The calorimeter is water cooled and calibrated for laser power input for the purpose of determining the amount of laser power transmitted by the plasma.

Not shown in the figure is the solenoid actuated tungsten rod insertion device. By remote command a 4 mm diameter tungsten rod ground flat on one side is inserted into the laser focal volume. Laser heating of the rod provides the necessary conditions for gas breakdown and plasma initiation. The rod is retracted as soon as the plasma is stabilized (the whole process takes milliseconds).

Also not shown in Figure 2.4 are the pressure transducer mounted through the absorption chamber wall and the thermocouple imbedded in the wall near the plasma. These signals along with the inlet and exhaust thermocouple signals and the calorimeter signal are monitored and recorded with a Fluke model 2240A data acquisition system. These data are saved to a Macintosh personal computer for later evaluation. Gas temperature rise through the plasma is needed for LSP thermal conversion efficiency calculation, as is the transmitted laser power for global LSP absorption calculation.

2.1.2. Spectroscopic Equipment

2.1.2.1. LSP Emission Collection Optics

Because axial as well as radial spectroscopic measurements are made in this investigation, special attention is paid to the collection optics. The spectrometer and detector combination is capable of gathering both spectral and radial information simultaneously, but axial measurements must be made sequentially by traversing the collection optics vertically through the LSP domain. The difficulty in designing an optical system like this is to maintain a focused

image on the spectrometer entrance slit while the overall optical path length changes as the optics are traversed vertically .

Figure 2.5 is a two-view schematic showing the relative positions of the plasma and laser absorption chamber, the collection optics, and the spectrometer. The first turning mirror is a 4 inch aluminum flat with a silicon monoxide overcoat for durability. The first lens is a 120 mm focal length, 2 inch diameter achromat to which a second achromat of 65 mm focal length and 25 mm diameter is matched so that collimated light results as output from the lens combination. This matching permits these first three optical components to be traversed vertically without altering the final image location.

The second coated aluminum mirror accepts the collimated light and turns the signal horizontal to the optical table and flips the plasma image to horizontal as well. The third and last achromatic lens images the plasma onto the vertically oriented spectrometer entrance slit. With a 120 mm focal length and 24 mm diameter, this last lens automatically stops down the light so that f/5 focusing results, thus matching the spectrometer f-number for all wavelengths studied. All lenses are achromatic so that emission lines widely separated in the visible spectrum are all focused to the same location.

The first lens is approximately 1.11 meters from the plasma centerline, although not on a straight line due to the first turning mirror. With the first lens having a focal length of 120 mm an intermediate plasma image is formed 134.5 mm below that lens. This is calculated using the well known lens formula:

$$\frac{1}{f.l.} = \frac{1}{x_o} + \frac{1}{x_i} \quad (2.1)$$

where f.l. is focal length, x_o is the distance from the object to the lens, and x_i is the distance from the lens to the image. If $x_o = 1110$ mm and f.l. = 120 mm, then $x_i = 134.5$ mm. This results in an intermediate magnification of:

$$M_1 = \frac{x_i}{x_o} = (8.253)^{-1} \quad (2.2)$$

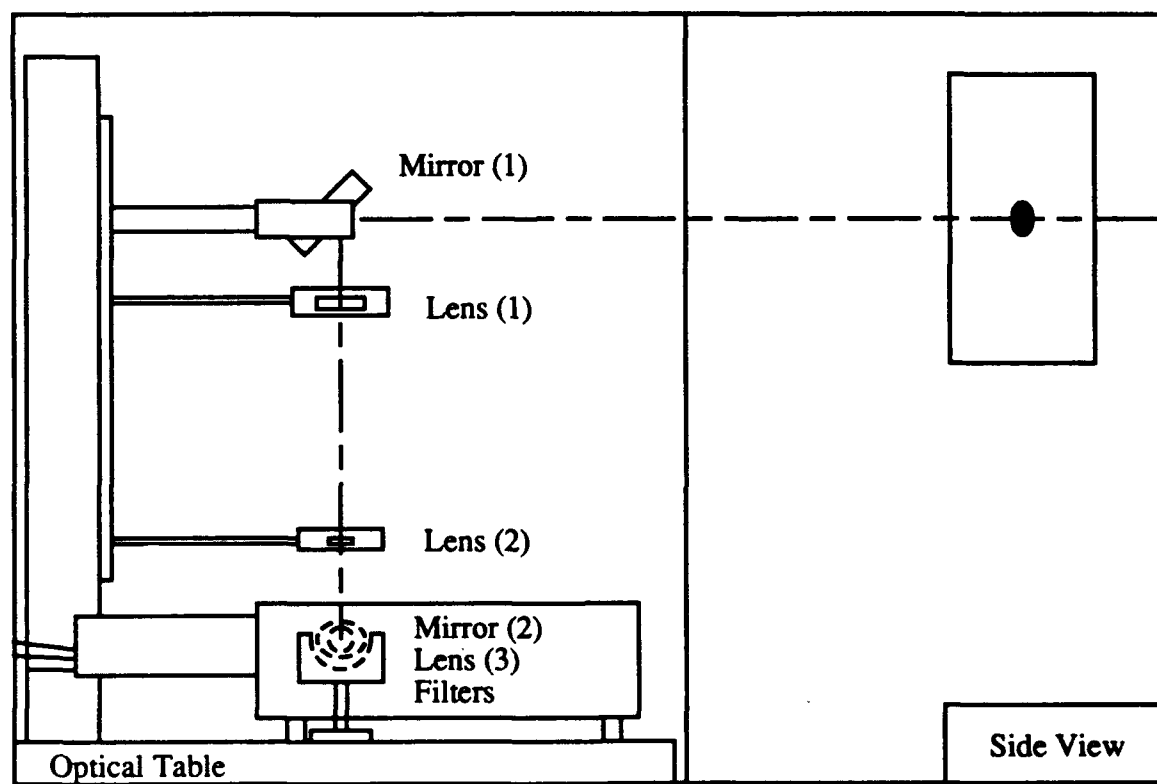
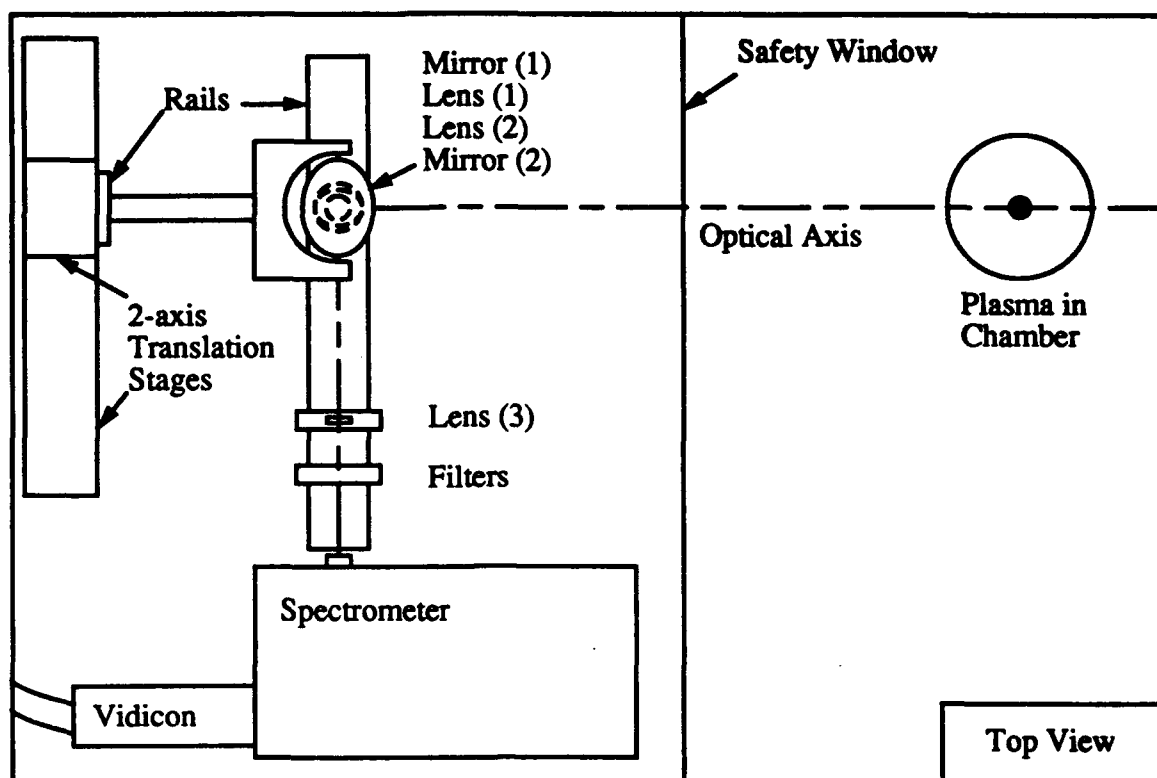


Figure 2.5 Schematic of the spectroscopic optical system and the plasma absorption chamber. Two views showing the top and side.

The second lens is positioned such that the first intermediate plasma image is one focal length, or 65 mm from the lens. Considering the first intermediate image to be the object at a distance $x_0 = f.l.$ from the second lens, a second intermediate image is formed at an infinite distance from the second lens, i.e. the signal is collimated. This collimated signal is turned by the second mirror and the third lens forms the final image at a distance of one focal length, or 120 mm. The effective magnification of the intermediate image going to the final image is then:

$$M_2 = \frac{120}{65} = 1.846 \quad (2.3)$$

resulting in an overall magnification of:

$$M = M_1 M_2 = (4.47)^{-1} \quad (2.4)$$

Thus an original plasma object 12 mm in width is imaged onto the spectrometer slit with a height of approximately 2.7 mm. This is smaller than is necessary to fit comfortably onto the 8 mm high entrance slit, but is the best possible result due to the necessarily large distance between the plasma and the first lens.

Neutral density filters are always required in this experiment and are placed in the optical path between the last lens and the spectrometer. Four filters of varying density are always used so that the focus location is not affected by refraction through the filters. In some cases filters of zero nominal density are used simply to account for diffraction.

Figures 2.6 and 2.7 are photographs of the optical system. A view looking towards the laser absorption chamber from inside the spectroscopic experiment room is shown in Figure 2.6. The spectrometer can be seen in the lower right hand corner of the photograph. In Figure 2.7 the laser absorption chamber is to the left and not seen in the photograph. The three movable optics are all mounted onto a vertical translation stage actuated by a remotely controlled stepper motor. The entire vertical assembly is mounted onto a horizontal stage with

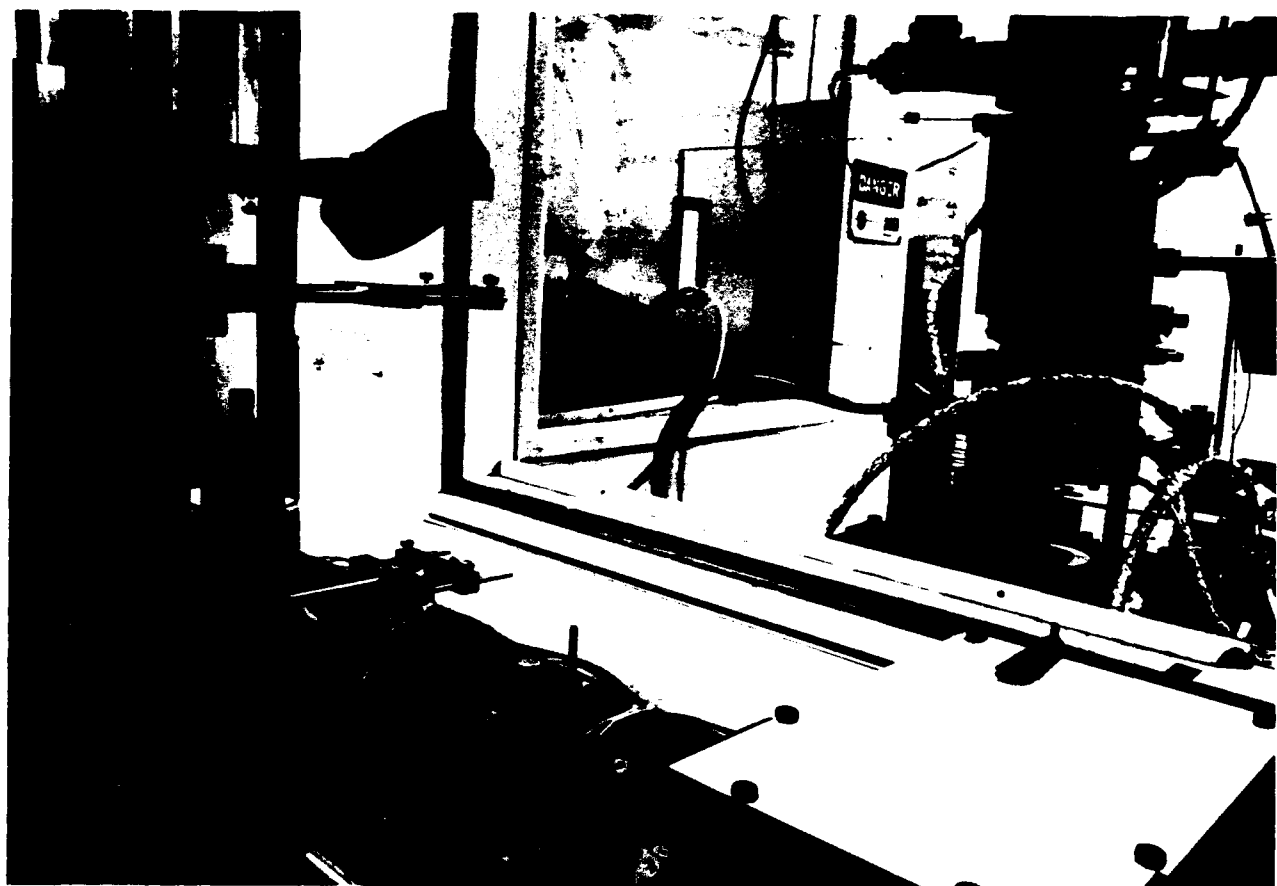


Figure 2.6 Photograph of LSP emission collection optics. The LSP absorption chamber is shown in the background, outside of the spectroscopic experiment room.



Figure 2.7 Photograph of LSP emission collection optics. The spectrometer can be seen in this view, but the LSP absorption chamber is out of the picture to the left.

its own stepper motor. This stage is used to locate the optical axis laterally onto the plasma centerline. This is done at the beginning of the experiment and need not be repeated.

This optical layout is an improvement over past spectroscopic efforts associated with this project [Rockstroh, 1986; Chen, 1988]. The original system had the spectrometer and collection optics both mounted onto the vertical translation stage and the whole system moved incrementally up or down. This lead to inaccuracies due to the wobbling of the excessively heavy assembly and slippage along the vertical translation stage lead screw. It was difficult to repeat experiments at a previous axial location, or to return to a known datum to begin a new experiment. In addition, the single collection lens suffered chromatic aberration. With the spectrometer now resting on the optical table and translating only the imaging optics, much of the difficulty in maintaining proper alignment and a consistent vertical datum is eliminated.

2.1.2.2. Spectrometer and Vidicon Detector

An Instruments S.A., Inc. HR-320 (320 mm focal length) coma corrected Czerny-Turner configuration spectrometer is used in this investigation. The f-number of this spectrometer is close to 5 over the entire range of wavelengths studied and is closely matched by the focusing geometry of the collection optics. A 1200 g/mm holographic diffraction grating is currently installed in the spectrometer, providing both high resolution and a bandpass large enough for these experiments. The system is operated in first order and the grating is blazed at 330 nm. The entrance slit of the spectrometer is 8 mm high and 0.025 mm wide. This results in an axial spatial resolution of 0.11 mm given the external magnification of $(4.47)^{-1}$.

A vidicon detector is mounted to the spectrometer housing at the exit focal plane. The two-dimensional array measures 500 pixels in the spectral dimension, and 512 pixels in the spatial direction. Because the plasma image is turned horizontal by the collection optics, the vertical entrance slit of the spectrometer resolves lateral position in the LSP. Vidicon control software allows pixel grouping, and in this experiment five rows of pixels are grouped to

represent a given lateral location. With each pixel measuring 25 microns in size, and external magnification being 4.47 (going backwards to plasma object), lateral spatial resolution is:

$$(5 \text{ pixels}) \times (.025 \text{ mm/pixel}) \times (4.47) = 0.5588 \text{ mm.} \quad (2.5)$$

The linear dispersion is nominally 2.2 nm/mm at approximately 550 nm for this grating-spectrometer combination. The actual spectral resolution of the vidicon detector array is determined more precisely for each wavelength of interest by scanning the emission of well characterized wavelength standard lamps. Spectral resolution ranges from 0.55 Å to 0.63 Å per pixel over the emission lines measured in this experiment.

The detector is calibrated for absolute spectral radiance by comparing plasma emission to the emission of an Optronic Laboratories, Inc. model 453-1 calibrated source of spectral radiance. This calibration source consists of a quartz halogen reflectorized lamp whose output is reflected into a six inch diameter integrating sphere. The sphere coating is highly reflective and diffuse, producing a very uniform radiance source over a 1 1/8 inch diameter region at the exit port (not directly illuminated by the lamp). Such a large calibration source is required for this experiment because of the need to calibrate the large detector area illuminated by plasma emission.

The detector is an EG&G PARC model 1254 intensified vidicon array. It is controlled and scanned by a EG&G PARC model 1216 detector controller, which is in turn controlled by an EG&G PARC model 1460 Optical Multichannel Analyzer (OMA III) console. More specifically, the 1216 detector controller accepts the scanning code from the 1460 console and drives the vidicon scanning sequence. It then receives and digitizes the signal from the vidicon and sends it to the 1460 console for display and storage.

A photograph of this equipment is shown in Figure 2.8. Also seen in this photograph are the Tandy computer and Velmex 8300 controller used for the programming and remote control



Figure 2.8 Photograph of the Optical Multichannel Analyzer (foreground) and stepper motor controller. The LSP emission collection optics and vidicon detector cables can be partly seen in the background.

of the three stepper motors used in this experiment. The cables connected to the end of the vidicon detector are just visible to the right of the motor controller equipment.

The EG&G PARC OMA III system is flexible and powerful in its ability to take spectroscopic data. The vidicon software executed on the 1460 console allows user friendly specification of scanning parameters such as spectral and spatial range, spatial resolution (to the limit of a single pixel), and pixel integration time. Whole frames can be summed sequentially in time during a single experiment for improved signal to noise ratio. OMA III software also supports plotting routines and data manipulation. This is very useful during preliminary studies aimed at determining useful emission lines or the spatial extent of emission.

2.2. EMISSION LINES

2.2.1. Argon

In this experiment both neutral and ionic argon line emissions are measured. The purpose is to determine as accurately as possible the absolute population of the upper level of each line transition. With this information upper level excitation temperature can be determined for both the neutral and ionic systems, as well as the population of the effective highest excited state. In addition, LTE analysis can be applied to each line for comparison to the non-LTE analysis undertaken in this investigation.

There are several criteria involved in the selection of argon emission lines to be studied. Spectral isolation from other emission structures, strong emission combined with weak self-absorption, and reliable spontaneous emission coefficient data are all desirable emission line qualities. In addition the lines chosen must have well spaced upper level energies so that meaningful Boltzmann plots may be drawn.

It is very difficult to match all the above criteria when considering even just two well spaced emission lines. The lines chosen for this experiment represent the most equitable compromise possible for the emission signature of the laser sustained plasma studied.

The selection procedure is as follows. For each system (neutral or ionic) a high energy line and a low energy line must be chosen. Within the high or low energy range, only lines with relatively well known spontaneous emission coefficients are considered ($\pm 25\%$ uncertainty or better on the NBS scale [Wiese, et al., 1969]). From preliminary plasma studies, emission lines strong enough to be easily measured are determined, as well as lines which appear to be isolated from other lines. Tabulated argon spectra are then checked to make sure no hidden interference exist in the lines remaining under consideration [Weise, et al., 1969]. Strength of self-absorption is then checked using oscillator strength considerations, and the lines most free of this drawback are chosen for study.

Because the collection optics vertically traverse the plasma in this experiment, the use of a stationary concave back mirror to correct for self-absorption cannot be used. A more complicated system in which the back mirror traverses in tandem with the collection optics could be employed in future studies, but cannot be made possible for this experiment. Minimizing the effect of self-absorption through the judicious choice of lines is currently the most practical approach.

Table 2.1 contains the pertinent information on the argon lines chosen for study. The spontaneous emission coefficients shown are not the NBS values, in general. Updated values for the neutral lines are taken from more recent literature considering the effects of non-LTE on measured transition probabilities [Sedghinasab, 1987]. The ion data are those of Olsen [1963] and fall within the stated uncertainty of the NBS values.

2.2.2. Hydrogen

The theory of line broadening by the Stark effect can be used to find electron number density independent of an assumption of LTE [Griem, 1974; p.227]. In this experiment the entire emission profile of the hydrogen Balmer series alpha line (H_{α}) is measured for the purpose of determining electron number density.

Table 2.1 Spectroscopic Data

λ (Å)	species	E_m (cm ⁻¹) - upper	gm	A_{mn} (10 ⁶ s ⁻¹)	A_{mn} (10 ⁶ s ⁻¹) (NBS)
7147	neutral	107132	3	0.462 \pm 4%	0.650 \pm 25%
6752	neutral	118907	5	3.015 \pm 10%	2.01 \pm 25%
4658	ionic	159706	2	69.5 \pm 10%	81.0 \pm 25%
4610	ionic	170530	8	90.6 \pm 5%	91.0 \pm 25%

Hydrogen is introduced into the primary argon flow in an amount small enough to have no effect on the plasma thermodynamic state. In this experiment 7 mg/s of hydrogen are added to 25 g/s of argon, which corresponds to about 1/2 % hydrogen by volume. The strength of argon emission lines measured with and without this trace hydrogen flow are the same, thus justifying the addition of this diagnostic seed.

The upper limit to the amount of hydrogen which can be added without affecting the plasma thermodynamic state is not known precisely. However, it is known that in order to produce the hydrogen Balmer series beta line (H β) in a strength great enough for Stark broadening evaluation, the effect on the argon line strength is significant. In general it is better to use H β for electron number density determination because better accuracy can be achieved [Griem, 1974; p.170-1].

In the plasma studied here, there are many argon ion lines overlaying H β . The usual procedure is to perform two experiments, one with the hydrogen seed and one without. The spectrum measured without hydrogen must then be subtracted from the spectrum with hydrogen to remove the interfering argon ion lines. This procedure results in a net H β line with many 'holes' where the argon ion lines were located when applied to the LSP in this study. The addition of sufficient hydrogen to produce reasonably strong H β cools the plasma enough to significantly diminish the argon ion emission, thus altering the original plasma thermodynamic state.

H_{α} is not only free of the above difficulty, but also has theoretical profile data to higher electron number densities than does H_{β} . The tables used in this experiment [Vidal, et al., 1973] extend only to an electron number density of $1 \times 10^{17} \text{ cm}^{-3}$ for H_{β} , but go up to $1 \times 10^{18} \text{ cm}^{-3}$ for H_{α} . Electron number densities in this laser sustained plasma are found to be as high as $2 \times 10^{17} \text{ cm}^{-3}$, thus the H_{α} tables are required in any case.

3. DATA ANALYSIS

More than 1×10^8 raw spectroscopic data points are considered in this investigation. The raw data consists of five different plasma emission line spectral profiles at fifty-one lateral locations at each of fifty-two axial locations. Four of the lines are from argon neutral and ionic species (two lines each) and the fifth is a hydrogen Balmer series line. The data reduction for the argon lines is slightly different than that for the hydrogen line.

The first task in the data reduction process is to transfer the raw data from the OMA system hard drive to the UIUC Convex mainframe computer. This is a two step process in which the data is first read into a BASIC array on the OMA and sent to a Compaq personal computer via serial communications. This step uses a program written in Heminway BASIC to read the raw data and send it to the OMA console serial port. This program is a modified version of a program written by Randy Lober [1989]. The serial data is captured onto the Compaq personal computer using Kermit, a public domain communications package. The Compaq computer is linked to the campus-wide ethernet, and step two of the data transfer process is to send it from the Compaq to the Convex using the File Transfer Program (FTP) supported by the network.

All further data reduction and analysis pertaining to this investigation is performed on the Convex. The program to perform the preliminary data reduction is called RAWOMA and is listed in Appendix A. The main functions of the program are to smooth the spectral profiles, determine and subtract the background signal, calibrate the net spectral profile, and to integrate the line and adjacent continuum signals. Integration is not performed on the hydrogen line because it is the spectral information which is required for electron number density determination, not total intensity. A section to perform a spectral to lateral transposition (required for Abel inversion) is substituted for integration in the hydrogen version of the data reduction program (not listed in Appendices).

3.1. DATA REDUCTION

3.1.1. Smoothing of Spectra

Data smoothing is accomplished by filtering the discrete Fourier transform of each emission line. Taking each line profile as a time sequence and performing a fast Fourier transform (FFT) results in a discrete sequence in Fourier space. A Butterworth-type low-pass filter is then applied and the inverse discrete Fourier transform taken to return a profile which contains less random noise. A typical argon emission line profile is shown both before and after smoothing in the upper plot in Figure 3.1. In this case the line is argon neutral at 7147 Å, and originates from a lateral location near the plasma centerline at the laser focus. All the major features are preserved while the small random variations are diminished. A close-up of a smaller spectral segment detailing the effect of smoothing is shown in the lower plot in Figure 3.1.

The Fourier transform of this emission line is shown both before and after low-pass filtering in the upper plot in Figure 3.2. All frequencies in Fourier space corresponding to variations periodic over approximately five pixels or less (in the original 'time' sequence) are suppressed, while more slowly varying features remain intact. A close-up of the region in discrete Fourier space in which the filtering becomes apparent is shown in the lower plot in Figure 3.2. Smoothing is performed on all data sequences used in this investigation. This includes the background and radiance calibration lamp signals. Similar discrete Fourier component strengths are found for nearly all data sequences, indicating that the noise is due mainly to detector or detector readout characteristics.

3.1.2. Background Correction

Measurements can only be made at approximately ten consecutive axial locations during an experiment. This is because radiative heating of the absorption chamber limits the length of any particular data taking period. Excessively long experiments result in burn damage to

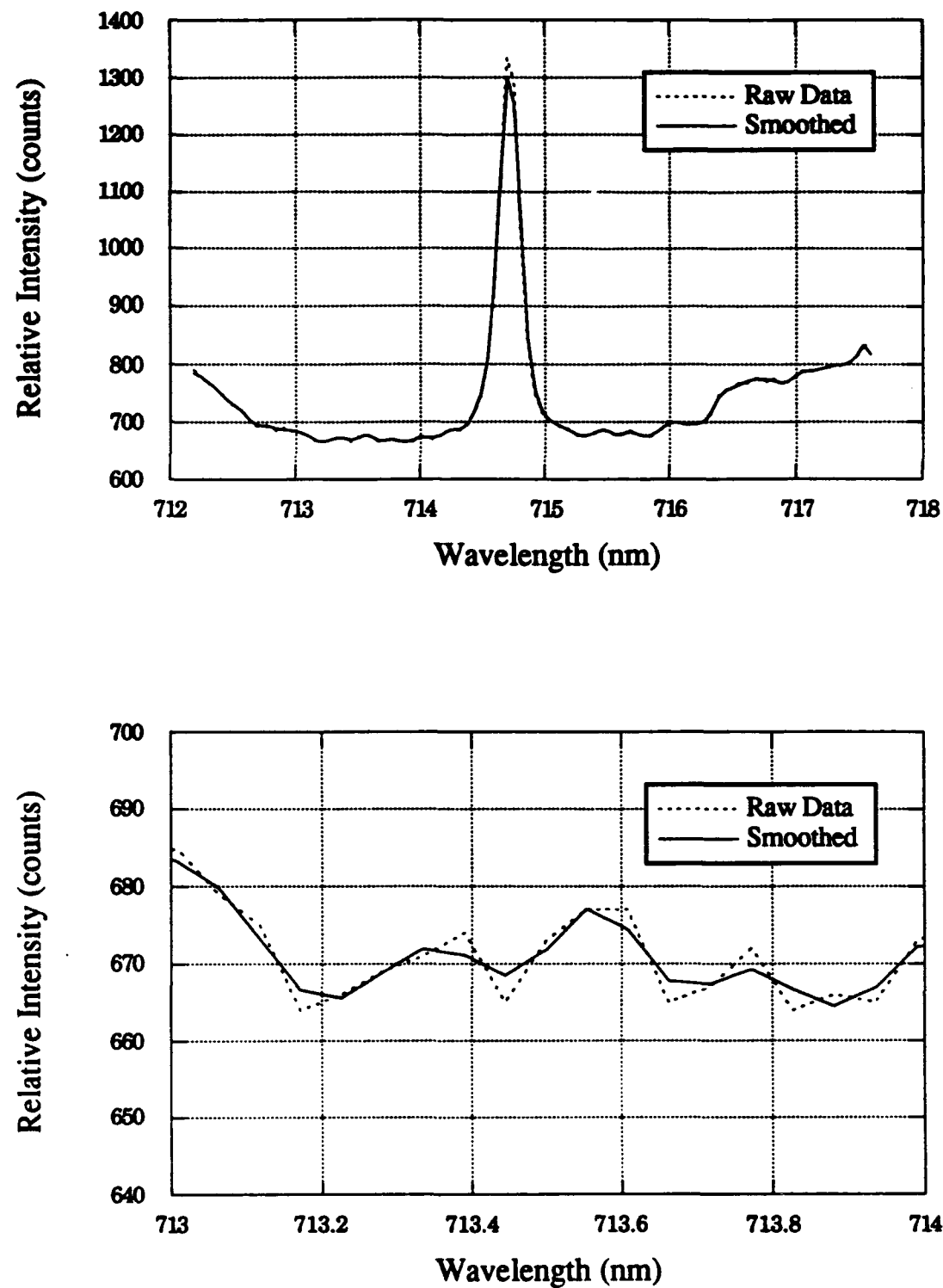


Figure 3.1 Upper plot: Neutral argon line profile centered on 7147 \AA shown with and without smoothing of noise fluctuations.
Lower plot: Expanded spectral scale to show a detailed section of filtered data.

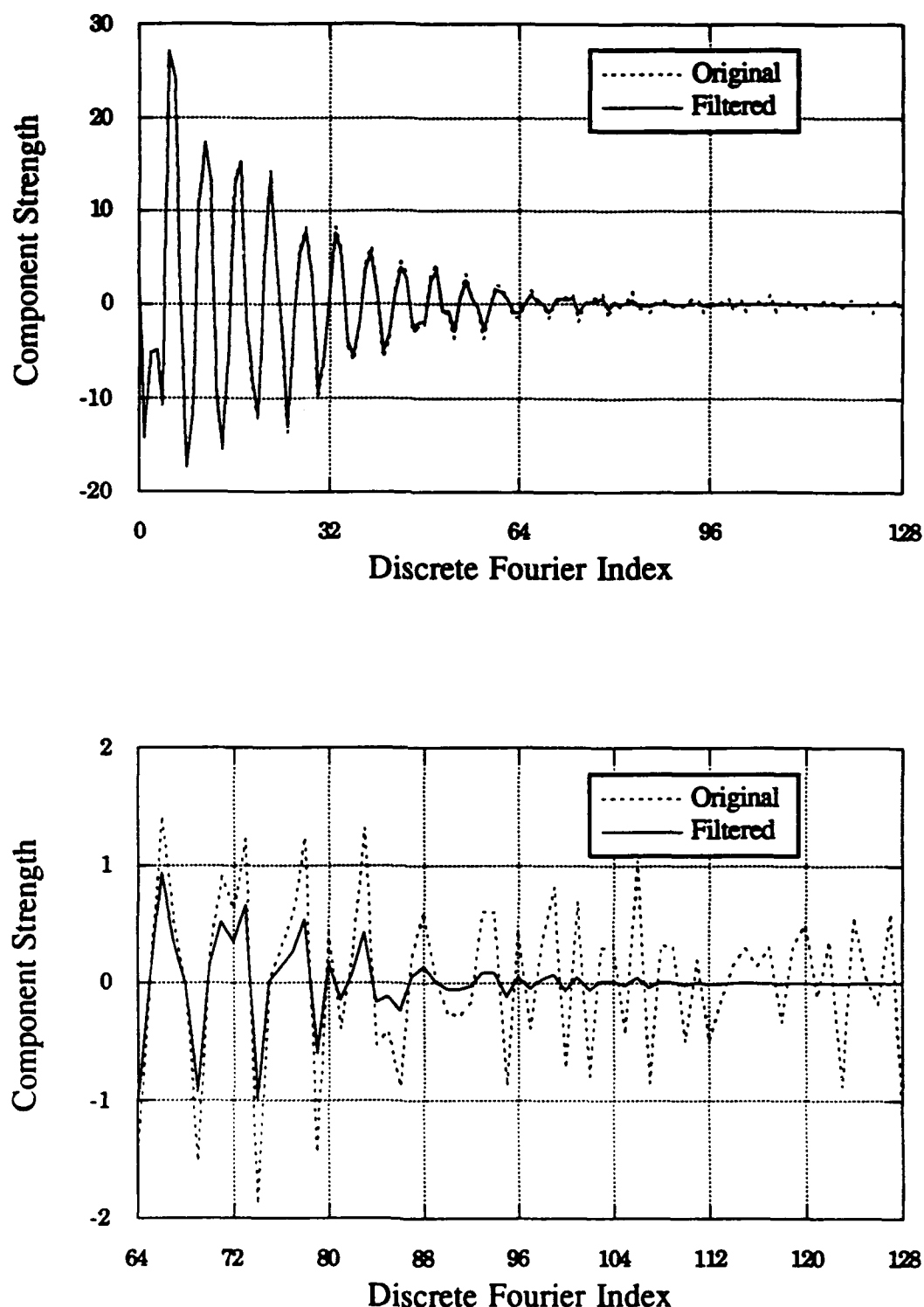


Figure 3.2 Upper plot: Discrete Fourier transform of the 7147 Å line profile shown with and without filtering.
 Lower plot: Expanded scale to show the detailed effect of filtering in the region where noise becomes dominant.

window seals. Another set of ten axial locations can be scanned after the chamber cools sufficiently. Background signals are taken at the beginning and end of each period to account for any possible variation in the background signal. These two signals are averaged after smoothing and subtracted from the plasma emission data taken in between. The background signal corresponding to the argon emission line discussed above is shown in the upper plot in Figure 3.3, and the profile resulting after background subtraction is shown in the lower plot. Background signals do not vary significantly over the course of the 5-10 minutes data taking periods, but there is evidence of significant variation of vidicon background signals over the course of hours [Azer, 1991].

3.1.3. Radiance Calibration

Signals from a source of standard radiance are measured for each of the wavelength regions considered in this experiment. These measurements are made for the purpose of calibrating the emission line profile for absolute spectral radiance. The calibration procedure accounts not only for the bulk conversion of pixel counts to radiance, but also for local variations in pixel sensitivity.

Experimental conditions are simulated exactly except for the neutral density filters required to get a satisfactory signal strength. Separate measurements must be made for each wavelength region due to spectral variations present in the standard lamp radiance, optical throughput, and bulk detector sensitivity. The spectral variation of the standard lamp radiance is documented as part of the lamp manufacturer's literature, and has been curve fit for all the wavelength regions considered in this experiment

The calibration procedure consists of taking the ratio of the plasma and standard lamp signals on each pixel, then multiplying by the lamp standard spectral radiance at the wavelength falling on that pixel, the wavelength increment represented by that pixel, and a scaling factor due to the difference in neutral densities required for the plasma and the lamp. The resulting quantity has the units of radiance:

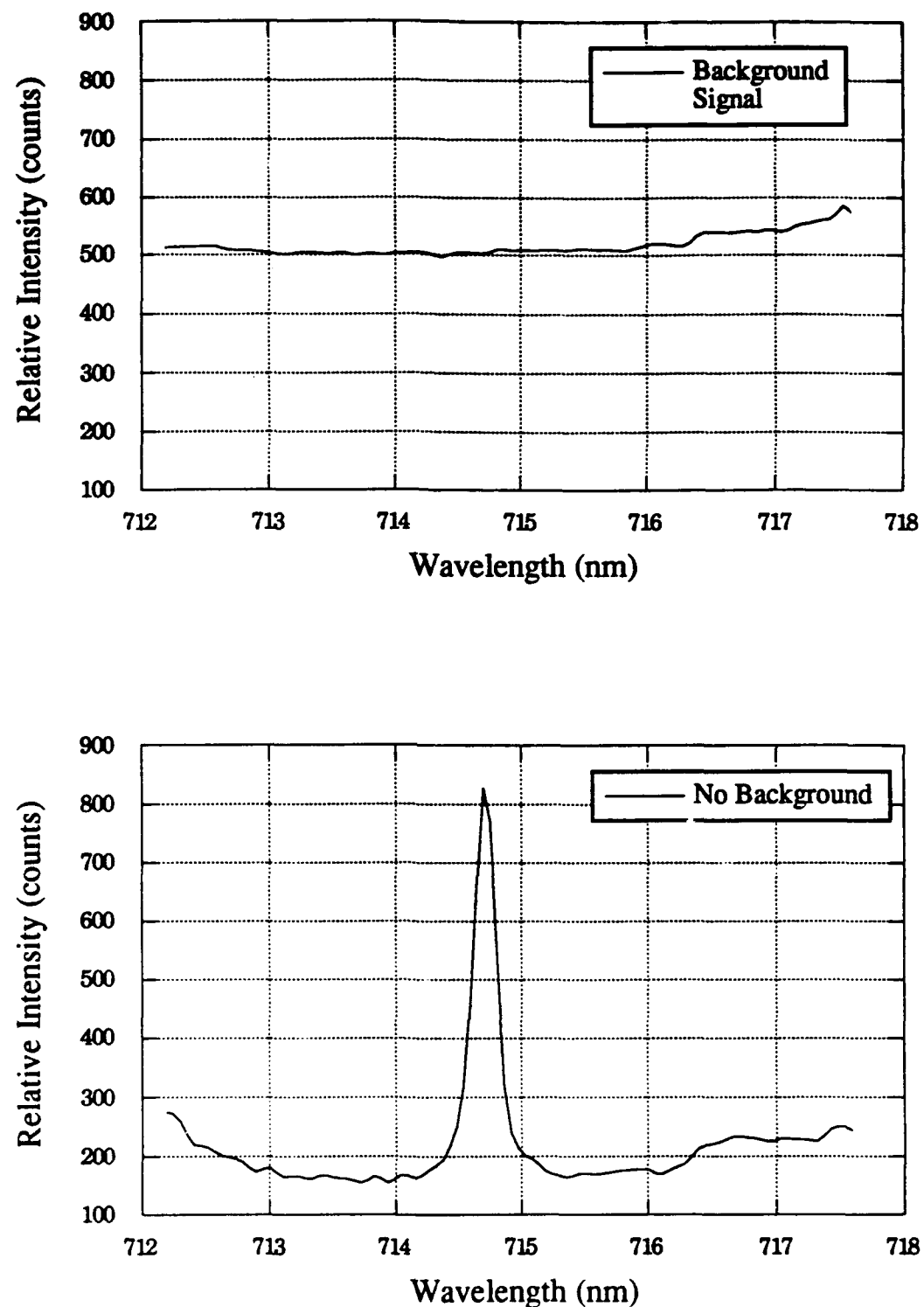


Figure 3.3 Upper plot: Background signal associated with the 7147 Å profile in Figure 3.1.
Lower plot: 7147 Å profile shown with background signal subtracted.

$$I_{exp} \left[\frac{\mu\text{W}}{\text{cm}^2 \text{ Sr}} \right] = S_{lmp} \left[\frac{\mu\text{W}}{\text{cm}^2 \text{ nm } \text{ Sr}} \right] \Delta\lambda \text{ [nm]} 10^{ND} \left(\frac{F_{exp}}{F_{lmp}} \right) \quad (3.1)$$

where I_{exp} is the absolute plasma radiance, S_{lmp} is the lamp standard spectral radiance, $\Delta\lambda$ is the pixel wavelength increment, ND is the difference between the neutral densities required during the plasma and lamp measurements, F_{exp} is the measured plasma pixel count, and F_{lmp} is the measured lamp pixel count.

The measured standard lamp signal for the region of the detector surface corresponding to the lateral position of the spectral profile discussed above is shown in the upper plot in Figure 3.4. The profile resulting from the calibration procedure is shown in the lower plot in Figure 3.4. It is apparent that the relatively high signal near the ends of the profile in the lower plot in Figure 3.3 are due to detector sensitivity variation rather than some significant plasma emission feature. These end regions flatten out nicely when calibrated, indicating that this line is indeed isolated in the observable argon emission spectrum.

3.1.4. Net Line Integration

The final task of the preliminary data reduction program (for argon lines) is to integrate the emission profile over wavelength, determine the adjacent continuum, and calculate the net total line radiance. The term 'net' refers to the fact that the underlying continuum has been estimated and subtracted, and the term 'total' means that the spectral lineshape information has been lost and the entire line emission power flux is represented by a single quantity. This quantity is sometimes called the net line-of-sight integrated intensity.

The argon emission line in the upper plot in Figure 3.4 is integrated from 714.0 nm to 715.4 nm to give the total line plus continuum radiance. The continuum is estimated from the sum of the emission from 1 nm bands on either side of the line. This sum is then prorated to the spectral width of the line to gauge the continuum under the line. The line plus continuum and estimated continuum are shown in the upper plot in Figure 3.5 for all the lateral positions measured at the axial position corresponding to the laser focus. The difference between these

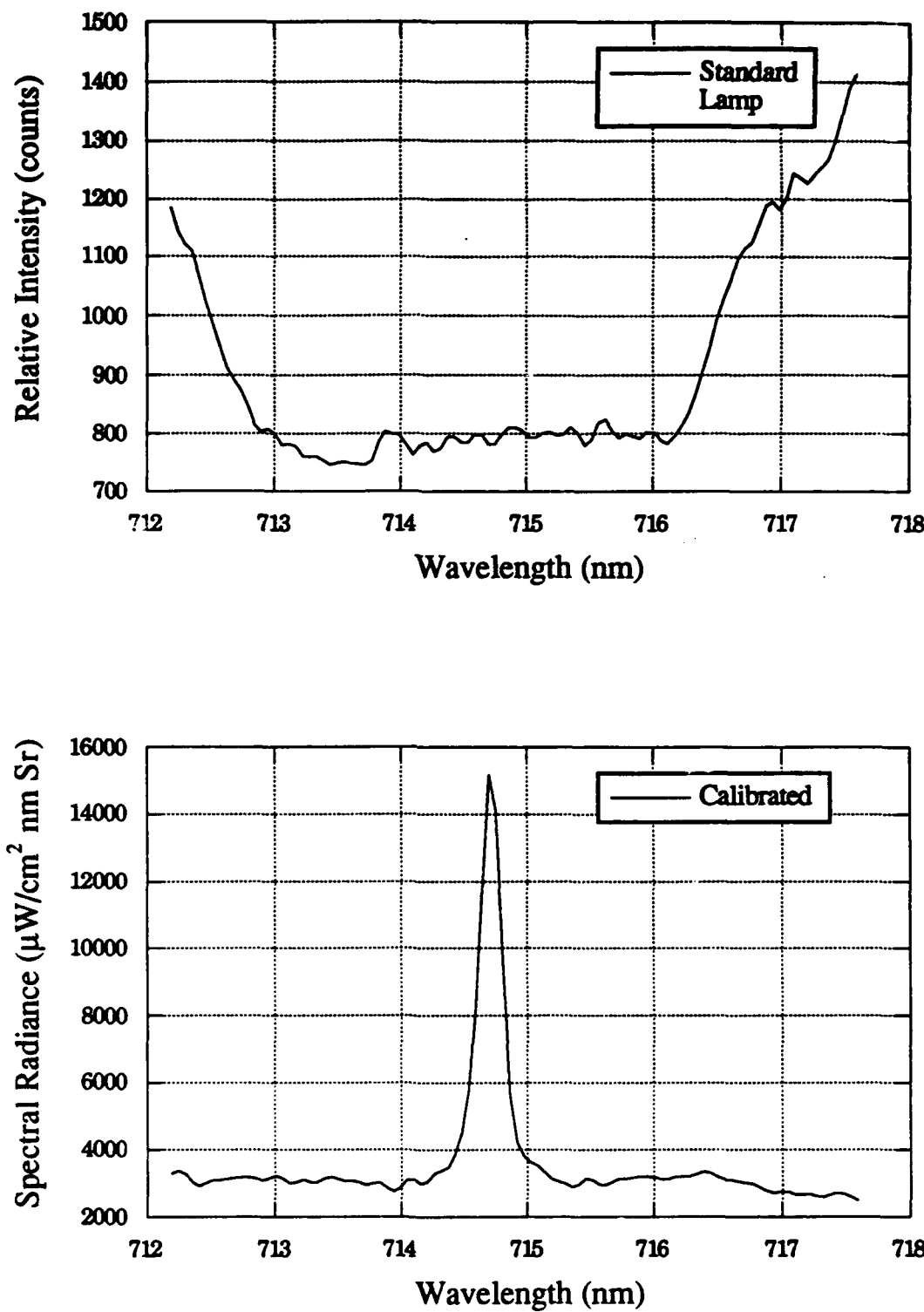


Figure 3.4 Upper plot: Calibration lamp signal for the region of the detector surface corresponding to the 7147 Å profile in Figure 3.1.
 Lower plot: 7147 Å profile after calibration for absolute spectral radiance.

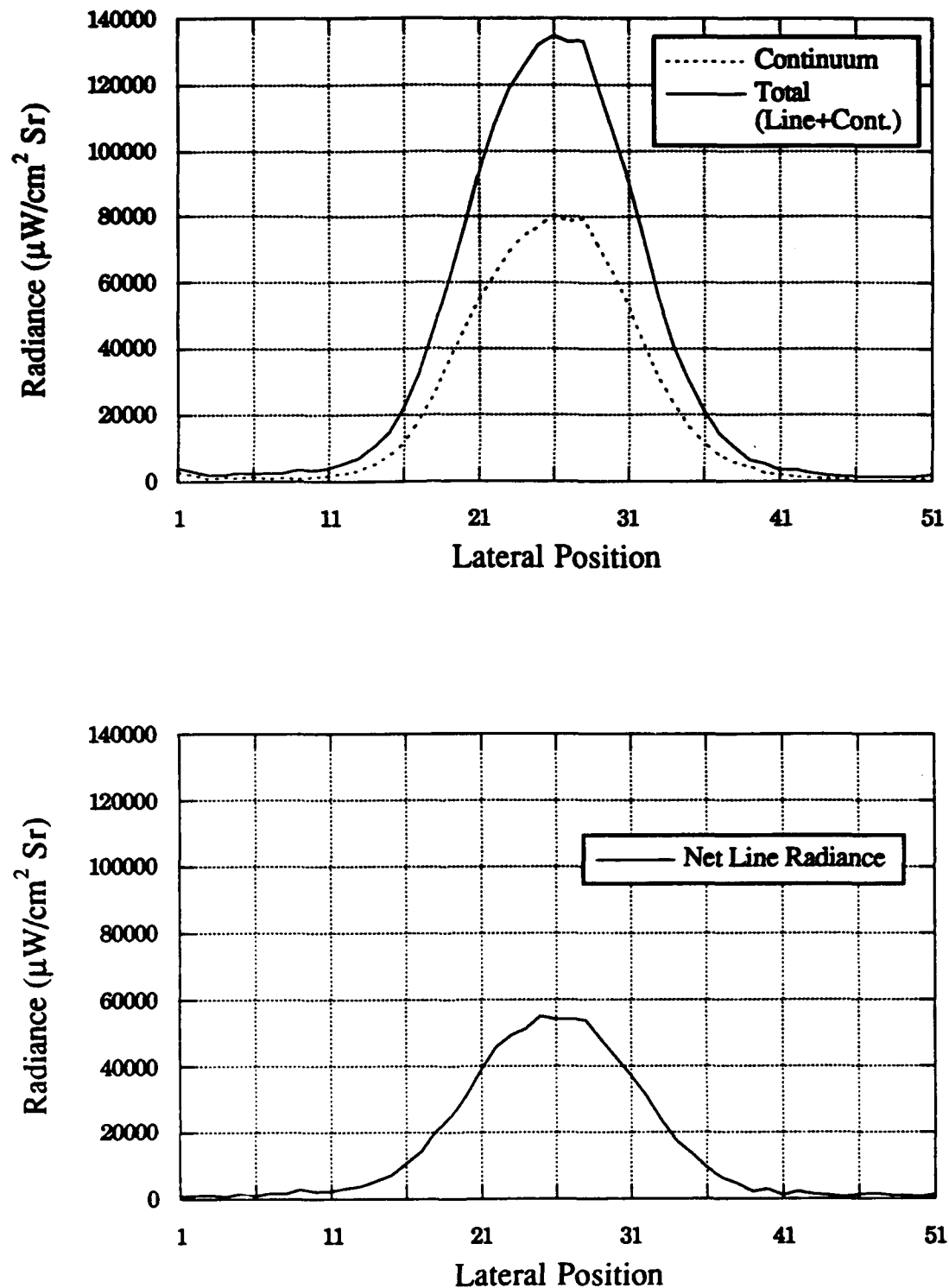


Figure 3.5 Upper plot: Total (line plus continuum) and continuum lateral radiance profiles for the 7147 Å line emitted near the laser focus.
 Lower plot: Net lateral radiance profile for the 7147 Å line (total minus continuum).

two quantities is the net total line radiance, and this quantity is shown in the lower plot of Figure 3.5. Similar lateral profiles are produced for all the plasma axial locations considered. It is these lateral profiles which undergo the Abel inversion procedure resulting in radial emissive power [$\mu\text{W}/\text{cm}^3 \text{ Sr}$]. Before a discussion of this inversion, the treatment of the hydrogen line preparation for this procedure will be described.

The hydrogen line profiles are processed in the same way as the argon lines up until the integration procedure. Each hydrogen profile is made up of 200 discrete wavelength increments, each collected on a separate pixel. The last step in the preliminary data reduction for hydrogen is to transpose the data field so that instead of spectral profiles at fifty-one lateral locations, lateral profiles for 200 separate wavelengths are stored. Figure 3.6 incorporates a photograph of the OMA console screen containing a number of hydrogen line spectral profiles. Only half of the profiles are shown for clarity. The wavelength increases going left to right in the figure, and the spectral profile at the plasma centerline is farthest toward the back. It is easy to imagine from the figure how the spectral profiles could be transposed into 200 lateral profiles running from the back of the figure to the front.

Following the Abel inversion of each of the 200 lateral profiles, the data field is again transposed to return the spectral profiles with units of emissive power [$\mu\text{W}/\text{cm}^3 \text{ Sr}$].

3.2. ABEL INVERSION

3.2.1. Overview

Abel inversion is a mathematical procedure for calculating the reconstruction of a circularly symmetric two-dimensional function from its lateral projection [Griem, 1964]. The lateral projection is usually the only type of information that can be measured in an emission spectroscopic experiment. It is then necessary to perform an Abel inversion to recover radial information, which in a circularly symmetric plasma represents a complete spatial description at a given axial location.

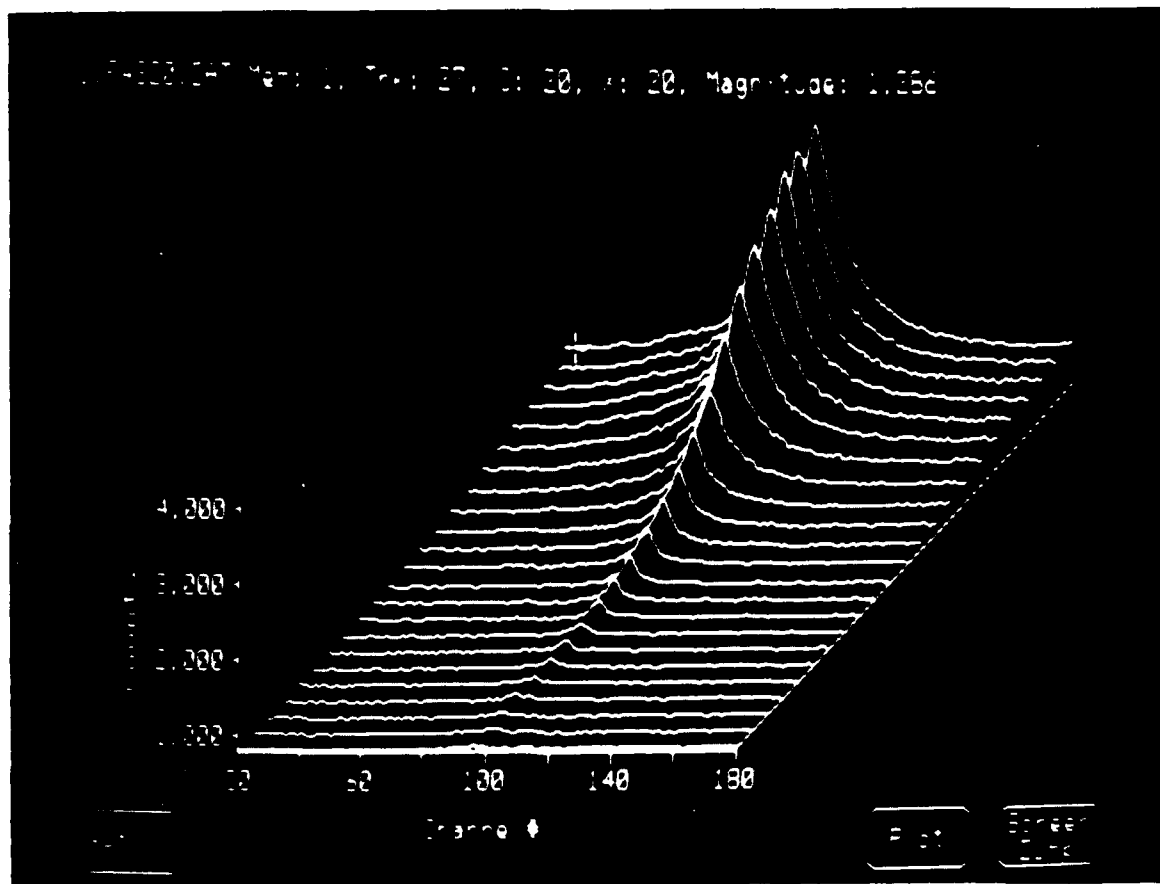


Figure 3.6 Photograph of OMA screen showing H_{α} spectral profiles at several lateral locations.

There are numerous methods available for the inversion of lateral profiles into radial profiles. Among the more popular are matrix inversion methods and numerical integration methods employing curve fitting of lateral profiles. For this investigation these methods have been overpassed in favor a method using integral transforms.

Matrix inversion methods are very useful in situations where there is a significant self-absorption of the measured emission. Unaccounted for self-absorption destroys the accuracy Abel inversion, and evidence of this might be the calculation of negative emissivity [Mork and Scheeline, 1987], or as jagged 'noisy' looking radial emission profiles [Scheeline and Walters, 1982]. These problems can be overcome with a high degree of success using a matrix inversion method of Mork and Scheeline, but additional measurements must be made to quantify the self-absorption. The presence of noise in the lateral profiles also has a fairly dramatic effect on the results of this method.

The choice of emission lines with minimal self-absorption for this experiment, the inconvenience and expense of performing back-lighting experiments, and the presence of significant noise in the measured lateral profiles makes other methods of Abel inversion more attractive than the matrix inversion method for this investigation. Cremers and Birkebak [1966] have compared several inversion techniques using numerical integration. They found that least squares curve fitting techniques are better than exact fit techniques. The integral transform method chosen for this investigation [Smith and Keefer, 1988] has several advantages that make it even more attractive than the least-squares curve-fitting technique.

The measured lateral profile, $I_{exp}(x)$, is given in terms of the radial emission coefficients, $\epsilon(r)$, through the Abel transform [Griem, 1964]:

$$I_{exp}(x) = 2 \int_x^{\infty} \frac{r\epsilon(r)}{\sqrt{r^2-x^2}} dr \quad (3.2)$$

where x is the lateral displacement from the plasma axis of symmetry, and r is the radial distance within the plasma from the axis of symmetry. The Abel inversion integral, or the inverse Abel transform, is given by:

$$\varepsilon(r) = \frac{-1}{\pi} \int_r^{\infty} \frac{\left(\frac{dI_{exp}(x)}{dx} \right)}{\sqrt{x^2 - r^2}} dx \quad (3.3)$$

The application of the above integral in its present form is difficult for a number of reasons. The denominator goes to zero at the lower limit of the integral, and taking the derivative of the measured lateral profile can amplify any noise present in the data. In addition, an assumption must be made concerning the functional form of the lateral profile because its value is known only at some number of discrete points. Curve-fitting to this assumed functional form is a type of low-pass filtering, but the extent of the smoothing is largely uncontrolled. There may also be some uncertainty concerning the actual, or 'best' axis of symmetry around which the integration is performed.

3.2.2. Inverse Hankel Transform

The integral transform method of Smith and Keefer [1988] avoids or removes many of the above problems. A discrete fast Fourier transform is taken of the original lateral profile and a user specified low-pass filter is applied in Fourier space. A procedure for determining the 'best' axis of symmetry is included in the method, and the Abel inversion is reformulated so that an inverse Hankel transform is used to reconstruct the radial emission profile.

A detailed description of the reformulation and application of Abel inversion by integral transforms is found in the article by Smith and Keefer referenced above. Some parts will be restated here for clarity. The computer program for performing the actual inversion is called ABEL and is listed in Appendix A.

The reformulation begins with the substitution $r = \sqrt{x^2+y^2}$ in equation (3.2). The lateral profile can then be written as:

$$I_{\text{exp}}(x) = \int_{-\infty}^{\infty} \epsilon(\sqrt{x^2+y^2}) dy \quad (3.4)$$

Taking the one-dimensional Fourier transform of (3.4) and changing from cartesian to polar coordinates gives (q is the Fourier index):

$$\text{FT}\{I_{\text{exp}}(x)\} = 2\pi \int_0^{\infty} r\epsilon(r)J_0(2\pi rq) dr \quad (3.5)$$

where J_0 denotes the zero-order Bessel function of the first kind. It so happens that the right hand side of (3.5) is the zero-order Hankel (also known as the Fourier-Bessel) transform of $\epsilon(r)$. The inverse Hankel transform of the left hand side of (3.5) will therefore result in the reconstruction of the radial emission profile. In other words, the inverse Hankel transform of the Fourier transform of the measured lateral profile results in the radial emission profile.

The inverse Hankel transform has the exact same form as the forward transform, and so the radial emission profile is expressed as:

$$\epsilon(r) = 2\pi \int_0^{\infty} qJ_0(2\pi rq) \int_{-\infty}^{\infty} I_{\text{exp}}(x)\exp(-j2\pi xq) dx dq \quad (3.6)$$

This equation is equivalent to the Abel inversion integral given in equation (3.3), but has several advantages according to Smith and Keefer. First there is no division by zero at the lower integration limit, and second the expression of the lateral profile in Fourier space allows the application of a noise reducing low-pass filter similar to the one used in the smoothing of the raw emission data. Smith and Keefer also outline an algorithm which can be applied to the Fourier transform which will center the data to a mathematically defensible axis of symmetry. An application of this method to the lateral profiles in Figure 3.5 will demonstrate the benefits of noise reduction. It will also help to confirm the insignificance of the effect self-absorption has on the measured lateral profiles and the calculated radial profiles.

The original lateral profiles along with the profiles resulting from an inverse Fourier transform of the filtered discrete Fourier transform of the original profiles are compared in Figure 3.7. A minimum degree of filtering is employed in order to preserve as much information as possible without corrupting the subsequent inverted profiles with noise. A comparison of the Abel inversion of the net total lateral profile in Figure 3.5 using the integral transform method with and without noise filtering and axis centering is shown in the upper plot of Figure 3.8. The axis of symmetry correction for this particular profile was very small, but the effect of noise filtering is quite evident, particularly near the axis.

The Abel inversion is linear when only emission occurs, that is, when self-absorption is insignificant [Scheeline and Walters, 1982]. In such a situation, the continuum may be subtracted before or after the Abel inversion without altering the final result. A comparison of the inverted profiles using these two mathematical paths is shown in the lower plot of Figure 3.8. The profile resulting from the inversion of the net lateral profile is virtually identical to the difference between the inversions of the total and continuum lateral profiles. It would seem then that the test of linearity is passed and only emission is occurring at this particular axial location in the plasma. This is a typical result for all the plasma axial locations studied, and one can conclude that self-absorption is not an important spectroscopic interference in this investigation.

3.3. PRELIMINARY DATA ANALYSIS

The result of the preliminary data reduction is a complete two-dimensional (radial and axial) set of emission coefficients for four integrated argon lines and the spectral profile of the hydrogen Balmer series alpha line, denoted H_{α} . The preliminary data analysis includes calculating the population of the upper electronic level involved in each of the four argon line transitions. Two of the lines are from neutral argon, and two are from ionic argon. Thus the upper level electronic excitation temperatures, $T_{ex\beta,a}$ for the neutrals and $T_{ex\beta,i}$ for the ions, are calculated from Boltzmann factors for each species.

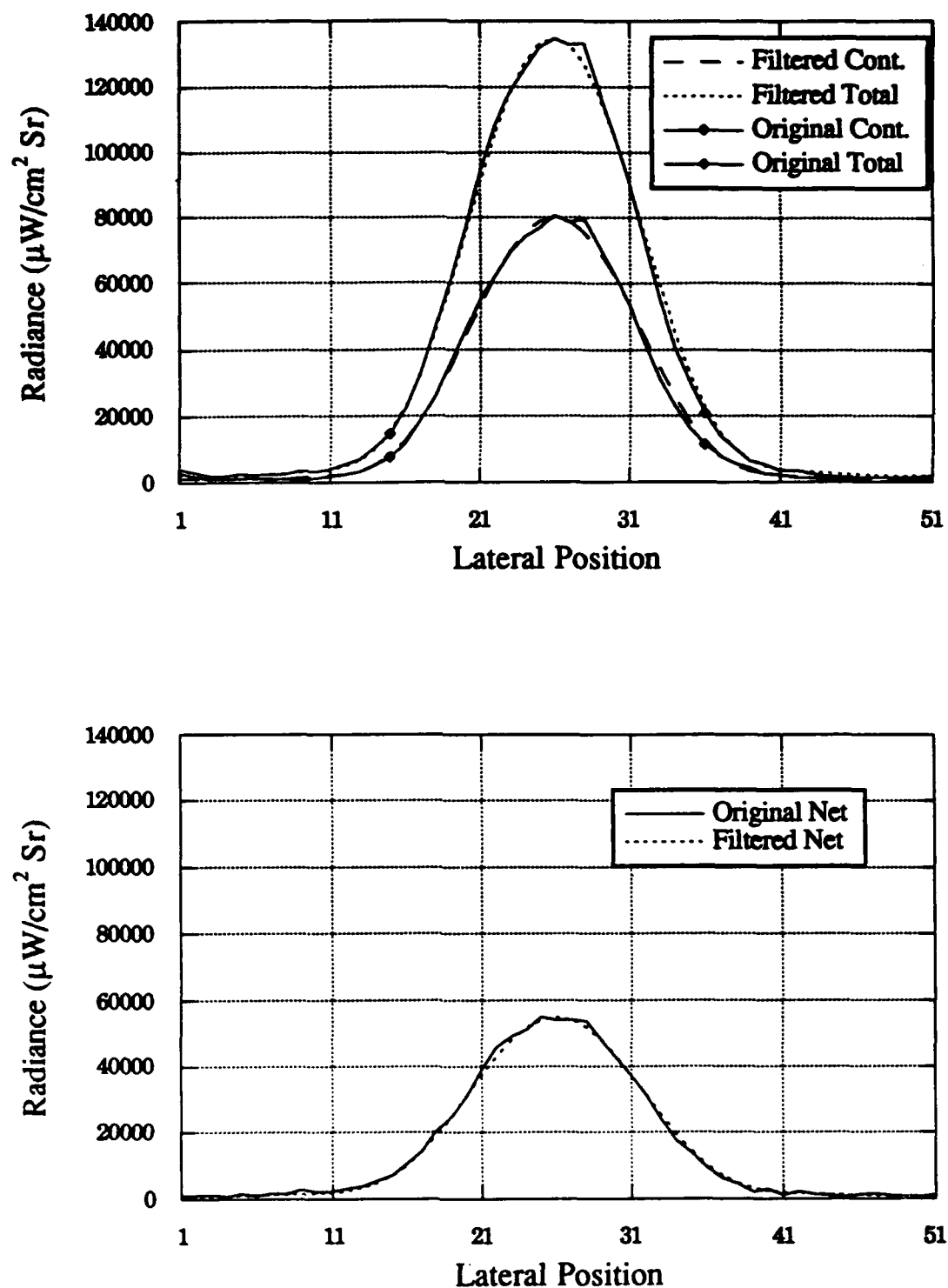


Figure 3.7 Upper plot: Comparison of the original 7147 Å total and continuum lateral radiance profiles to the smoothed profiles.
 Lower plot: Comparison of the original 7147 Å net lateral radiance profile to the smoothed profile.

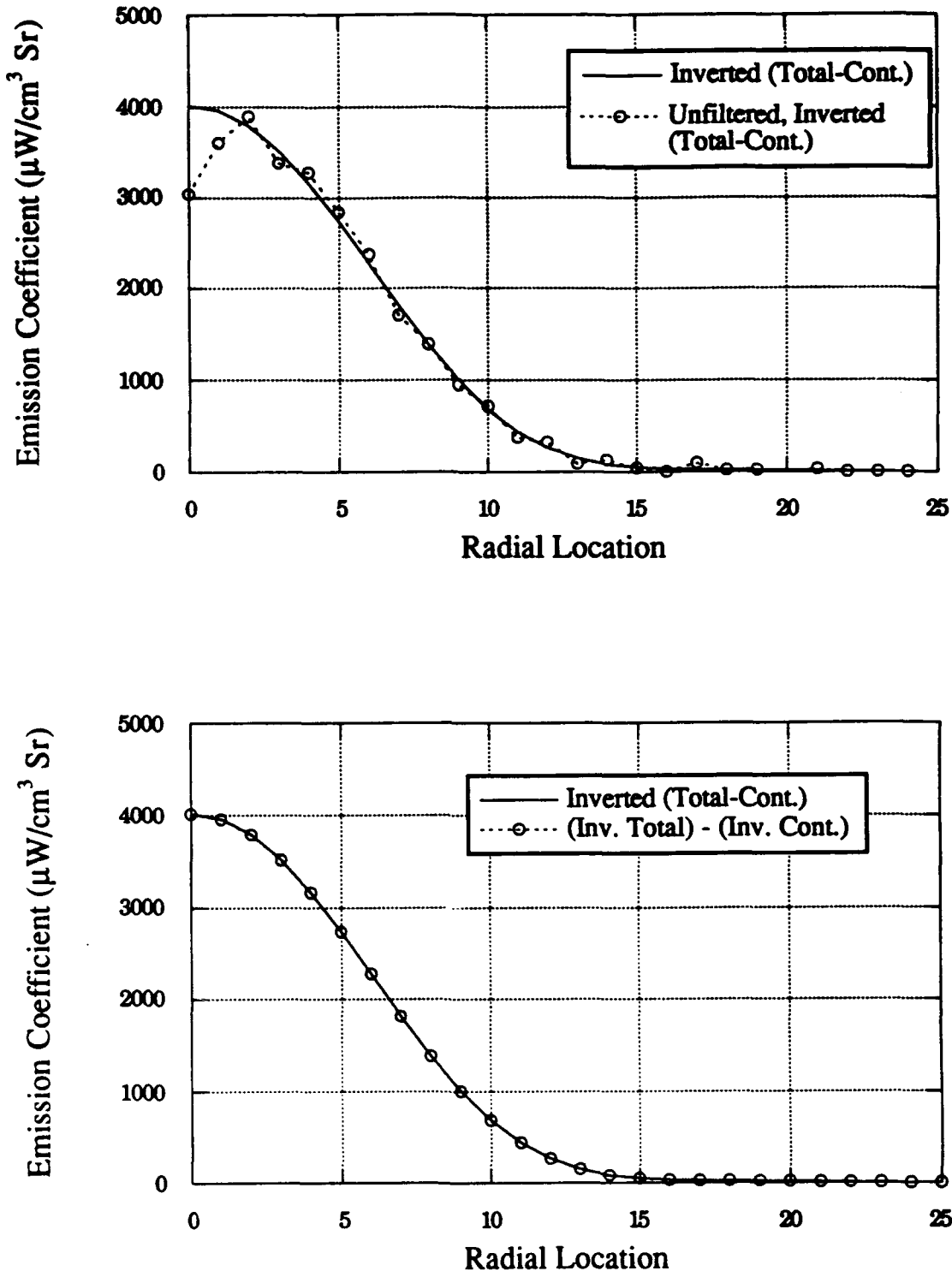


Figure 3.8 Upper plot: Comparison of filtered and unfiltered inverse Hankel transforms of the 7147 Å lateral radiance profile.
 Lower plot: Comparison of the inverse Hankel transform of the net 7147 Å lateral radiance profile, and the difference between the inverse Hankel transforms of the 7147 Å total and continuum lateral radiance profiles.

Preliminary analysis also involves using the H_{α} spectral profile to determine electron number density, n_e , at each of the points in the two-dimensional plasma domain. The unified theory of hydrogen line Stark broadening [Vidal, Cooper, and Smith, 1973] is employed in a computer program written by Chan and Montaser [1989] to calculate n_e from the spectral shape of H_{α} . The program was written in BASIC for execution on IBM compatible personal computers, but has been converted to FORTRAN by this researcher for execution on the Convex mainframe computer on the University of Illinois campus. The FORTRAN version of this program is called NE and is listed in Appendix A (with permission). The original TURBO BASIC program was provided by Professor Alexander Scheeline [1990].

The populations of the upper levels of the argon line transitions are also used to calculate plasma temperature and composition based on the assumption of local thermodynamic equilibrium (LTE). This relatively simple analysis requires only the measurement of a single upper level population, and thus has enjoyed great popularity. For example see Keefer, et al. [1990] for both absolute and relative line intensity temperature determination techniques, or Drellishak et al., [1963] for LTE argon compositions and thermodynamic properties. It will be shown, however, that non-LTE analysis is required for the purpose of determining the thermodynamic state of the laser sustained plasma (LSP) studied in this investigation. Comparisons are made between the LTE temperature and composition, and the excitation temperatures and Stark-based electron number density.

The radial emission coefficient for an argon line transition, $\epsilon(r)_L$, is related to the population of the upper level of the transition, n_m , as follows [Griem, 1964]:

$$n_m = \frac{4\pi\lambda_{mn}\epsilon(r)_L}{hcA_{mn}} \quad [m^{-3}] \quad (3.7)$$

where λ_{mn} [m] is the center wavelength of the line transition, h [J s] is Planck's constant, c [m/s] is the speed of light, and A_{mn} [1/s] is Einstein's coefficient for spontaneous emission

from level m to level n . The units of $\epsilon(r)_L$ are officially $[W/m^3 \text{ Sr}]$, but that is numerically equivalent to $[\mu W/cm^3 \text{ Sr}]$.

3.3.1. Upper Level Excitation Temperature

The upper level excitation temperatures are determined from the ratios of the Boltzmann factors corresponding to the energy levels considered. The population of at least two levels in each argon species must be known in order to calculate an excitation temperature. In this investigation exactly two are known for each species and excitation temperature is found from the relation:

$$\frac{n_m}{g_m} = \frac{n_n}{g_n} \exp\left(\frac{-(E_m - E_n)}{k_b T_{ex\beta}}\right) \quad (3.8)$$

which is similar to equation (1.8) but has the excitation temperature in the exponential rather than an equilibrium temperature. Recall that equation (1.8) is valid for all energy levels in a given species if complete Boltzmann equilibrium holds, not just the higher lying levels described by (3.8). It is assumed in (3.8) that the populations of all the upper levels in a given species are in equilibrium amongst themselves and can be related to each other by the excitation temperature, $T_{ex\beta}$.

Taking the natural logarithm of (3.8) gives a form convenient for examination on a Boltzmann plot:

$$\frac{-1}{T_{ex\beta}} = \frac{\ln\left(\frac{n_m}{g_m}\right) - \ln\left(\frac{n_n}{g_n}\right)}{(E_m - E_n)/k_b} \quad (3.9)$$

The Boltzmann plot then consists of a $\ln(n/g)$ ordinate and an E/k_b abscissa, and the plotted points fall on a line with slope $-1/T_{ex\beta}$. If more than two populations are known, then a least squares fitted line gives the slope and therefore the excitation temperature.

The equation (3.9) is evaluated at every point in the two-dimensional plasma domain for both the neutral and ionic argon species. In addition the line described by the slope of the Boltzmann plot is extrapolated to the lowered ionization limit, E_I , and the population of the effective highest excited level, (n_I/g_I) , is calculated from this intercept. This population is related to the population of the ground state by the total excitation temperature, T_{exa} for neutrals, and T_{exi} for ions, by the relation (for neutrals):

$$\frac{n_a}{Z_{\text{exa}}} = \left(\frac{n_I}{g_I} \right)_a \exp\left(\frac{E_{Ia}}{k_b T_{\text{exa}}} \right) \quad (3.10)$$

where Z_{exa} is the electronic excitation partition function for the neutral species (in this case) evaluated at T_{exa} . This temperature is important for the non-LTE data analysis described in a later section. An example of a Boltzmann plot relating the quantities $T_{\text{ex}\beta}$, (n_I/g_I) , T_{exa} , and n_a was shown in Chapter 1.

3.3.2. H_α Electron Number Density

Prior to successful execution of program NE, another program must be executed so that raw experimental hydrogen profiles are converted into the necessary format. This pre-processing program was also written in BASIC and has been converted to FORTRAN for execution on the Convex computer. It is listed in Appendix A and is called CONVERT. The primary tasks of CONVERT are to read in a raw profile, either hydrogen data or instrument profile data, read in the wavelength increment corresponding to a single data point in the profile, determine the peak center, upper limit, and lower limit wavelengths, and to store the converted profiles in the proper format for use in NE.

The NE program requires that the theoretical profiles of Vidal, et al. [1973] be interpolated such that the theoretical profiles correspond in wavelength increment to the converted experimental profile. There is a subroutine within NE to read in the Vidal profiles and perform this interpolation, with the results being stored as STARK files. NE will also calculate

theoretical Doppler profiles at a user specified heavy particle temperature and wavelength increment. The program convolutes the Doppler profile and a user specified instrument profile with an interpolated theoretical STARK profile, then compares the result to the experimental profile. Different theoretical profiles corresponding to different electron number densities are used in succession until the convoluted Doppler/instrument/STARK profile matches the shape of the experimental profile.

The theoretical profiles of Vidal, et al. are available at only a certain number of electron temperatures, those being 2500, 5000, 10000, 20000, and 40000 K. All evaluations of electron number density in this investigation use the profiles corresponding to 10000 K, which mostly closely agrees with the electron kinetic temperatures determined in this investigation. The dependence of Stark broadened hydrogen line shape on electron temperature is very weak compared to its dependence on electron number density [Griem, 1964]. It is found in this investigation that the final electron number density determined with this method does not vary significantly with the assumed electron or heavy particle temperatures.

A comparison of a typical experimental hydrogen profile and its theoretical best-fit profile is shown in the upper plot in Figure 3.9. The electron and heavy particle temperatures are assumed to be 10000 K in this example, and the corresponding electron number density is $1.89 \times 10^{17} \text{ cm}^{-3}$. As is apparent in the figure, the theoretical profile matches the experimental profile quite well. The same experimental profile is analyzed assuming various combinations of electron and heavy particle temperatures, and the results are compared in the lower plot in Figure 3.9 along with the corresponding electron number densities. There is practically no difference in the results due to the weak dependence of Stark-broadened line shape on electron temperature, and the insignificance of Doppler broadening at this relatively high electron number density.

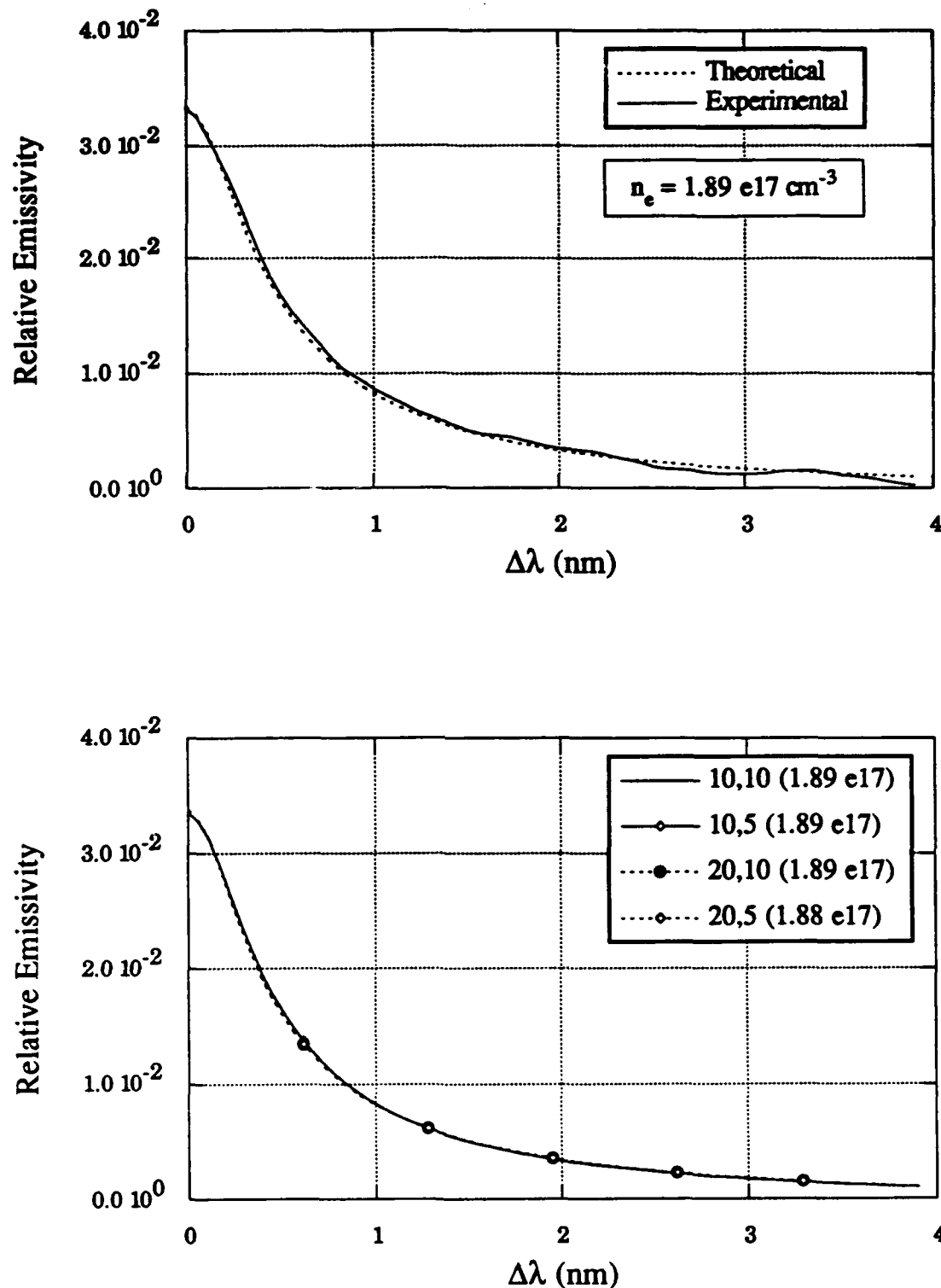


Figure 3.9 Upper plot: Comparison of experimental and theoretical H_α profiles. Both T_e and T_g are 10000 K for this example.
 Lower plot: Comparison of theoretical H_α profiles for several combinations of T_e and T_g showing that the corresponding electron densities do not change.

3.3.3. LTE Temperature and Composition

In LTE the temperature and composition of a plasma can be determined from the measurement of a single excited level population and the system pressure. The procedure for this determination involves a number of equations and relations which require some explanation.

Key to the procedure is the calculation of the electronic excitation partition functions for neutral argon and a number of its ions. This calculation requires knowing the energies and degeneracies of all the levels of each species below the ionization limit. The ionization limit itself must also be determined, it being somewhat lowered in a plasma due to Coulomb interactions. The Ph.D. thesis of Sedghinasab [1987] lists a program for the calculation of partition functions and it is used in this investigation. Sedghinasab also provides the energies and degeneracies needed for the calculation. The partition function is of the form:

$$Z_{ex} = \sum_{i=1}^m g_i \exp\left(\frac{-E_i}{kT_{ex}}\right) \quad (3.11)$$

where $i=1$ is the ground state, $i=m$ is the highest effective bound level, g_i is the degeneracy of energy level E_i , and T_{ex} is the excitation temperature. T_{ex} is the same as the plasma temperature for this LTE based calculation.

In an isolated atom the number of bound levels approaches infinity as energy level increases, and the partition function sum does not converge. The highest effective bound level in a plasma atom is determined by the lowering of the ionization potential. Only levels with energy below the lowered limit need be considered in the sum. The lowering calculated by Griem [1964] is used throughout this investigation and is given by:

$$\Delta E_{\infty} = \frac{ze^2}{\rho_D} \quad (3.12)$$

where z is the effective nuclear charge seen by the excited electron and e is the electronic charge. The plasma Debye length is given by Shkarofsky, et al. [1966] for a multitemperature plasma as:

$$\rho_D = \left[4\pi e^2 \left(\frac{n_e}{k_b T_e} + \sum_j \frac{z_j^2 n_j}{k_b T_g} \right) \right]^{-1/2} \quad (3.13)$$

where the summation is over the heavy charged species, T_e is the electron kinetic temperature, and T_g is the heavy particle kinetic temperature.

The calculation of partition functions is vital to the procedure for calculating LTE based plasma temperature and composition from the measured excited level population. The program for this LTE based analysis is called LTE and is listed in Appendix A. The logic proceeds as follows:

- 1) Make an initial estimate of temperature and composition, making certain that the temperature estimate is too low, say 5000 K.
- 2) Calculate the plasma Debye length and the lowered ionization potential for all the heavy species considered in the plasma (up to fourth degree ionization).
- 3) Calculate the partition function for each of the heavy species.
- 4) Calculate the neutral argon number density from the measured population, n_m , and the Boltzmann factors using,

$$n_a = \left(\frac{n_m}{g_m} \right) Z_{exa} \exp\left(\frac{E_m}{k_b T} \right) \quad (3.14)$$

- 5) Species number density ratios are calculated from the Saha equation written for each ionization reaction:

$$\frac{n_e n_j}{n_{j-1}} = C_j = 2 \left(\frac{2\pi m_e k_b T_e}{h^2} \right)^{3/2} \frac{Z_{ex(j)}}{Z_{ex(j-1)}} \exp\left(\frac{-E_{I(j)}}{k_b T} \right) \quad (3.15)$$

where a zero subscript denotes the neutral particle. Combining the species density ratios with the expression for plasma quasi-neutrality:

$$n_e = \sum j n_j \quad j = 1, 2, 3, 4 \quad (3.16)$$

results in the following relation for determining electron number density:

$$n_e = \{ n_e^{-3} n_a C_1 + n_e^{-2} n_a C_2 C_1 + n_e^{-1} n_a C_3 C_2 C_1 + n_a C_4 C_3 C_2 C_1 \}^{1/5} \quad (3.17)$$

where n_e^{-} is the last calculated value and n_e is the next calculated value. This equation is solved by repetitive substitution for n_e while all other species number densities remain unchanged.

- 6) Ion number densities are calculated from the latest n_a , n_e , and appropriate C_j 's:

$$n_j = \frac{n_{j-1} C_j}{n_e} \quad (3.18)$$

- 7) The ideal gas equation of state is used to calculate a system pressure:

$$P_{\text{calc}} = k_b T (n_e + \sum_{j=0}^4 n_j) (1 - P_c^{\text{DH}}) \quad (3.19)$$

where P_c^{DH} is the Debye-Huckel pressure correction term [Cambel, et al., 1962] to account for the non-ideal gas behavior of charged particles. It is given by the expression:

$$P_c^{\text{DH}} = \left[24\pi \rho_D^3 \left(n_e + \sum_{j=0}^4 n_j \right) \right]^{-1} \quad (3.20)$$

which typically results in a 1-2 % reduction in pressure.

- 8) The calculated system pressure is compared to the actual system pressure to check if the guessed temperature and calculated number densities are consistent with this known constraint. *If they are not, temperature is incremented upward and the procedure is repeated starting at step 2).*

3.3.4. LTE Level Population

A slight modification to the above algorithm allows the calculation of the population of any plasma species energy level and the plasma composition for an assumed plasma LTE temperature. The results of the modified algorithm are plotted in Figures 3.10 and 3.11. The population of the upper level of the 7147 Å transition in neutral argon is plotted versus temperature in the upper portion of Figure 3.10. The energy of this level is 107132 cm^{-1} . Notice the temperature is double valued for a given population, and that the peak is near 15000 K. This is known as the normal temperature for this line. A similar variation is shown in the lower plot in Figure 3.10 for the 4610 Å argon ion transition. The energy of this transition's upper level is 170530 cm^{-1} . The normal temperature is much greater than for the neutral line; approximately 26000 K.

Plasma species number densities are plotted versus temperature in Figure 3.11. The total particle density decreases with increasing temperature as required by the equation of state at constant pressure. The neutral particle density drops steadily as ionization takes place, accompanied by an increase in electron number density. The number density of singly charged ions is practically equivalent to the electron number density until the temperature exceeds 20000 K. Above this temperature higher degrees of ionization become significant as well.

3.4. NON-LTE DATA ANALYSIS

3.4.1. Equations and Assumptions

The goal of non-LTE data analysis is to determine, independent of an explicit LTE assumption, the kinetic temperatures of the electrons and heavy species, T_e and T_g , the total excitation temperatures of neutral and ionic argon, T_{exa} and T_{exi} , and the number densities of the neutral and ionic species, n_a and n_i . The electron number density, n_e , determined from the Stark broadened line shape of the hydrogen Balmer series alpha line, is taken as a quantity known independent of an LTE assumption.

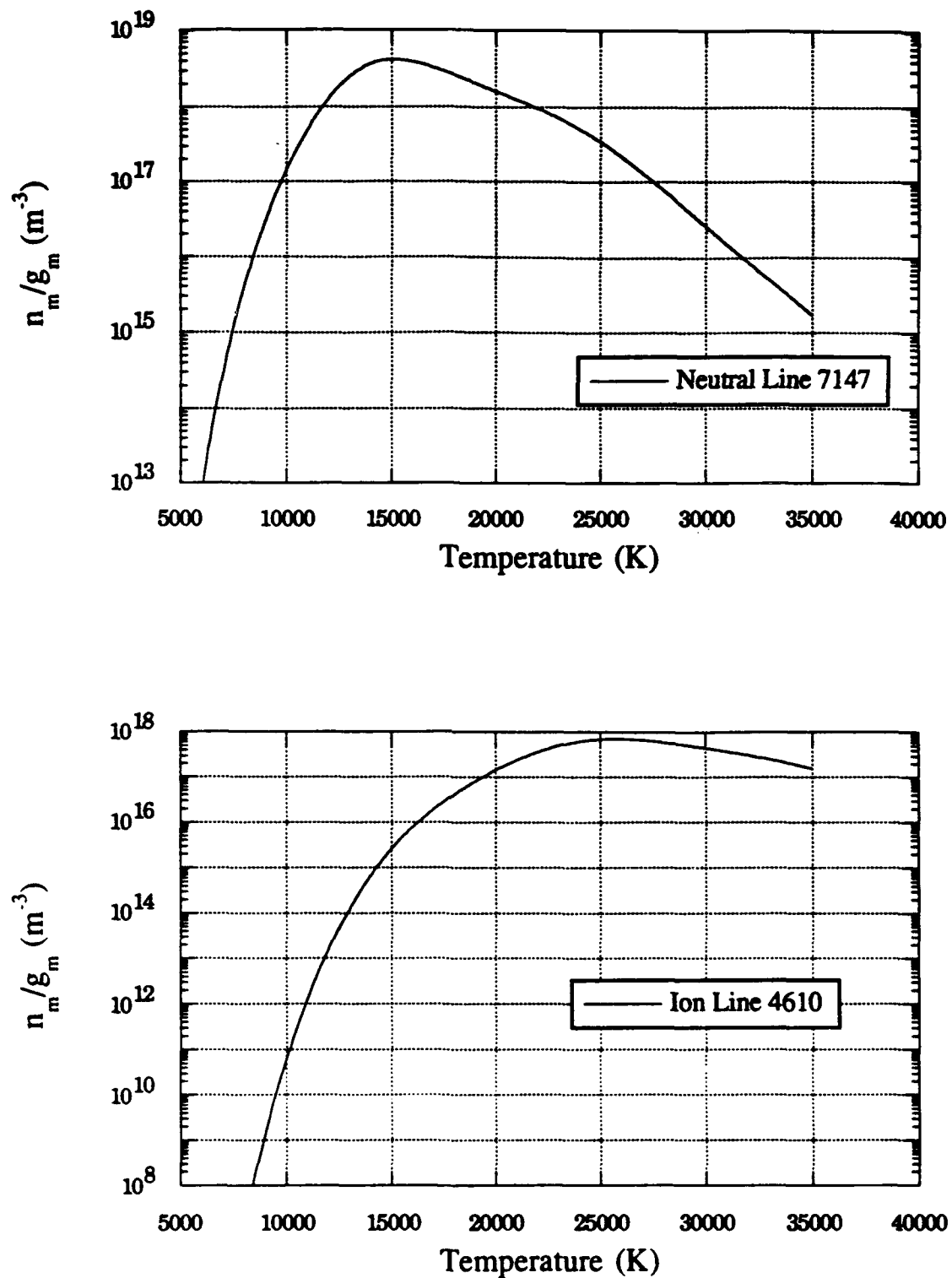


Figure 3.10 Upper plot: LTE relationship between the population of the upper level of the 7147 Å argon neutral transition and temperature.
 Lower plot: LTE relationship between the population of the upper level of the 4610 Å argon ion transition and temperature.

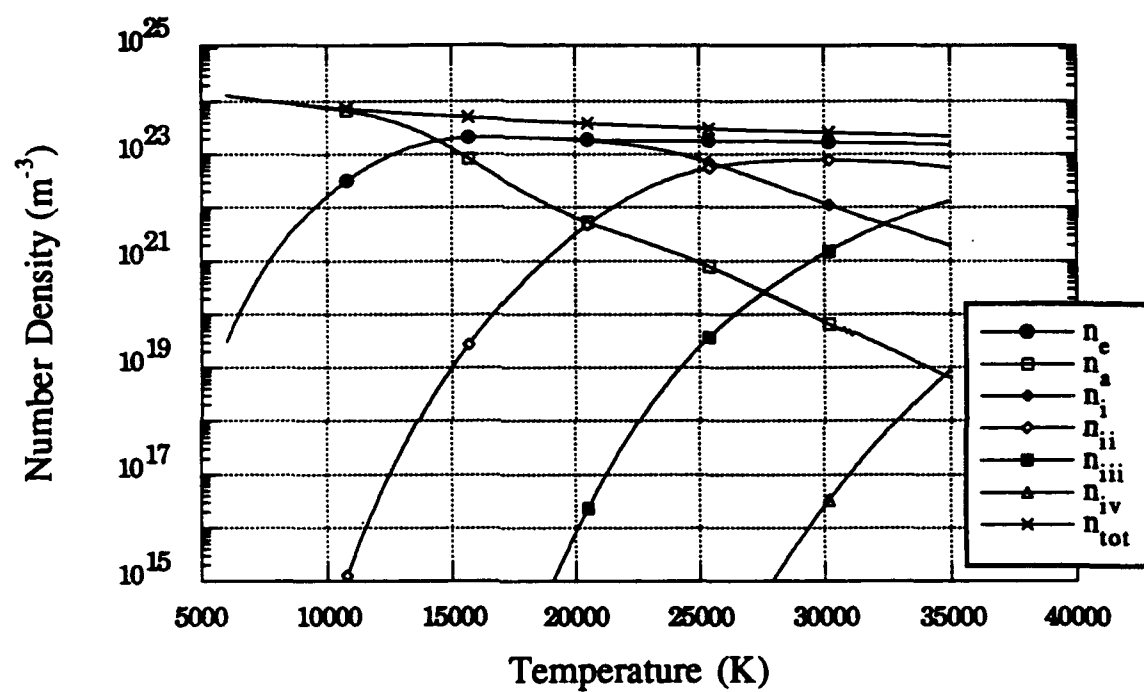


Figure 3.11 LTE composition of argon plasma as a function of temperature.

There are then six unknowns which must be calculated, and so six equations and/or simplifying assumptions are required to arrive at a unique solution. The following equations are assumed valid for the LSP studied in this investigation:

1) Gas Equation of State:

$$P = k_b [n_e T_e + (n_a + n_i) T_g] (1 - P_c^{DH}) \quad (3.21)$$

2) Non-LTE Ionization:

$$n_e \left(\frac{n_i}{n_a} \right) \frac{T_g}{T_e} = 2 \frac{Z_{exi} \left(\frac{T_{exi}}{T_e} \right)}{Z_{exa} \left(\frac{T_{exa}}{T_e} \right)} \left(\frac{2\pi m_e k_b T_e}{h^2} \right)^{3/2} \exp \left(\frac{-E_{Ia}}{k_b T_e} \right) \quad (3.22)$$

3) Neutral Boltzmann Factors:

$$\frac{n_a}{Z_{exa}} = \left(\frac{n_i}{g_i} \right)_a \exp \left(\frac{E_{Ia}}{k_b T_{exa}} \right) \quad (3.10)$$

4) Ionic Boltzmann Factors:

$$\frac{n_i}{Z_{exi}} = \left(\frac{n_i}{g_i} \right)_i \exp \left(\frac{E_{Ii}}{k_b T_{exi}} \right) \quad (3.23)$$

Two more equations and/or assumptions are required, and in this study the following assumptions are made:

1) Quasi-neutrality:

$$n_i = n_e \quad (3.24)$$

2) Neutral Boltzmann Approximation:

$$T_{exa} = T_{LTE,a} \quad (3.25)$$

Assumption (1) can be used with equation (3.23) to determine T_{exi} , and assumption (2) allows the determination of n_a through equation (3.10). Quasi-neutrality to include only the first ion is a very good assumption at the temperatures found in this study. The LTE composition shown Figure 3.11 indicates that below 20000 K n_i is virtually equivalent to n_e , and that the densities of the higher order ions are much lower. The highest temperature of any kind determined for this LSP is less than 17000 K.

The validity of assumption (2) is the most suspect of this investigation, as it implies complete Boltzmann equilibrium in the neutral electronic system. However, it has been shown that the total excitation temperature is approximately equal to the LTE temperature determined from the population of an upper energy level if the total excitation temperature is relatively low compared to the LTE normal temperature [Sedghinasab, 1987; Eddy, 1989]. This is the case regardless of the type and extent of non-equilibrium persisting in a plasma. The upper plot in Figure 3.12 will help to demonstrate the validity of this claim.

Shown in the figure are curves relating the population of the upper level of the 7147 Å argon neutral line transition, to the total excitation temperature for different non-equilibrium conditions. The temperature ratios shown in the plot legend correspond to the range of non-equilibrium combinations found in this investigation. The key feature of this plot is that all the curves collapse onto the LTE curve (all ratios = 1.00) on the low temperature side of the normal temperatures. So for level populations below the normal points of the curves, the predicted total excitation temperature is approximately the same for each nonequilibrium condition. In this investigation LTE temperatures calculated are always below the normal temperature, and assumption (2) appears justified. The lower plot in Figure 3.12 shows the same type of behavior for the 4610 Å argon ion line.

To take advantage of the relationship between T_{ex} and T_{LTE} for both the neutrals and ions, in this investigation both T_{exa} and T_{exi} have been assumed equivalent to their respective LTE counterparts. This is especially important for calculating the neutral particle density, which is now found from the expression:

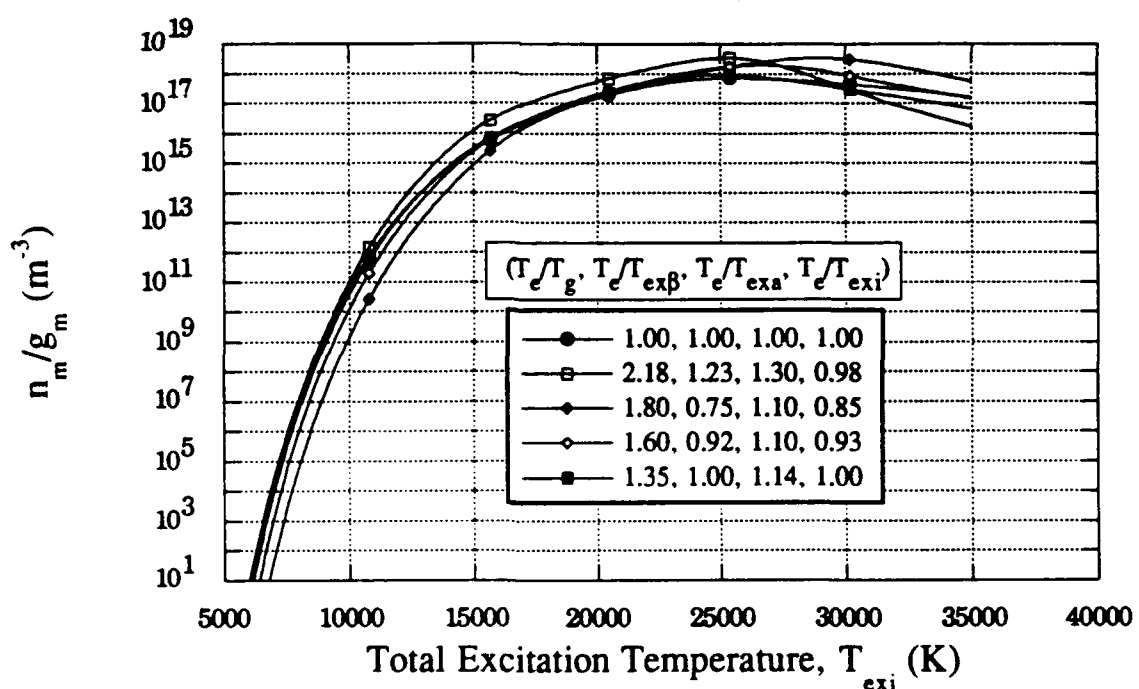
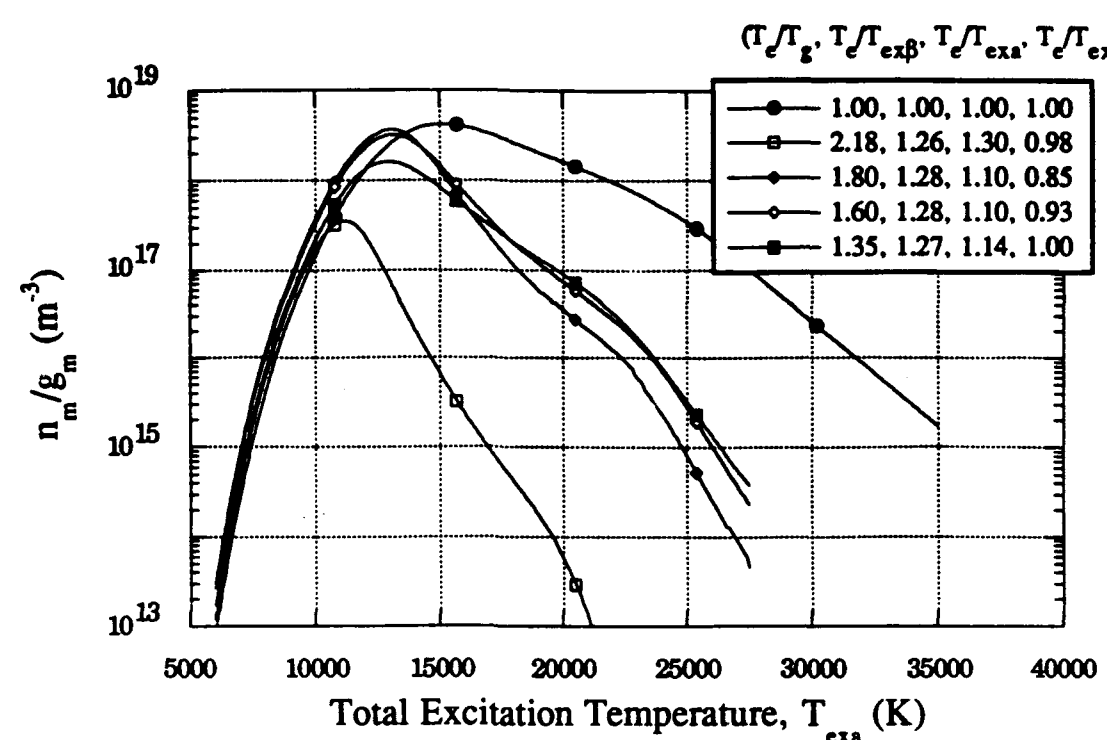


Figure 3.12 Upper plot: 7147 Å neutral line upper level population as a function of total excitation temperature, T_{exa} , for several non-LTE cases.
Lower plot: 4610 Å ion line upper level population as a function of total excitation temperature, T_{exi} , for several non-LTE cases.

$$n_a = \left(\frac{n_m}{g_m} \right)_{7147} Z_{exa}(T_{LTE}) \exp \left[\frac{E_m}{k_b T_{LTE}} \right] \quad (3.26)$$

which is the same as (3.10) except that the level population of the 7147 Å line is used rather than the population of the effective highest excited level, and $T_{LTE,7147}$ (calculated from n_m/g_m) is used in place of T_{exa} . The 7147 Å line is used rather than the 6753 Å line because the uncertainty in the spontaneous emission coefficient is lower for the 7147 Å line.

This type of calculation is not necessary to determine the ion density because it is assumed equivalent the the measured electron number density. However, it is an interesting check on the assumption to carry out the calculation and to compare the resultant ion density to the electron density. This has been done and the results shown in the next chapter indicate a very favorable comparison.

This fact is important because the spatial extent of the argon ion spectroscopic data is less than the spatial extent of the neutral argon and hydrogen data. In order to apply equation (3.22) throughout the larger measurement domain, a value of T_{exi} is required. Inside the ion data domain, $T_{LTE,4610}$ is used, while outside the domain the LTE temperature corresponding to the measured electron density value is used for T_{exi} . Again, the 4610 Å line is used because its spontaneous emission coefficient is known more precisely than is that of the 4658 Å argon ion line.

Referring to Figure 3.11, it is shown that the electron number density curve flattens out above approximately 15000 K. This small variation with temperature makes it very difficult to predict LTE temperature given an electron number density at high temperature. Fortunately, outside the ion data domain, the measured electron number densities are low enough that LTE temperature, and therefore T_{exi} , can be uniquely determined from the steeper portion of the curve in Figure 3.11.

3.4.2. Solution Algorithm

Of the original six unknowns, T_e , T_g , T_{exa} , T_{exi} , n_a , and n_i , the only ones remaining to be calculated after the simplifying assumptions are applied are T_e , T_g , and n_a . Equations (3.21), (3.22), and (3.26) are used in the algorithm to solve for these quantities. The program for this non-LTE based analysis is called NONLTE and is listed in Appendix A. The logic proceeds as follows:

- 1) Read the values of n_e , $T_{LTE,7147}$, $T_{LTE,4610}$, and $(n_m/g_m)_{7147}$ from preliminary results data files. Set $T_{exa} = T_{LTE,7147}$, $T_{exi} = T_{LTE,4610}$, and $n_i = n_e$.
- 2) Make an initial estimate for n_a from (3.26) with $Z_{exa} = 1$.
- 3) Make an initial estimate of electron kinetic temperature, $T_e = 16000$ K, and an initial estimate of the heavy kinetic temperature, $T_g = 5000$ K.
- 4) Calculate the plasma Debye length from (3.13) and the lowered ionization potential with (3.12).
- 5) Calculate the partition functions.
- 6) Calculate n_a from (3.26) with the new lowered ionization potential and partition function.
- 7) Calculate T_e from (3.22), rearranged so that the new T_e comes from the electron translational partition function and appears as a function of the T_e from the previous iteration:

$$T_e = \left(\frac{h^2}{2\pi m_e k_b} \right) \left[\frac{n_e}{2} \left(\frac{n_i}{n_a} \right)^{(T_g/T_e)} \frac{Z_{exa}^{(T_{exa}/T_e)}}{Z_{exi}^{(T_{exi}/T_e)}} \exp\left(\frac{E_{ia}}{k_b T_e}\right) \right]^{(2/3)} \quad (3.27)$$

where T_e is from the previous iteration.

- 8) Calculate n_i from quasi-neutrality.
- 9) Calculate the Debye-Hückel pressure correction from (3.20).

10) Calculate the system pressure from (3.21). If the calculated pressure is not close enough to the known system pressure to satisfy a convergence criterion, then T_e is under-relaxed so that:

$$T_e = T_e^* + R (T_{e,calc} - T_e^*) \quad (3.28)$$

T_g is incremented upward, and the procedure is repeated starting at step 4).

3.4.3. Alternative Solution Methods

The purpose of the neutral Boltzmann approximation is to facilitate the calculation of the neutral particle number density in the absence of an independent equation. It is possible to calculate all of the above quantities without having to make the neutral Boltzmann approximation. In order to do that, at least one more equation needs to be presented and solved. The most obvious choice is an electron energy conservation equation.

Assuming that n_e is still known from experimental results, as are the highest effective level populations of both the neutrals and ions, an alternative algorithm might proceed as follows:

- 1) Guess initial values for all quantities, except T_g .
- 2) Calculate T_g from the gas equation of state (3.21).
- 3) Calculate n_a from the non-LTE ionization equation (3.22).
- 4) Calculate T_{exa} from neutral Boltzmann factors (3.10).
- 5) Calculate T_{exi} from ionic Boltzmann factors (3.23).
- 6) Calculate n_i from quasi-neutrality (3.24).
- 7) Calculate T_e from the electron energy equation (3.29) (see below).
- 8) Repeat from step 2) if the calculated variables have not converged.

The problem with this algorithm lies in the formulation of the electron energy equation for this LSP. It is typically hypothesized that the plasma flow field is two-dimensional and axisymmetric [Jeng and Keefer, 1986; Eguiguren, 1989]. Therefore the convection terms in

the electron energy equation require knowledge of the plasma bulk velocity components in the axial and radial directions.

The axisymmetric electron energy equation for variable electron thermal conductivity is [Mertogul, 1992]:

$$\begin{aligned} \frac{\partial}{\partial x} \left(\left(\frac{3}{2} n_e k_b u \right) T_e \right) + \frac{1}{r} \frac{\partial}{\partial r} \left(\left(\frac{3}{2} r n_e k_b v \right) T_e \right) = \\ \frac{\partial}{\partial x} \left(\lambda_e \frac{\partial T_e}{\partial x} \right) + \frac{1}{r} \frac{\partial}{\partial r} \left(r \lambda_e \frac{\partial T_e}{\partial r} \right) - \left(n_e k_b \frac{\partial u}{\partial x} \right) T_e - \left(\frac{n_e k_b}{r} \frac{\partial}{\partial r} (r v) \right) T_e + \end{aligned} \quad (3.29)$$

(Absorption - Elastic + Inelastic - Radiation)

where the last four terms are source terms representing laser beam absorption, elastic collision transfer, inelastic collision transfer, and radiation loss. The velocity components, u for the axial and v for the radial, must then be found from the full solution of the two-dimensional axisymmetric equations of motion along with the conservation of mass equation. These are written out as follows, for example by Mertogul [1992]:

The mass conservation equation for a variable density axisymmetric cylindrical system is:

$$\frac{\partial}{\partial x} (\rho u) + \frac{1}{r} \frac{\partial}{\partial r} (r \rho v) = 0 \quad (3.30)$$

The axisymmetric axial momentum equation for variable density and viscosity is:

$$\frac{\partial}{\partial x} (\rho u u) + \frac{1}{r} \frac{\partial}{\partial r} (r \rho u v) = \quad (3.31)$$

$$\frac{4}{3} \frac{\partial}{\partial x} \left(\mu \frac{\partial u}{\partial x} \right) + \frac{1}{r} \frac{\partial}{\partial r} \left(\mu r \frac{\partial u}{\partial r} \right) - \frac{2}{3} \frac{\partial}{\partial x} \left(\mu \frac{\partial v}{\partial r} \right) - \frac{2}{3r} \frac{\partial}{\partial x} \left(\mu v \right) + \frac{1}{r} \frac{\partial}{\partial r} \left(\mu r \frac{\partial v}{\partial x} \right) - \frac{\partial p}{\partial x} - \rho g$$

The axisymmetric radial momentum equation for variable density and viscosity is:

$$\begin{aligned}
 & \frac{\partial}{\partial x}(\rho uv) + \frac{1}{r} \frac{\partial}{\partial r}(r \rho vv) = \\
 & \frac{\partial}{\partial x}\left(\mu \frac{\partial v}{\partial x}\right) + \frac{4}{3r} \frac{\partial}{\partial r}\left(\mu r \frac{\partial v}{\partial r}\right) + \frac{\partial}{\partial x}\left(\mu \frac{\partial u}{\partial r}\right) \\
 & - \frac{2}{3r} \frac{\partial}{\partial r}\left(\mu r \frac{\partial u}{\partial x}\right) + \frac{2\mu}{3r} \frac{\partial u}{\partial x} - \frac{\partial p}{\partial r} - \frac{4\mu v}{3r^2} - \frac{2v}{3r} \frac{\partial \mu}{\partial r}
 \end{aligned} \tag{3.32}$$

These equations can be solved using the SIMPLE (Semi-IMplicit Pressure Linked Equations) algorithm of Patankar [1980] without too much difficulty for simple flowfields. However, the fields for which this algorithm converge do not correspond to physical plasma flows, i.e., the gas is uniformly hot throughout the calculation domain, with correspondingly high electron number densities and kinetic equilibrium.

When cold gas is allowed to enter the inlet of the domain, as it would in a physical flow, and the measured values of electron number density are imposed on the plasma domain interior, the algorithm becomes unstable. This seems to be due to the algorithm's sensitivity to the initial values guessed for the flow variables T_e , u , v , and ρ (bulk mass density), which are extremely difficult to know in advance for a non-LTE flow.

This method was not pursued further in this investigation because the time and expense required to arrive at a stable algorithm were not justified in light of the relative simplicity of the non-LTE analysis described in the previous section. Fully numerical two-dimensional non-LTE plasma simulations, i.e. those not relying on measured values of electron number density or level populations, are required as future work in this field and will be discussed in Chapter 5.

3.4.4. Thermal Conversion Efficiency

The biggest drawback of not solving for the velocity field as part of a solution algorithm in this investigation is that the thermal conversion efficiency of the LSP cannot be calculated.

Knowing only the various temperatures associated with the non-LTE LSP allows the calculation of energy density, [J/m³], at any point in the plasma measurement domain, but not the total power of the flow, [J/s], entering or leaving the domain as a combined result of conduction or convection. The conversion of energy density to power goes as follows, assuming the flow is one-dimensional (axial) at the domain inlet and outlet:

$$\text{Power [W]} = (\text{E-Density [J/m}^3\text{]}) \times (\text{Flow Speed [m/s]}) \times (\text{Area [m}^2\text{]}) \quad (3.33)$$

The increase in flow power between the inlet and the outlet gives the thermal conversion efficiency when divided by the incident laser power:

$$\eta_{th} = \left(\frac{\text{Power}_{out} - \text{Power}_{in}}{P_{laser}} \right) = \frac{\dot{m} C_p \Delta T}{P_{laser}} \quad (3.34)$$

where ΔT is the mass averaged increase in temperature that might be measured with thermocouples in a laboratory LSP.

As a result no comparisons will be made concerning LSP thermal conversion efficiency. None the less the global absorption which is calculated in this investigation provides a very useful comparison standard for the non-LTE analysis and other methods for predicting or measuring LSP performance.

4. RESULTS AND DISCUSSION

There are two main bodies of results which are discussed. The preliminary results include the argon line emission coefficients, electron number density from H_{α} , and LTE temperature and composition. The non-LTE results include the kinetic temperatures T_e and T_g . Global absorption is calculated from the non-LTE analysis as are the various energy density pools. Comparisons are made to the results of the LTE numerical model of Eguiguren [1989]. The LSP conditions for which all analyses are based are 5 kW incident laser power, an f/4 beam focusing geometry, and $13.8 \text{ kg/m}^2\text{s}$ incident argon mass flux. This mass flux corresponds to a flow velocity of 8.5 m/s at one atmosphere system pressure.

4.1. PRELIMINARY RESULTS

4.1.1. Argon Line Emission Coefficients.

Contour plots of the emission coefficient for the argon neutral lines at 6753 Å and 7147 Å are shown in Figure 4.1. The quantity actually plotted is that which results from the Abel inversion of the lateral radiance profiles. The conversion to line emission coefficient requires dividing the values on the plot by the radial scaling factor 0.05588 cm. The origin of the horizontal axis represents the laser focus, and the dashed lines show the path of the laser beam's inner and outer diameters through the plasma. The axes are scaled equally so that the actual proportions of the plasma emission are preserved. Both the gas flow and laser propagation are left to right in all contour plots.

Similar contour plots for the 4610 Å and 4658 Å argon ion lines are shown in Figure 4.2. The most significant feature of Figures 4.1 and 4.2 is that the two neutral line plots have approximately the same shape and size, as do the two ion line plots, but the spatial extent of the ion emission is much smaller than the neutral, and almost completely upstream of the laser focus. The line emission coefficients are directly related to the heavy particle number densities through equations (3.7) and (3.26).

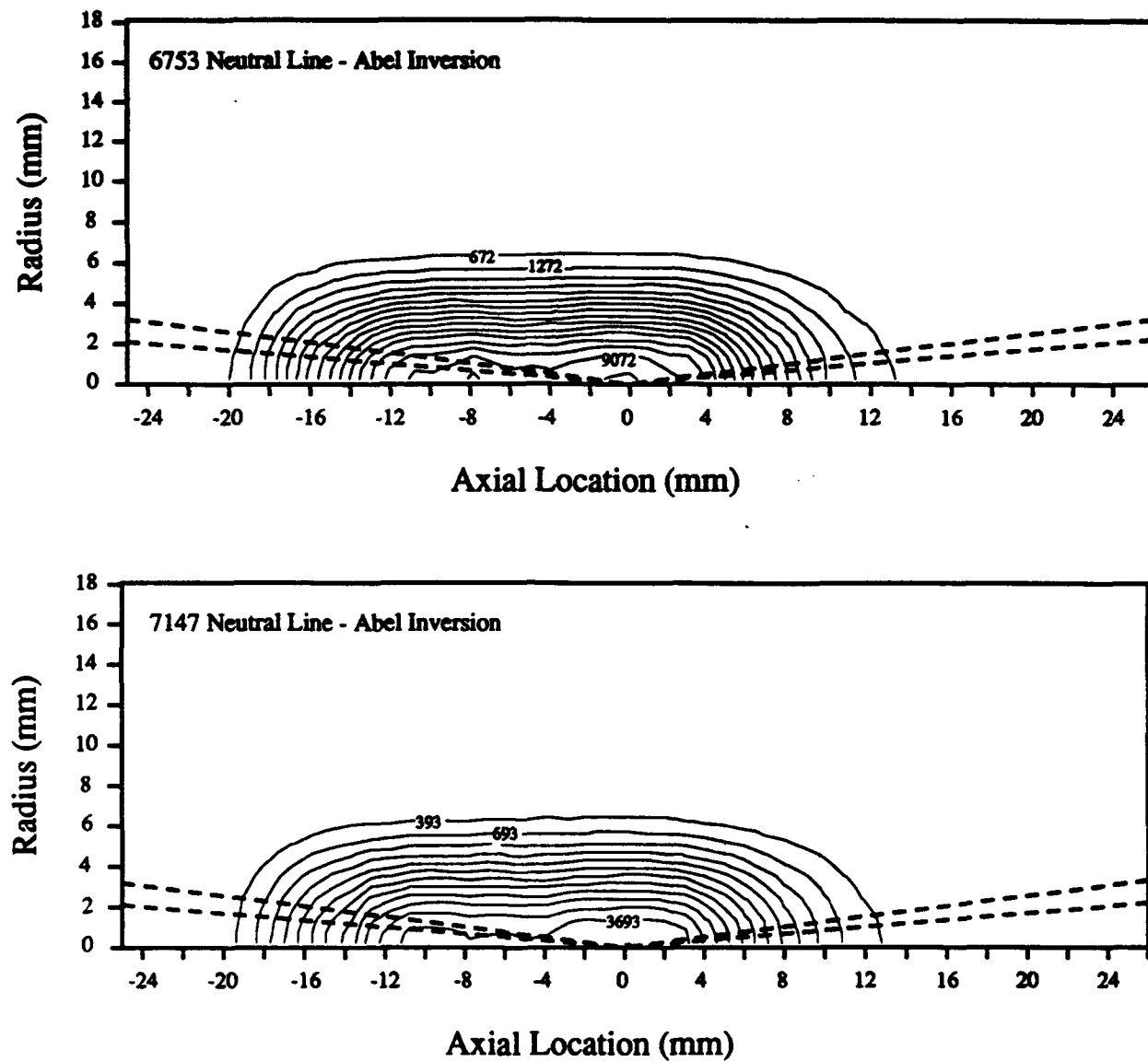


Figure 4.1 Neutral argon emission coefficient contours for the 6753 Å and 7147 Å lines. Divide by 0.05588 cm for units of [$\mu\text{W}/\text{cm}^3\text{Sr}$].

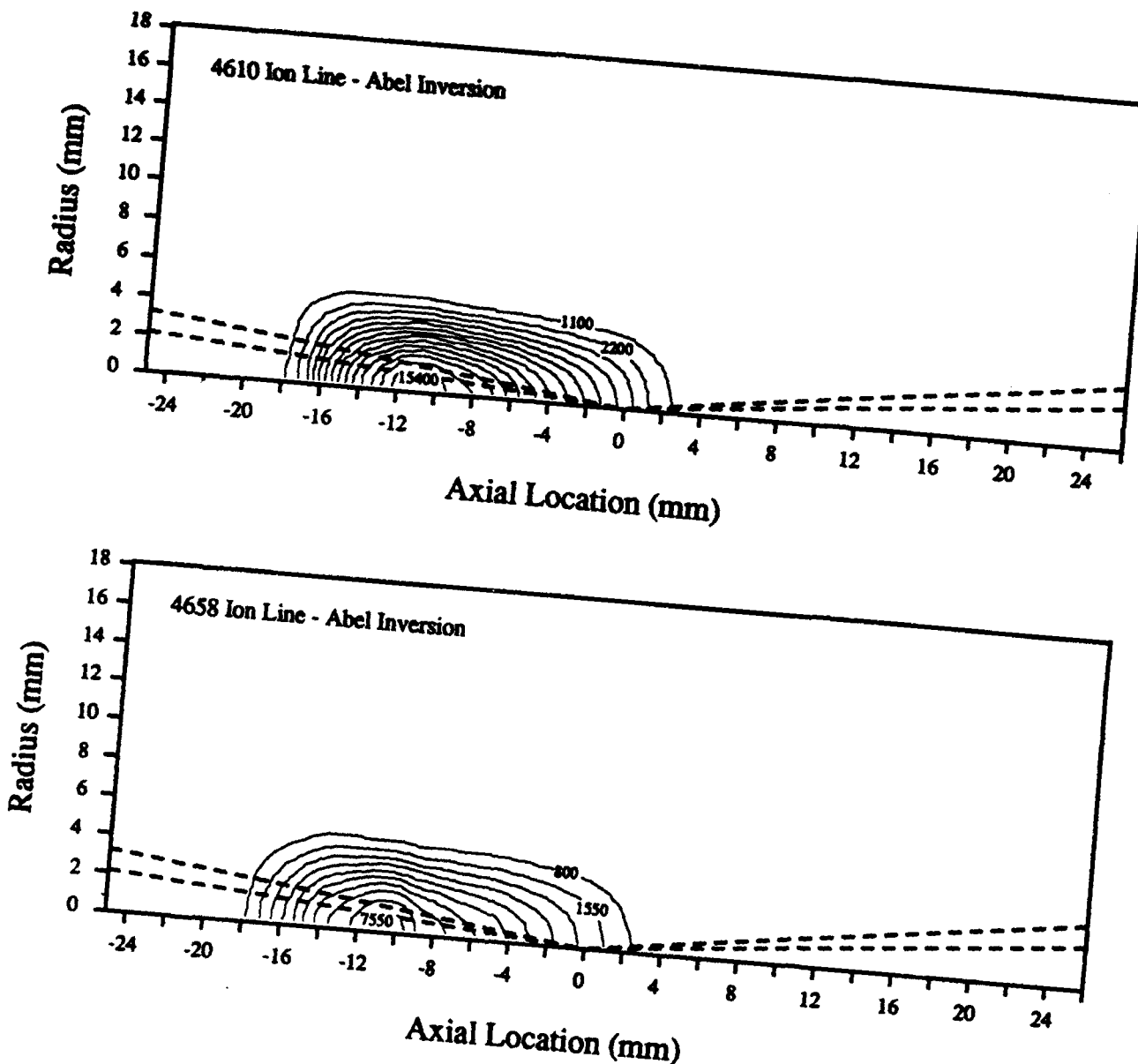


Figure 4.2 Ionic argon emission coefficient contours for the 4610 \AA and 4658 \AA lines.
Divide by 0.05588 cm for units of $[\mu\text{W}/\text{cm}^3\text{Sr}]$.

In LTE, changes in the number densities of neutrals and ions are inversely related by the Saha equation (1.11), but as can be seen by comparing the centerline values of emission coefficient at axial locations -10 mm and +2 mm in Figures 4.1 and 4.2, this is not the case in this plasma. Notice the line emission and therefore the neutral particle density is approximately unchanged between these two axial locations, whereas the ion density decreases significantly. This non-LTE effect will be explained in the context of the kinetic temperature nonequilibrium results appearing later in this chapter, as the two effects are closely related.

4.1.1.1. Boltzmann Plots

Figures 4.3 - 4.6 contain Boltzmann plots made using the populations of the upper levels in the 6753 Å and 7147 Å transitions in neutral argon. Figures 4.3 and 4.4 show a progression of plots at 6 mm increments along the plasma centerline starting at 12 mm downstream of the laser focus and ending 18 mm upstream of the laser focus. The slope between the two upper level points corresponds to the upper level excitation temperature, $T_{ex\beta,a}$. The slope between the lower energy level and the ground state corresponds to the LTE temperature of that level (also assumed to be the total excitation temperature, $T_{ex,a}$). There are two points plotted at the ground state corresponding to natural $\log(n_a/Z_{ex,a})$ calculated from the LTE temperatures of the two upper energy level populations. These two ground level densities are virtually indistinguishable on the Boltzmann plot, but small differences will be apparent when plotted on a linear ordinate. Figures 4.5 and 4.6 are similar except that they contain plots corresponding to a radius of 3.9 mm.

The key feature of all these Boltzmann plots is the near equivalence of the LTE temperatures and of the neutral densities predicted from these temperatures. The estimated error in the LTE temperature and neutral particle density determinations are $\pm 3\%$ and $\pm 9\%$ respectively. (All error analyses are shown in Appendix B). $T_{ex\beta,a}$ does not agree as well with the LTE temperatures, but has a larger estimated error of $\pm 7\%$. More importantly, $T_{ex\beta,a}$ is lower than both LTE temperatures at every point in the LSP. This indicates that the error may

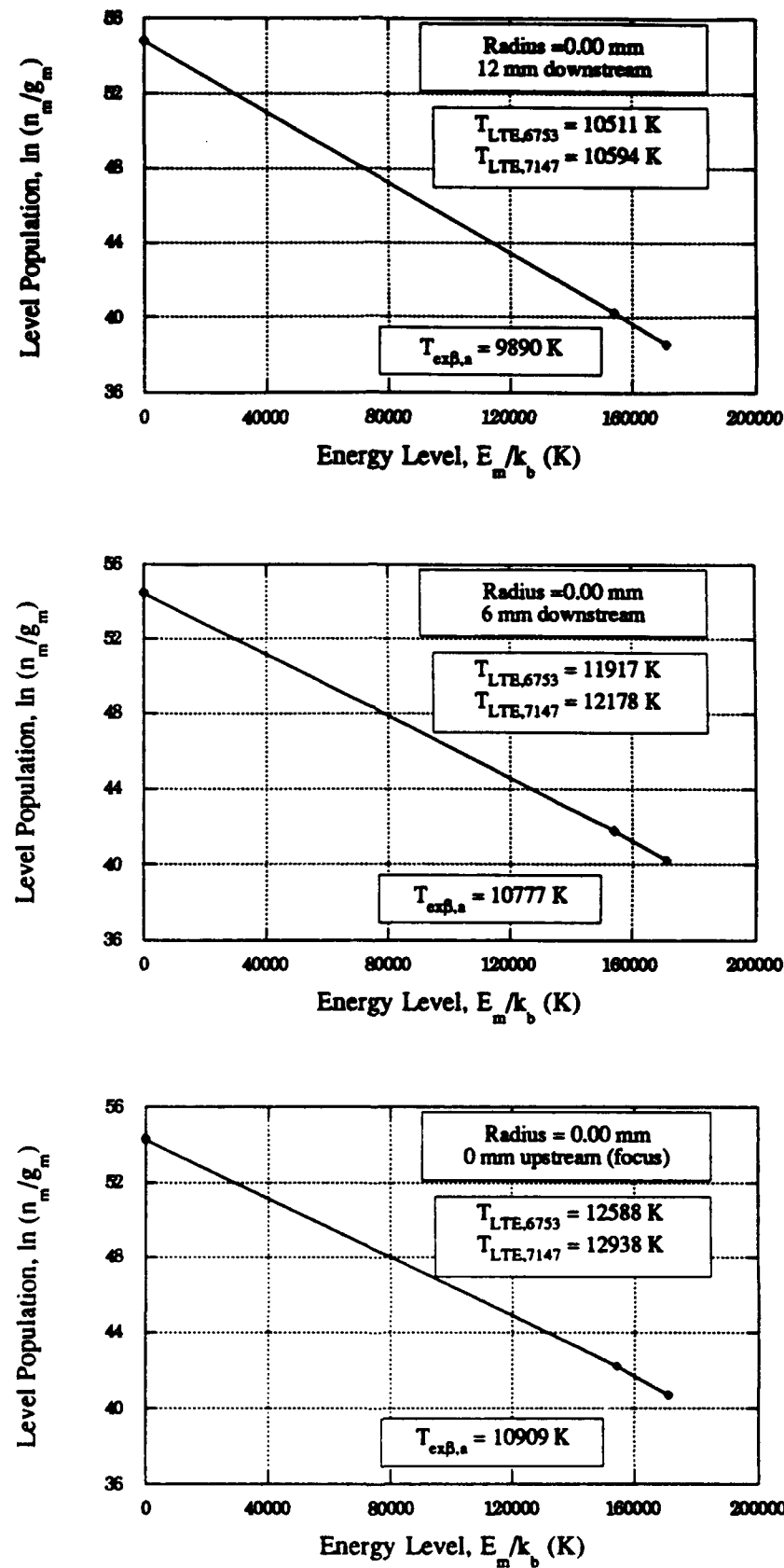


Figure 4.3 Boltzmann plots for neutral argon showing $T_{\text{exB,a}}$ and the LTE temperatures for the 6753 Å and 7147 Å lines. Three axial locations shown for 0 mm radius.

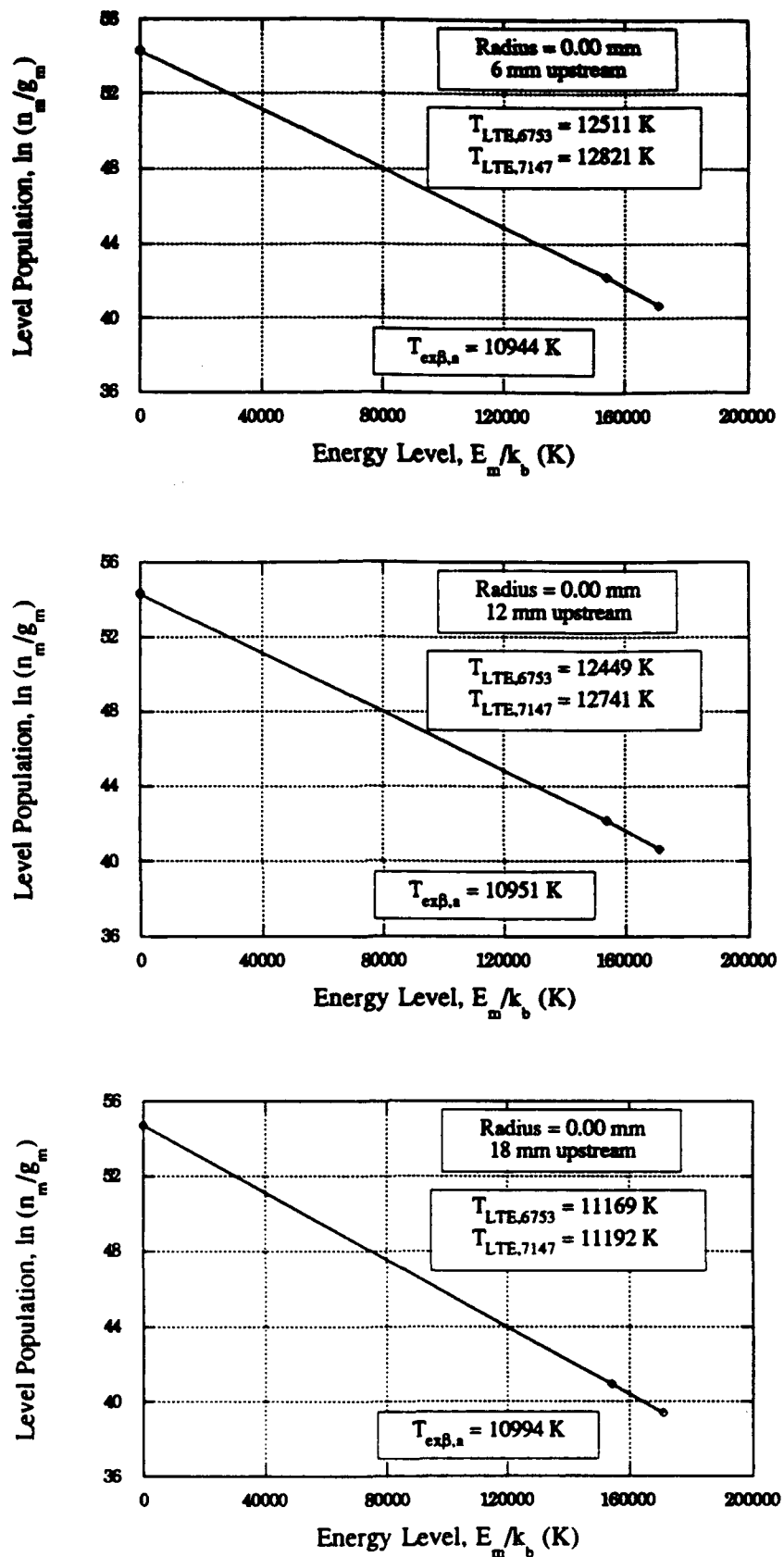


Figure 4.4 Boltzmann plots for neutral argon showing $T_{\text{ex}\beta,a}$ and the LTE temperatures for the 6753 Å and 7147 Å lines. Three axial locations shown for 0 mm radius.

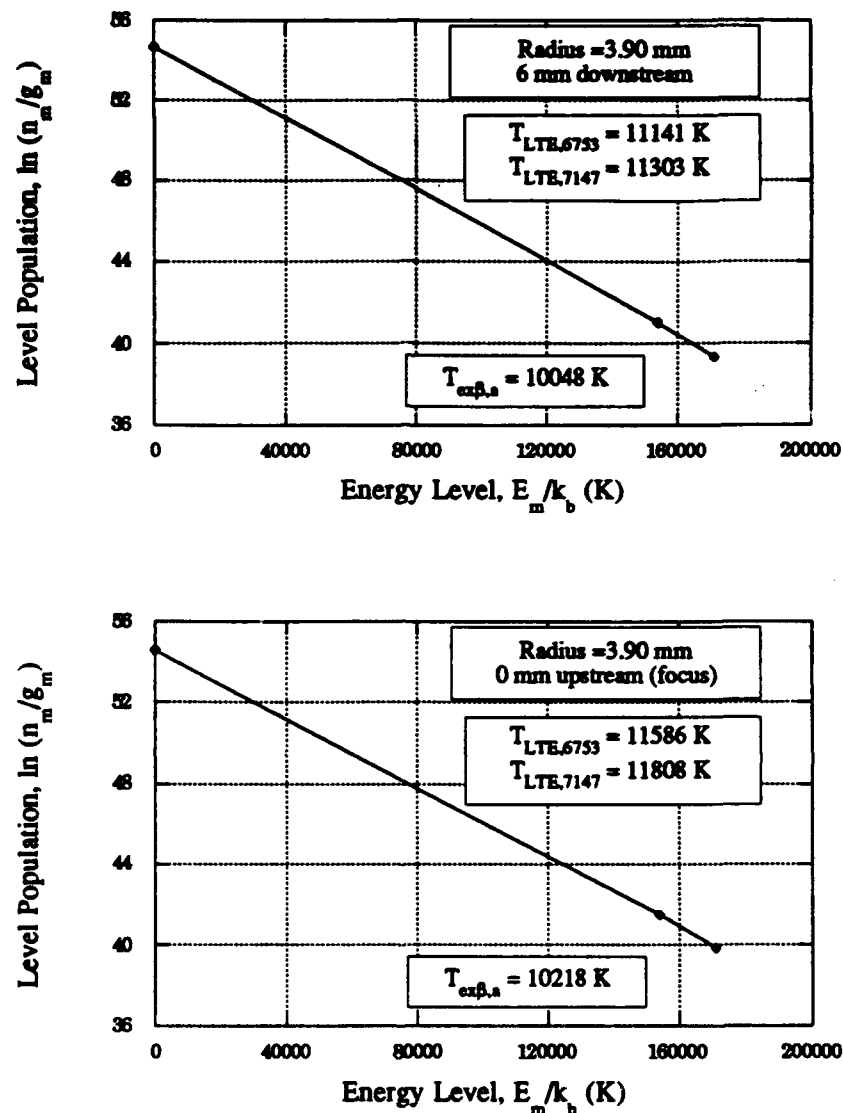


Figure 4.5 Boltzmann plots for neutral argon showing $T_{ex\beta,a}$ and the LTE temperatures for the 6753 Å and 7147 Å lines. Two axial locations shown for 3.9 mm radius.

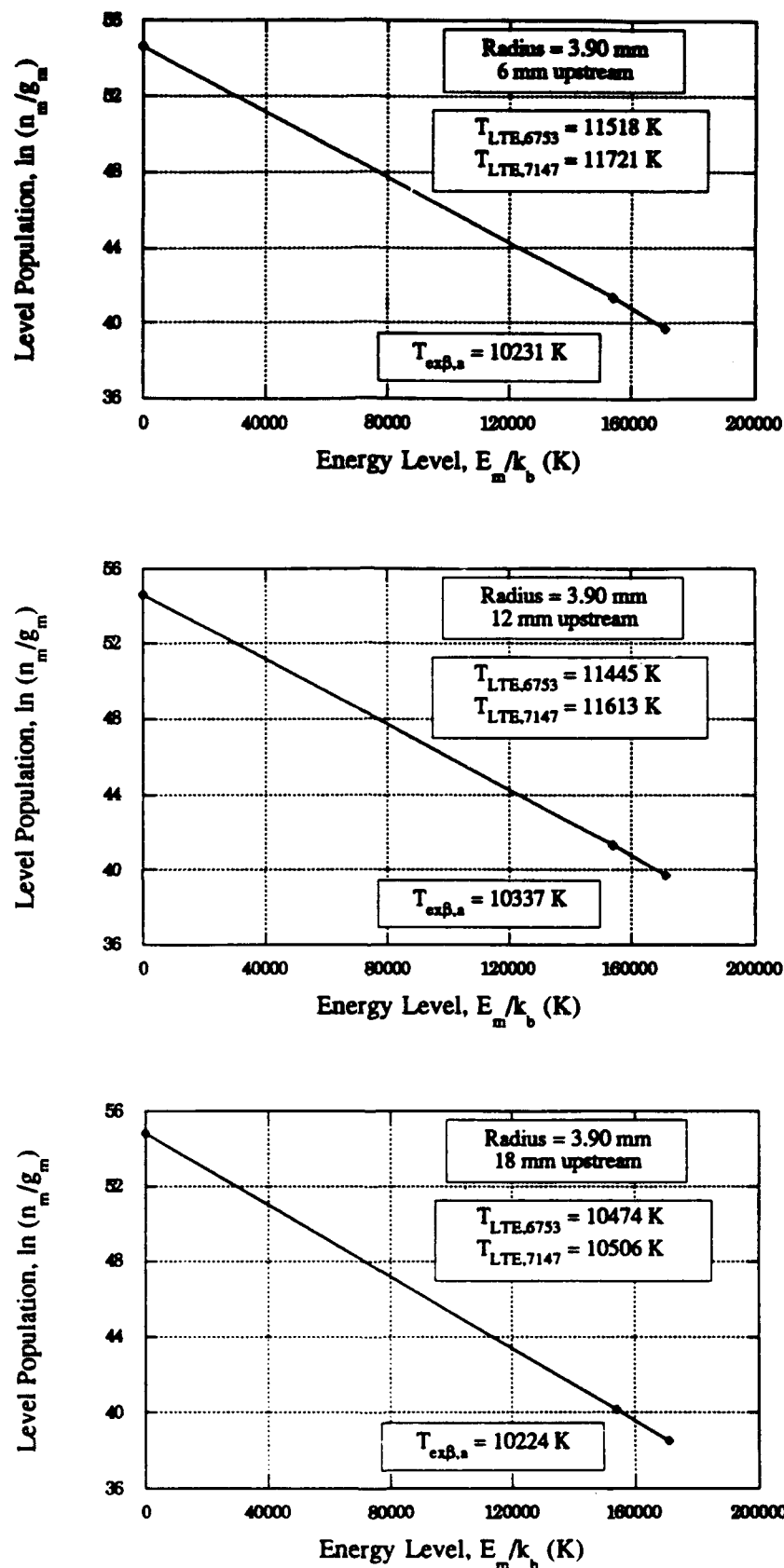


Figure 4.6 Boltzmann plots for neutral argon showing $T_{\text{ex}\beta,a}$ and the LTE temperatures for the 6753 Å and 7147 Å lines. Three axial locations shown for 3.9 mm radius.

be systematic in nature and possibly due to inaccuracy in the spontaneous emission coefficients for these argon lines. Although this is not necessarily true, it seems none the less that the neutral particle electronic system is in near Boltzmann equilibrium. The significance of this conclusion is that the neutral Boltzmann approximation used to calculate n_a from the 7147 Å line LTE temperature can be used with greater confidence.

A comparison of $T_{ex\beta,a}$ and the LTE temperature from the 6753 Å line is shown in Figure 4.7 for the entire neutral line measurement domain. The contours in the excitation temperature plot are less smooth due to the higher uncertainty in the calculation of $T_{ex\beta,a}$ as compared to T_{LTE} .

Figures 4.8 and 4.9 contain Boltzmann plots made using the populations of the upper levels in the 4610 Å and 4658 Å transitions in ionic argon. The axial progression is similar to that of the neutral Boltzmann plots, except that the domain is shorter and the radial location shown in Figure 4.9 is only 2.9 mm off the centerline. Again, the LTE temperatures are very close together, even more so than for the neutral lines, and the ground state populations predicted from each line are completely indistinguishable on the Boltzmann plot. The upper level excitation temperature is generally quite higher than the LTE temperatures, but the estimated error is $\pm 12\%$ due to large uncertainty in the spontaneous emission coefficients and the relatively close spacing of the upper levels of the transitions as compared to the calculated excitation temperature. Figure 4.10 contains a comparison of the upper level excitation and LTE temperature contours for the entire ion measurement domain.

A similar conclusion can be drawn from the ionic Boltzmann plots as is drawn from the neutral plots above. It is clear that the ion electronic system is in near Boltzmann equilibrium, and that n_i can be determined with confidence from an LTE analysis of a single ion line. A comparison of the ion number density calculated in this way to the electron number density calculated from H_α Stark broadening confirms this claim.

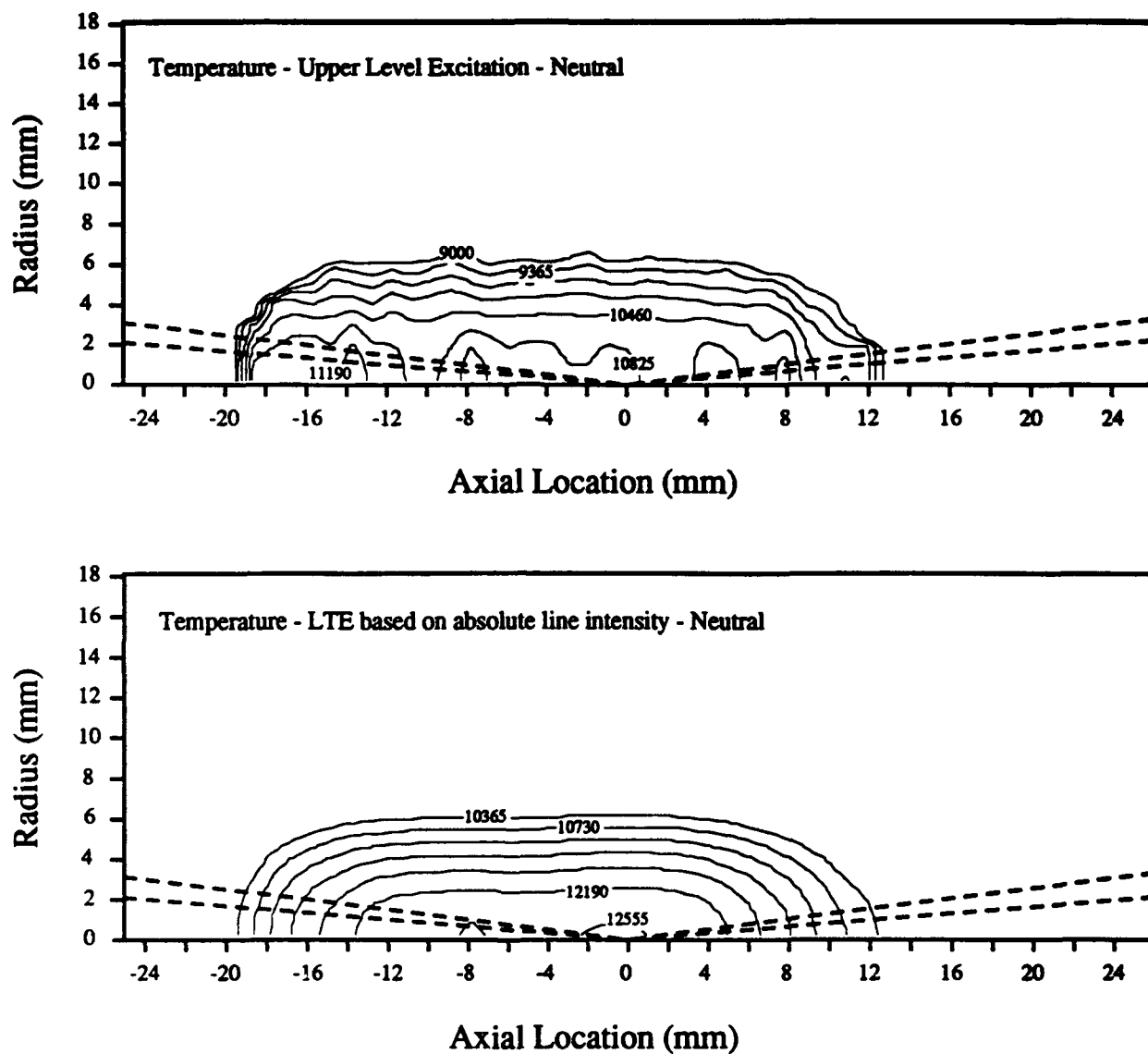


Figure 4.7 A comparison of the temperature contours for $T_{\text{ex}\beta,a}$ and $T_{\text{LTE},6753}$

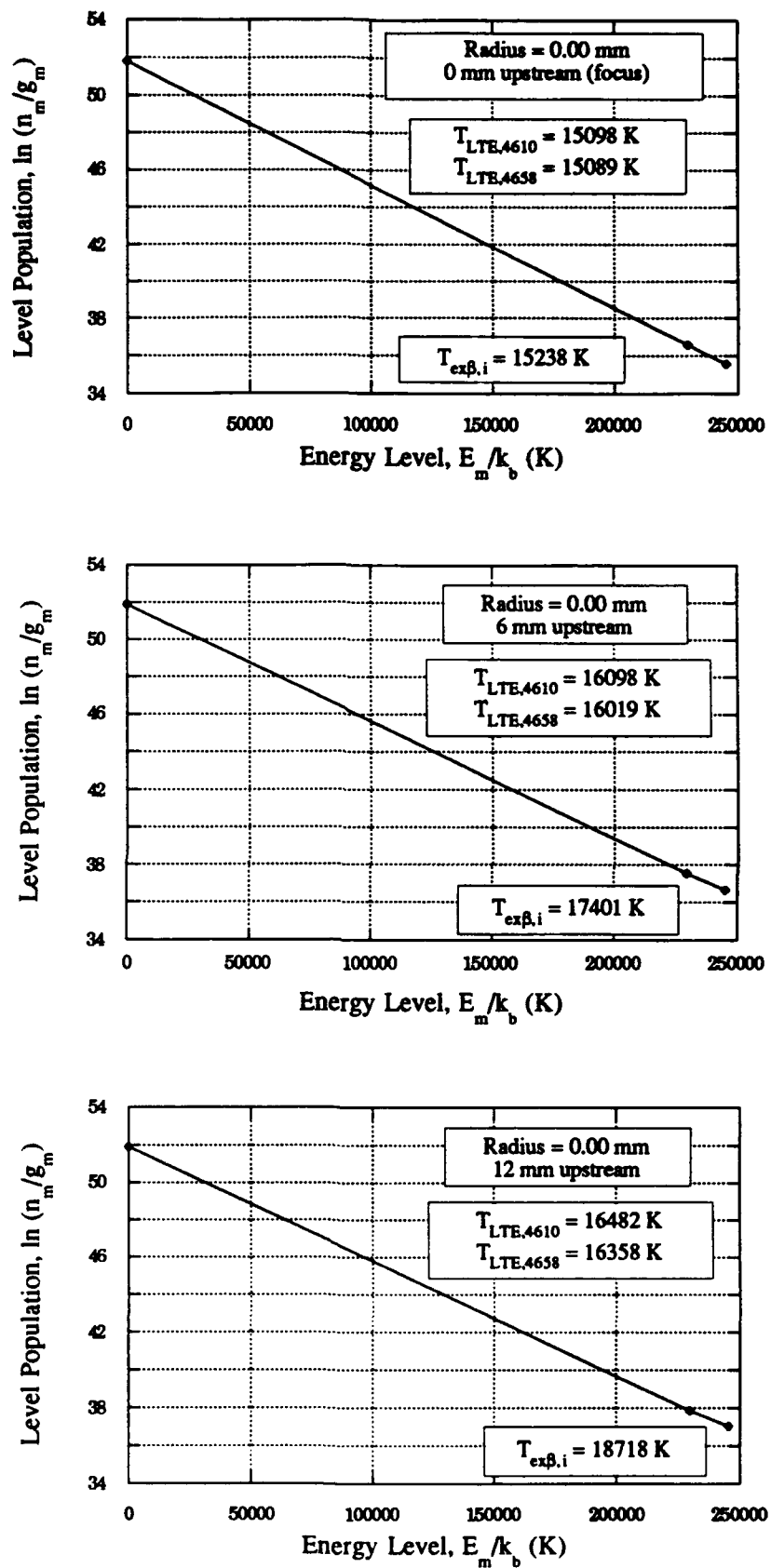


Figure 4.8 Boltzmann plots for ionic argon showing $T_{ex\beta,i}$ and the LTE temperatures for the 4610 Å and 4658 Å lines. Three axial locations shown for 0 mm radius.

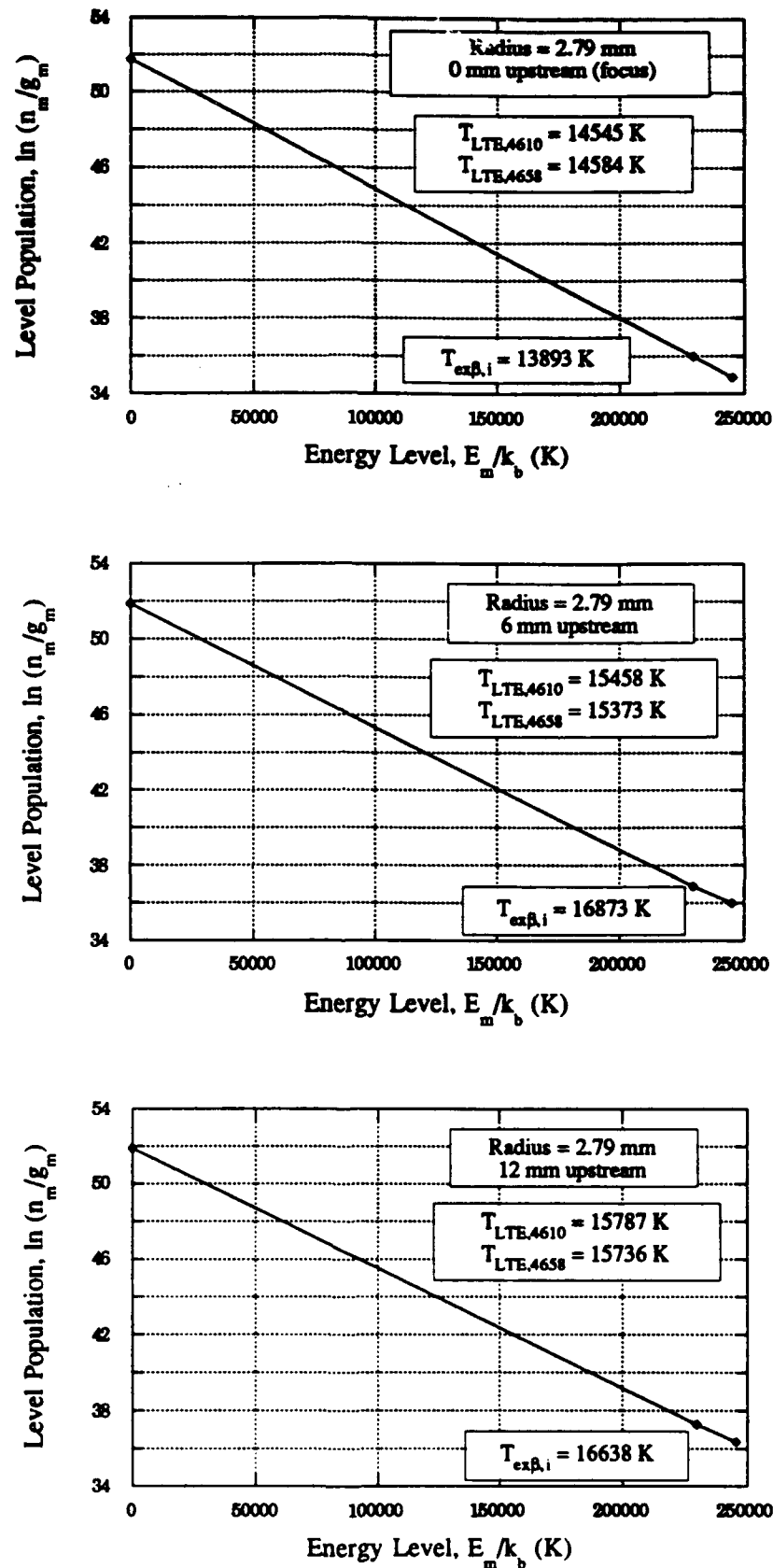


Figure 4.9 Boltzmann plots for ionic argon showing $T_{\text{exp},i}$ and the LTE temperatures for the 4610 Å and 4658 Å lines. Three axial locations shown for 2.9 mm radius.

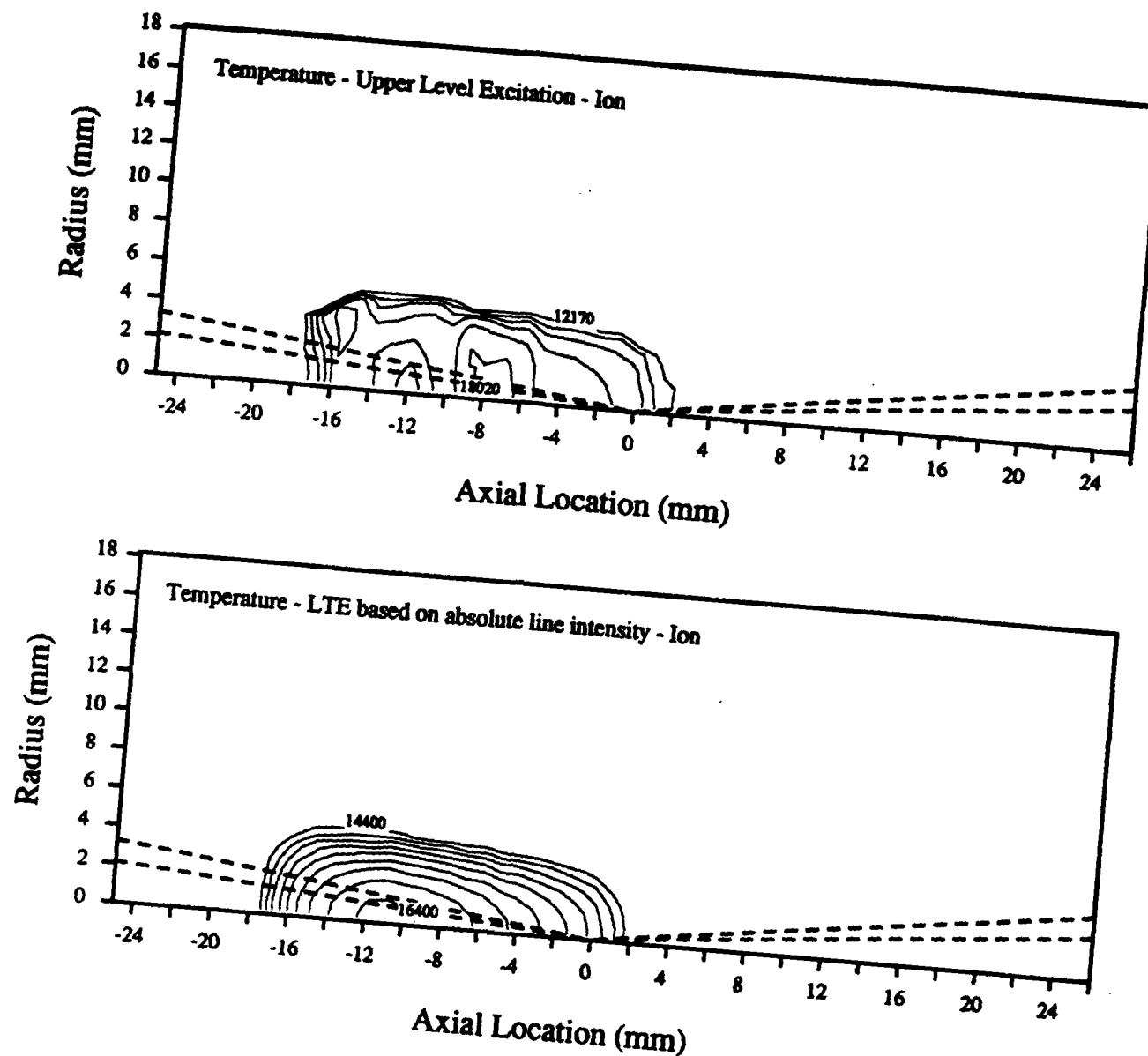


Figure 4.10 A comparison of the temperature contours for $T_{\text{ex}\beta,i}$ and $T_{\text{LTE},4610}$.

4.1.2. Number Densities

4.1.2.1. Electron Number Density

Figure 4.11 contains contour plots of electron number density as calculated by H_{α} Stark broadening analysis and by LTE analysis of the 4610 Å argon ion line emission. The agreement between these two contours is excellent. The radial and axial extent of the contour corresponding to $1.65 \times 10^{23} \text{ m}^{-3}$ in the H_{α} plot is almost identical to the $1.6 \times 10^{23} \text{ m}^{-3}$ contour on the ion LTE plot. The central contours near $2 \times 10^{23} \text{ m}^{-3}$ on each plot also agree quite well. The estimated error in the H_{α} electron number density determination is $\pm 7\%$. It is assumed that if the vidicon detector range allowed more extensive ion measurements, the results in the downstream region of the LSP would agree with the H_{α} results as well.

Figures 4.12 - 4.14 are a series of plots comparing the radial variation of electron number density as calculated by three different methods. The six plots show an axial progression starting at the laser focus (0 mm) and going to 15 mm upstream of the focus at increments of 3 mm. The H_{α} and ion LTE determinations agree quite well at all axial and radial locations, but the neutral LTE determination is clearly not in agreement.

The agreement between two completely independent methods for determining electron number density tends to confirm the validity of both methods. The disagreement with a third method is also significant. These results are important for two main reasons. First, it shows the large error that is introduced into the LSP electron number density determination if only LTE analysis of neutral argon emission is used. This is a rather simple method, but should be avoided in similar investigations due to its inaccuracy. Second, for argon LSP's at atmospheric pressure it may be necessary to use only the LTE analysis of a suitable argon ion line for electron number density determination (assuming quasi-neutrality with $n_e = n_i$). This eliminates the need for the somewhat involved calculations required for the undertaking of Stark broadening analysis. Also, the conditions on critical electron number density set out by Drawin [1969] and Griem [1964] (equations (1.15) and (1.16), respectively) seem to be valid

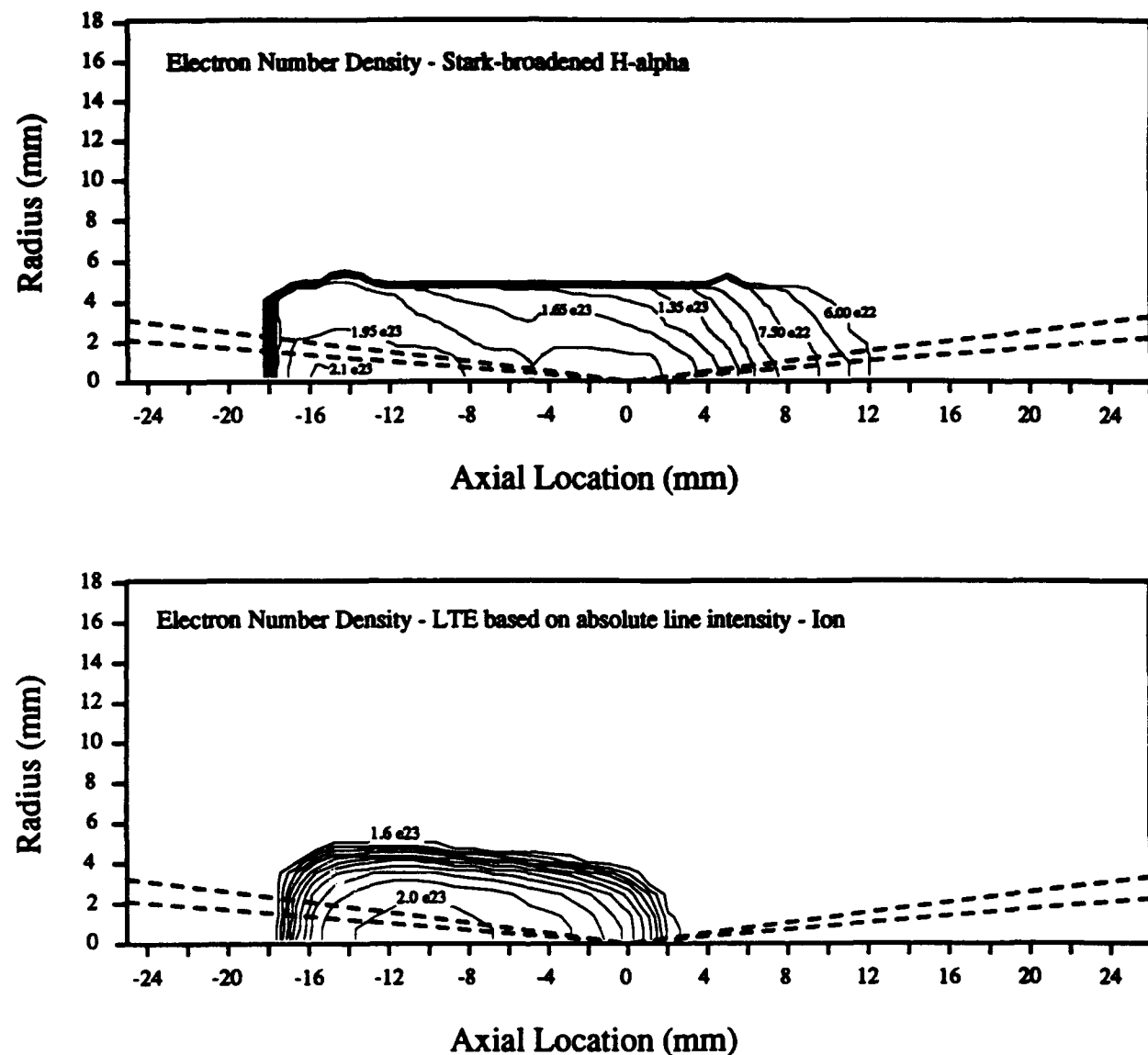


Figure 4.11 A comparison of the electron number density contours from Stark-broadened H_{α} and the 4610 Å argon ion line.

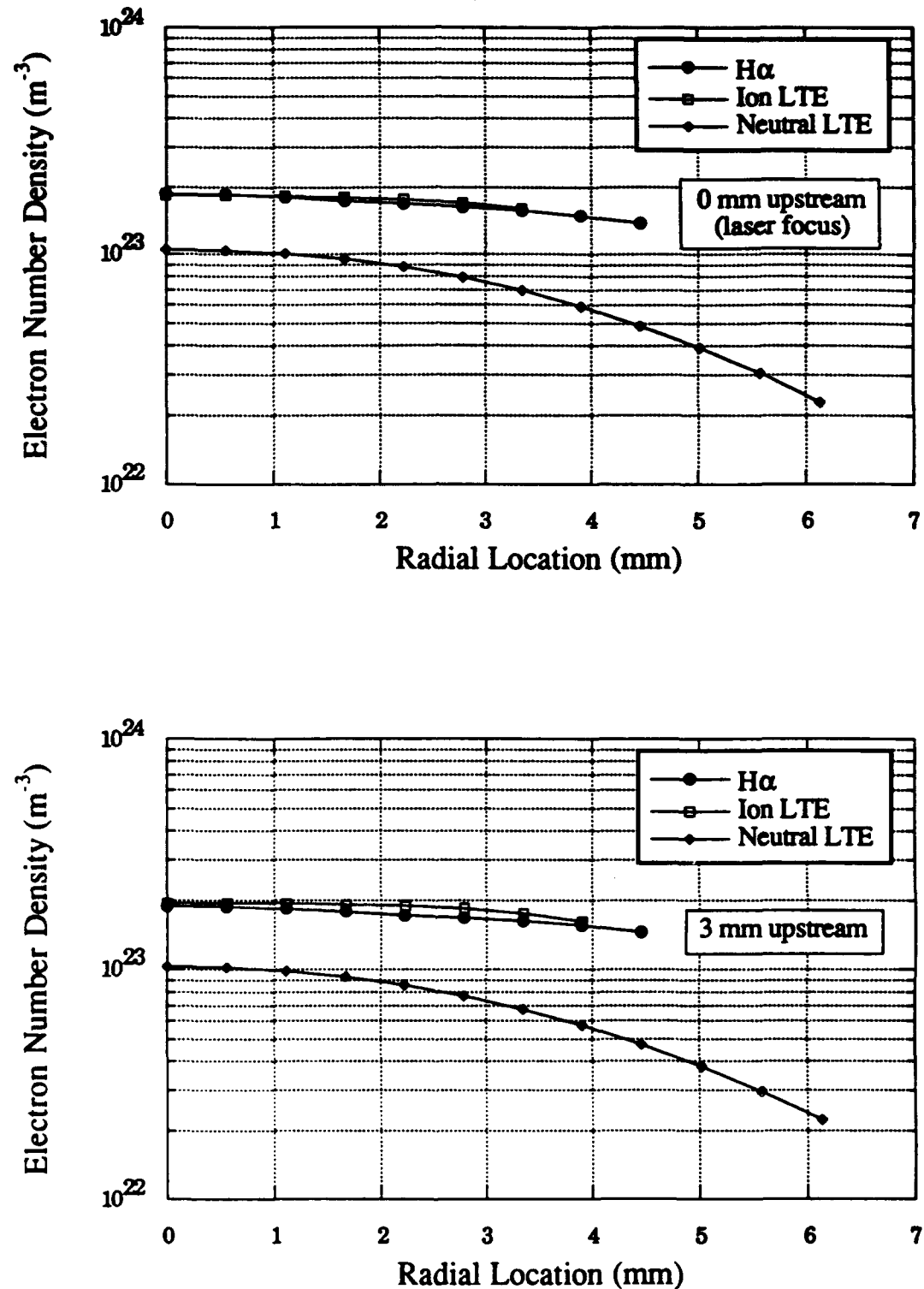


Figure 4.12 Radial comparisons of electron number density calculated by three methods. Two axial locations are shown.

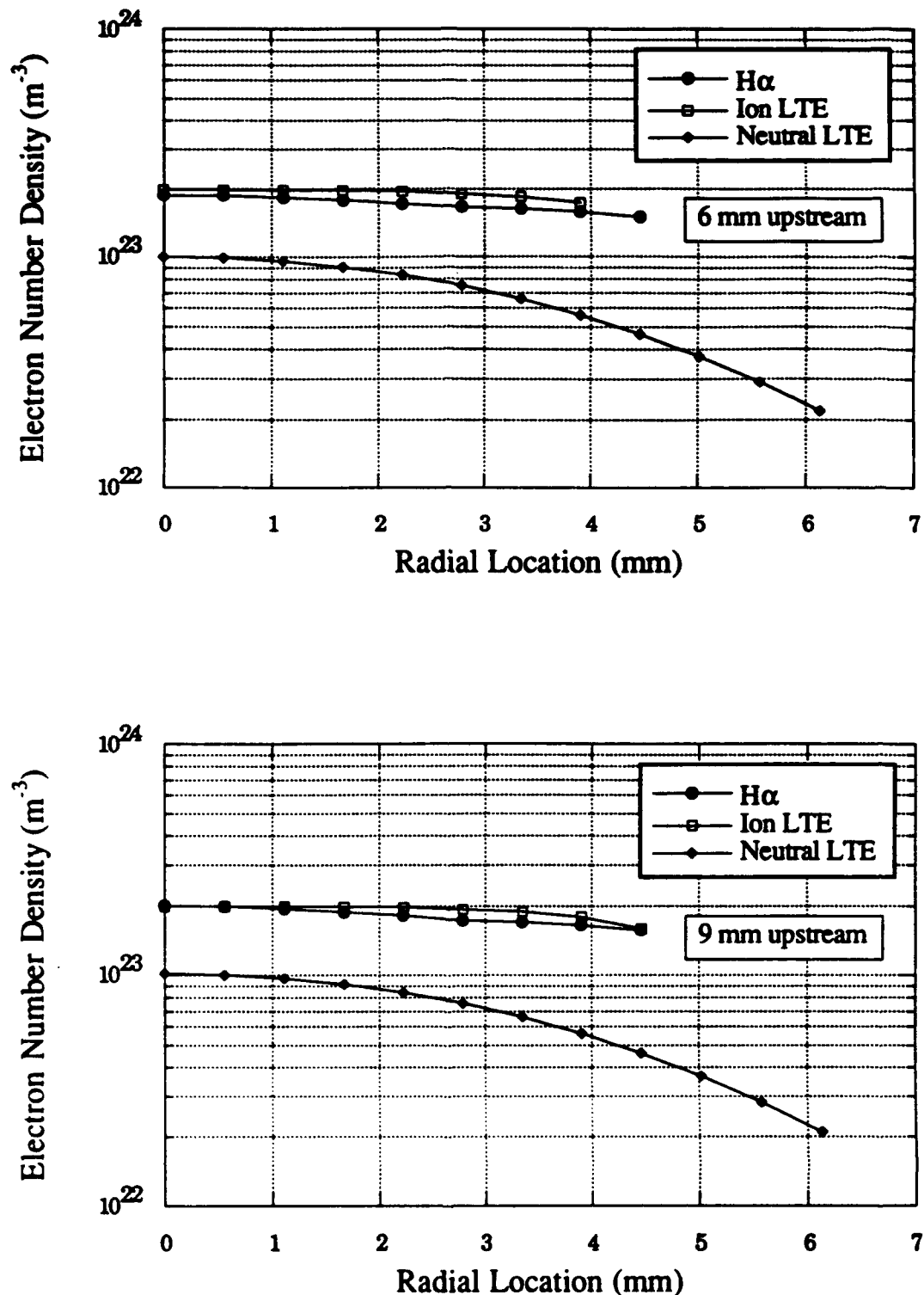


Figure 4.13 Radial comparisons of electron number density calculated by three methods. Two axial locations are shown.

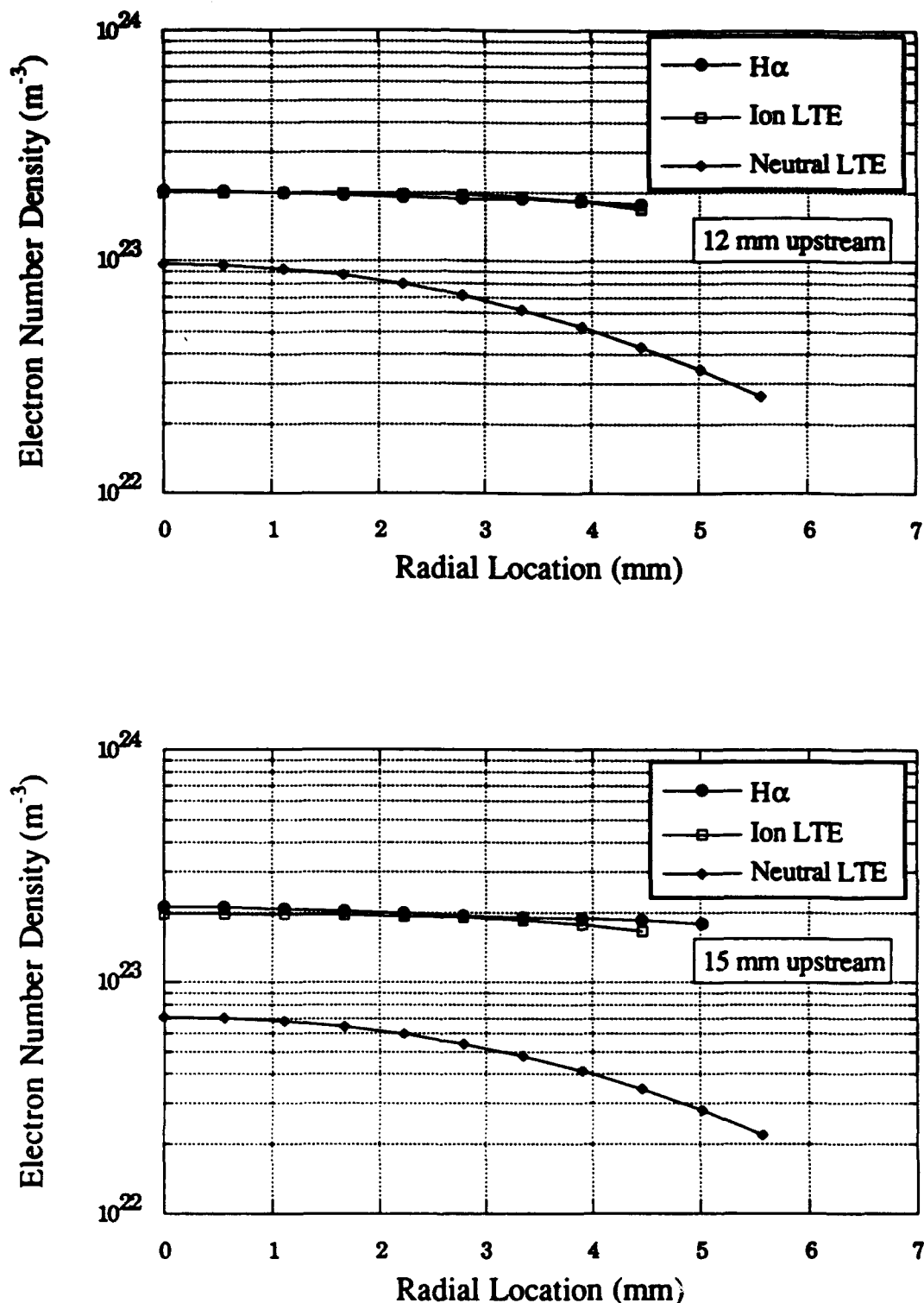


Figure 4.14 Radial comparisons of electron number density calculated by three methods. Two axial locations are shown.

for this LSP as applied to the ions, and may be used as a check before using the ion LTE electron number density determination.

4.1.2.2. Neutral Particle Number Density

Figures 4.15 - 4.17 are a series of plots comparing the radial variation of neutral particle number density as calculated from the LTE analysis of the two neutral lines. The six plots show an axial progression starting 12 mm downstream of the laser focus and going to 18 mm upstream of the focus at increments of 6 mm. The difference between the two densities not detectable on the earlier Boltzmann plots is clearly visible on these linear ordinates. Again, the error in the determination from any one line is approximately $\pm 9\%$, which nearly encompasses the difference between the two lines at all locations. The neutral particle number density values determined from the 7147 Å line LTE analysis are the ones used in this investigation because the estimated error is slightly smaller due to a more precise spontaneous emission coefficient. There is currently no independent check on the validity of this neutral density determination method.

4.2. NON-LTE RESULTS

4.2.1. Kinetic Temperatures

4.2.1.1. Contour Plots

Figure 4.18 contains the contour plots of the electron and heavy particle kinetic temperatures. It is immediately obvious that significant kinetic nonequilibrium persists in this LSP, and that it is likely due to the presence of the laser beam. A temperature difference is driven by the continuous laser beam because electrons absorb the laser photon energy during the inverse bremsstrahlung absorption process, and the heavy particles are heated secondarily through electron collisions. The difference contours ($T_e - T_g$) are shown in Figure 4.19 along with the ratio contours (T_e/T_g). The kinetic nonequilibrium is greatest near the plasma front, where T_e is at its highest and T_g at its lowest. This is because near the plasma front the laser

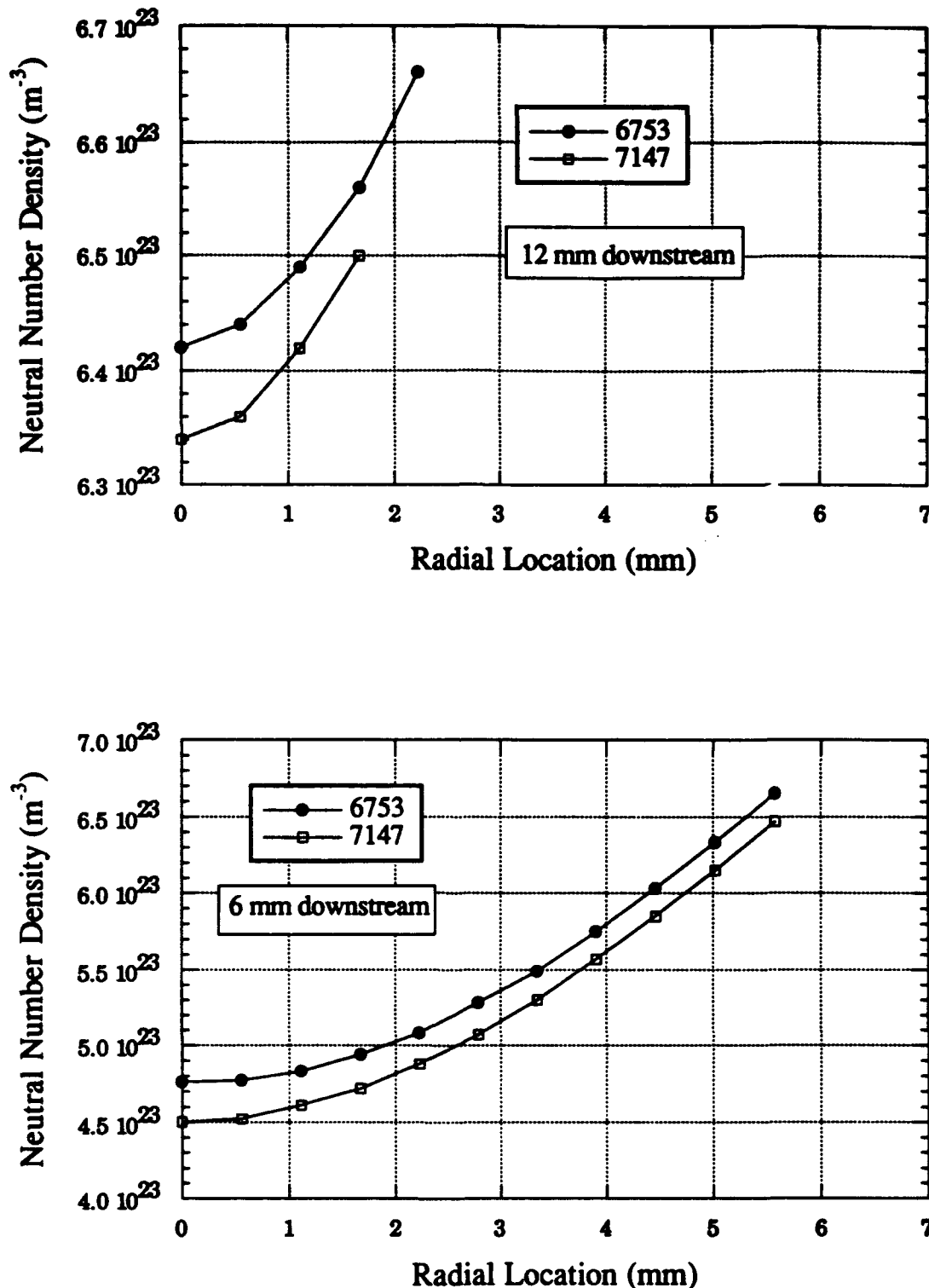


Figure 4.15 Radial comparison of the LTE neutral particle number densities corresponding to the 6753 Å and 7147 Å argon neutral lines. Two axial locations are shown.

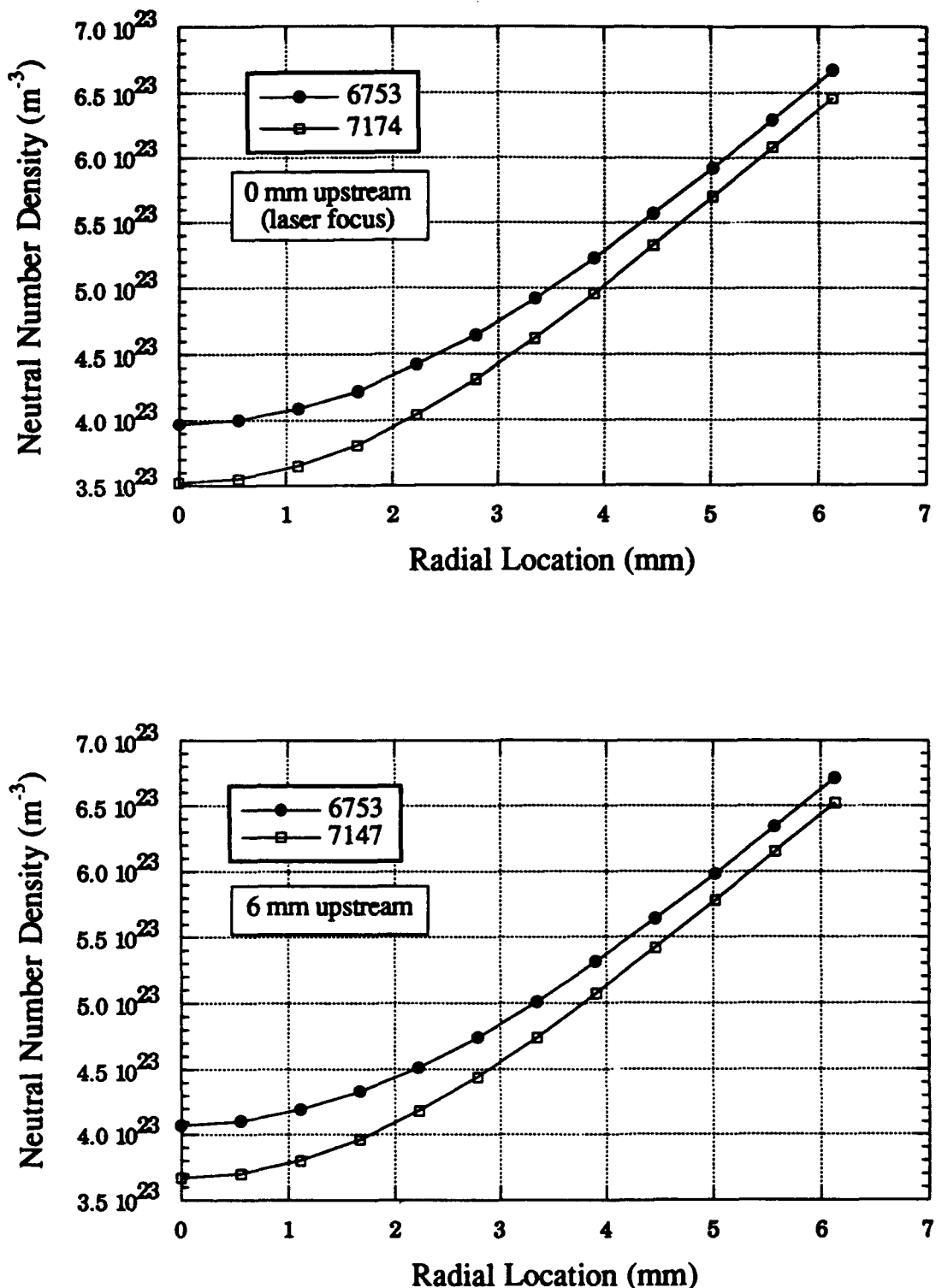


Figure 4.16 Radial comparison of the LTE neutral particle number densities corresponding to the 6753 \AA and 7147 \AA argon neutral lines. Two axial locations are shown.

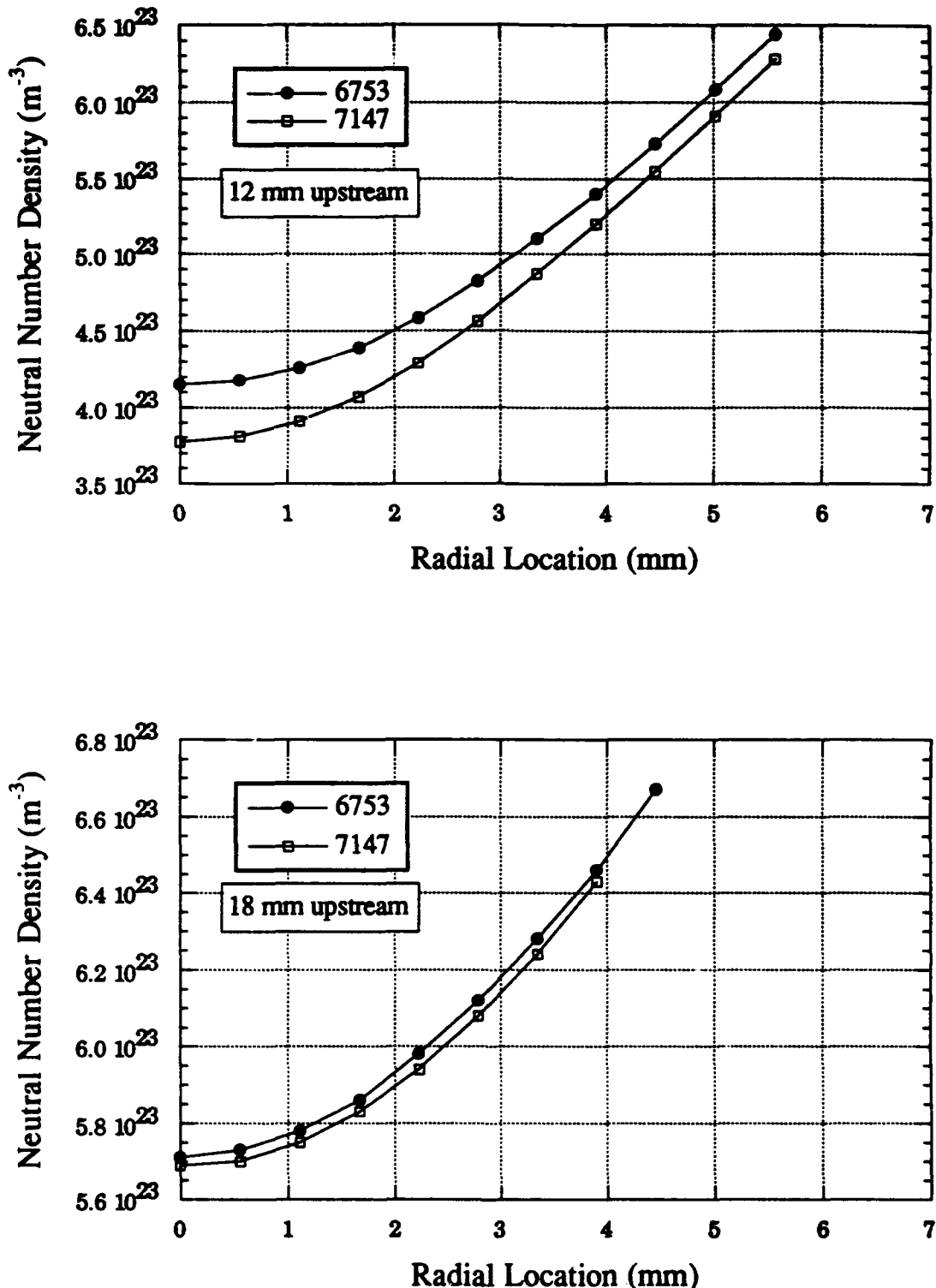


Figure 4.17 Radial comparison of the LTE neutral particle number densities corresponding to the 6753 Å and 7147 Å argon neutral lines. Two axial locations are shown.

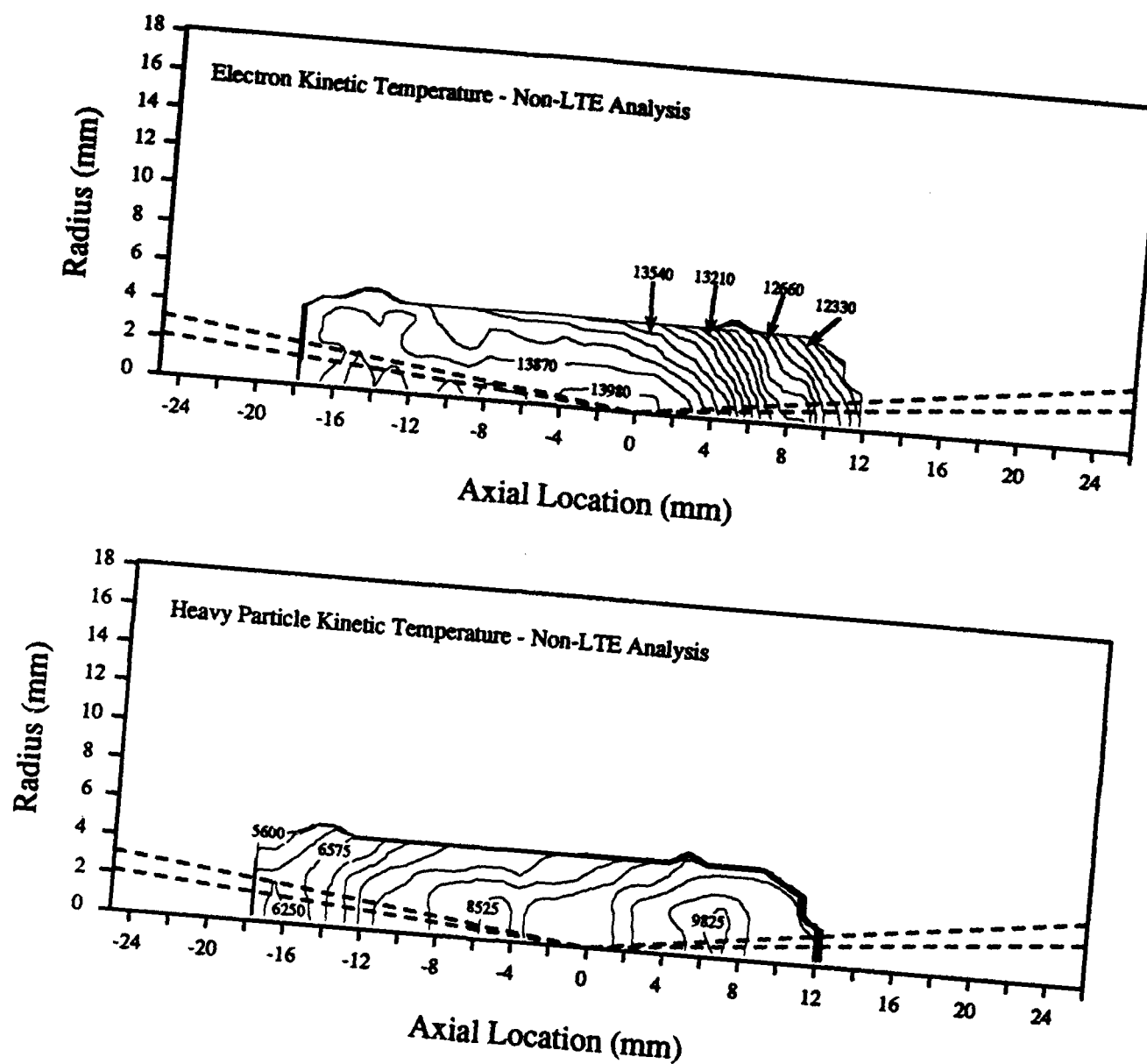


Figure 4.18 A contour comparison of the electron and heavy particle kinetic temperatures.
Based on non-LTE analysis.

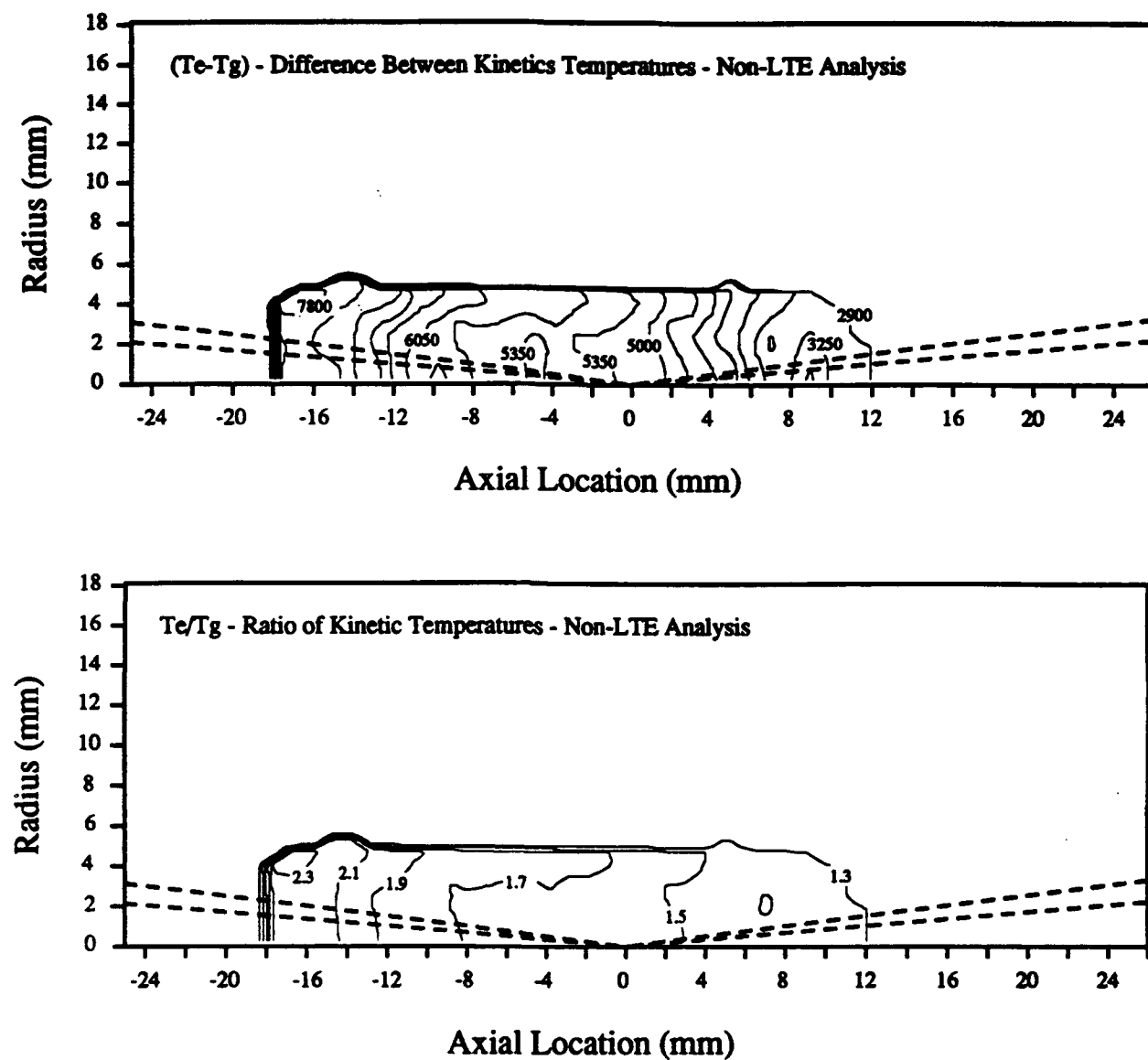


Figure 4.19 Contour plots showing kinetic nonequilibrium. $(Te-Tg)$ and (Te/Tg) are shown.

beam power is at its maximum, and it is attenuated as it propagates downstream. Near the plasma tail the laser beam is severely weakened, and the heavy species have had a longer interaction time with the electrons so that the kinetic nonequilibrium is diminished. The estimated errors in the determination of T_e and T_g are $\pm 1\%$ and $\pm 10\%$, respectively.

Kinetic nonequilibrium helps to explain why the neutral line emission remains strong well downstream of the laser focus, while the ion emission does not. Recalling Figures 4.1 and 4.2, consider axial locations at -10 mm and +2 mm. In the upstream region the laser beam is strong and the electrons are hot. Ionization events are frequent and the electron and ion densities are high. However, due to the relatively low kinetic temperature of the neutral particles, their density is allowed to remain higher than it would be in Saha equilibrium, and still satisfies the gas equation of state. Downstream in the LSP the electron temperature is lower, as are the electron and ion densities. Because the heavy particle kinetic temperature is higher than it is upstream, the neutral number density can remain nearly the same so that the equation of state is still satisfied.

Recalling equation (3.21):

$$P = k_b[n_e T_e + n_i T_g + n_a T_g] (1 - P_c^{DH}) \quad (3.21)$$

A qualitative look at the three terms in the first bracket shows the first term is smaller downstream than upstream because both n_e and T_e are smaller downstream. The second term may remain approximately unchanged because n_i is lower downstream, but T_g is higher. Therefore the last term must be larger downstream than upstream to maintain system pressure. This is indeed the case as n_a remains approximately unchanged between the two axial locations considered, while T_g is increased.

Some thought should be given to the cause and effect relationship between the line emission strengths and the kinetic nonequilibrium. In this investigation the line emission strengths are measured and the kinetic temperatures calculated so that they are consistent with the measurements and the imposed thermodynamic model. In this case the model includes the

equation of state (3.21) and the non-LTE ionization equation (3.22). So it comes as no surprise that the calculated kinetic temperatures can be used with the model equations to 'explain' the experimental observations. From a physical standpoint the kinetic temperatures are the determining factor for the particle number densities and electronic level populations, and therefore the observed plasma emission.

4.2.1.2. Radial Plots

Figures 4.20 - 4.30 show comparisons of all the various temperatures calculated as part of this investigation. The plots are for axial locations spaced 3 mm apart, starting at 18 mm upstream of the focus and ending at 12 mm downstream. The ion upper level excitation temperature, $T_{ex\beta,i}$, is generally the highest, followed by ion LTE temperature, $T_{LTE,4610} = T_{xi}$, and electron kinetic temperature, T_e . The neutral upper level excitation temperature, $T_{ex\beta,a}$, and the neutral LTE temperature, $T_{LTE,7147} = T_{xa}$, are always between the ion/electron temperatures and the heavy particle kinetic temperature, T_g , which is always the lowest.

The most significant trend found in these plots is that the curves seem to be collapsing towards a single temperature when viewed in a streamwise progression. The difference between the highest and lowest centerline temperatures is 10900 K 12 mm upstream of the focus, 6400 K at the focus, and 2900 K 12 mm downstream of the focus. Because the laser beam is strongly attenuated in the upstream portion of the LSP, the downstream portion tends to relax towards an equilibrium state. At 12 mm downstream of the focus the estimated errors on T_e and T_g can account for approximately half of the difference between the two temperatures.

4.2.2. LTE Numerical Model

The numerical LSP model of Eguiguren [1989] is based on the assumption of LTE. Results from this model executed for the same conditions as for the LSP studied spectroscopically are presented in this section. Figure 4.31 shows the temperature contours for

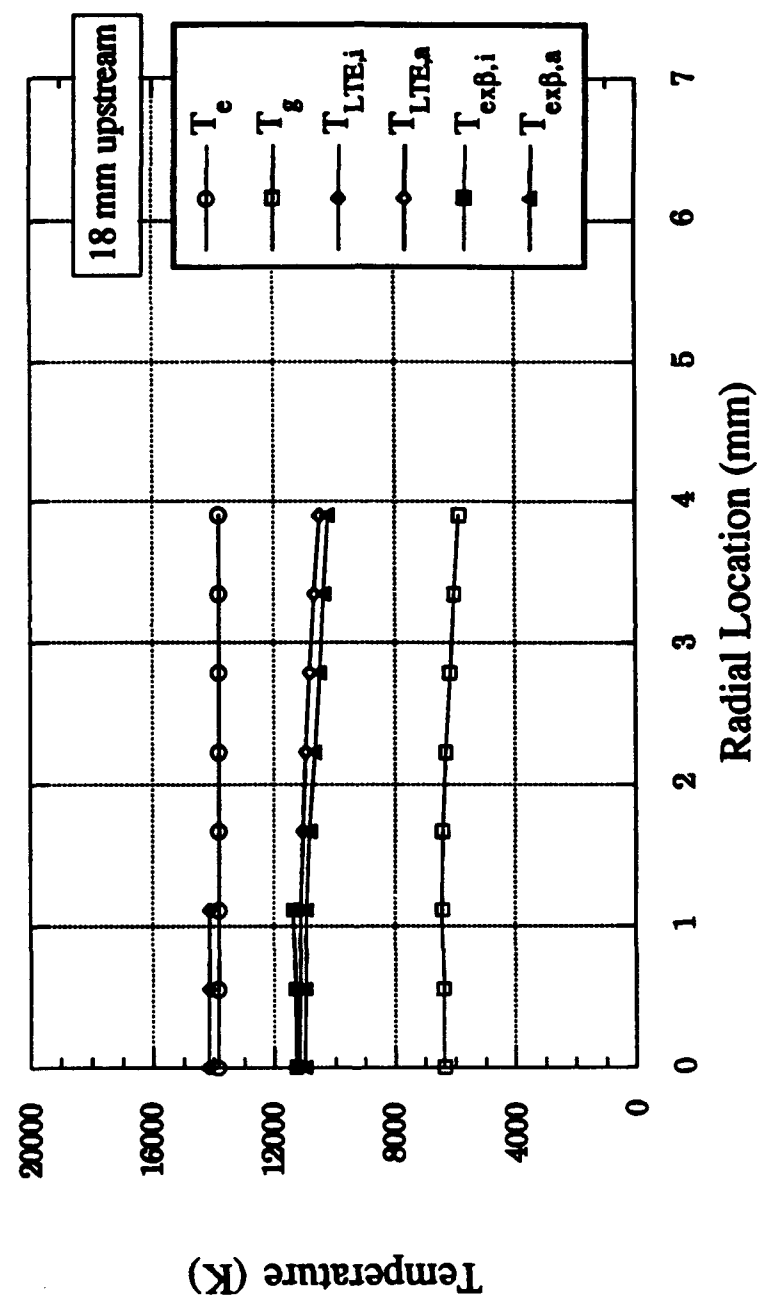


Figure 4.20 Radial variation of the various non-LTE temperatures. Axial location is 18 mm upstream of the laser focus

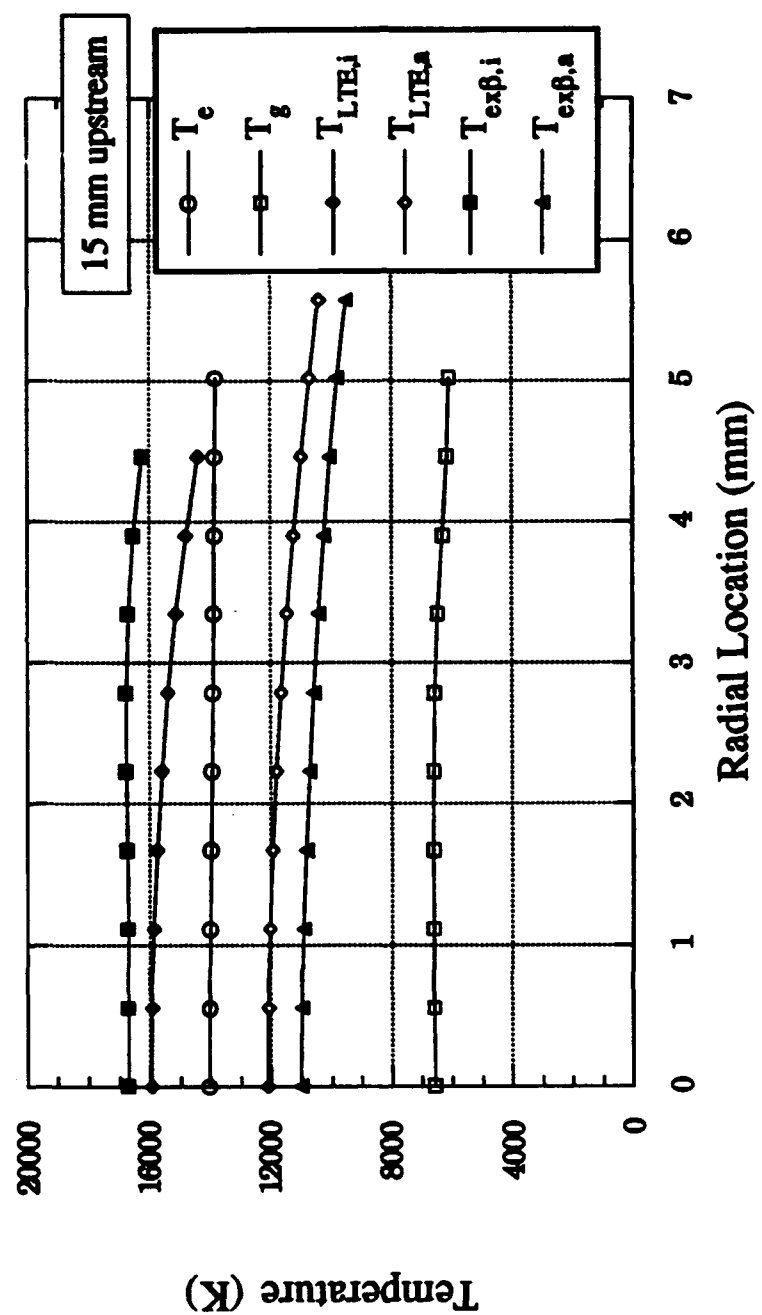


Figure 4.21 Radial variation of the various non-LTE temperatures. Axial location is 15 mm upstream of the laser focus

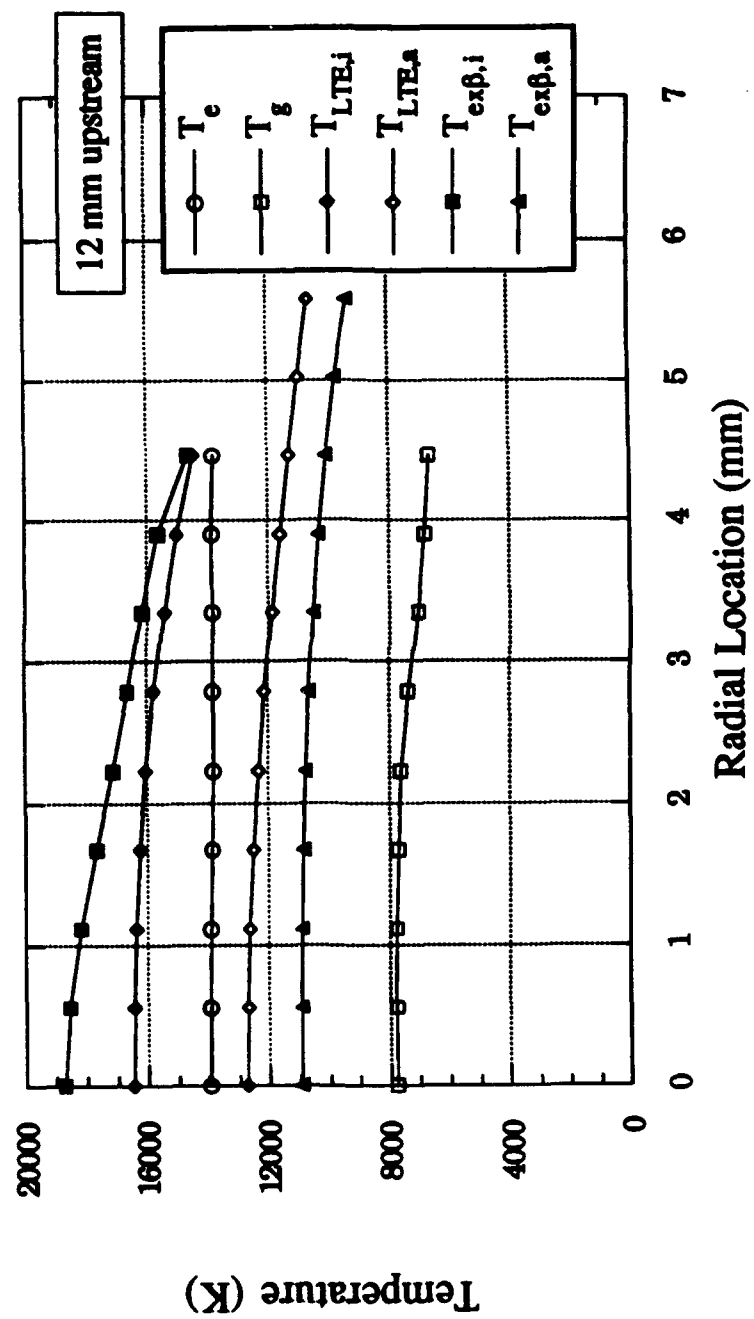


Figure 4.22 Radial variation of the various non-LTE temperatures. Axial location is 12 mm upstream of the laser focus.

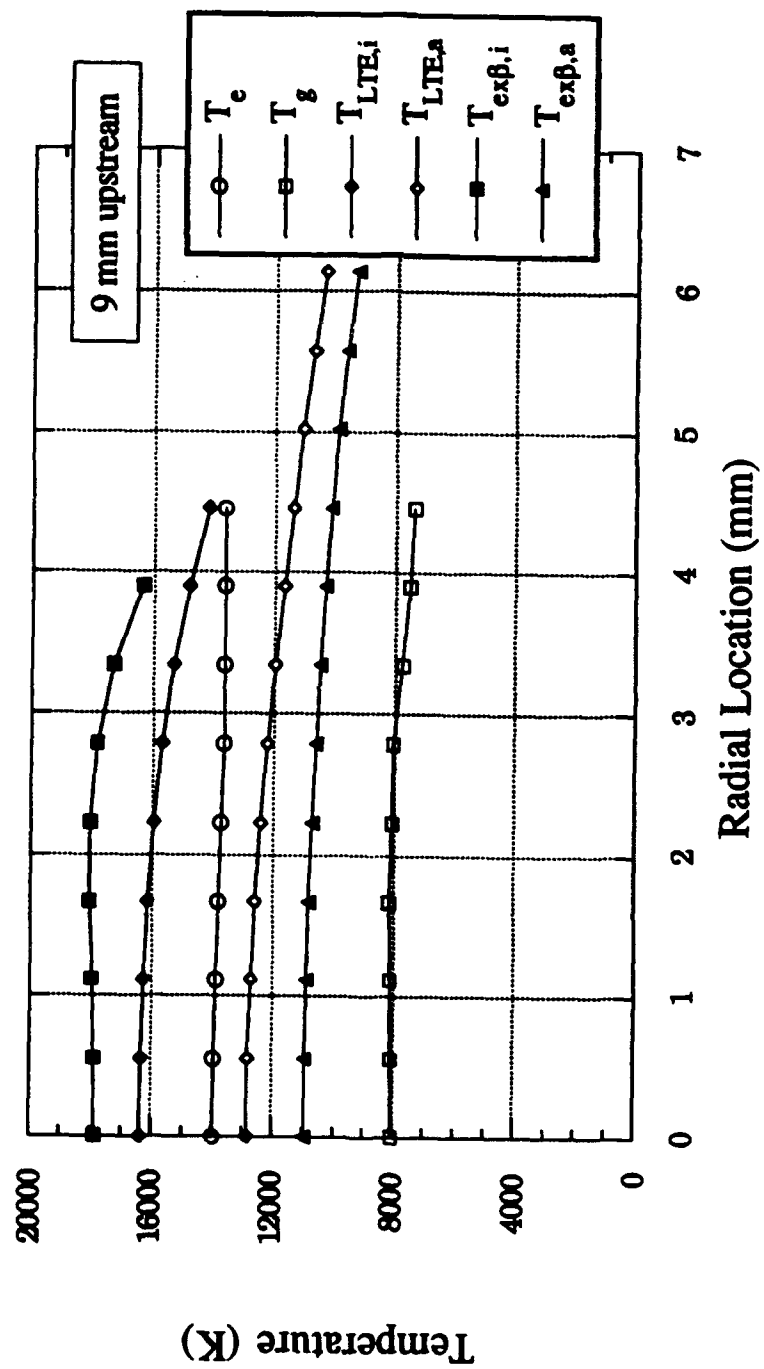


Figure 4.23 Radial variation of the various non-LTE temperatures. Axial location is 9 mm upstream of the laser focus.

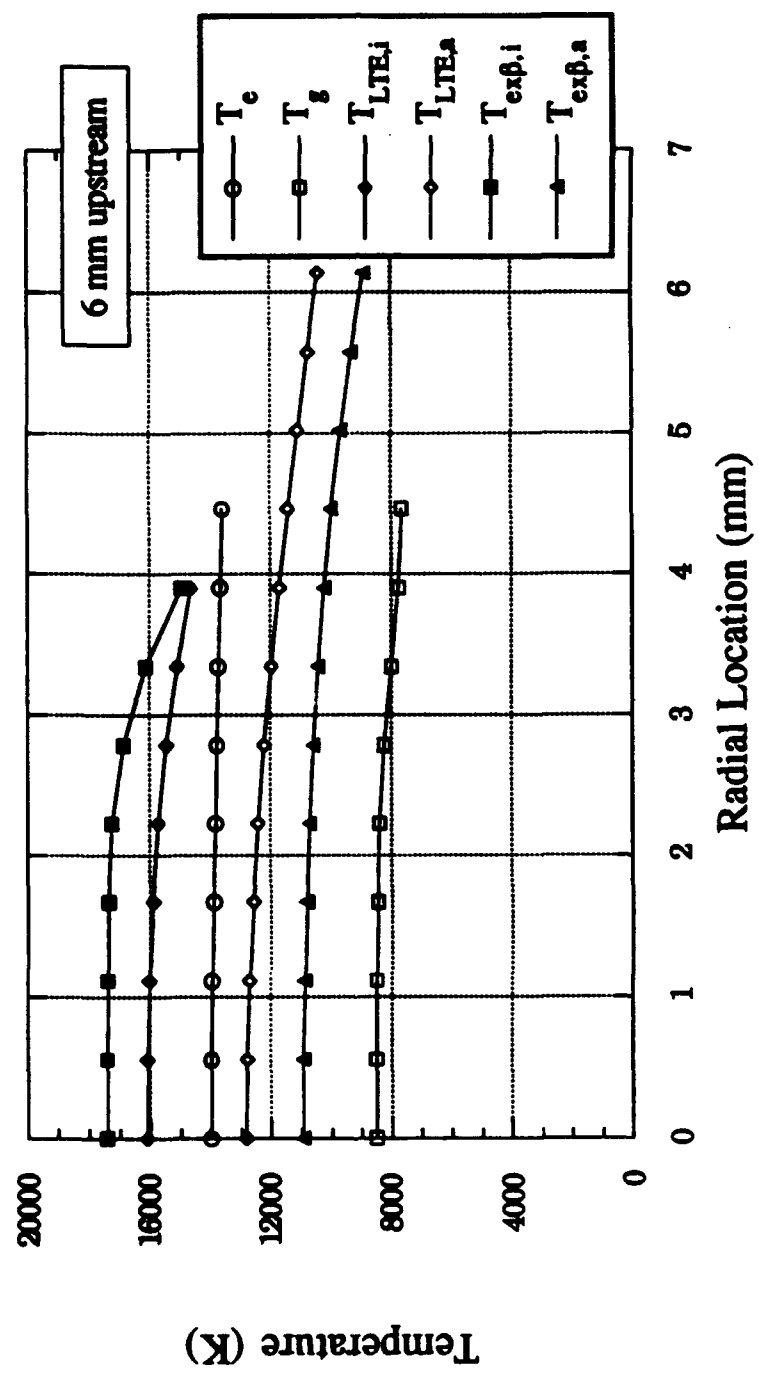


Figure 4.24 Radial variation of the various non-LTE temperatures. Axial location is 6 mm upstream of the laser focus.

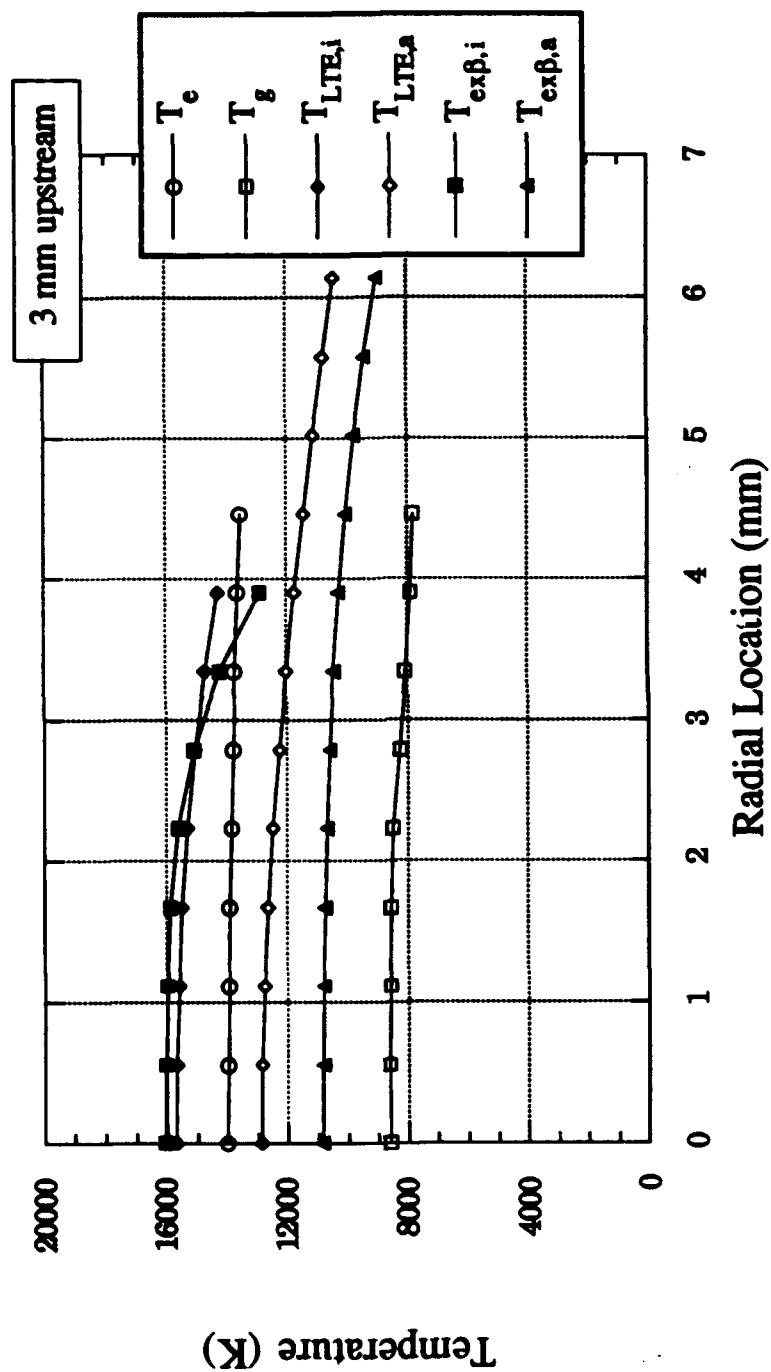


Figure 4.25 Radial variation of the various non-LTE temperatures. Axial location is 3 mm upstream of the laser focus.

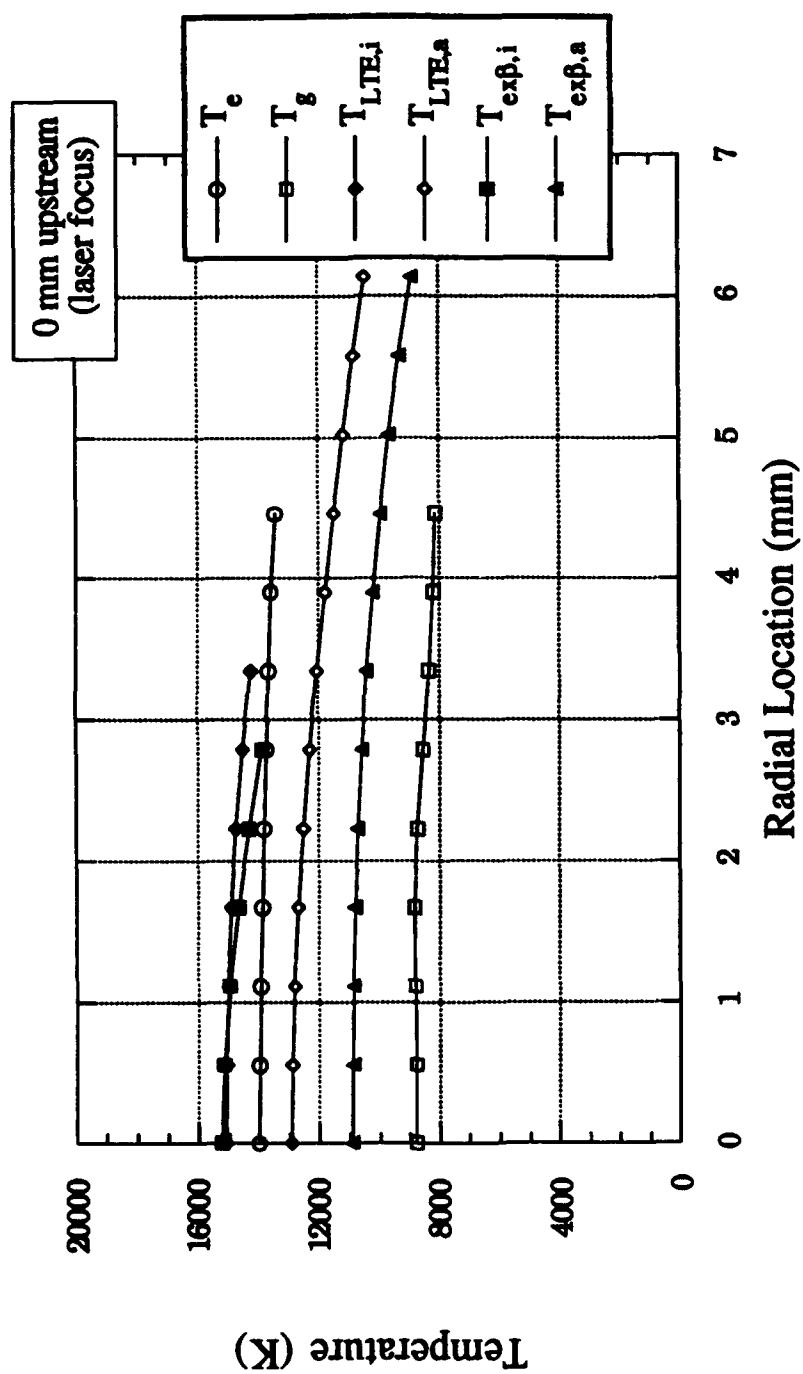


Figure 4.26 Radial variation of the various non-LTE temperatures. Axial location is 0 mm upstream of the laser focus.

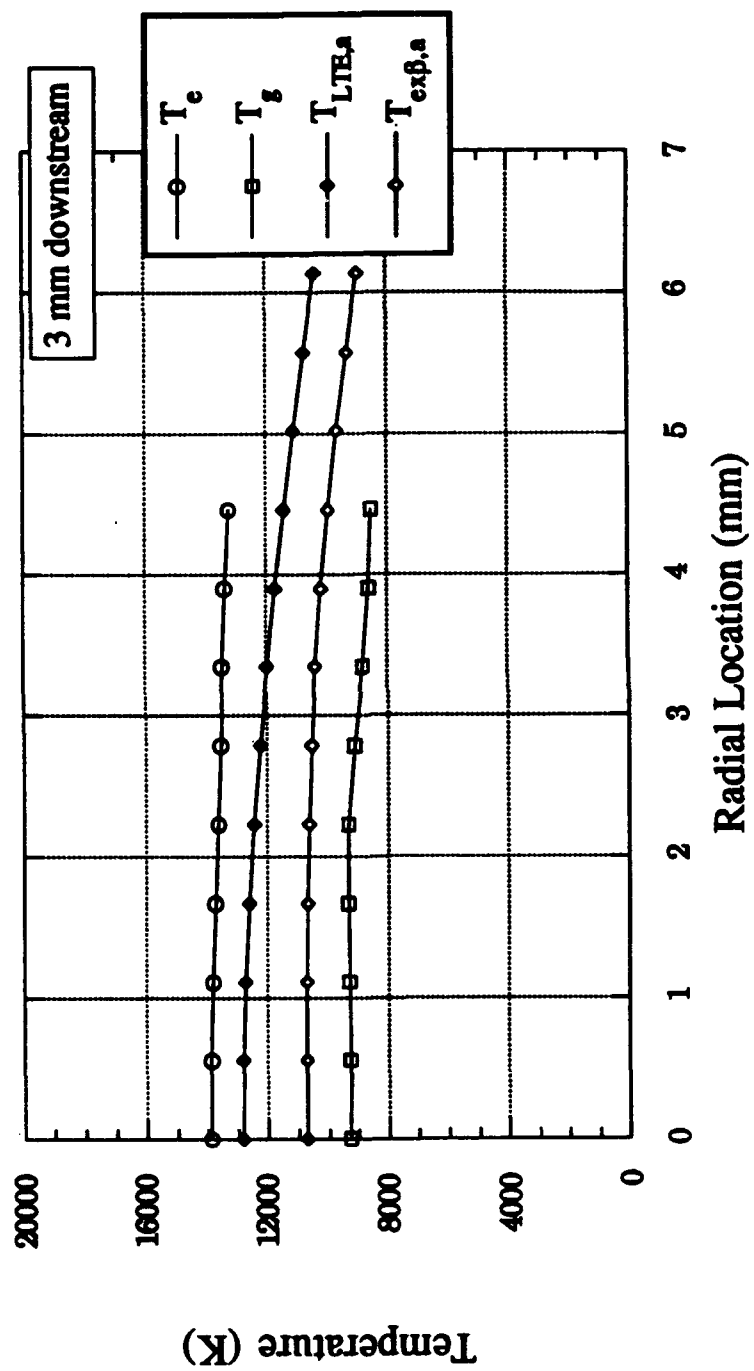


Figure 4.27 Radial variation of the various non-LTE temperatures. Axial location is 3 mm downstream of the laser focus.

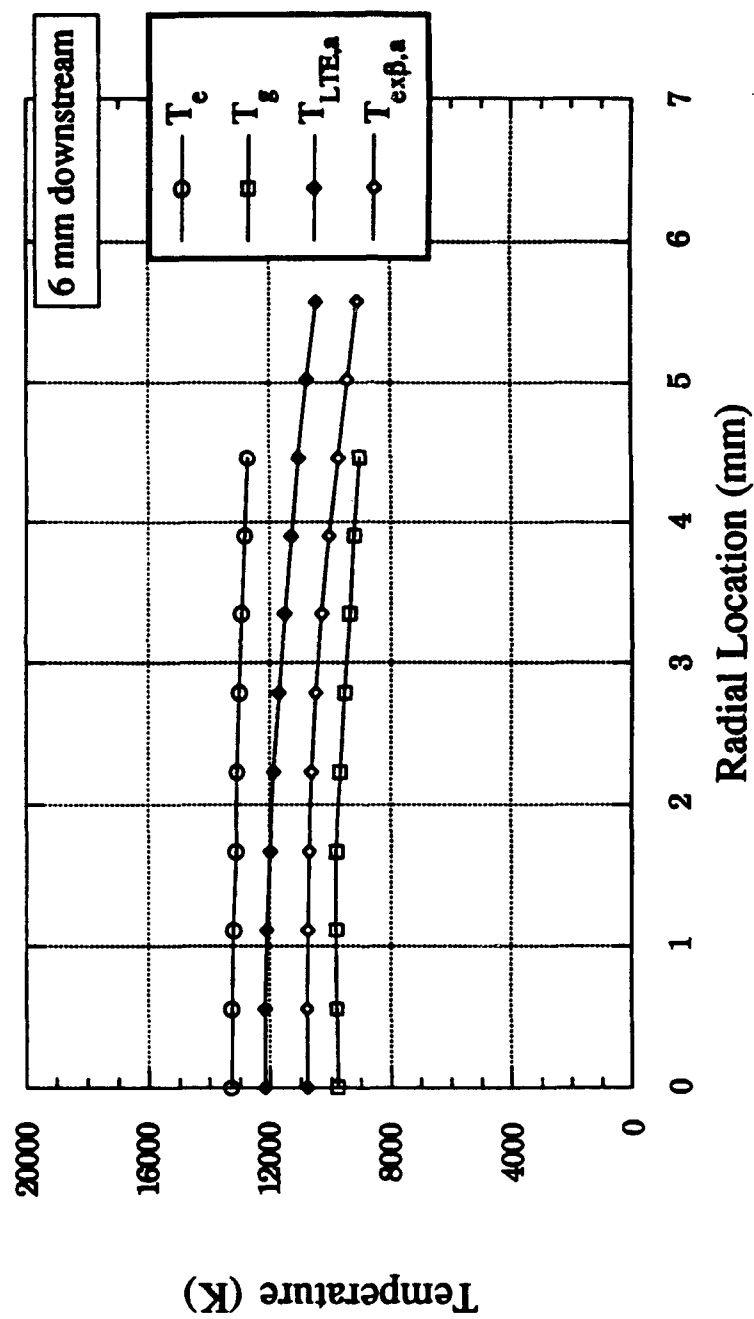


Figure 4.28 Radial variation of the various non-LTE temperatures. Axial location is 6 mm downstream of the laser focus.

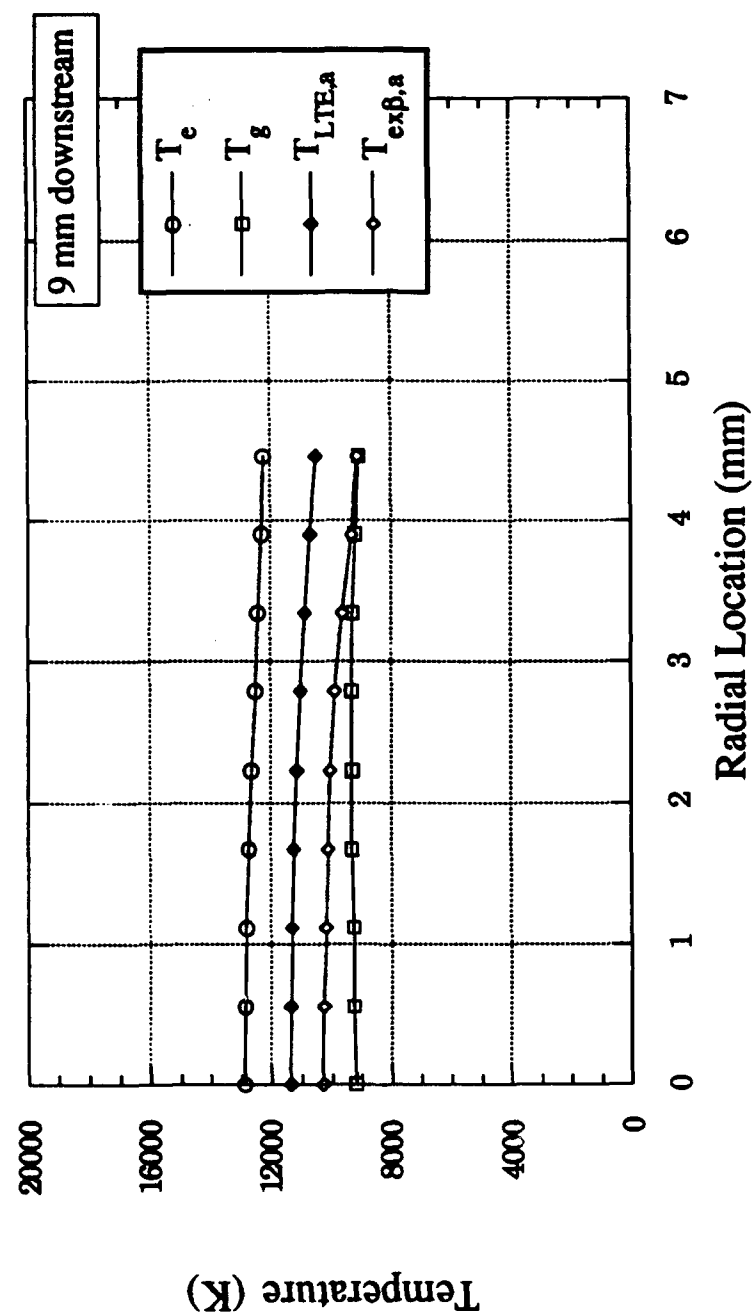


Figure 4.29 Radial variation of the various non-LTE temperatures. Axial location is 9 mm downstream of the laser focus.

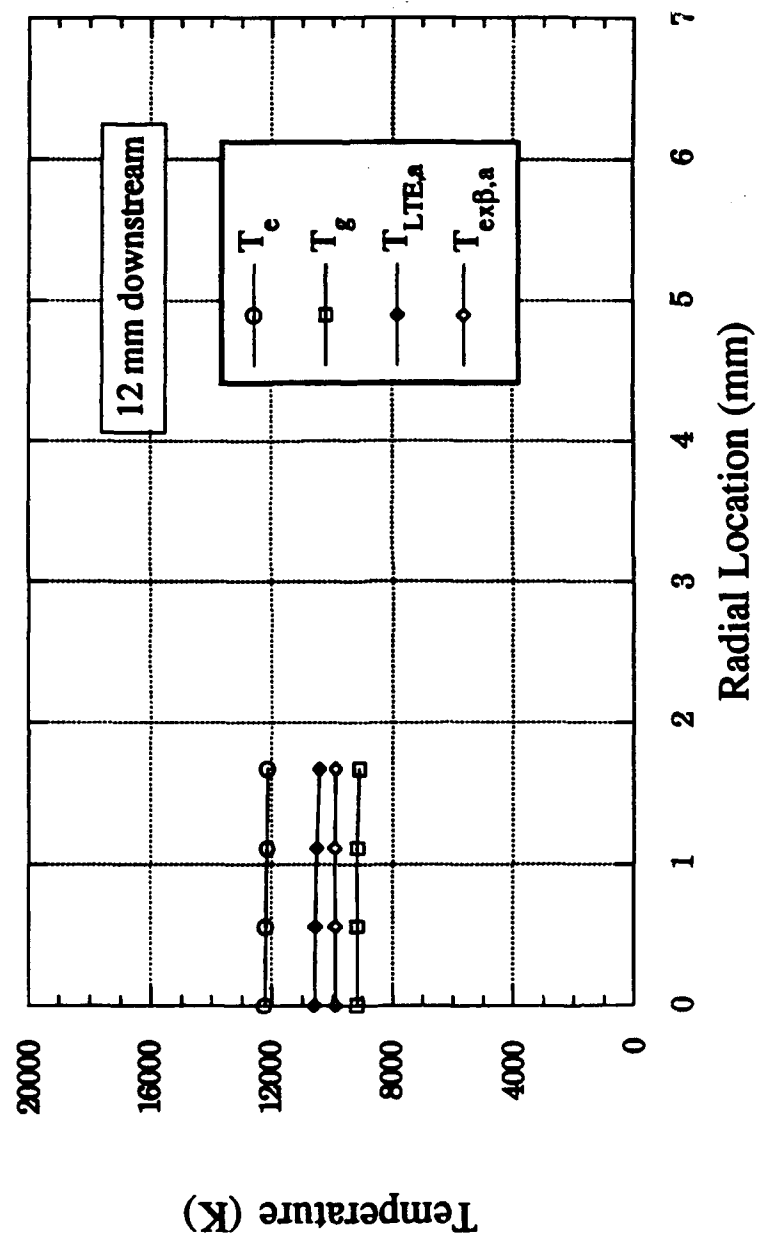


Figure 4.30 Radial variation of the various non-LTE temperatures. Axial location is 12 mm downstream of the laser focus.

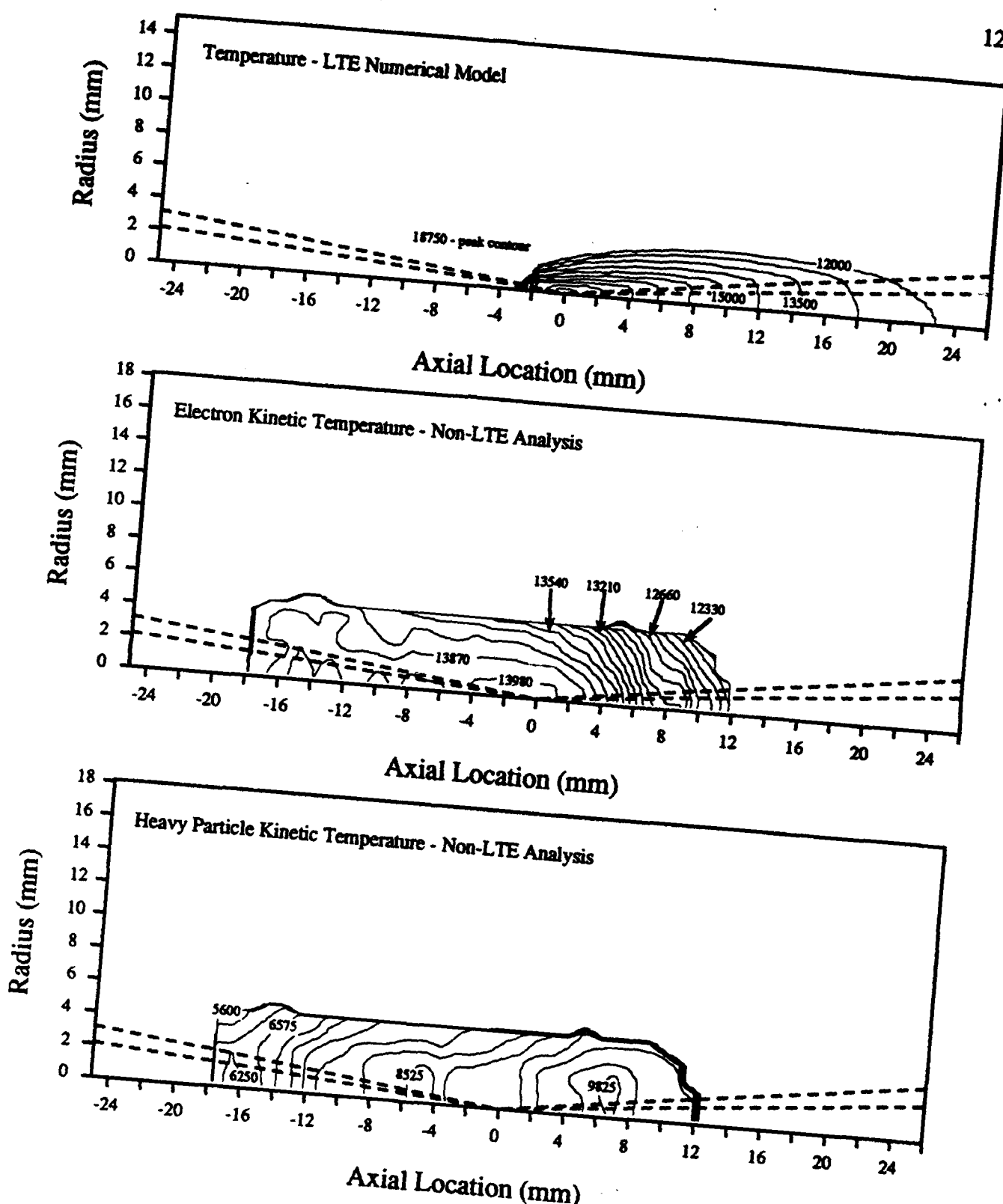


Figure 4.31 Temperature contour plots comparing the results of the LTE numerical model of Eguiguren [1989], to the electron and heavy particle kinetic temperatures.

the numerical model compared to the electron and heavy particle kinetic temperature contours determined with the non-LTE analysis. The most striking observation is the LTE model's poor prediction of LSP position relative to the laser focus. The peak temperature is somewhat higher than even the electron kinetic temperature, but the predicted length of the plasma bounded by the 12000 K contour is approximately the same for both contour plots.

Figure 4.32 shows contours of electron number density determined by the LTE model and by the H_{α} spectroscopic method. Again, the plasma location is much different, but the range of electron number density is approximately the same on both contour plots. The electron number density is a key element in the calculation of local laser beam absorption coefficient, and the overall plasma length is a factor in the total laser power absorption (or global absorption).

The laser beam absorption coefficient used in this investigation is due to Stallcop [1974]. It is expressed as follows in units of m^{-1} :

$$\alpha_{IB} = \frac{256}{3} \sqrt{\frac{\pi}{3}} \pi^2 (fsc) a_0 \left(\frac{E_H}{hc} \right)^3 \left(\frac{E_H}{k_b} \right)^{1/2} n_e^2 \lambda^3 (T_e)^{-1/2} \exp \left[\frac{hc}{\lambda k_b T_e} \right] \left[1 - \exp \left(\frac{-hc}{k_b \lambda T_e} \right) \right] \left(\frac{hc}{\lambda k_b T_e} + g_{ff} \right)$$

This coefficient is calculated at every point in the LSP and the amount of beam power absorbed is calculated using a program written by Mertogul [1992]. A small coefficient for electron-neutral IB is added to (4.1) and is curve fit from Geltman [1973]. Figure 4.33 contains contour plots of local beam power absorption for both the non-LTE analysis and the LTE numerical model. Figure 4.34 is the same data shown with the radial scale expanded by a factor of two. It is clear that most of the absorption takes place near the plasma front using either analysis, but that the plasma front is much closer to the laser focus in the LTE numerical analysis. The pocket-like appearance of the beam power absorption is due to the discrete nature of the spectroscopic measurement points or numerical grid points and is therefore not a completely accurate physical description. However, the overall picture presented by the non-LTE analysis contours is an excellent representation of reality.

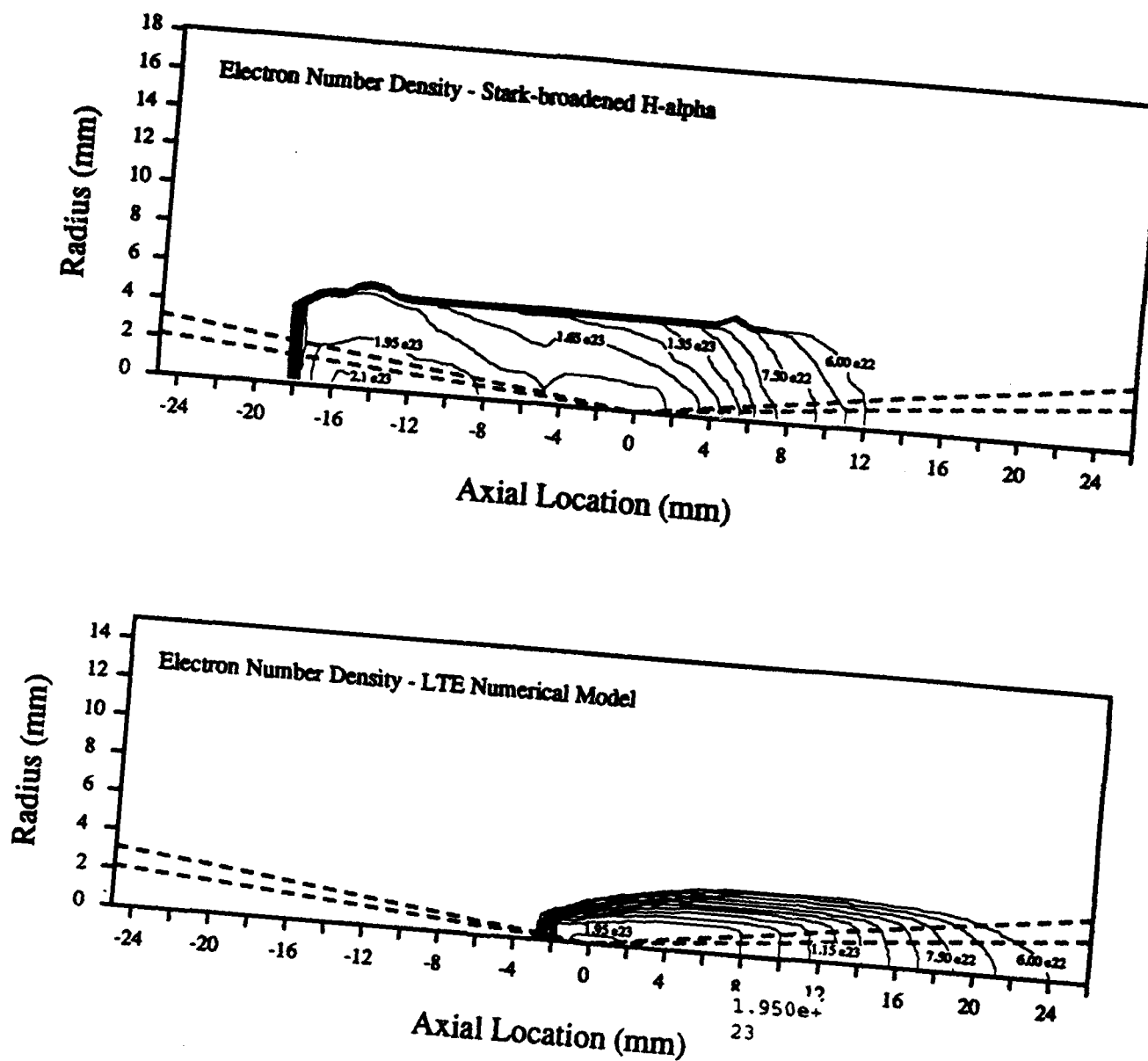


Figure 4.32 Electron number density contour plots comparing the results of the LTE numerical model of Eguiguren [1989] to the H_{α} Stark broadening results.

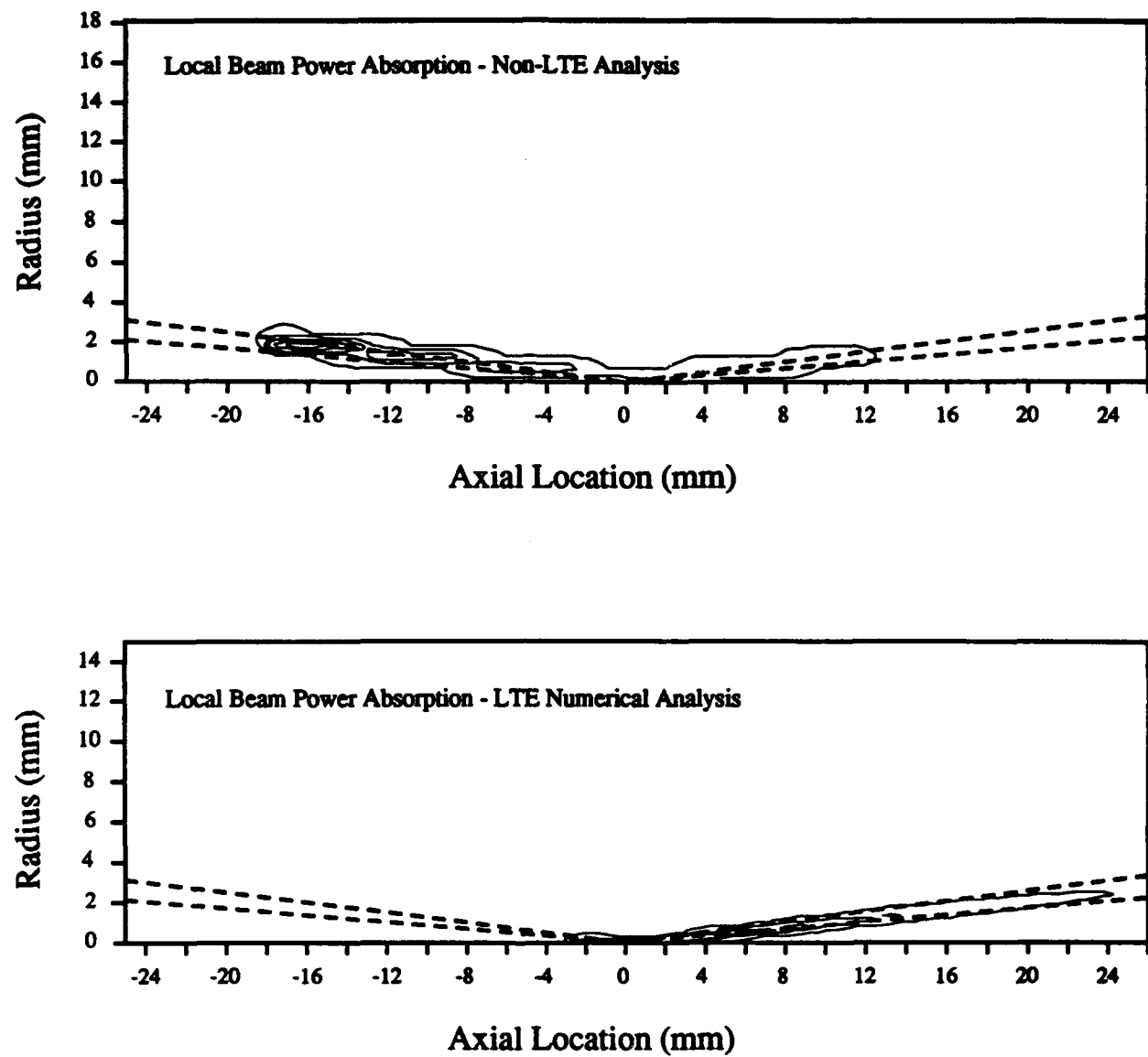


Figure 4.33 Local laser beam power absorption contour plots comparing the results of the non-LTE analysis to the results of the LTE numerical model of Eguiguren [1989].

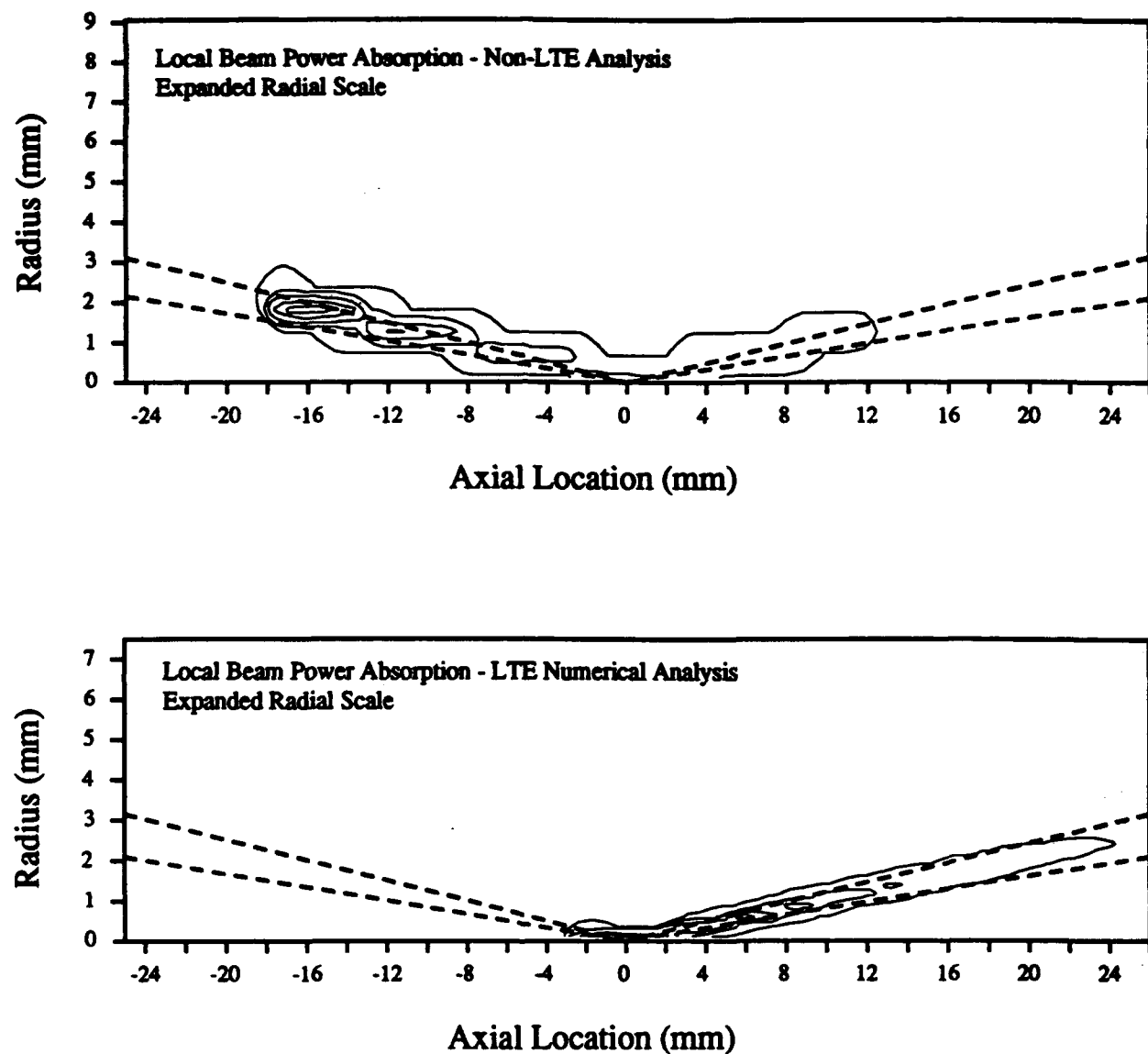


Figure 4.34 Local laser beam power absorption contour plots comparing the results of the non-LTE analysis to the results of the LTE numerical model of Eguiguren [1989]. Radial scale expanded to show details.

The total beam power absorption is calculated from the non-LTE analysis, the LTE numerical analysis, the LTE analysis of a single neutral emission line, and from calorimetric measurements of actual laser beam transmission through the LSP. Global absorption is calculated as the ratio of this absorbed power to the incident laser power, and is expressed as a percentage of the incident power. Figure 4.35 is a bar graph comparing the global absorption corresponding to each analysis. The non-LTE analysis, LTE numerical analysis, and calorimetric measurement all agree fairly well, given the uncertainty of the measurements. The non-LTE and calorimetric global absorptions are accurate to $\pm 6\%$ and $\pm 4\%$, respectively. The errors are expressed as absolute percent global absorption. The neutral line LTE analysis results in an extremely poor measure of global absorption due to the low electron number density associated with it.

The fact that the LTE numerical analysis results in a global absorption very close to that which is measured calorimetrically originally lead to the belief that the physics of LSP's were being accurately modeled [Eguiguren, 1989]. Due to the poor prediction of plasma location with respect to the laser focus, it is now clear that this is not the case, and that the numerical analysis is by no means guaranteed to produce similarly accurate results if extended to LSP operating conditions beyond those available in the laboratory. It seems clear that improved numerical modeling is required. This topic will be discussed further in the next chapter.

4.2.4. Energy Densities

The final calculations and comparisons made in this study concern the energy densities in each of the various energy modes in the LSP. Considered are the ionization energy, electron kinetic energy, heavy particle kinetic energy, and neutral particle electronic excitation energy. The ionization energy density is simply the neutral argon ionization energy multiplied by the ion number density. The kinetic energy densities are calculated from the following expressions:

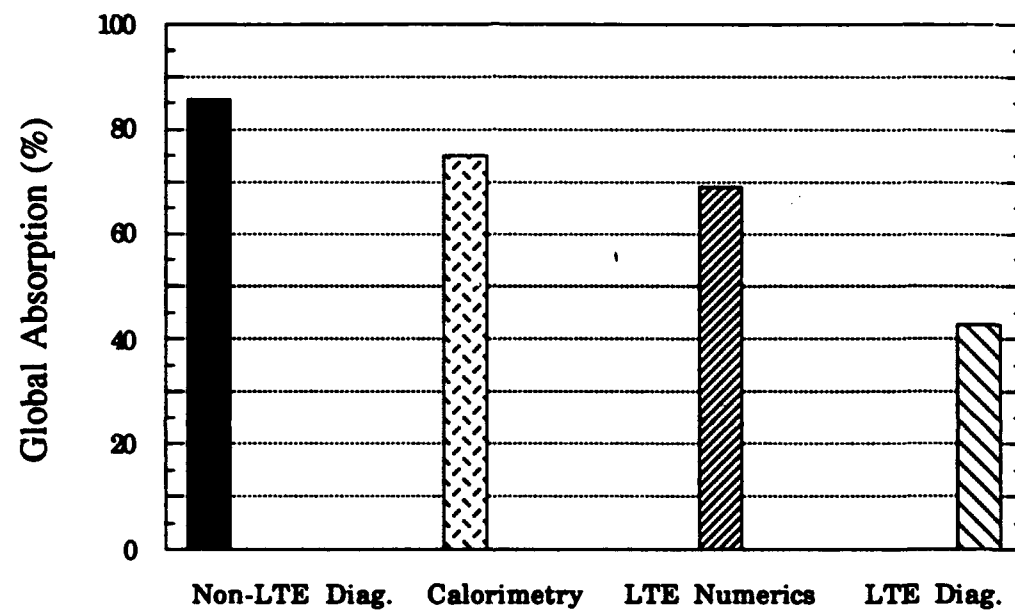


Figure 4.35 Global absorption calculated by four different methods.

$$\text{electron kinetic energy density} = \frac{3}{2} n_e k_b T_e \quad [\text{J/m}^3] \quad (4.2)$$

$$\text{heavy particle kinetic energy density} = \frac{3}{2} (n_a + n_i) k_b T_g \quad [\text{J/m}^3] \quad (4.3)$$

The electronic excitation energy density is calculated from:

$$\sum_{m=1}^I E_m n_m = n_a k_b T_{exa}^2 \frac{d}{dT_{exa}} [\ln(Z_{exa})] \quad [\text{J/m}^3] \quad (4.4)$$

This expression is derived in Appendix C.

Figures 4.36 - 4.39 contain contour plots of the energy densities of ionization, electron kinetic, heavy particle kinetic, and the total of all four energy densities. The excitation energy density is excluded because its magnitude is very small compared to the others. The results corresponding to the LTE numerical analysis are also shown for comparison.

The ionization energy density is the largest, and like the electron kinetic energy density, peaks near the plasma front and decreases toward the tail in a manner very similar to the electron number density. The heavy particle energy density has an inverse behavior, increasing towards the plasma tail due to increasing heavy particle kinetic temperature. The shapes of the heavy energy density contours still resemble those of the ionization and electron kinetic energy densities because of the ion number density component in equation (4.3). The total of the four energy densities has a contour plot almost identical in shape to the ionization energy density plot because it is the largest term in the sum.

Figure 4.40 contains two plots. The lower plot shows the axial variation in total energy density $[\text{J/m}^3]$ at various radii. The upper plot shows the axial variation in energy density along the plasma centerline for the various components. The key feature of this plot is that the decreases in ionization and electron kinetic energy densities past the focus coincide with the increase in heavy particle kinetic energy density. The energy of ionization is lost to a combination of continuum radiation and heavy particle kinetic energy. As the electrons and ions recombine rapidly in the LSP tail, the number density of neutrals increases as does their

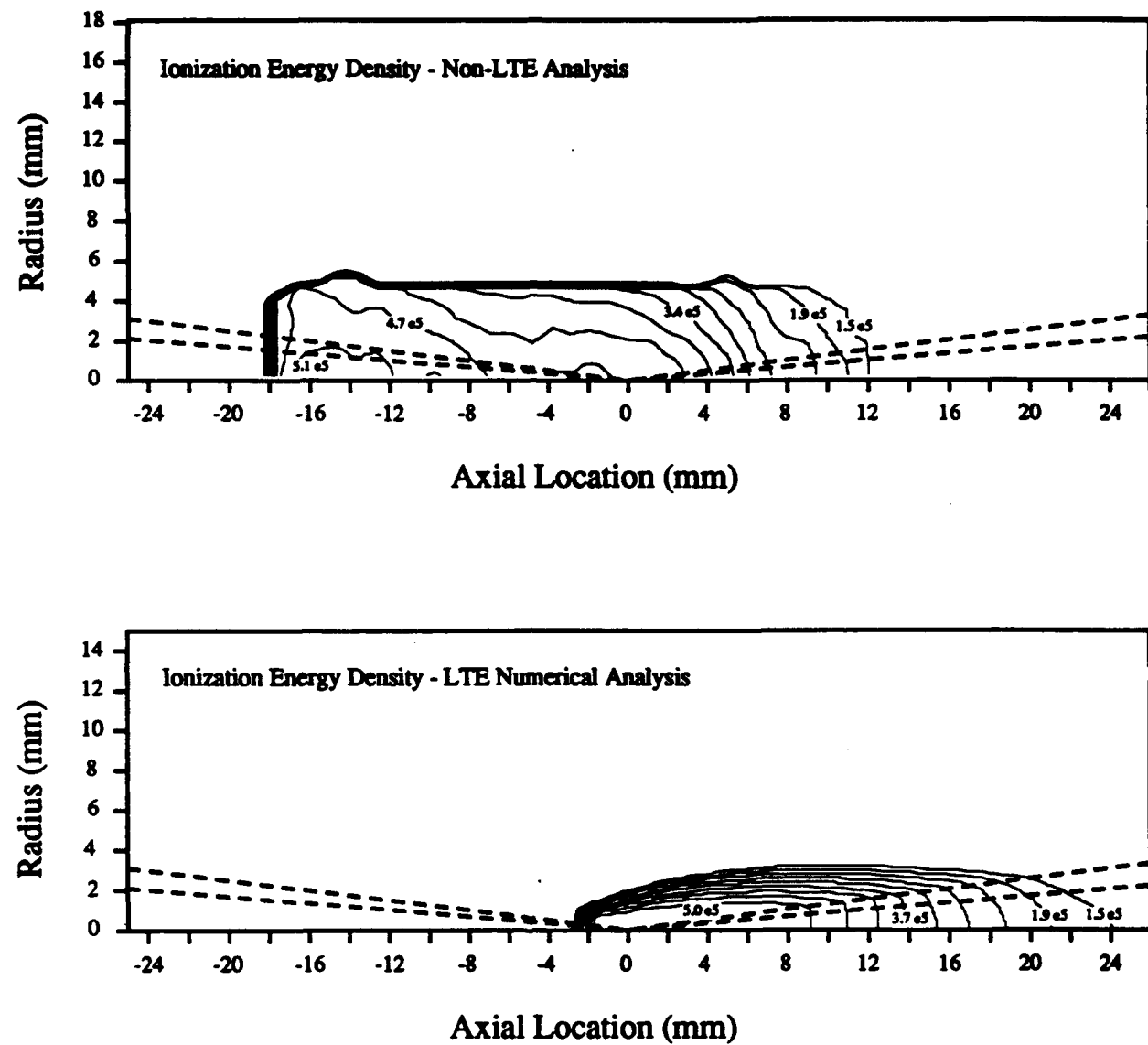


Figure 4.36 Contours of ionization energy density. Comparing the non-LTE analysis to the LTE numerical model of Eguiguren [1989].

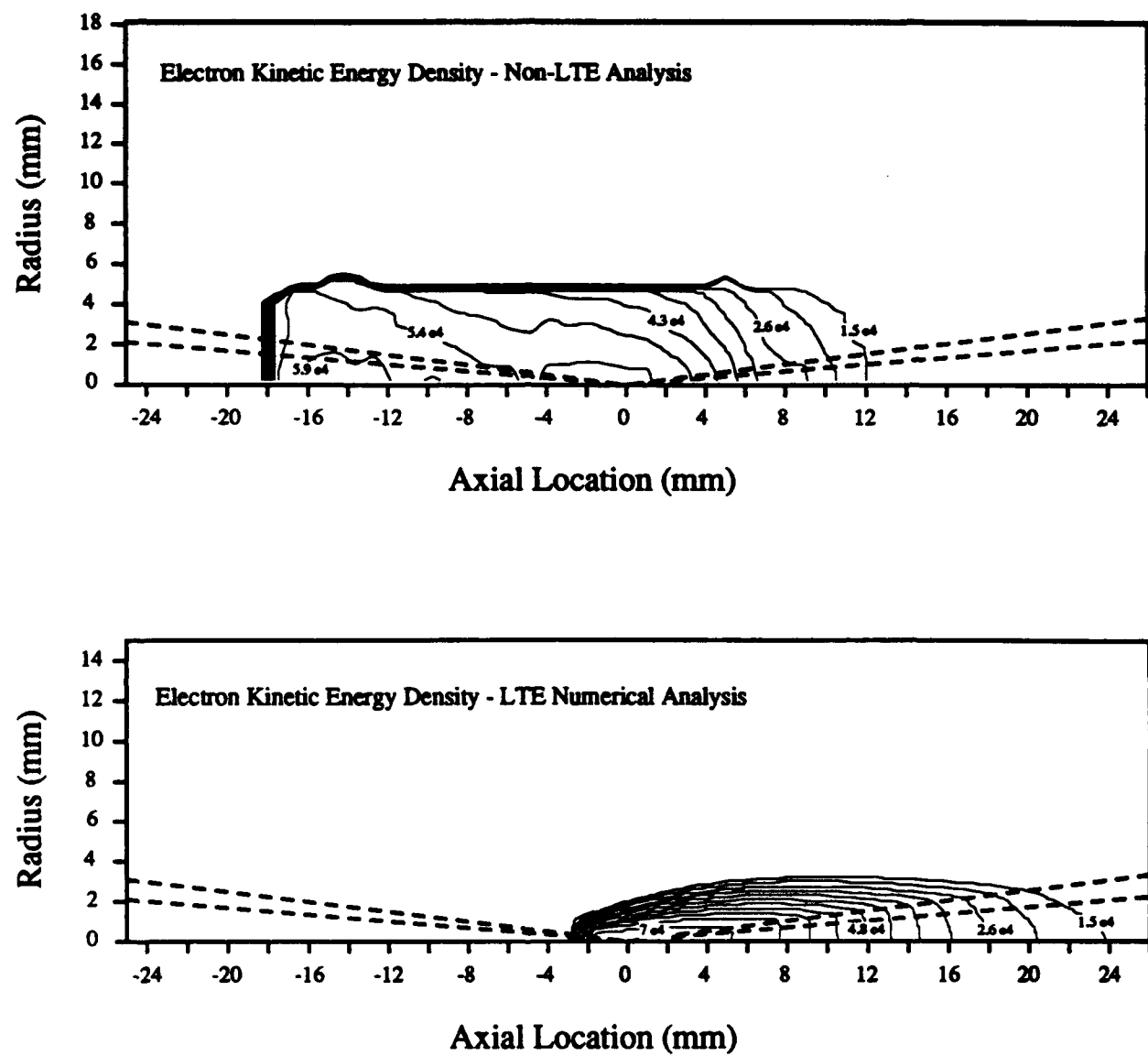


Figure 4.37 Contours of electron kinetic energy density. Comparing the non-LTE analysis to the LTE numerical model of Eguiguren [1989].

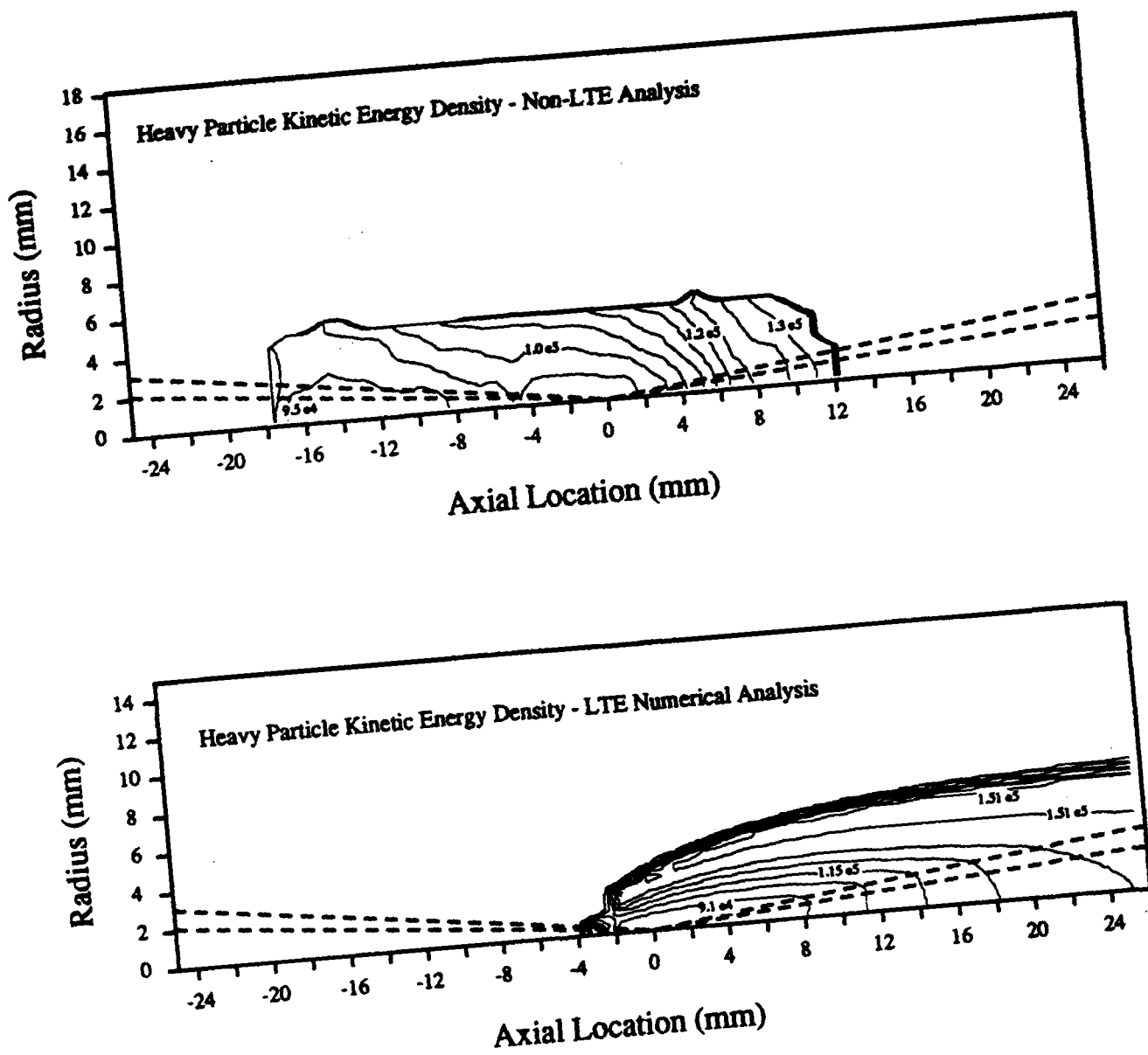


Figure 4.38 Contours of heavy particle kinetic energy density. Comparing the non-LTE analysis to the LTE numerical model of Eguiguren [1989].

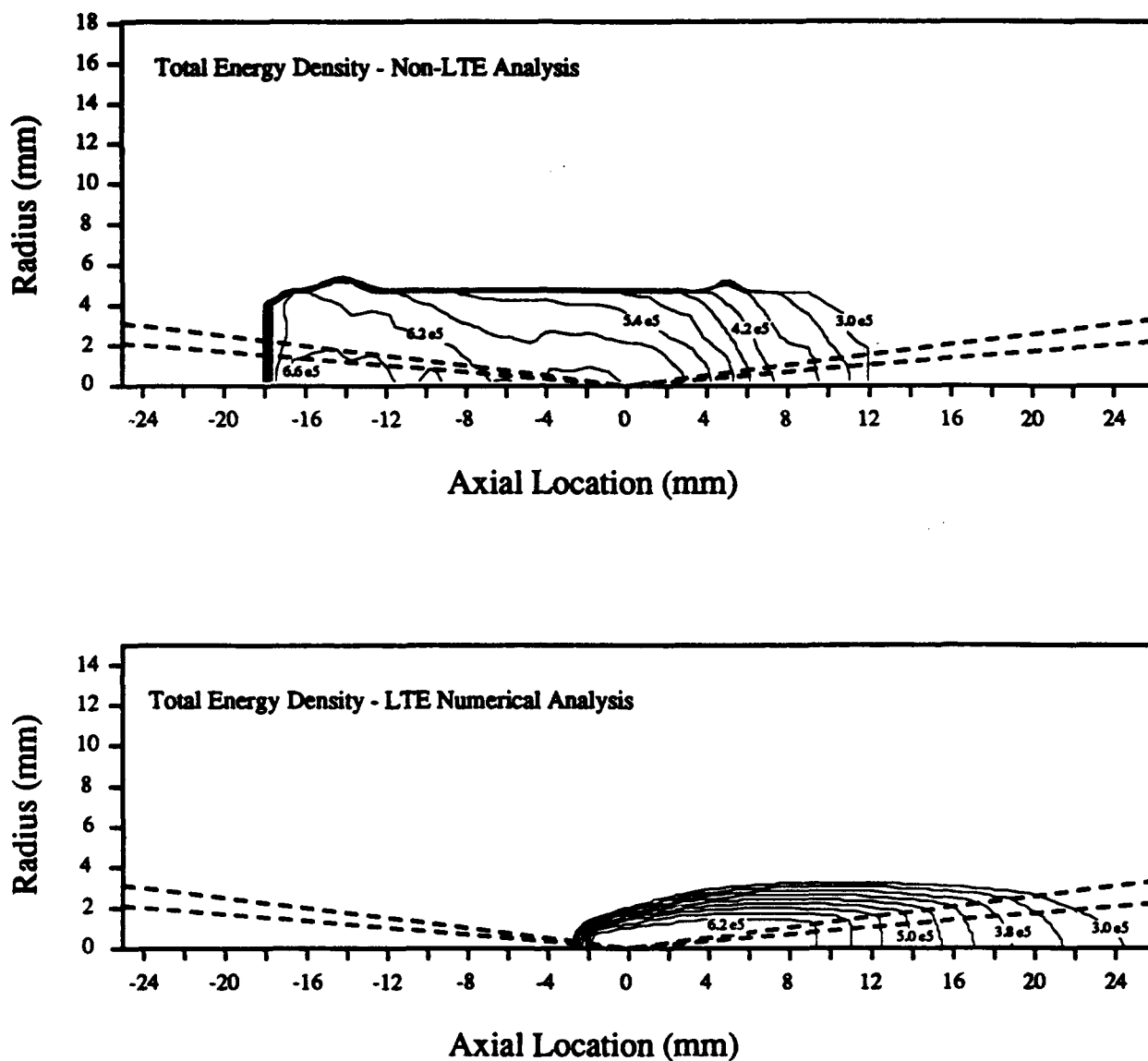


Figure 4.39 Contours of total energy density. Comparing the non-LTE analysis to the LTE numerical model of Eguiguren [1989].

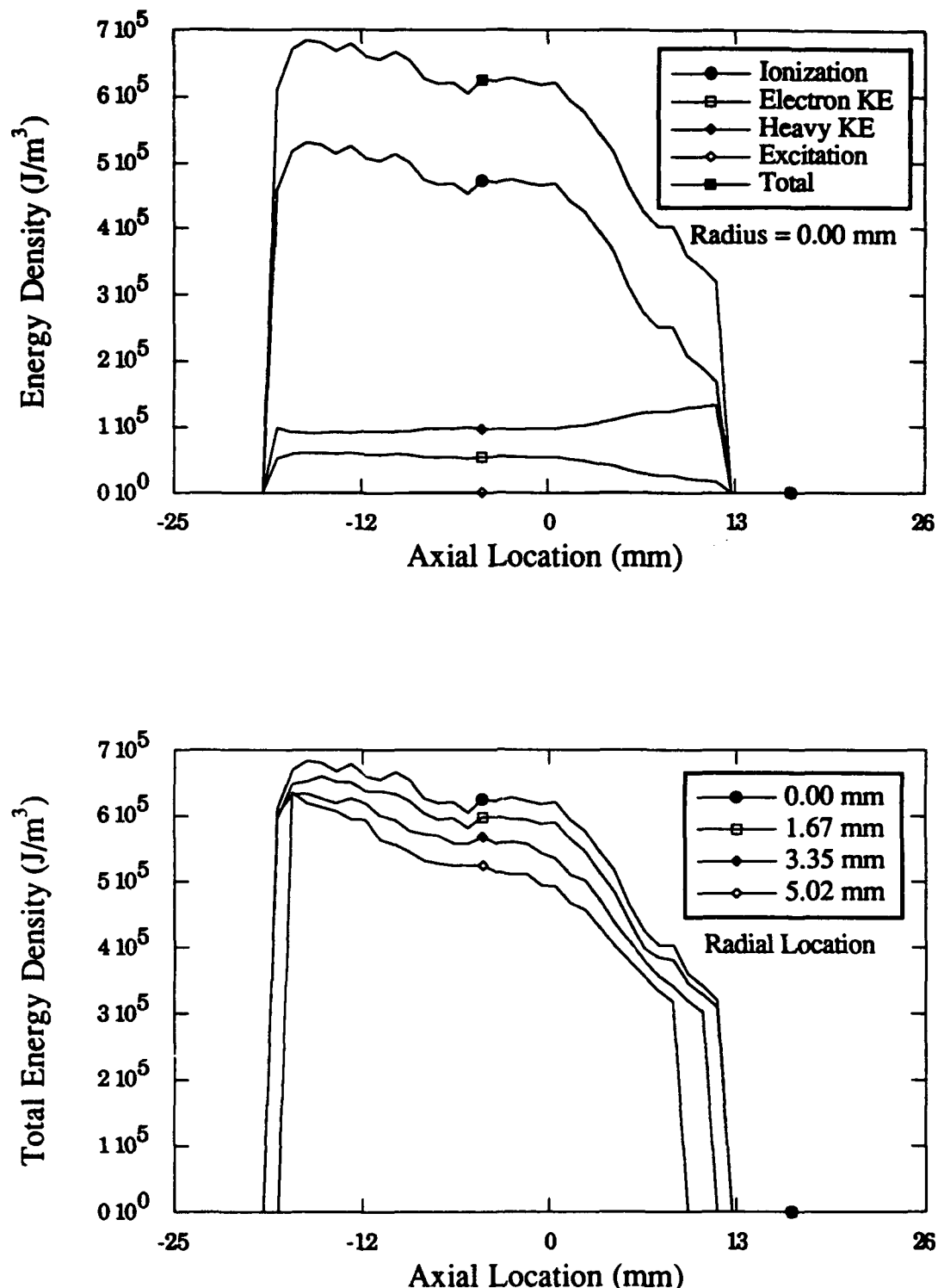


Figure 4.40 Upper plot: Axial variation of the various energy densities along the centerline.
 Lower plot: Axial variation of total energy density at several radii.

kinetic temperature. At some point past the spectroscopic measurement domain, the electrons and ions will fully recombine, the radiation field will decrease to near zero, and the net power absorbed from the laser beam will be contained in the flow of neutral argon atoms as they make their way towards a laser thruster exhaust nozzle.

5. CONCLUSIONS AND RECOMMENDATIONS

5.1. CONCLUSIONS

Non-local thermodynamic equilibrium is a significant effect in laboratory laser sustained argon plasmas. The most important factor is kinetic nonequilibrium between the electrons and the heavy particles. The electron kinetic temperature can be more than twice as large and as much as 8000 K higher than the heavy particle kinetic temperature in the LSP studied in this investigation. The greatest deviation between kinetic temperatures occurs near the plasma front, where the laser power flux is high. The beam is attenuated as it passes through the plasma and kinetic nonequilibrium is not as severe in the plasma tail.

Nonequilibrium between the electron kinetic temperature and the electronic excitation temperatures is another significant effect in this LSP. Often the electron kinetic temperature is assumed to be equivalent to the upper level excitation temperature of the neutral particles. This is a very poor approximation in this LSP because $T_{ex\beta,a}$ is typically 3000 K-5000 K lower than the electron kinetic temperature. In addition, $T_{ex\beta,a}$ is subject to large errors due to both uncertainties in the spontaneous emission coefficients, and systematic error associated with the accuracy of these coefficients.

A better approximation is that the temperature resulting from an LTE analysis of a neutral particle upper energy level population can be used to calculate the neutral particle number density. This allows the determination of electron and heavy particle kinetic temperatures through application of the non-LTE thermodynamic model described in this work. This approximation is valid due to the near Boltzmann equilibrium existing among the neutral particle electronic energy levels, and the weak dependence of total excitation temperature on various LSP nonequilibrium effects.

A similar approximation is valid for the ion electronic system. A quasi-neutral plasma at the temperatures found in this LSP will have very nearly equivalent electron and ion number

densities. The ion number density determined from an LTE analysis of an ion upper energy level population in this LSP agrees extremely well with the electron number density determined through a Stark broadening analysis of the hydrogen Balmer series alpha line spectral profile. This result validates the ion LTE analysis as a means for determining electron number density in this LSP. The critical electron number density criteria for Boltzmann equilibrium due to Drawin [1969] and Griem [1964] seem to be valid indicators for this LSP. The result for the ion electronic system is especially convincing.

Although the LTE analysis of a neutral line upper level population can be accurately used to determine neutral particle number density, it should not be used to determine electron number density. Nor should the neutral particle number density be determined from an LTE analysis of an ion line upper level population. These misapplications would result in an extremely poor determination of the LSP thermodynamic state.

It is somewhat inconsistent that the ion total excitation temperature is greater than the calculated electron kinetic temperature. It could be that the ion excitation temperature is inaccurate due to inaccurate spontaneous emission coefficients, but its value is validated by the accurate prediction of ion number density. Evidence of Boltzmann equilibrium indicates that the ion level population excitation and de-excitation rates are collision dominated. In this case there is no means by which the excitation temperature could exceed the electron kinetic temperature.

A possible explanation for the $T_{\text{exi}} > T_e$ inconsistency is that the argon ionization reaction is not in chemical equilibrium as assumed in the derivation of equation (1.20) from equation (1.19). If chemical nonequilibrium is considered, then $\alpha \neq 0$ and it appears in the exponential term of equation (1.20). The ionization equation written with $\alpha \neq 0$ is as follows:

$$n_e \left(\frac{n_i}{n_a} \right) \frac{T_g}{T_e} = 2 \frac{Z_{\text{exi}} \left(\frac{T_{\text{exi}}}{T_e} \right)}{Z_{\text{exa}} \left(\frac{T_{\text{exa}}}{T_e} \right)} \left(\frac{2\pi m_e k_b T_e}{h^2} \right)^{3/2} \exp \left(\frac{-E_{\text{la}} + \alpha}{k_b T_e} \right) \quad (5.1)$$

The effect is of altering the ionization potential of neutral argon by an amount equal to the chemical affinity, α . If the values of n_e , n_i , n_a , T_{exa} , and T_{exi} are known, then increasing T_e to equal T_{exi} requires a decrease in T_g to satisfy the equation of state. Some non-zero value of α is then required to satisfy equation (5.1). For example, on the plasma centerline near the plasma front; $n_e = n_i = 2.10 \times 10^{23} \text{ m}^{-3}$, $n_a = 4.68 \times 10^{23} \text{ m}^{-3}$, $T_{exa} = 12041 \text{ K}$, and $T_{exi} = 15923 \text{ K}$. The corresponding T_e and T_g with chemical equilibrium are $T_e = 14036 \text{ K}$ and $T_g = 6626 \text{ K}$. If T_e is increased to 15923 K, then T_g decreases to 6048 K, and $\alpha = -15606 \text{ cm}^{-1}$ is required. This represents an effective increase of approximately 12% in the ionization potential.

In other words, the chemical nonequilibrium is a result of the plasma not being able to ionize fast enough, thus the seemingly higher ionization potential. This conclusion does not seem at all unreasonable at this location near the plasma front, and chemical nonequilibrium may be indicated in this LSP.

Some question remains concerning the values for the spontaneous emission coefficients used for argon line transitions. The values used for neutral argon in this investigation do not agree well with the more commonly accepted National Institute of Standards and Technology (NIST) values [Wiese, et al., 1989]. However, use of the NIST values changes only the degree of the kinetic nonequilibrium calculated. NIST values of neutral argon spontaneous emission coefficient lead to an even higher prediction of neutral particle number density, thus the heavy particle kinetic temperature is lowered even further. More recent values for the argon ion spontaneous emission coefficients [Garcia and Campos, 1985] have better agreement with the values used in this investigation, almost to within the stated uncertainties.

In other investigations where the kinetic nonequilibrium is not as easily observed, or where it is important to accurately calculate the upper level excitation temperature, it will be necessary to arrive at a universally consistent set of argon spontaneous emission coefficients. However, for the purposes of this investigation, the accuracy of these coefficients is not of utmost concern.

5.2. RECOMMENDATIONS

Based on the conclusions presented above, the following recommendations are made:

- 1) Future spectroscopic diagnostics of laboratory laser sustained plasmas be performed using non-LTE methods. LTE analysis can be used judiciously if the appropriate conditions are met, e.g. critical electron number density for ionic Boltzmann equilibrium. However, determining the entire plasma thermodynamic state from an LTE temperature or upper level excitation temperature alone results in large errors.
- 2) Future numerical modeling of laser sustained plasmas should include non-LTE effects. Based on this investigation, the most important effect to include is kinetic nonequilibrium. Also of value would be the inclusion of some method for tracking optically thick radiative transport through the plasma. Current LTE models use experimentally determined values of 'radiative conductivity' which may or may not be applicable to every (or *any*) general plasma geometry.

These improvements in a numerical model may help to better predict LSP position relative to the laser focus. This investigation has shown how kinetic nonequilibrium affects the relative plasma particle number densities. Increased electron and ion number densities are possible in regions near the plasma front, thus the laser power absorption coefficient is larger. The overall effect is the movement of the plasma front farther upstream of the laser focus than it would be if kinetic equilibrium were held.

In addition, if the radiative conductivity used by the current LTE numerical model is too low, then the radiative/conductive preheating of the cold inlet gas is underestimated. This would have the effect of pushing the plasma front back closer to the laser focus.

Another valuable characteristic of a non-LTE model would be the ability to account for nonequilibrium excited electronic energy level populations. This would require a collisional-radiative model to be incorporated into the algorithm [Cho,1988], and is a very involved undertaking [Mertogul, 1992].

APPENDICES

A. COMPUTER CODE LISTINGS

A.1. Raw Spectroscopic Data Reduction

```

program RAWOMA
c
c*****THIS PROGRAM WILL READ IN A FILE TRANSFERRED FROM THE OMA WHICH
c CONTAINS BACKGROUND FILES EMBEDDED AT USER SPECIFIED LOCATIONS.
c DATA IS TAKEN AT A PARTICULAR MONOCHROMATOR SETTING. THE DATA
c THEREFORE REPRESENTS A THREE DIMENSIONAL DATA SET INCLUDING
c SPECTRAL INFORMATION ON THE 'CHANNELS', SPATIAL INFORMATION
c (RADIAL) ON THE 'TRACKS', AND SPATIAL INFORMATION (AXIAL) ON
c THE 'AXIAL STATIONS'. EACH DATA (not BG) FILE REPRESENTS AN AXIAL
c LOCATION IN THE PLASMA.
c THE PROGRAM WILL SMOOTH THE DATA TO WITH A FOURIER TRANSFORM
c TECHNIQUE, SUBTRACT OFF THE APPROPRIATE BACKGROUND SIGNAL
c FROM EACH PLASMA DATA SCAN, CALIBRATE THE PLASMA DATA RESULTING
c IN (MICROWATTS/CM**2 SR) ON EACH CHANNEL, AND INTEGRATE ALL
c THE IMPORTANT LINE AND CONTINUUM SPECTRAL REGIONS. THE RESULT WILL
c BE TWO FILES FOR EACH LINE REPRESENTED, EACH CONTAINING EITHER
c INTEGRATED LINE OR CONTINUUM DATA IN TWO DIMENSIONS, RADIAL
c AND AXIAL. THIS DATA IS THEN TO BE INPUT TO AN ABEL INVERSION CODE
c TO RESOLVE POINT INTENSITIES (MICROWATTS/CM**3 SR).
c*****LAST MODIFIED BY DKZ ON 11/20/90
c MODIFIED TO RAWOMA2 BY DKZ ON 4/18/91
c      User input background file locations
c      Removal of wavelength calibration section (assumed linear)
c MODIFIED BY DKZ ON 9/18 91 for FFT smoothing of noise
c
c*****DESCRIPTION OF SOME VARIABLES USED IN THIS PROGRAM
c
c      Alam: Input; HR-320 center wavelength; tells program which
c              calibration constants are to be used. (in Angstroms)
c      nmlamvec: Array containing the wavelength on each channel
c      back: Array to read in the background scans to be subtracted
c              from the plasma data scans. (in nanometers)
c      block: Number of DAT-BG-DAT sequences present in the .dat file
c      c1-c4: curve fit constants for calculating nmlamvec.
c      cal: Character variable naming the file containing the
c              calibrated intensity data (i.e. prefix.cal)
c      calden: Input; optical density of the filters used to take
c              intensity calibration lamp data.
c      con: Character variable naming the file containing the
c              integrated continuum data (i.e. lambda.cal)
c      dens: Calibration factor accounting for the difference in the
c              optical densities of the plasma and lamp data filters.
c      Dlamvec: Array containing the wavelength interval falling on
c              each channel.

```

```

c dumdeal: Array to read in the whole data set (for smoothing)
c dumfile: Character variable to read in the OMA files names
c           from the data set.
c dumscan: Array to read in a plasma scan before background subtraction
c exp: Character variable naming the file containing the
c       experimental information data (i.e. prefix.exp)
c expden: Input; optical density of the filters used to take
c           plasma data.
c Fexp: Array to read in the entire smoothed and background
c       subtracted data set.
c Flmp: Array to read in the calibration lamp data set.
c Icon: Array containing the integrated continuum intensities
c       corresponding to the spectral lines.
c Iexp: Array containing the final, calibrated data set.
c Iinteg: Array contains the integrated spectral line intensities.
c int: Character variable naming the file containing the
c       integrated line data (i.e. lambda.int)
c lambda: Array containing the prefixes for the integrated
c           line and continuum intensities.
c lmp: Character variable naming the file containing the
c       calibration lamp data (i.e. prefix.lmp)
c nbg: Character variable naming the file containing the
c       background subtracted data (i.e. prefix.nbg)
c nchan: Input; number of vidicon channels used.
c ncl: Array containing the 'lefthand' pixel of the line wings.
c ncr: Array containing the 'righthand' pixel of the line wings.
c ndiff: ncr-ncl.
c nline: Input; number of lines integrated from the data set.
c nscan: Input; total number of scans (background+data).
c ntot: total number of pixels used per scan (nchan*ntrak)
c ntrak: Input; number of tracks used on the vidicon.
c nvstat: Input; number of axial stations in the data set.
c dat: Character variable naming the file containing the
c       raw oma data (i.e. prefix.dat)
c prefix: Input; general name for all files used or created during
c           the data set reduction.
c peakchn: Channel on which the line center falls
c r1-r5: curve fit constants for calculating intensity
c           calibration factors.
c Slmp: Array containing the intensity calibration factors
c           for each pixel.
c smo: Character variable naming the file containing the
c       smoothed data (i.e. prefix.smo)
c ****
c
c common/expdat/Alam,nvstat,nscan,nchan,ntrak,expden,calden,Dlam
c common/files/smo,exp,dat,nbg,lmp,cal,prefix
c common/bacscn/nbacs(60)
c common/noise/peakchn,ncon
c character*6 prefix
c character*10 exp,dat,smo,nbg,cal,lmp
c character*4 s1/'.smo'/
c character*4 s2/'.dat'/
c character*4 s3/'.nbg'/
c character*4 s4/'.lmp'/
c character*4 s5/'.cal'/
c character*4 s6/'.exp'/

```

```
      write(6,*) 'What is the .dat filename prefix?'
      read(5,95) prefix

c
      smo=prefix//s1
      exp=prefix//s6
      dat=prefix//s2
      nbg=prefix//s3
      lmp=prefix//s4
      cal=prefix//s5

c
      call experiment
      call smooth
      call backsub
      call calibrate
      call integrate

c
95  format(A)
c
      stop
      end

c*****READ IN THE EXPERIMENT INFO AND WRITE TO .EXP FILE
      subroutine experiment

c
      common/expdat/Alam,nvstat,nscan,nchan,ntrak,expden,calden,Dlam
      common/files/smo,exp,dat,nbg,lmp,cal,prefix
      common/bacscn/nbacs(60),nbacscn
      common/noise/peakchn,ncon

c
      character*10 exp,dat,smo,nbg,cal,lmp
      integer nchan,nvstat,ntrak,nscan,nbacs,nbacscn

c
      open(unit=8,file=exp)

c
      read(8,*) Alam
      read(8,*) Dlam
      read(8,*) nvstat
      read(8,*) nscan
      read(8,*) nchan
      read(8,*) ntrak
      read(8,*) expden
      read(8,*) calden
      read(8,*) nbacscn
      do 10 i=1,nbacscn
10      read(8,*) nbacs(i)
      read(8,*) peakchn
      read(8,*) ncon

c
      close(8)
      return
      end

c*****READ IN THE RAW OMA DATA, REMOVE THE OMA SCAN NAMES
c*****AND PERFORM CHANNEL NOISE SMOOTHING. THE FFT WAS
c*****FIRST WRITTEN BY MAGDI AZER AND MODIFIED FOR USE
c*****IN THIS PROGRAM.
      subroutine smooth

c
      common/expdat/Alam,nvstat,nscan,nchan,ntrak,expden,calden,Dlam
      common/files/smo,exp,dat,nbg,lmp,cal,prefix
```

```

common/bacsxn/nbacs(60),nbacsxn
common/noise/peakchn,ncon

c
character*10 exp,dat,smo,nbg,cal,lmp
character*11 dumfile
complex*16 fk(0:1024),W,temp,r,b,sum,xx,fwk(0:1024),frk(0:1024),sum1
complex*16 fyk(0:1024),g(0:1024),backgr(64,300)
real*4 ran
real*8 f,fc,x
real*8 dm,test
real*8 ang,pi,fkint(0:1024),dint,ang2
real*8 Alam,expden,calden
integer nchan,nvstat,ntrak,nscan
dimension dumdeal(500)

c
open(unit=7,file=dat)
open(unit=9,file=smo)
open(unit=20,file='backgr')

c
pi = dacos(-1.d0)
n1=nchan

c
***** calculate the power of two required for this sequence
xln=dlog10(n1*1.)/dlog10(2.)
12n=nint(xln)
if (12n.lt.xln) 12n=12n+1c
***** np is the number of points in the transformed sequence
***** n2 is the number of points in the mirrored-double sequence
np=2**12n
n2=np*2
ndn=np-n1+1
ii=1

c
do 66 nn=1,nscan
  read(7,97)dumfile
  write(6,97)dumfile
  do 77 mm=1,ntrak
***** read in the data, leaving room to pad with zeroes
  total=0.
  do 12 i=0,n1-1
    read(7,*) fwxk(i)
12  total=total+fxk(i)
  avg=total/n1
***** Window the edge with a cosine attenuator
  do 16 i=n1,n1+9
16  fk(i)=(fxk(n1-1)-avg)*dcos((110-i)*pi/20.)
***** Subtract the mean value from all points (kills dc component)
***** Pad zeroes to the end of the sequence
***** Mirror the sequence to create a symmetric profile
  do 13 i=0,n1-1
13  fk(i)=fxk(i)-avg
  do 14 i=n1+10,np
14  fk(i)=(0.d0,0.d0)
  do 15 i=np+1,n2-1
    j=i-2*(i-np)
    fk(i)=fk(j)
15  n=n2*2
    j=1

```

```

***** perform bit reversal
do 11 i=1,n,2
  if (j.gt.i) then
    l = (j-1)/2
    k = (i-1)/2
    temp = fk(l)
    fk(l) = fk(k)
    fk(k) = temp
  endif
  m=n/2
1      if((m.ge.2).and.(j.gt.m)) then
    j=j-m
    m=m/2
    goto 1
  endif
  j=j+m
11    continue
  k=1
***** perform fast Fourier transform
do 30 l=1,12n+1
  m=k
  bm=m
  k=2*k
  w = (1.d0,0.d0)
  do 20 j = 1,m
    bj = j
    do 10 i = j,n2,k
      i2 = i + m - 1
      b = fk(i2)*w
      fk(i2) = fk(i-1) - b
      fk(i-1) = fk(i-1) + b
10    continue
    ang = pi*bj/bm
    w = dcplx(dcos(ang),-dsin(ang))
20    continue
30    continue
  do 31 i=0,n2-1
31    fk(i)=fk(i)/n2
***** Apply Butterworth-type low-pass filter
  filter=1
  fc=80.
  xf=6.
  if (filter.ne.1) goto 65
  do 19 i=0,n2-1
    f=float(i)
    x2=float(n2/2)
    if (i.gt.(n2/2)) f=f-2.* (f-x2)
    g(i)=dcplx(dcos(pi*f/r2)*(1.+(f/fc)**(2.*xf))**-.5,
    &           dsin(pi*f/n2)*(1.+(f/fc)**(2.*xf))**-.5)
    fk(i)=fk(i)*g(i)
19    continue
65    continue
***** Set imaginary component of the transform to zero (due to noise)
  do 111 i=0,n2-1
111    fk(i)=dcplx(dreal(fk(i)),0.0)
***** Perform inverse Fourier transform
***** Add back the mean value of the sequence
  j=1

```

```

***** perform bit reversal
do 511 i=1,n,2
  if (j.gt.i) then
    l = (j-1)/2
    k = (i-1)/2
    temp = fk(l)
    fk(l) = fk(k)
    fk(k) = temp
  endif
m=n/2
2      if((m.ge.2).and.(j.gt.m)) then
        j=j-m
        m=m/2
        goto 2
      endif
      j=j+m
511    continue
      k=1
***** perform fast inverse Fourier transform
do 530 l=1,12n+1
  m=k
  bm=m
  k=2*k
  W = (1.d0,0.d0)
do 520 j = 1,m
  bj = j
  do 510 i = j,n2,k
    i2 = i + m - 1
    b = fk(i2)*w
    fk(i2) = fk(i-1) - b
    fk(i-1) = fk(i-1) + b
510    continue
    ang = pi*bj/bm
    W = dcplx(dcos(ang),dsin(ang))
520    continue
530    continue
***** Check for background scan (add for averaging) or write to file
  if (nn.eq.nbacs(ii)) then
    do 1100 jj=0,n1-1
      fxk(jj)=fk(jj)+avg
1100    backgr(mm,jj)=backgr(mm,jj)+fxk(jj)
  else
    do 1101 jj=0,n1-1
      fxk(jj)=fk(jj)+avg
1101    write(9,1102) dreal(fxk(jj))
  endif
77    continue
  if (nn.eq.nbacs(ii)) ii=ii+1
66    continue
***** Calculate the average background and write it to file 'backgr'
  do 1103 jj=1,ntrak
    do 1103 kk=0,n1-1
      backgr(jj,kk)=backgr(jj,kk)/float(nbacsnn)
1103    write(20,1102) dreal(backgr(jj,kk))
97    format(A)
1102  format(f6.1)
  close(7)
  close(9)

```

```

      close(20)
c
      return
      end
c*****PERFORM BACKGROUND SUBTRACTION AND SAVE RESULTS (.NBG)
      subroutine backsub
c
      common/expdat/Alam,nvstat,nscan,nchan,ntrak,expden,calden,Dlam
      common/files/smo,exp,dat,nbg,lmp,cal,prefix
      common/bacscn/nbacs(60),nbacscn
      common/noise/peakchn,ncon
      character*10 exp,dat,smo,nbg,cal,lmp,tab
      integer nscan,nchan,ntrak,nvstat,nbacscn,nbacs
      dimension dumscan(15000),back(15000)
c
      open(unit=9,file=smo)
      open(unit=10,file=nbg)
      open(unit=20,file='backgr')
      rewind(20)
      rewind(9)
c
      ntot=ntrak*nchan
      do 70 i=1,ntot
         read(20,120)back(i)
      do 80 i=1,nvstat
      do 90 j=1,ntot
         read(9,120)dumscan(j)
      90      write(10,120)dumscan(j)-back(j)
      80      continue
      close(9)
      close(10)
      close(20)
120      format(f6.1)
      return
      end
c*****CALCULATE THE WAVELENGTH VECTOR ASSOCIATED WITH THIS DATA
c*****SET, CALCULATE THE WAVELENGTH INTERVAL ON EACH CHANNEL,
c*****CALCULATE THE INTENSITY CALIBRATION FACTOR FOR EACH CHANNEL,
c*****AND CALCULATE THE CALIBRATED INTENSITY FOR EACH CHANNEL
      subroutine calibrate
c
      common/expdat/Alam,nvstat,nscan,nchan,ntrak,expden,calden,Dlam
      common/files/smo,exp,dat,nbg,lmp,cal,prefix
      common/noise/peakchn,ncon
c
      character*10 exp,dat,smo,nbg,cal,lmp
      integer ntrak,nchan,nvstat,nscan,nstrt,nend
      real*8 Fexp(60,51,500),Flmp(51,500)
      real*8 c1,c2,c3,c4,r1,r2,r3,r4,r5
      real*8 Alam,expden,calden
      real*8 nmllamvec(500),Slmp(500),Iexp(60,51,500)
      real*8 nmllamin,nmllamax
c
      open(unit=10,file=nbg)
      rewind(10)
      open(unit=11,file=lmp)
      open(unit=12,file=cal)
c

```

```

do 190 i=1,nchan
190  nmlamvec(i)=0.1*(Alam+(i-peakchn)*10.*Dlam)
c*****READ IN THE OMA FILE CONTAINING THE INTENSITY CALIBRATION
c      DATA FILE (.LMP), DETERMINE THE CORRECT LAMP CURVE FIT,
c      AND CALIBRATE THE PLASMA DATA FOR ABSOLUTE SPECTRAL RADIANCE*****
c
nmlamin=nmlamvec(1)
nmlamax=nmlamvec(nchan)
c
do 202 i=1,nvstat
do 205 j=1,ntrak
do 210 k=1,nchan
210  read(10,122) Fexp(i,j,k)
205  continue
202  continue
c
do 206 j=1,ntrak
do 211 k=1,nchan
211  read(11,*) Flmp(j,k)
206  continue
c
if (350. .le. nmlamin .and. nmlamax .lt. 490.) then
  r1=56.677795897
  r2=-0.37004906185
  r3=0.00070547019574
  r4=-3.0597649765e-7
  r5=0.0
  edge=490.
elseif (490. .le. nmlamin .and. nmlamax .lt. 670.) then
  r1=33.914311834
  r2=-0.28980959708
  r3=0.00066275118741
  r4=-3.5968909308e-7
  r5=0.0
  edge=670.
elseif (670. .le. nmlamin .and. nmlamax .lt. 830.) then
  r1=95.777041634
  r2=-0.45056871965
  r3=0.00075578518507
  r4=-3.4614990423e-7
  r5=0.0
  edge=830.
elseif (830. .le. nmlamin .and. nmlamax .lt. 990.) then
  r1=-6637.1270333
  r2=29.867198599
  r3=-0.05025358659
  r4=3.7633379499e-5
  r5=-1.0549585806e-8
  edge=990.
elseif (990. .le. nmlamin .and. nmlamax .le. 1110.) then
  r1=1514.4134258
  r2=-4.8113899083
  r3=0.0051846187885
  r4=-1.8272409409e-6
  r5=0.0
  edge=1110.
elseif (350. .le. nmlamin .and. nmlamax .ge. 490.) then

```

```

r1=56.677795897
r2=-0.37004906185
r3=0.00070547019574
r4=-3.0597649765e-7
r5=0.0
x1=33.914311834
x2=-0.28980959708
x3=0.00066275118741
x4=-3.5968909308e-7
x5=0.0
edge=490.
elseif (490. .le. nmlamin .and. nmlamax. ge. 670.) then
  r1=33.914311834
  r2=-0.28980959708
  r3=0.00066275118741
  r4=-3.5968909308e-7
  r5=0.0
  x1=95.777041634
  x2=-0.45056871965
  x3=0.00075578518507
  x4=-3.4614990423e-7
  x5=0.0
  edge=670.
elseif (670. .le. nmlamin .and. nmlamax. ge. 830.) then
  r1=95.777041634
  r2=-0.45056871965
  r3=0.00075578518507
  r4=-3.4614990423e-7
  r5=0.0
  x1=-6637.1270333
  x2=29.867198599
  x3=-0.05025358659
  x4=3.7633379499e-5
  x5=-1.0549585806e-8
  edge=830.
elseif (830. .le. nmlamin .and. nmlamax. ge. 990.) then
  r1=-6637.1270333
  r2=29.867198599
  r3=-0.05025358659
  r4=3.7633379499e-5
  r5=-1.0549585806e-8
  x1=1514.4134258
  x2=-4.8113899083
  x3=0.0051846187885
  x4=-1.8272409409e-6
  x5=0.0
  edge=990.
else
  write(6,*) 'Wavelength not in lamp range.'
  write(6,*) 'Enter the ten (five if not split) Scal canstants,
+ each followed by a carriage return.'
  read(5,*) r1
  read(5,*) r2
  read(5,*) r3
  read(5,*) r4
  read(5,*) r5
  read(5,*) x1
  read(5,*) x2

```

```

    read(5,*) x3
    read(5,*) x4
    read(5,*) x5
  endif
C
  dens=10** (expden-calden)
C
  do 220 i=1,nchan
    if (nmlamvec(i) .lt. edge) then
      Slmp(i)=r1+nmlamvec(i)*r2+nmlamvec(i)**2*r3+nmlamvec(i)**3*r4
+          +nmlamvec(i)**4*r5
    else
      Slmp(i)=x1+nmlamvec(i)*x2+nmlamvec(i)**2*x3+nmlamvec(i)**3*x4
+          +nmlamvec(i)**4*x5
    endif
220  continue
C
  do 222 i=1,nvstat
  do 225 j=1,ntrak
  do 230 k=1,nchan
    Iexp(i,j,k)=Slmp(k)*Fexp(i,j,k)*Dlam*dens/Flmp(j,k)
230  write(12,113) Iexp(i,j,k)
225  continue
222  continue
C
122  format(f8.1)
113  format(f9.2)
C
  close(10)
  close(11)
  close(12)
C
  return
end
C*****SUBROUTINE TO INTEGRATE THE SPECTRAL LINE PROFILE.
subroutine integrate
C
  common/expdat/Alam,nvstat,nscan,nchan,ntrak,expden,calden,Dlam
  common/files/smo,exp,dat,nbg,lmp,cal,prefix
  common/noise/peakchn,ncon
C
  integer ndiff(10),ncl(10),ncr(10),nchan,ntrak,nvstat
  real*8 Icon(10,60,51),Iinteg(10,60,51),Iexp(60,51,500)
  real*8 totint(51,500),Inet(60,51,500)
  character*4 s7/'.con'/
  character*4 s8/'.int'/
  character*4 s9/'.net'/
  character*10 con,int,cal,exp,dat,smo,lmp,nbg,net
  character*6 prefix
C
  open(unit=12,file=cal)
  rewind(12)
C
  xcon=float(ncon)
C
  do 700 i=1,nvstat
  do 710 j=1,ntrak
  do 720 k=1,nchan

```

```

      read(12,114) Iexp(i,j,k)
720  continue
710  continue
700  continue
c
114  format(f9.2)
c
      write(6,*)'how many lines to be integrated (max of 10) ?'
      read(5,*)nline
c
      do 400 k=1,nline
      write(6,*)'enter the left channel for line number ',k
      read(5,410)ncl(k)
      write(6,*)'enter the right channel for line number ',k
      read(5,410)ncr(k)
400  continue
c
410  format(i3)
c*****INTEGRATE Iexp VS LAMBDA*****
      do 785 j=1,nvstat
      do 780 k=1,ntrak
      do 789 i=1,nline
      Icon(i,j,k)=0.0
      Iinteg(i,j,k)=0.0
789  continue
780  continue
785  continue
c
      do 1000 i=1,nline
      ndiff(i)=ncr(i)-ncl(i)
      xdiff=float(ndiff(i))+1.0
c
      do 950 j=1,nvstat
      do 900 k=1,ntrak
c*****INTEGRATE LINE AND CORRESPONDING CONTINUUM*****
      do 101 nc=ncl(i),ncr(i)
      Iinteg(i,j,k)=Iinteg(i,j,k)+Iexp(j,k,nc)
      do 102 ll=ncl(i)-ncon,ncl(i)-1
      Icon(i,j,k)=Icon(i,j,k)+Iexp(j,k,ll)
      do 103 jj=ncr(i)+1,ncr(i)+ncon
      Icon(i,j,k)=Icon(i,j,k)+Iexp(j,k,jj)
103  continue
c
      Icon(i,j,k)=(1./(2.*xcon))*Icon(i,j,k)*xdiff
c*****SUBTRACT THE CONTINUUM FROM THE LINE*****
      Inet(i,j,k)=Iinteg(i,j,k)-Icon(i,j,k)
900  continue
950  continue
1000 continue
c
      con=prefix//s7
      int=prefix//s8
      net=prefix//s9
      open(unit=14,file=con)
      open(unit=13,file=int)
      open(unit=15,file=net)
      do 300 i=1,nline
      do 310 j=1,nvstat
      do 320 k=1,ntrak

```

```

      write(15,*) Inet(i,j,k)
      write(14,*) IIcon(i,j,k)
320    write(13,*) Iinteg(i,j,k)
310    continue
300    continue
C
      close(12)
      close(14)
      close(13)
      close(15)
      close(21)
C
      return
end

```

A.2. Abel Inversion by Inverse Hankel Transform

```

program ABEL
C
C THIS PROGRAM PERFORMS A FOURIER-BESSEL TRANSFORM, ALSO KNOWN
C AS AN INVERSE HANKEL TRANSFORM, FOR THE PURPOSE OF ACQUIRING
C THE SPATIALLY RESOLVED 'ABEL INVERSION' OF THE INPUT PROFILES.
C
      complex*16 fk(0:1024),W,tempb,sum,xx,fxk(0:1024),frk(0:1024),suml
      complex*16 fyk(0:1024),g(0:1024),base
      real*4 ran
      real*8 f,fc,x,Imax
      real*8 dm,Re(0:1024),Im(0:1024),test
      real*8 ang,pi,fkint(0:1024),dint,ang2
      character*6 prefix
      character*3 suffix
      character*10 RAW,IFT,FFT,IHT
C
      print*, 'Enter the raw data file name prefix (6 characters)'
      read(5,'(A)') prefix
      print*, 'Enter the raw data file name suffix (3 characters)'
      read(5,'(A)') suffix
      print*, 'Enter the number of vertical stations'
      read(5,*) nvstat
      print*, 'apply filter? (1=yes)'
      read(5,*) ans2
      print*, 'fc='
      read(5,*) fc
      print*, 'n='
      read(5,*) xf
C
      RAW=prefix//'.'//suffix
      FFT=prefix//'.FFT'
      IHT=prefix//'.IHT'
      pi = dacos(-1.d0)
C
      open(unit=7,file=RAW)
      open(unit=8,file=FFT)

```

```

open(unit=10,file=INT)
C***** Set the number of points in the sequence
n1=51
C
xln=dlog10(n1*1.)/dlog10(2.)
12n=nint(xln)
if (12n.lt.xln) 12n=12n+1
np=2**12n
ndn=int((np-n1)/2.)
n2=int(n1/2.)
C
do 122 nn=1,nvstat
C***** Read in the lateral profile sequence for this station
Imax=0.
do 12 i=0,n1-1
read(7,*) fk(i)
if (dreal(fk(i)).gt.Imax) Imax=dreal(fk(i))
12 continue
C*****set baseline to zero
base=(0.d0,0.d0)
do 121 i=2,6
121 base=base+fk(i)
base=base/5.
Imax=Imax-base
C
do 14 i=0,n2
14   fxk(i)=fk(i+n2)-base
do 15 i=n2,n2+2*ndn
15   fxk(i)=(0.d0,0.d0)
do 13 i=np-n2,np-1
13   fxk(i)=fk(i-np+n2)-base
C
do 16 i=0,np-1
16   fk(i)=fxk(i)
16 continue
n=np*2
j=1
C*****perform bit reversal
do 11 i=1,n,2
  if (j.gt.i) then
    l = (j-1)/2
    k = (i-1)/2
    tempor = fk(l)
    fk(l) = fk(k)
    fk(k) = tempor
  endif
  m=n/2
11  if((m.ge.2).and.(j.gt.m)) then
      j=j-m
      m=m/2
      goto 1
  endif
  j=j+m
11 continue
k=1
C*****perform fast Fourier transform
do 30 l=1,12n
  m=k

```

```

bm=m
k=2*k
w = (1.d0,0.d0)
do 20 j = 1,m
  bj =j
  do 10 i = j,np,k
    i2 = i + m - 1
    b = fk(i2)*w
    fk(i2) = fk(i-1) - b
    fk(i-1) = fk(i-1) + b
10    continue
    ang = pi*bj/bm
    W = dcmplx(dcos(ang),-dsin(ang))
20    continue
30    continue
c*****print the transformed sequence to file .FFT
  do 1000 i=0,np-1
    write(8,*)dreal(fk(i)),      ',dimag(fk(i))
1000 continue
c*****apply Butterworth-type low-pass filter
  if (ans2.ne.1) goto 65
  do 19 i=0,np-1
    f=float(i)
    x2=float(np/2)
    if (i.gt.(np/2)) f=f-2.* (f-x2)
    g(i)=dcmplx(dcos(pi*f/np)*(1.+(f/fc)**(2.*xf))**-.5,
    &           dsin(pi*f/np)*(1.+(f/fc)**(2.*xf))**-.5)
    fk(i)=fk(i)*g(i)
19    continue
c***** Perform axis shifting
  KK=np/2+1
  do 120 i=0,np-1
    Re(i)=dreal(fk(i))
    Im(i)=dimag(fk(i))
120 continue
  delm=1.
  st=1e-6
  dm=0.
  dir=0
c
  y=test(dm,Re,Im,KK,np)
  x=test(dm+st,Re,Im,KK,np)
  if(y.lt.x) then
    dum=x
    x=y
    y=dum
    delm=-delm
    dir=-1
  endif
  x=y
  ncount=0
99  ncount=ncount+1
  dm=dm+delm
  y=x
  x=test(dm,Re,Im,KK,np)
  if(y.gt.x)goto 99
  nsdp=-1
  if(dir.ne.-1) st=-st

```

```

deldm=1.
xdel=1e-4
98  ncount=ncount+1
    if(nsdp.eq.-1) then
        delm=-0.5*delm
        nsdp=1
    endif
    dmold=dm
    dm=dm+delm
    y=test(dm,Re,Im,KK,np)
    x=test(dm+st,Re,Im,KK,np)
    if(x.gt.y) then
        nsdp=-1
        st=-st
    endif
    deldm=dabs((dmold-dm)/(dmold+1e-8))
    if(deldm.gt.xdel) goto 98
    print*, 'dm=',dm
c
    do 111 i=0,np-1
        yy=i*1.
        if(i.gt,np/2) yy=-yy-2.*yy-(np/2))
        ang2=-2*pi*yy*dm/np
        fk(i)=fk(i)*dcmplx(dcos(ang2),dsin(ang2))
        fk(i)=dcmplx(dreal(fk(i)),0.0)
111  continue
65   continue
c*****perform inverse Hankel transform
c*****calculate interpolation points (based on Bessel zeroes)
    fkint(0)=2.4048/pi
    fkint(1)=5.5201/pi-1
    fkint(2)=8.6537/pi-2
    fkint(3)=11.7915/pi-3
    fkint(4)=14.9309/pi-4
    fkint(5)=18.0711/pi-5
    fkint(6)=21.2116/pi-6
    do 117 i=7,np/2
        fkint(i)=0.751609672
117  continue
c
    sum1=0.
    do 200 k=0,np/2
        sum=0.
        do 210 i=0,np/2
            yy=i+fkint(i)
            dint=1.-fkint(i)
c            if(i.gt.(np/2)) yy=yy-2.*yy-(np/2))
            ang=2.*pi*k*yy/np
210   sum=sum+dbsj0(ang)*(yy/np)*(fk(i+1)+dint*(fk(i)-fk(i+1)))
        frk(k)=2.*pi*sum
        sum1=sum1+frk(k)
        write(10,*)dreal(frk(k)), ' ', dimag(fk(k))
200   continue
        do 211 i=0,int(n1/2.)
211   sum1=sum1+frk(i)
        print*, 'Icheck(0)=',2.*sum1-frk(0)
        print*, 'Imax=',Imax
        c
        write(10,*)2.*sum1-frk(0)
        endif

```

```

122  continue
c
  close(7)
  close(8)
  close(9)
  close(10)
c
  stop
end
c
  real function test *8 (xm,Rel,Ima,LLL,ip)
  real*8 Rel(0:1024),Ima(0:1024)
  test=0.
  pi=dacos(-1.0)
  do 10 i=0,LLL-1
    ang=4.*pi*i*xm/ip
    test=test+i*(2.*Rel(i)*Ima(i)*dcos(ang)-
  &           (Rel(i)**2-Ima(i)**2)*dsin(ang))**2
10  continue
  return
end

```

A.3. Electron Number Density by Stark Broadening

```

program NE
c
c  THIS PROGRAM IS A FORTRAN VERSION OF THE ORIGINAL TURBO BASIC
c  PROGRAM WRITTEN BY SHI-KIT CHAN (SEE BELOW)
c
  common/subint/TRIAL,NETRY(80),XIN,P,SB(15,80),SC(15,80),
+           SD(15,80),DATA2,L1,Y(80),X(80),B(80),C(80),D(80),
+           EDATA,RESID(80),DATA1,PROFILE1(80),CONVL(80),
+           STARK(15,80),PROFILE2(80),EXPER
  common/subnor/NORM(80),LPOINT,MAX,M,INTENS(160),
+           NPOINT,CENTER,NETAVG(80)
c
  integer TRIAL,DATA2,L1,EDATA,DATA1,LPOINT,M,NPOINT,CENTER,P
  real*8 NETRY,X,STARK,XIN,Y,SD,SC,SB,PROFILE1,PROFILE2
  real*8 CONVL,NORM,INTENS,MAX,RESID,NETAVG,B,C,D,EXPER(80)
  PRINT*, '*****'
  PRINT*, '** NE.BAS (VER 1.0), (c) Copyright 1989 **'
  PRINT*, '** CALCULATES ELECTRON NUMBER DENSITY **'
  PRINT*, '** VIA STARK BROADENING **'
  PRINT*, '** WRITTEN BY SHI-KIT CHAN, 3/20/1988 **'
  PRINT*, '** RESEARCH DIRECTOR, AKBAR MONTAISER **'
  PRINT*, '** THE GEORGE WASHINGTON UNIVERSITY **'
  PRINT*, '*****'
c
10  PRINT*, '1=VIDAL 2=STARK 3=DOPPL 6=NeCALC 7=QUIT'
  read(5,*) key
  if (key.eq.1) call vidalr
  if (key.eq.2) call starkr

```

```

if (key.eq.3) call dopplr
if (key.eq.6) call necalcr
if (key.eq.7) goto 999
goto 10
999 stop
end
C*****VIDAL : CREATE/EDIT VIDAL PROFILES *
subroutine vidalr
real*8 NE(15),F0(15),DALPHA(15,80),VIDAL(15,80)
integer nprofile,lprofile,VDATA(15),LDATA(15),ans
character*12 filename
character*60 title
character*5 profile/'VIDAL'/
PRINT*, 'CREATE/EDIT VIDAL PROFILES'
lprofile=0
20 PRINT*, '1=CREATE NEW FILE, 2=EDIT SAVED FILE'
read(5,*) ans
if (ans.eq.1) goto 167
if (ans.eq.2) goto 142
goto 20
C-----READ SAVED VIDAL PROFILES
142 PRINT*, 'FILENAME OF EXISTING VIDAL FILE (VIDALxxx.DAT)'
read(5,'(A)') filename
open(unit=2,file=filename,status='old',err=144)
goto 145
144 write(6,'(A)')'FILE NOT FOUND, TRY AGAIN'
goto 142
145 read(2,'(A)') title
read(2,146) nprofile
146 format(I2)
lprofile=nprofile
do 150 N=1,nprofile
read(2,*) NE(N),F0(N),VDATA(N)
LDATA(N)=VDATA(N)
do 151 M=1,VDATA(N)
151    read(2,*) DALPHA(N,M),VIDAL(N,M)
150 continue
close(2)
C-----INPUT/EDIT INITIAL INFORMATION
PRINT*, 'VIDAL FILE = ',filename
PRINT*, 'TITLE = ',title
PRINT*, '# OF VIDAL ELECTRON NUMBER DENSITY PROFILES = ',nprofile
goto 172
C
167 PRINT*, 'FILENAME OF NEW VIDAL FILE (VIDALxxx.DAT)'
read(5,'(A)') filename
PRINT*, 'TITLE = '
read(5,'(A)') title
170 PRINT*, '# OF VIDAL ELECTRON NUMBER DENSITY PROFILES (MAX 15) = '
read(5,*) nprofile
if (nprofile.lt.1.or. nprofile.gt.15) goto 170
172 PRINT*, 'ANY CORRECTION TO ABOVE DATA (Y=1/N=any #) ?'
read(5,*) ans
if (ans.eq.1) goto 167
C-----INPUT/EDIT VIDAL PROFILES
do 180 N=1,nprofile
PRINT*, 'VIDAL PROFILE #',N
if (N.gt.lprofile) goto 190

```

```

PRINT*, 'ELECTRON NUMBER DENSITY (/cm3)= ',NE(N)
PRINT*, 'F0 = DLAMDA/DALPHA = ',F0(N)
PRINT*, '# OF DATA IN THIS PROFILE =',VDATA(N)
GOTO 195
C
190 PRINT*, 'ELECTRON NUMBER DENSITY (/cm3) = '
  read(5,*) NE(N)
  PRINT*, 'F0 = DLAMBDA/DALPHA = '
  read(5,*) F0(N)
193 PRINT*, '# OF DATA IN THIS PROFILE (MAX 80) = '
  read(5,*) VDATA(N)
  IF (VDATA(N).lt.1.or.VDATA(N).gt.80) goto 193
195 PRINT*, 'ANY CORRECTION TO ABOVE DATA (Y=1/N=any #) ?'
  read(5,*) ans
  if (ans.eq.1) goto 190
C
PRINT*, 'FILENAME, PROFILE # = ',filename,N
PRINT*, '    Ne (/cm3) ',NE(N)
PRINT*, '    F0; ',F0(N)
PRINT*, 'M DALPHA INT. M DALPHA INT. M DALPHA INT.'
PRINT*, '0,0,0 TO END INPUT/EDIT DATA, M=1 TO ',VDATA(N)
210 PRINT*, 'M,DALPHA,INTENSITY = '
  read(5,*) M,DALPHA(N,M),VIDAL(N,M)
  IF(M.eq.0.and.DALPHA(N,M).eq.0.and.VIDAL(N,M).eq.0) goto 180
  IF (M.gt.VDATA(N)) PRINT*, 'error; M.gt.VDATA(N)'
  GOTO 210
180 continue
C-----SAVE VIDAL PROFILES
open(unit=1,file=filename)
write(1,'(A)') title
write(1,*) nprofile
do 220 N=1,nprofile
  write(1,221) NE(N),F0(N),VDATA(N)
  do 222 M=1,VDATA(N)
222 write(1,223) DALPHA(N,M),VIDAL(N,M)
220 continue
221 format(2(g9.3,x),2I)
223 format(2(g9.3,x))
  CLOSE(1)
  do 225 N=1,nprofile
    NE(N)=0
    F0(N)=0
    VDATA(N)=0
    LDATA(N)=0
    do 226 M=1,VDATA(N)
      DALPHA(N,M)=0
226 VIDAL(N,M)=0
225 continue
  RETURN
END
C*****F2 : CREATE STARK PROFILES FROM VIDAL PROFILES *
subroutine starkr
common/subint/TRIAL,NETRY(80),XIN,P,SB(15,80),SC(15,80),
+           SD(15,80),DATA2,L1,Y(80),X(80),B(80),C(80),D(80),
+           EDATA,RESID(80),DATA1,PROFILE1(80),CONVL(80),
+           STARK(15,80),PROFILE2(80),EXPER
  real*8 NE(15),F0(15),waveincr,MAX,XIN,DX,EXPER(80)
  real*8 NETRY,SD,SC,SB,PROFILE1,PROFILE2,CONVL,RESID

```

```

integer P1,TRIAL,DATA2,DATA1,EDATA,L1
real*8 X,Y,B,C,D
real*8 DALPHA(15,80),DLAMDA(15,80),VIDAL(15,80),STARK
integer VDATA(15),P,nprofile,ans,adv
character*5 profile/'STARK'
character*12 filename
character*60 title
C-----READ SAVED VIDAL PROFILES
PRINT*, 'READ SAVED VIDAL PROFILES'
249 write(6,*) 'FILENAME OF EXISTING VIDAL FILE (VIDALxxxx.DAT)= '
read(5,'(A)') filename
PRINT*, 'filename= ',filename
open(unit=2,file=filename,status='old',err=250)
goto 251
250 write(6,*) 'FILE NOT FOUND, TRY AGAIN'
goto 249
251 read(2,'(A)') title
read(2,*) nprofile
do 257 N=1,nprofile
read(2,*) NE(N),F0(N),VIDAL(N)
do 258 M=1,VIDAL(N)
258 read(2,*) DALPHA(N,M),VIDAL(N,M)
257 continue
CLOSE(2)
C-----INPUT INITIAL INFORMATION
PRINT*, 'TITLE = ',title
PRINT*, 'CREATE STARK PROFILES'
PRINT*, 'FILENAME OF STARK FILE (STARKxxxx.DAT) = '
read(5,'(A)') filename
PRINT*, 'WAVELENGTH INCREMENT (Angstroms) = '
read(5,*) waveincr
PRINT*, 'ANY CHANGE TO ABOVE DATA (Y=1/N=any #) ?'
read(5,*) ans
if (ans.eq.1) goto 249
282 PRINT*, 'AUTOMATIC (1) OR MANUAL (2) ADVANCEMENT ?'
read(5,*) adv
IF (adv .ne. 1 .and. adv .ne. 2) goto 282
C-----CONVERT DALPHA TO DLAMDA
PRINT*, 'FILENAME, PROFILE # = ',filename,N
PRINT*, '    Ne (/cm3)',NE(N)
PRINT*, '    F0 ',F0(N)
PRINT*, 'M DLAMDA INT. M DLAMDA INT. M DLAMDA INT.'
PRINT*, 'CONVERTING DALPHA TO DLAMDA'
do 296 M=1,VIDAL(N)
296 DLAMDA(N,M)=F0(N)*DALPHA(N,M)
call return(adv)
C-----CALCULATE SPLINE COEFFICIENTS FROM VIDAL PROFILES
C-----INTERPOLATE AT EACH WAVEINCR FOR STARK PROFILES
PRINT*, 'FILENAME, PROFILE # = ',filename,N
PRINT*, '    Ne (/cm3)',NE(N)
PRINT*, '    F0 ',F0(N)
PRINT*, 'M DLAMDA INT. M DLAMDA INT. M DLAMDA INT.'
PRINT*, 'INTERPOLATING DATA'
P=VIDAL(N)
MAX=0
do 315 M=1,P
X(M)=DLOG(DLAMDA(N,M)+2.939E-39)/DLOG(10.)
Y(M)=VIDAL(N,M)

```

```

315 IF (VIDAL(N,M) .gt. MAX) MAX=VIDAL(N,M)
    call spline
    do 320 M=1,80
      XIN=DLOG(waveincr*(M-1)+2.939E-39)/DLOG(10.)
      IF (XIN.lt.X(2)) THEN
        STARK(N,M)=(Y(2)-Y(1))*XIN/(X(2)-X(1))+Y(1)
        GOTO 329
      ENDIF
      do 323 IZ=3,P
        IF (XIN.lt.X(IZ)) goto 326
323 continue
326 IZ=IZ-1
      DX=XIN-X(IZ)
      STARK(N,M)=Y(IZ)+DX*(B(IZ)+DX*(C(IZ)+DX*D(IZ)))
329 IF (STARK(N,M) .gt. MAX) MAX=STARK(N,M)
320 continue
      call return(adv)
290 continue
C-----SAVE STARK PROFILES
      PRINT*, 'SAVING ',filename
      OPEN (unit=1,file=filename)
      write(1,'(A)') title
      write(1,*) waveincr
      write(1,*) nprofile
      do 363 N=1,nprofile
        write(1,*) NE(N)
        do 365 M=1,80
          write(1,*) STARK(N,M)
          IF (M/5..eq.INT(M/5.)) write(1,'(A)') ''
365 continue
363 continue
      CLOSE(1)
      do 373 N=1,15
        NE(N)=0
        F0(N)=0
        VDATA(N)=0
        do 374 M=1,80
          X(M)=0
          Y(M)=0
          B(M)=0
          C(M)=0
          D(M)=0
          DALPHA(N,M)=0
          DLAMDA(N,M)=0
          VIDAL(N,M)=0
374 STARK(N,M)=0
373 continue
      RETURN
      END
C*****F3 : CREATE DOPPLER PROFILE *
      subroutine dopplr
      real*8 DOPPL(80),WAVEL,TEMP,ATOMWT,waveincr,LAMDAD,VEL,R,C
      integer ans,DDATA
      character*60 title
      character*12 filename
      character*5 profile/'DOPPL'
C-----INPUT INITIAL INFORMATION
      PRINT*, 'CREATE DOPPLER PROFILE'

```

```

390 PRINT*, 'FILENAME OF DOPPLER FILE (DOPPLxx.DAT) = '
  read(5, '(A)') filename
  PRINT*, 'TITLE = '
  read(5, '(A)') title
  PRINT*, 'HP TEMPERATURE (K) = '
  read(5, *) TEMP
  PRINT*, 'WAVELENGTH (Angstroms) = '
  read(5, *) WAVEL
  PRINT*, 'ATOMIC WEIGHT (amu) = '
  read(5, *) ATOMWT
  PRINT*, 'WAVELENGTH INCREMENT (Angstroms) = '
  read(5, *) waveincr
  PRINT*, 'ANY CORRECTION TO ABOVE DATA (Y=1/N=any #) ?'
  read(5, *) ans
  if (ans .eq. 1) goto 390
  PRINT*, filename
  PRINT*, 'TEMP = ', TEMP
  PRINT*, 'WAVELENGTH = ', WAVEL
  PRINT*, 'AW = ', ATOMWT

C-----CALCULATE THEORETICAL PROFILE
  PRINT*, 'M DLAMDA INT. M DLAMDA INT. M DLAMDA INT.'
  PRINT*, 'CREATING PROFILE'
  R=8.3144
  C=2.9979E+08
  VEL=SQRT(2000.*R*TEMP/ATOMWT)
  LAMDAD=(VEL/C)*WAVEL
  do 413 M=1,80
  DOPPL(M)=EXP(-(waveincr*(M-1)/LAMDAD)**2)/(SQRT(3.1415926)*LAMDAD)
  IF (DOPPL(M) .lt. 0.01*DOPPL(1) .or. M.eq.80) goto 418
  413 continue
  418 DDATA=M
  if (DDATA.gt.80) DDATA=80
  call return(2)

C-----SAVE DOPPLER PROFILE
  PRINT*, 'SAVING ',filename
  open(unit=1,file=filename)
  write(1, '(A)') title
  write(1, *) waveincr
  write(1, *) DDATA
  do 443 M=1,DDATA
  write(1, *) DOPPL(M)
  IF (M/5..eq.INT(M/5.)) write(1, '(A)') ''
  443 continue
  close(1)
  do 450 N=1,80
  450 DOPPL(N)=0
  RETURN
  END

C*****F6 : CALCULATE ELECTRON NUMBER DENSITY *
  subroutine necalcr
  common/subint/TRYAL,NETRY(80),XIN,P,SB(15,80),SC(15,80),
  + SD(15,80),DATA2,L1,Y(80),X(80),B(80),C(80),D(80),
  + EDATA,RESID(80),DATA1,PROFILE1(80),CONVL(80),
  + STARK(15,80),PROFILE2(80),EXPER
  common/subnor/NORM(80),LPOINT,MAX,M,INTENS(160),
  + NPOINT,CENTER,NETAVG(80)
  real*8 NE(15),NORM,NETAVG,PROFILE1,PROFILE2
  real*8 STARK,DOPPL(80),INTENS,INSTU(80),EXPER(80),CONVL

```

```

real*8 RESID,X,Y,B,C,D
real*8 SB,SC,SD,MAX,EMAX
real*8 RESIDE,RESIDA,RESIDC,RESIDD,RESIDB,XIN,waveincr
real*8 NTRY,NEA,NEB,NEC,NED,NEE,MINRESID,BESTNE
integer P,T,TRIAL,adv,L1,nprofile,query,CENTER,M
integer DDATA,NPOINT,LPOINT,DATA1,DATA2,IData,EDATA
character*12 STARKs,DOPPLs,INSTUs,EXPERs,NeOUT
character*25 title,filename
character*6 profile/'NECALC'/
PRINT*, 'CALCULATE Ne'
580 PRINT*, 'FILENAME OF STARK FILE (STARKxxx.DAT) = '
read(5,'(A)') STARKs
if (query.eq.5) goto 590
581 PRINT*, 'FILENAME OF DOPPLER FILE (DOPPLxxx.DAT) = '
read(5,'(A)') DOPPLs
if (query.eq.3) goto 629
582 PRINT*, 'FILENAME OF INSTRUMENTAL FILE (INSTUxxx.DAT) = '
read(5,'(A)') INSTUs
if (query.eq.4) goto 644
PRINT*, 'ANY CORRECTION TO THE ABOVE DATA (Y=1/N=any #) ?'
read(5,*) query
if (query.eq.1) goto 580
c-----READ STARK PROFILES
query=0
PRINT*, 'READING ',STARKs
590 open(unit=2,file=STARKs,status='old',err=595)
goto 596
595 PRINT*, 'STARK FILE NOT FOUND, TRY AGAIN'
query=5
goto 580
596 read(2,'(A)') title
read(2,*) waveincr
read(2,*) nprofile
do 598 N=1,nprofile
  read(2,*) NE(N)
  do 600 M=1,80
600   read(2,*) STARK(N,M)
598 continue
CLOSE(2)
PRINT*, 'STARK FILE = ',STARKs
PRINT*, 'TITLE = ',TITLE
PRINT*, 'WAVELENGTH INCREMENT = ',waveincr
c-----CALCULATE SPLINE COEFFICIENTS FROM STARK PROFILES
PRINT*, 'CALCULATING SPLINE COEFFICIENTS FROM STARK PROFILES'
P=nprofile
do 613 M=1,80
do 614 N=1,P
  X(N)=DLOG(NE(N))/DLOG(10.)
614  Y(N)=STARK(N,M)
call spline
do 618 N=1,P
  SB(N,M)=B(N)
  SC(N,M)=C(N)
618 SD(N,M)=D(N)
613 continue
c-----READ DOPPLER PROFILE
629 query=0
PRINT*, 'READING ',DOPPLs

```

```

open(unit=2,file=DOPPLs,status='old',err=630)
goto 631
630 PRINT*, 'DOPPL FILE NOT FOUND, TRY AGAIN'
query=3
goto 581
631 read(2,'(A)') title
read(2,*) waveincr
read(2,*) DDATA
do 632 M=1,DDATA
632 read(2,*) DOPPL(M)
CLOSE(2)
PRINT*, 'DOPPLER FILE = ',DOPPLs
PRINT*, 'TITLE = ',TITLE
PRINT*, 'WAVELENGTH INCREMENT = ',waveincr
C-----READ, BACKGROUND-SUBSTRACT, & AVERAGE INSTRUMENTAL PROFILE
644 query=0
PRINT*, 'READING ',INSTUs
open(unit=2,file=INSTUs,status='old',err=645)
goto 646
645 PRINT*, 'INSTU FILE NOT FOUND, TRY AGAIN'
query=4
goto 582
646 read(2,'(A)') title
read(2,*) waveincr
read(2,*) NPOINT,CENTER
do 647 M=1,NPOINT
647 read(2,*) INTENS(M)
CLOSE(2)
call netavgr
IDATA=LPOINT
do 651 M=1, IDATA
651 INSTU(M)=NETAVG(M)
PRINT*, 'INSTRUMENTAL FILE = ',INSTUs
PRINT*, 'TITLE = ',title
PRINT*, 'WAVELENGTH INCREMENT = ',waveincr
call return(2)
C-----CONVOLUTE DOPPLER & INSTRUMENTAL PROFILES
PRINT*, 'INSTU+DOPPL'
C   PRINT*, 'M DLAMDA INT. M DLAMDA INT. M DLAMDA INT.'
PRINT*, 'CONVOLUTING INSTRUMENTAL & DOPPLER PROFILES'
DATA1=DDATA
DATA2=IDATA
do 679 M=1,DATA1
679 PROFILE1(M)=DOPPL(M)
do 680 M=1,DATA2
680 PROFILE2(M)=INSTU(M)
call convlr
DATA2=L1
do 683 M=1,DATA2
683 PROFILE2(M)=CONVL(M)
call return(2)
C-----READ, BACKGROUND-SUBSTRACT, AVERAGE, & NORMALIZE EXPERIMENTAL PROFILE
PRINT*, 'PROCESS EXPERIMENTAL FILE FOR COMPARISON'
709 PRINT*, 'EXPERIMENTAL FILE (EXPERxxx.DAT) = '
read(5,'(A)') EXPERS
PRINT*, 'READING ',EXPERS
open(unit=2,file=EXPERS,status='old',err=710)
goto 711

```

```

710 PRINT*, 'EXPER FILE NOT FOUND, TRY AGAIN'
      goto 709
711 PRINT*, 'Ne OUTPUT FILE= '
      read(5,'(A)') NeOUT
      open(unit=3,file=NeOUT)
      read(2,'(A)') title
      read(2,*) waveincr
      read(2,*) nvstat
      print*, 'Enter ntrak'
      read(5,*) ntrak
      do 1711 ii=1,nvstat
          do 1712 jj=1,ntrak
              print*, 'trak=',jj
              read(2,*) NPOINT,CENTER
              do 712 M=1,NPOINT
    712 read(2,*) INTENS(M)
      call netavgr
      do 713 M=1,LPOINT
    713 NORM(M)=NETAVG(M)
      call normal
      EMAX=MAX
      EDATA=M
      do 717 M=1,EDATA
    717 EXPER(M)=NORM(M)
      C PRINT*, 'EXPERIMENTAL FILE = ',EXPER
      C PRINT*, 'TITLE = ',TITLE
      C PRINT*, 'WAVELENGTH INCREMENT = ',waveincr
      C 724 PRINT*, 'AUTOMATIC (1) OR MANUAL (2) ADVANCEMENT ?'
      C read(5,*) adv
      C IF (adv.ne.1 .and. adv.ne.2) goto 724
      adv=1.
      C-----SET UP INITIAL NE SET (A,B,C,D,E) & CALCULATE RESIDUALS
      TRIAL=0
      do 732 N=1,P
    732 X(N)=DLOG(NE(N))/DLOG(10.)
      NEB=NE(1)
      NED=NE(P)
      NEC=10**((DLOG(NEB)/DLOG(10.)+DLOG(NED)/DLOG(10.))/2)
      XIN=DLOG(NEB)/DLOG(10.)
      call interp(adv)
      RESIDB=RESID(TRIAL)
      XIN=DLOG(NED)/DLOG(10.)
      call interp(adv)
      RESIDD=RESID(TRIAL)
      XIN=DLOG(NEC)/DLOG(10.)
      call interp(adv)
      RESIDC=RESID(TRIAL)
      NEA=NEB
      RESIDA=RESIDB
      NEE=NED
      RESIDE=RESIDD
      C----COMPARE RESIDUALS FOR CURRENT NE SET (B,C,D) & FIND NEW NE SET (A,C,E)
      750 IF ((NEC-NEB).lt.(.005*NEC).and.(NED-NEC).lt.(.005*NEC)) goto 782
          IF (RESIDB.ge.RESIDC) goto 755
          NEE=NEC
          RESIDE=RESIDC
          NEC=NEB
          RESIDC=RESIDB

```

```

GOTO 766
755 IF (RESIDD.ge.RESIDC) goto 759
    NEA=NEC
    RESIDA=RESIDC
    NEC=NED
    RESIDC=RESIDD
    GOTO 766
759 NEA=NEB
    RESIDA=RESIDB
    NEE=NED
    RESIDE=RESIDD
C-----CALCULATE RESIDUALS FOR THE NEW NE SET (B,C,D)
766 IF (NEA.eq.NEC) THEN
    NEB=NEC
    RESIDB=RESIDC
    GOTO 771
    endif
    NEB=10**((DLOG(NEA)/DLOG(10.)+DLOG(NEC)/DLOG(10.))/2)
    XIN=DLOG(NEB)/DLOG(10.)
    call interp(adv)
    RESIDB=RESID(TRIAL)
771 IF (NEE.eq.NEC) THEN
    NED=NEC
    RESIDD=RESIDC
    GOTO 750
    endif
    NED=10**((DLOG(NEC)/DLOG(10.)+DLOG(NEE)/DLOG(10.))/2)
    XIN=DLOG(NED)/DLOG(10.)
    call interp(adv)
    RESIDD=RESID(TRIAL)
    goto 750
C-----FIND MINIMUM RESIDUAL FOR THE FINAL NE SET (B,C,D) & ESTIMATE BEST NE
782 MINRESID=RESIDC
    BESTNE=NEC
    IF (RESIDB.lt.MINRESID) THEN
        MINRESID=RESIDB
        BESTNE=NEB
    endif
    IF (RESIDD.lt.MINRESID) THEN
        MINRESID=RESIDD
        BESTNE=NED
    endif
    C PRINT*, 'EXPERIMENTAL FILE = ',EXPERS
    C do 787 T=1,TRIAL
    C PRINT*, 'TRIAL = ',T
    C PRINT*, 'NE = ',NETRY(T)
    C787 PRINT*, 'RESID = ',RESID(T)
    IF (BESTNE.eq.NE(1)) THEN
        C PRINT*, 'THE ESTIMATED ELECTRON NUMBER DENSITY (/cm3) =< ',BESTNE
        GOTO 794
    endif
    IF (BESTNE.eq.NE(P)) THEN
        C PRINT*, 'THE ESTIMATED ELECTRON NUMBER DENSITY (/cm3) => ',BESTNE
        GOTO 794
    endif
    C PRINT*, 'THE BEST ESTIMATED ELECTRON NUMBER DENSITY (/cm3) = ',BESTNE
794 continue
    C

```

```

do 801 N=1,15
  X(N)=0
  Y(N)=0
801 continue
  do 802 M=1,80
    NORM(M)=0
    NETAVG(M)=0
    PROFILE1(M)=0
    EXPER(M)=0
    CONVL(M)=0
    RESID(M)=0
    NTRY(M)=0
802 continue
  do 803 N=1,160
803  INTENS(N)=0
c
1712 continue
1711 continue
c
  do 8011 N=1,15
    NE(N)=0
    X(N)=0
    Y(N)=0
    B(N)=0
    C(N)=0
    D(N)=0
8011 continue
  do 8021 M=1,80
    NORM(M)=0
    NETAVG(M)=0
    PROFILE1(M)=0
    PROFILE2(M)=0
    DOPPL(M)=0
    INSTU(M)=0
    EXPER(M)=0
    CONVL(M)=0
    RESID(M)=0
    NTRY(M)=0
  do 18021 N=1,15
    STARK(N,M)=0
    SB(N,M)=0
    SC(N,M)=0
18021  SD(N,M)=0
8021 continue
  do 8031 N=1,160
8031  INTENS(N)=0
c
  CLOSE(2)
  CLOSE(3)
  RETURN
  end
*****SUBROUTINE COMPUTE SPLINE COEFFICIENTS USING CUBIC SPLINE ****
subroutine spline
common/subint/TRIAL,NTRY(80),XIN,P,SB(15,80),SC(15,80),
+           SD(15,80),DATA2,L1,Y(80),X(80),B(80),C(80),D(80),
+           EDATA,RESID(80),DATA1,PROFILE1(80),CONVL(80),
+           STARK(15,80),PROFILE2(80),EXPER
  real*8 X,Y,B,C,D,EXPER(80)

```

```

real*8 NTRY, STARK, XIN, SD, SC, SB, PROFILE1, PROFILE2, CONVL, RESID
integer P, P1, TRIAL, DATA2, DATA1, EDATA, L1
P1=P-1
C-----SET UP MATRIX
D(1)=X(2)-X(1)
C(2)=(Y(2)-Y(1))/D(1)
do 821 I=2,P1
D(I)=X(I+1)-X(I)
B(I)=2.* (D(I-1)+D(I))
C(I+1)=(Y(I+1)-Y(I))/D(I)
C(I)=C(I+1)-C(I)
821 continue
C-----FIND BOUNDARY CONDITIONS
B(1)=-D(1)
B(P)=-D(P1)
C(1)=C(3)/(X(4)-X(2))-C(2)/(X(3)-X(1))
C(P)=C(P-1)/(X(P)-X(P-2))-C(P-2)/(X(P-1)-X(P-3))
C(1)=C(1)*D(1)**2/(X(4)-X(1))
C(P)=-C(P)*D(P-1)**2/(X(P)-X(P-3))
C-----FORWARD ELIMINATION
do 839 I=2,P
Q=D(I-1)/B(I-1)
B(I)=B(I)-Q*D(I-1)
C(I)=C(I)-Q*C(I-1)
839 continue
C-----BACK SUBSTITUTION
C(P)=C(P)/B(P)
do 848 J=1,P1
I=P-J
C(I)=(C(I)-D(I)*C(I+1))/B(I)
848 continue
C-----COMPUTE SPLINE COEFFICIENTS
B(P)=(Y(P)-Y(P1))/D(P1)+D(P1)*(C(P1)+2*C(P))
do 856 I=1,P1
B(I)=(Y(I+1)-Y(I))/D(I)-D(I)*(C(I+1)+2*C(I))
D(I)=(C(I+1)-C(I))/D(I)
C(I)=3*C(I)
856 continue
C(P)=3*C(P)
D(P)=D(P-1)
RETURN
END
C*****INTERPOLATE, CONVOLUTE, NORMALIZE & CALCULATE RESIDUALS *
subroutine interp(adv)
common/subint/TRIAL,NTRY(80),XIN,P,SB(15,80),SC(15,80),
+ SD(15,80),DATA2,L1,Y(80),X(80),B(80),C(80),D(80),
+ EDATA,RESID(80),DATA1,PROFILE1(80),CONVL(80),
+ STARK(15,80),PROFILE2(80),EXPER
common/subnor/NORM(80),LPOINT,MAX,M,INTENS(160),
+ NPOINT,CENTER,NETAVG(80)
real*8 Y,B,C,D,PROFILE2,INTENS
integer LPOINT,L1,DATA1,CDATA,EDATA,TRIAL,P,adv,DATA2,M,NPOINT,CENTER
real*8 NTRY,X,PROFILE1,STARK,CONVL,NETAVG
real*8 SB,SC,SD,NORM,RESID
real*8 EXPER(80),XIN,MAX,DX,RESIDa(80)
TRIAL=TRIAL+1
NTRY(TRIAL)=10***(XIN)
C PRINT*, 'M DLAMDA INT. M DLAMDA INT. M DLAMDA INT.'

```

```

C-----INTERPOLATE
  MAX=0
  do 877 IZ=1,P
  877 IF (XIN.lt.X(IZ)) goto 880
  880 IZ=IZ-1
  DX=XIN-X(IZ)
  do 882 M=1,80
    PROFILE1(M)=STARK(IZ,M)+DX*(SB(IZ,M)+DX*(SC(IZ,M)+DX*SD(IZ,M)))
    IF (PROFILE1(M).gt.MAX) MAX=PROFILE1(M)
    IF (PROFILE1(M).lt..01*MAX .or. M.eq.80) goto 890
  882 continue
  if (M.gt.80) M=80
C-----CONVOLUTE
  890 DATA1=M
  call convlr
C-----NORMALIZE
  LPOINT=L1
  do 896 M=1,LPOINT
  896 NORM(M)=CONVL(M)
  call normal
  CDATA=M
C-----CALCULATE RESIDUAL
  RESID(TRIAL)=0
  do 903 M=1,EDATA
    IF (M.gt.CDATA) NORM(M)=0
  903 RESID(TRIAL)=RESID(TRIAL)+(EXPER(M)-NORM(M))**2
  call return(adv)
  RETURN
  END
C*****SUBROUTINE CONVOLUTE PROFILES *
subroutine convlr
common/subint/TRY,NETRY(80),XIN,P,SB(15,80),SC(15,80),
+           SD(15,80),DATA2,L1,Y(80),X(80),B(80),C(80),D(80),
+           EDATA,RESID(80),DATA1,PROFILE1(80),CONVL(80),
+           STARK(15,80),PROFILE2(80),EXPER
common/subnor/NORM(80),LPOINT,MAX,M,INTENS(160),
+           NPOINT,CENTER,NETAVG(80)
real*8 X,Y,B,C,D,EXPER(80),NORM,NETAVG,INTENS
real*8 NETRY,STARK,XIN,SD,SC,SB,CONVL,RESID
integer P,P1,TRY,EDATA,LPOINT,M,NPOINT,CENTER
integer DATA1,DATA2,RIGHT,LEFT,L1,L2
real*8 PROFILE2,PROFILE1,MAX
MAX=0
do 931 L1=1,DATA1+DATA2-1
CONVL(L1)=0
  do 933 L2=1,DATA2
    RIGHT=L1+L2-1
    LEFT=L1-L2+1
    IF (RIGHT.gt.DATA1) goto 938
    CONVL(L1)=CONVL(L1)+PROFILE2(L2)*PROFILE1(RIGHT)
  938 IF (LEFT.gt.DATA1 .or. LEFT.lt.(2-DATA1)) goto 933
    IF (LEFT.lt.1) LEFT=(2-LEFT)
  933 CONVL(L1)=CONVL(L1)+PROFILE2(L2)*PROFILE1(LEFT)
  M=L1
  IF (CONVL(L1).gt.MAX) MAX=CONVL(L1)
  IF (CONVL(L1).lt..01*MAX .or. L1.eq.80) goto 946
  931 continue
  if (L1.gt.DATA1+DATA2-1) L1=DATA2+DATA2-1

```

```

946 RETURN
end
*****SUBROUTINE CALCULATE NET AVERAGE INTENSITY *
subroutine netavgr
common/subnor/NORM(80),LPOINT,MAX,M,INTENS(160),
+           NPOINT,CENTER,NETAVG(80)
real*8 INTENS,NETAVG,MIN,MAX,NORM
integer NPOINT,CENTER,LPOINT,M
MIN=INTENS(1)
MAX=INTENS(1)
do 953 M=2,NPOINT
  IF (INTENS(M).lt.MIN) MIN=INTENS(M)
  IF (INTENS(M).gt.MAX) MAX=INTENS(M)
953 continue
LPOINT=CENTER
IF (NPOINT-CENTER+1.lt.CENTER) LPOINT=NPOINT-CENTER+1
do 959 M=1,LPOINT
959 NETAVG(M)=(INTENS(CENTER-M+1)+INTENS(CENTER+M-1))/2-MIN
RETURN
END
*****SUBROUTINE NORMALIZATION *
subroutine normal
common/subnor/NORM(80),LPOINT,MAX,M,INTENS(160),
+           NPOINT,CENTER,NETAVG(80)
integer LPOINT,M,CENTER,NPOINT
real*8 NORM,MAX,EVEN,ODD,AREA,INTENS,NETAVG
EVEN=0
ODD=0
MAX=0
do 969 M=2,LPOINT-1
  IF ((M/2.).eq.INT(M/2.)) EVEN=EVEN+NORM(M)
  IF ((M/2.).ne.INT(M/2.)) ODD=ODD+NORM(M)
969 continue
AREA=2*(NORM(1)+4*EVEN+2*ODD+NORM(LPOINT))/3
if (area.le.0) area=1e-6
do 974 M=1,LPOINT
  NORM(M)=NORM(M)/AREA
  IF (NORM(M).gt.MAX) MAX=NORM(M)
  IF (NORM(M).lt..01*MAX .or. M.eq.80) goto 979
974 continue
if (M.gt.LPOINT) M=LPOINT
979 RETURN
end
*****SUBROUTINE HIT RETURN TO CONTINUE *
subroutine return(adv)
integer adv,query
IF (adv .eq. 1) goto 1021
1018 PRINT*, 'ENTER 1 TO CONTINUE'
read(5,*) query
if (query .eq. 1) goto 1021
goto 1018
1021 continue
RETURN
END

```

A.4. Hydrogen Profile Conversion (required for NE)

```

program CONVERT
C
C***** This program reads in the Abel inverted Balmer line and converts
C* it for processing in NE.f. This entails removing data
C* not actually part of the line wings. The maximum number of
C* channels in the converted spectrum is 160.
C*****
C
      character*25 title,filename,convint
      real*8 wavincr,intens(50,75,160),intensity(50,75,500)
      real*8 max(50,75),minl(50,75),minr(50,75),maxdum,Rcm(50,101)
      integer nrad(50)
      integer nvstat,nchan,npoint(50,75),center(50,75)
      integer nl(50,75),nr(50,75),chr(50,75),chl(50,75),ndum(50,75)
      data waveincr/.5285/
      data nvstat,nchan/36,180/
C-----Specify the files for original and converted spectra
9       write(6,*)"enter the original Balmer line filename"
      read(5,'(A)') filename
      open(unit=2,file=filename,status='old',err=10)
      goto 11
10      write(6,*)"FILE NOT FOUND, TRY AGAIN."
      goto 9
11      continue
      write(6,*)"enter the converted spectrum filename"
      read(5,'(A)') convint
      open(unit=3,file=convint)
      write(6,*)"enter the title of the data file (25 characters max)"
      read(5,'(A)') title
C-----write the title and waveincr to the converted spectrum data file
      write(3,'(A)') title
      write(3,*) waveincr
      write(3,111) nvstat
111     format(i3,x,i3)
C-----Find the maximum intensity on each track and the channel it lies on
      do 20 i=1,nvstat
        do 20 j=1,nrad(i)
          read(2,201) nrad(i)
          do 20 k=1,nrad(i)
            read(2,231) Rcm(i,j,k)
            max(i,j)=0.
            center(i,j)=1
            do 20 l=1,nchan
              read(2,23) intensity(i,j,k)
              if(intensity(i,j,k).lt.0.0) intensity(i,j,k)=intensity(i,j,k-1)
              if(intensity(i,j,k).gt.max(i,j)) then
                center(i,j)=k
                max(i,j)=intensity(i,j,k)
              endif
20      continue
C
23      format(13.6)
201     format(I3)
231     format(e10.4)

```

```

close(2)
c-----Find the minimum intensities on each side and their channels.
c-----Consider only the central 160 channels.
do 25 i=1,nvstat
  do 26 j=1,nrad(i)
    nl(i,j)=center(i,j)-79
    nr(i,j)=center(i,j)+80
    if(nl(i,j).lt.1) nl(i,j)=1
    if(nr(i,j).gt.180) nr(i,j)=180
    minl(i,j)=intensity(i,j, nl(i,j))
    minr(i,j)=intensity(i,j, nr(i,j))
c-----Check the left side of the center
  do 27 k=nl(i,j),center(i,j)-1
    if(intensity(i,j,k).le.minl(i,j)) then
      chl(i,j)=k
      minl(i,j)=intensity(i,j,k)
    endif
27  continue
c-----Check the right side of the center
  do 28 k=center(i,j)+1,nr(i,j)
    if(intensity(i,j,k).le.minr(i,j)) then
      chr(i,j)=k
      minr(i,j)=intensity(i,j,k)
    endif
28  continue
26  continue
25  continue
c-----Find the 1 percent clip channels on either side of the center
  do 30 i=1,nvstat
    write(3,301) nrad(i)
    do 31 j=1,nrad(i)
      write(3,311) Rcm(i,j)
c-----Left side
  m=chl(i,j)
  do 32 k=m,center(i,j)-1
    maxdum=max(i,j)-minl(i,j)
    clip=0.01*maxdum
    if(intensity(i,j,k)-minl(i,j).lt.clip) then
      chl(i,j)=k
    endif
32  continue
c-----Right side
  m=chr(i,j)
  do 33 k=m,center(i,j)+1,-1
    maxdum=max(i,j)-minr(i,j)
    clip=0.01*maxdum
    if(intensity(i,j,k)-minr(i,j).lt.clip) then
      chr(i,j)=k
    endif
33  continue
c-----calculate the number of points in the converted spectrum
c-----and reset the converted intensity spectrum within the new bounds
  npoint(i,j)=chr(i,j)-chl(i,j)+1
  icens=center(i,j)
  center(i,j)=center(i,j)-chl(i,j)+1
  write(3,111) npoint(i,j),center(i,j)
  if(icens.lt.80.or.icens.gt.100) then
    do 997 nn=1,npoint(i,j)

```

```

997      intensity(i,j,nn+chl(i,j)-1)=nn
        endif
        do 34 k=1,npoin(i,j)
        intens(i,j,k)=intensity(i,j,k+chl(i,j)-1)
34      write(3,23) intens(i,j,k)
31      continue
30      continue
c
301     format(I3)
311     format(e10.4)
        close(3)
c
        stop
end

```

A.5. LTE Temperature and Composition

```

      program LTE
c
c***** *****
c      The subroutine to calculate partition functions has been removed.
c      The common blocks and associated variables have been
c      retained in the main program.
c
c      Elevels.dat is a data file containing argon energy leve
c      information. It can be found in the Ph.D. thesis of A. Sedghinasab.
c      See note at bottom of program for more information.
c*****
c
      real*8 Tlow,Thigh,T,na,ne,ni,niii,P,Pcalc
      real*8 Eanf,Einf,Eiinf,Eiiinf
      real*8 me,pi,h,kb,Zte,Zexe,exp1,exp2,exp3
      real*8 debhuk1,debhuk3,debhuk2,e,jev,kc,pcdh
      real*8 Ea,Ei,Eii,Eiii,gg(4,400),Eml(4,400),Zex(4),kj
      integer nw(4,70),nlevs(4)
      character words
      character*10 filename,outfile
      character*6 prefix
      real*8 Esinf(4)
      real*8 linem,wavel,Amn,c,nm,gm,const,neold
      real*8 nallow,nilow,nelow,niilow,niilow
c
      common/Zpart/Esinf,nw,nlevs,gg,Eml,Zex,T,kb
      common/Elower/Ea,Ei,Eii,Eiii
c
      data kj,me,kb,h,e,kc,c/1.986307e-23,9.10953e-31,1.38066e-23,
      &           6.62618e-34,1.60219e-19,8.9875518e9,2.997925e8/
c
      open(unit=7,file='Elevels.dat')
c*****Read the data file description and first 3 ionization potentials
      read(7,'(A)') words
      read(7,7) Eanf,Einf,Eiinf,Eiiinf
7       format(4(f10.3,2x))

```

```

*****Convert to Joules and fill array for subroutine Zpart
Eanf=Eanf*kj
Einf=Einf*kj
Eiinf=Eiinf*kj
Eiiinf=Eiiinf*kj
Esinf(1)=Eanf
Esinf(2)=Einf
Esinf(3)=Eiinf
Esinf(4)=Eiiinf
*****Read the particle name and the number of level pairs (g,E)
*****Read the level pairs, convert cm-1 to Joules
do 8 nn=1,4
  read(7,10) words,nlevels
8   read(7,11) (gg(nn,j),Eml(nn,j),j=1,nlevels)
do 2 nn=1,4
do 2 j=1,400
2   Eml(nn,j)=Eml(nn,j)*kj
c
10  format(A6,I3)
11  format(4(f7.0,x,f9.2,2x))
*****Read the number of level pairs for each particle into an array
read(7,12) (nlevs(i),i=1,4)
12  format(4I3)
*****Read the break points for increasing energy series
read(7,13) ((nw(i,j),j=1,70),i=1,4)
13  format(7I4)
c
pi=dacos(-1.)
c
print*, 'Enter the emission coefficient data file name prefix'
read(5,125) prefix
125 format(A6)
print*, 'Enter the number of vertical stations'
read(5,*) nvstat
print*, 'Enter the number of radial locations'
read(5,*) nrad
print*, 'Enter the wavelength (Angstroms)'
read(5,*) wavel
wavel=wavel*1e-10
print*, 'Enter the Einstein emission coefficient (1/s)'
read(5,*) Amn
print*, 'Enter the upper level energy (1/cm)'
read(5,*) Em
Em=Em*kj
print*, 'Enter the upper level degeneracy'
read(5,*) gm
c
Zte=(2*pi*me*kb/h**2)**1.5
***** Read in the line emission coefficients
filename=prefix//'.IHT'
outfile=prefix//'.LTE'
open(unit=8,file=filename)
open(unit=9,file=outfile)
***** Set the radial spatial scaling factor
radscale=.05588
do 126 ii=1,nvstat
do 127 jj=1,nrad
read(8,*) linem

```

```

c*****Converts to units of W/m3sr
linem=linem/radscale
nm=4.*pi*wavel*linem/(h*c*Am)
c*****Initialize some variables and set some constants
T=5000
Tinc1=50
Tinc2=5
Tinc=Tinc1
P=100000
c
Zex(1)=1.000
Zex(2)=5.325
Zex(3)=7.904
Zex(4)=4.023
c*****Calculate na based on nm/gm and the Boltzmann factors
hitest=0
na=nm*Zex(1)*dexp(Em/(kb*T))/gm
c*****Estimate the initial ne
ne=dsqrt(2.*na*Zex(2)*Zte*T**1.5*dexp(-Eanf/(kb*T))/Zex(1))
ni=ne
nii=0.0
niii=0.0
niter=0
c
199  if(hitest.eq.0) then
      Pcalc=1e6
    else
      Pcalc=0.0
    endif
    delP=Pcalc-P
    delPs=delP
    jdone=0
c*****Iterate until convergence of P
99   do while(abs(delPs+delP).gt.abs(delPs-delP))
      T=T+Tinc
      if (T.ge.35000.) then
        write(9,'(A)') 'Temperature over 35,000 K'
        goto 999
      endif
      nelast=ne
c
      call Zpart
c
      debye=((4.*pi*e*kc/kb)*(ne/T+(ni+4.*nii+9.*niii)/T))**-.5
      debhuk1=e*e*kc/debye
      debhuk2=2.*debhuk1
      debhuk3=3.*debhuk1
      debhuk4=4.*debhuk1
      Ea=Eanf-debhuk1
      Ei=Einf-debhuk2
      Eii=Eiinf-debhuk3
      Eiii=Eiiinf-debhuk4
      exp1=dexp(-Ea/(T*kb))
      exp2=dexp(-Ei/(T*kb))
      exp3=dexp(-Eii/(T*kb))
      na=nm*Zex(1)*dexp(Em/(kb*T))/gm
      const=Zte*T**1.5*2.
      c1=const*exp1*Zex(2)/Zex(1)

```

```

c2=const*exp2*Zex(3)/Zex(2)
c3=const*exp3*Zex(4)/Zex(3)

c
testne=1e6
do while(testne.gt.1e-6)
  neold=ne
  ne=(na*c1*neold**2+2.*na*c1*c2*neold+3.*na*c1*c2*c3)**(1./4.)
  testne=(abs(neold-ne)/ne)
enddo

c
ni=na*c1/ne
nii=ni*c2/ne
niii=nii*c3/ne
pcdh=1./(24.*pi*(ne+na+ni+nii+niii)*debye**3)
Pcalc=kb*T*(ne+na+ni+nii+niii)*(1.-pcdh)
c
delPs=delP
delP=Pcalc-P
niter=niter+1

c
enddo
if(jdone.eq.0)then
  jdone=1
  T=T-Tinc
  Tinc=Tinc2
  ne=nelast
  delP=delPs
  goto 99
endif
T=-delPs*Tinc/(delP-delPs)+T-Tinc

c
call Zpart

c
debye=((4.*pi*e**kc/kb)*(ne/T+(ni+4.*nii+9.*niii)/T))**-.5
debhuk1=e**kc/debye
debhuk2=2.*debhuk1
debhuk3=3.*debhuk1
debhuk4=4.*debhuk1
Ea=Eanf-debhuk1
Ei=Einf-debhuk2
Eii=Eiinf-debhuk3
Eiii=Eiiiinf-debhuk4
exp1=dexp(-Ea/(T*kb))
exp2=dexp(-Ei/(T*kb))
exp3=dexp(-Eii/(T*kb))
na=nm*Zex(1)*dexp(Em/(kb*T))/gm
const=Zte*T**1.5*2.
c1=const*exp1*Zex(2)/Zex(1)
c2=const*exp2*Zex(3)/Zex(2)
c3=const*exp3*Zex(4)/Zex(3)

c
testne=1e6
do while(testne.gt.1e-6)
  neold=ne
  ne=(na*c1*neold**2+2.*na*c1*c2*neold+3.*na*c1*c2*c3)**(1./4.)
  testne=(abs(neold-ne)/ne)
enddo

c
ni=na*c1/ne

```

```

nii=ni*c2/ne
niii=nii*c3/ne
pcdh=1./(24.*pi*(ne+na+ni+nii+niii)*debye**3)
Pcalc=kb*T*(ne+na+ni+nii+niii)*(1.-pcdh)
if(hitest.eq.0) then
  Pcalclow=kb*T*(ne+na+ni+nii+niii)*(1.-pcdh)
  Tlow=T
  nelow=ne
  nalow=na
  nilow=ni
  niilow=nii
  niiilow=niii
  jdone=0
  hitest=1
  Tinc=Tinc1
    call Zpart
  goto 199
endif
c
Thigh=T
Pcalchi=kb*T*(ne+na+ni+nii+niii)*(1.-pcdh)
nahi=na
nehi=ne
nihii=ni
nihiihi=nii
nihiihihi=niii
c
999  write(9,131) linem,nm/gm,Thigh,ne,na,ni,nii,niii
continue
if (Tlow.eq.0.0) then
  write(9,'(A)') 'No solution for this emission coefficient'
  goto 998
endif
c
131  write(9,131) linem,nm/gm,Tlow,nelow,nalow,nilow,niilow,niiilow
      format(E10.4,x,E12.6,x,F7.1,x,5(E8.2,x))
c
998  continue
127  continue
126  continue
close(7)
close(8)
close(9)
stop
end
c
c*****SUBROUTINE TO CALCULATE PARTITION FUNCTIONS*****
c      This routine can be found in A. Sedghinasab's PhD. thesis.
c      Georgia Institute of Technology, 1987.
c*****

```

A.6. Non-LTE Analysis

```

program NONLTE
c
c***** The subroutine to calculate partition functions has been removed.
c***** The common blocks and associated variables have been
c***** retained in the main program.
c
c***** Elevels.dat is a data file containing argon energy leve
c***** information. It can be found in the Ph.D. thesis of A. Sedghinasab.
c***** See note at bottom of program for more information.
c*****
c
real*8 Te,Tg,Texa,Texi,na,ne,ni,nii,niii,P
real*8 Eanf,Einf,Eiinf,Eiiinf,neion,Nmogm
real*8 NIogIa,niogii,me,pi,h,kb,Zte,Zexe,exp1,exp2,exp3
real*8 debhuk1,debhuk3,debhuk2,e,jev,kc,pcdh
real*8 Ea,Ei,Eii,Eiii,gg(4,400),Eml(4,400),Zex(4),kj
integer nw(4,70),nlevs(4),radnecut,radnacut
character words
real*8 Esinf(4)
real*8 tarray(2),dtime
real*8 TeTg,TeTexa,xil,Texap
character*1 tab
c
common/Zpart/Esinf,nw,nlevs,gg,Eml,Zex,Texa,Texi,kb
common/Elower/Ea,Ei,Eii,Eiii,Eanf,Einf,Eiinf,Eiiinf
common/TEMP/Te,ne,Tg
common/TEXAb1k/TeTg,TeTexa,xil,Texap,Texaf,TeTexb
c
open(unit=2,file='Texup.neu')
open(unit=7,file='Elevels.dat')
open(unit=8,file='6562.NE')
open(unit=9,file='ion.LTE')
open(unit=11,file='neu.LTE')
open(unit=14,file='radcuts')
c
tab=char(9)
c*****Read the data file description and first 3 ionization potentials
kj=1.986307147e-23
read(7,'(A)') words
read(7,7) Eanf,Einf,Eiinf,Eiiinf
7 format(4(f10.3,2x))
c*****Convert to Joules and fill array for subroutine Zpart
Eanf=Eanf*kj
Einf=Einf*kj
Eiinf=Eiinf*kj
Eiiinf=Eiiinf*kj
Esinf(1)=Eanf
Esinf(2)=Einf
Esinf(3)=Eiinf
Esinf(4)=Eiiinf
c*****Read the particle name and the number of level pairs (g,E)
c*****Read the level pairs, convert cm-1 to Joules
do 8 nn=1,4

```

```

      read(7,10) words,nlevels
8       read(7,11)(gg(nn,j),Em1(nn,j),j=1,nlevels)
      do 2 nn=1,4
      do 2 j=1,400
2       Em1(nn,j)=Em1(nn,j)*kj
C
10      format(A6,I3)
11      format(4(f7.0,x,f9.2,2x))
C*****Read the number of level pairs for each particle into an array
      read(7,12) (nlevs(i),i=1,4)
12      format(4I3)
C*****Read the break points for increasing energy series
      read(7,13) ((nw(i,j),j=1,70),i=1,4)
13      format(7I4)
6601      format(E10.4,x,E12.7,x,F7.1,x,5(E8.3,x))
6602      format(E10.4,x,E12.7,x,F7.1,x,3(E13.6,x))
C*****Set some constants
      me=9.10953e-31
      pi=dacos(-1.)
      kb=1.38066e-23
      h=6.62618e-34
      e=1.60219e-19
      jev=1.6021917e-19
      kc=8.9875518e9
C
      Zte=(2*pi*me*kb/h**2)
C*****Loop to read in the data one point at a time
      do 6599 ii=1,52
          read(14,*) radnecut
          read(14,*) radnacut
      do 6605 jj=1,33
          read(2,*) Texb
          read(8,*) ne
          read(9,6602) dum1,dum2,Texi,neion,dum4,dum5
          read(11,6601) xil,Nmogm,Texaf,dum3,dum4,dum5,dum6,dum7
C
      Texa=Texaf
      Em=107132*kj
C
      ne=ne*1e6
C*****Calculate na (with Zexa=1.0)
      na=Nmogm*dexp(Em/(kb*Texa))
C*****Initialize some variables
      P=100000
      Tinc=200.
      Tbase=5000
      Tg=Tbase
C
      Zex(1)=1.003
      Zex(2)=5.684
      Zex(3)=9.405
      Zex(4)=4.881
      Zexe=(2./ne)
C
      Te=16000
      ni=ne
      nii=.29988e17
      niii=.1e6

```

```

c
  if (ne.eq.1e22) then
    Te=9485
    Tg=5000
    aff=0
    goto 6598
  endif
c
  if (jj.gt.radnacut) then
    call LTEne
    Tg=5000
    aff=0
    goto 6598
  endif
c
  if (ne.ge..1994351e24.and.jj.gt.radnecut) then
    Texi=16674.76
  elseif (jj.gt.radnecut) then
    call LTEne
    Texi=Te
    Texa=Texaf
  endif
c
  Teold=Te
  Telast=Te
  delp=1e10
  Tinc=200
  Tbase=4000
  Tg=Tbase
c
  niter=0
  test=1.0
c*****
  do while(test.gt.1e-7)
  delpold=delp
  Te=relax*Te+(1-relax)*Teold
  Teold=Te
  Tbase=Tbase+Tinc
  Tg=Tbase
c*****Calculate the Debye length and Debye-Hueckel lowering of the
c      ionization potentials
  debye=((4.*pi*e*e*k/c/kb)*(ne/Teold+(ni+4.*nii+9.*niii)/Tg))**-.5
  debhuk1=2.30686169e-28/debye
  debhuk2=2.*debhuk1
  debhuk3=3.*debhuk1
  debhuk4=4.*debhuk1
  Ea=Eanf-debhuk1
  Ei=Einf-debhuk2
  Eii=Eiinf-debhuk3
  Eiii=Eiiiinf-debhuk4
  exp1=dexp((-Ea+aff)/(Teold*k))
  exp2=dexp(-Ei/(Teold*k))
  exp3=dexp(-Eii/(Teold*k))
c*****Recalculate partitions functions
  call Zpart
c*****Recalculate na with new Ea
  na=Nmogn*Zex(1)*dexp(Em/(kb*Texa))
c*****Calculate the Debye-Hueckel pressure correction

```

```

pcdh=1./(24.*pi*(ne+na+ni+nii+niii)*debye**3)
      Te=(1./Zte)*((1./Zexe)*(ni/na)**(Tg/Teold)*Zex(1)**(Texa/Teold)/
      (Zex(2)**(Texi/Teold)*exp1))**2./3.)
1      nii=ni*((Zte*Te)**1.5*Zexe*exp2*(Zex(3)/Zex(2))
1      **(Texi/Te))**2./3.)
1      niii=nii*((Zte*Te)**1.5*Zexe*exp3*(Zex(4)/Zex(3))
1      **(Texi/Te))**2./3.)
1      ni=ne-2.*nii-3.*nii
Pcalc=(1.-pcdh)*kb*(ne*Te+(na+ni+nii+niii)*Tg)
delp=dabs(Pcalc-P)
if(delp.gt.delpold.and.niter.gt.5) then
  Tinc=-Tinc*.5
endif
  test=delp/P
  niter=niter+1
if (dabs(tinc).lt.1e-4.or.niter.gt.1000) then
  print*, 'No Convergence',ii,jj
  goto 299
endif
c
enddo
299 continue
6598 write(13,6510) Texi,Te,Tg,Texa,Texaf,ne,na
6605 continue
6599 continue
6510 format(5(F8.2,x),2(E13.6,x))
c
close(2)
close(7)
close(8)
close(9)
close(11)
close(14)
c
stop
end
c
c***** Subroutine to calculate a LTE temperature corresponding
c to the measured value of electron number density
c*****
subroutine LTEne
c
real*8 Tlow,Thigh,T,na,ne,ni,nii,niii,P,Pcalc
real*8 Eanf,Einf,Eiinf,Eiiinf
real*8 me,pi,h,kb,Zte,Zexe,exp1,exp2,exp3
real*8 debhuk1,debhuk3,debhuk2,e,jev,kc,pcdh
real*8 Ea,Ei,Eii,Eiii,gg(4,400),Eml(4,400),Zex(4),kj
integer nw(4,70),nlevs(4)
character words
character*10 filename,outfile
character*6 prefix
real*8 Esinf(4)
real*8 linem,wavel,Amn,c,nm,gm,const,neold
real*8 nallow, nilow, nelow, nielow, niiallow
real*8 TeTg,TeTexa,xil,Texap
c
common/Zpart/Esinf,nw,nlevs,gg,Eml,Zex,Texa,Texi,kb

```

```

common/Elower/Ea,Ei,Eii,Eiii,Eanf,Einf,Eiinf,Eiiinf
common/TEMP/Te,ne,Tg
common/TEXAb1k/TeTg,TeTexa,xil,Texap,Texaf,TeTexb

c
  data kj,me,kb,h,e,kc,c/1.986307e-23,9.10953e-31,1.38066e-23,
  &           6.62618e-34,1.60219e-19,8.9875518e9,2.997925e8/
  pi=dacos(-1.)
c
  Zte=(2*pi*me*kb/h**2)**1.5
c*****Initialize some variables and set some constants
  T=11000
  Tinc1=50
  Tinc2=5
  Tincz=Tinc1
  P=100000
  Zex(1)=1.001
  Zex(2)=5.658
  Zex(3)=9.221
  Zex(4)=4.689
  hitest=0
  na=5.993e23
  ni=ne
  nii=0.0
  niii=0.0
  niter2=0
c
  if(hitest.eq.0) then
    Pcalc=1e6
  else
    Pcalc=0.0
  endif
  delP=Pcalc-P
  delPs=delP
  jdone=0
c*****Iterate until convergence of P
99  do while(abs(delPs+delP).gt.abs(delPs-delP))
  T=T+Tincz
  if (T.ge.35000.) then
    print*, 'Temperature over 35,000 K'
    goto 999
  endif
c
  Texa=T
  Texi=T
  call Zpart
c
  debbye=((4.*pi*e*e*kc/kb)*(ne/T+(ni+4.*nii+9.*nnii)/T))**-.5
  debhuk1=e*e*kc/debbye
  debhuk2=2.*debhuk1
  debhuk3=3.*debhuk1
  debhuk4=4.*debhuk1
  Ea=Eanf-debhuk1
  Ei=Einf-debhuk2
  Eii=Eiinf-debhuk3
  Eiii=Eiiinf-debhuk4
  exp1=dexp(-Ea/(T*kb))
  exp2=dexp(-Ei/(T*kb))
  exp3=dexp(-Eii/(T*kb))

```

```

const=Zte*T**1.5*2.
c1=const*exp1*Zex(2)/Zex(1)
c2=const*exp2*Zex(3)/Zex(2)
c3=const*exp3*Zex(4)/Zex(3)
ni=ne-2.*nii-3.*niii
na=ni*ne/c1
nii=ni*c2/ne
niii=nii*c3/ne
pcdh=1./(24.*pi*(ne+na+ni+nii+niii)*debye**3)
Pcalc=kb*T*(ne+na+ni+nii+niii)*(1.-pcdh)
delPs=delP
delP=Pcalc-P
niter2=niter2+1
c
enddo
if(jdone.eq.0)then
  jdone=1
  T=T-Tincz
  Tincz=Tinc2
  delP=delPs
  goto 99
endif
c
T=-delPs*Tincz/(delP-delPs)+T-Tincz
c
if(hitest.eq.0) then
  Pcalc_low=kb*T*(ne+na+ni+nii+niii)*(1.-pcdh)
  Tlow=T
  jdone=0
  hitest=1
  Tincz=Tinc1
endif
999 continue
c
Te=Tlow
c
return
end
c
*****SUBROUTINE TO CALCULATE PARTITION FUNCTIONS*****
c      This routine was taken from A. Sedghinasab's PhD. thesis.
c      Georgia Institute of Technology, 1987.
*****
```

B. ERROR ANALYSIS

All of the error analysis performed for the calculations made in this investigation follow the method of Kline and McClintock [1953]. The method accounts for the propagation of error through the functional relationships between variables. That is, if a given variable is a function of several others, then the estimated error on that variable can be expressed as a function of the estimated errors on the variables it depends upon.

If a variable F depends on a number of other variables x_i , ($i = 1, n$), then the general equation for relationship between estimated errors is as follows:

$$\Delta F = \sqrt{\sum_{i=1}^n \left(\frac{\partial F}{\partial x_i} \Delta x_i \right)^2} \quad (B.1)$$

where ΔF is the estimated error of F (in units of F), and the Δx_i are the estimated errors of the other variables.

Throughout this appendix the term estimated error is meant to express the *precision* of a given variable's stated value. It is hoped that the values are *accurate* as well, meaning that they are a true representation of the physical quantities being determined. The term error is often used interchangeably with the term estimated error. In some cases the estimated error is quite small. However, we know through experience that systematic errors, or errors due to assumptions and approximations, tend to render the accuracy of the calculation worse than predicted. In some cases the estimated error of a certain variable is taken to be larger than the error calculated, if that variable is to be used in a further calculation.

B.1. LINE EMISSION COEFFICIENT

The error on almost every quantity calculated in this investigation is a function of the error on the argon line emission coefficients, $\epsilon(r)$. Recall that this quantity is calculated from the

Abel inversion of a lateral radiance profile. Lateral radiance, $I_{exp}(x)$, is a function of several variables as was shown in equation (3.1).

The fractional error on the pixel count quantities F_{exp} and F_{imp} is estimated at less than $\pm 1\%$ based on measurement repeatability. The fractional error on the calibration of standard radiance, S_{imp} , is $\pm 1\%$ based on manufacturer's specifications. The fractional error on $\Delta\lambda$ is estimated at less than $\pm 0.1\%$ and doesn't have much impact on the final error. The error on neutral density is estimated at less than $\pm 0.1\%$, but has the largest effect on the final error due to the exponential dependence of $I_{exp}(x)$ on neutral density. The final estimated fraction error on $I_{exp}(x)$ is between $\pm 1\%$ and $\pm 2\%$ for typical LSP conditions.

It is assumed that the Abel inversion of the lateral radiance profile imparts no additional error onto the calculated radial emission coefficients. The final estimated fractional error on radial line emission coefficients is then taken to be $\pm 2\%$. This quantity generally enters into further calculations involving the spontaneous emission coefficients of argon. Because the error on the spontaneous emission coefficients is always relatively large and dominates further error calculation, the propagation of error analysis required for the Abel inversion is not justified.

B.2. TEMPERATURES AND DENSITIES

All of the temperatures calculated in this investigation can be formulated in the following way [Eddy, 1976], with the exception of T_g :

$$\frac{1}{T} = \frac{-k_b}{\Delta E} \ln \left[\prod_i^n C_i \right] \quad (B.2)$$

where ΔE and the C_i 's depend on the temperature to be calculated. This proves to be a convenient form for error propagation analysis.

B.2.1. Upper Level Excitation Temperature

Substituting equation (3.7) for the level populations, and carrying through the partial differentiation in equation (B.1) on equation (3.9), the fraction error on upper level excitation temperature is written as:

$$\frac{\Delta T_{\text{ex}\beta}}{T_{\text{ex}\beta}} = \frac{k_b T_{\text{ex}\beta}}{E_{m1} - E_{m2}} \sqrt{\left(\frac{\Delta \varepsilon_{L1}(r)}{\varepsilon_{L1}(r)}\right)^2 + \left(\frac{\Delta \varepsilon_{L2}(r)}{\varepsilon_{L2}(r)}\right)^2 + \left(\frac{\Delta A_{mn1}}{A_{mn1}}\right)^2 + \left(\frac{\Delta A_{mn2}}{A_{mn2}}\right)^2} \quad (\text{B.3})$$

Taking the fractional errors on the A_{mn} from Table 2.1, the fractional error on $T_{\text{ex}\beta,a}$ is approximately $\pm 7\%$, and the fractional error on $T_{\text{ex}\beta,i}$ is approximately $\pm 12\%$.

B.2.2. LTE Temperature and Neutral Number Density

A similar manipulation performed on equation (3.26) for LTE temperature results in the fractional error written as:

$$\frac{\Delta T_{\text{LTE}}}{T_{\text{LTE}}} = \frac{k_b T_{\text{LTE}}}{E_m} \sqrt{\left(\frac{\Delta Z_{\text{ex}a}}{Z_{\text{ex}a}}\right)^2 + \left(\frac{\Delta n_a}{n_a}\right)^2 + \left(\frac{\Delta A_{mn}}{A_{mn}}\right)^2 + \left(\frac{\Delta \varepsilon_L(r)}{\varepsilon_L(r)}\right)^2} \quad (\text{B.4})$$

It is assumed that the fractional error on partition functions are negligibly small for the temperature range in this investigation. The fractional error on n_a is not known in advance, and another equation is required so that both ΔT_{LTE} and Δn_a can be determined uniquely. The gas equation of state (3.19) works very well for this purpose. From it n_a is expressed as:

$$n_a = \frac{P}{k_b T_{\text{LTE}}} - 2n_e \quad (\text{B.5})$$

where it is assumed that the Debye-Huckel correction is negligible for the error analysis, and that $n_i = n_e$. The fractional error on n_a is then expressed as:

$$\frac{\Delta n_a}{n_a} = \frac{1}{n_a} \sqrt{(2n_e + n_a)^2 \left(\frac{\Delta T_{\text{LTE}}}{T_{\text{LTE}}}\right)^2 + 4(\Delta n_e)^2} \quad (\text{B.6})$$

where it is assumed also that $\Delta n_i = \Delta n_e$, and that pressure is known exactly. The error on n_e is not determined from this analysis, but is based on the considerations in Chan and Montaser [1989] concerning the accuracy of the theoretical hydrogen Stark broadened profiles and their algorithm. A fractional error of $\pm 7\%$ is assigned to n_e for this investigation.

Equations (B.6) and (B.4) are solved simultaneously to arrive at the fractional errors for T_{LTE} and n_a , and they are $\pm 0.6\%$ and $\pm 5.3\%$, respectively. The bulk of the error is introduced by the error on n_e . If n_e were known to $\pm 1\%$, as it would be if $H\beta$ were used rather than $H\alpha$, then the fractional errors on T_{LTE} and n_a would be, $\pm 0.4\%$ and $\pm 1\%$ respectively. Solving an equation similar to (B.4) for $\Delta T_{LTE,i}$ using $\Delta n_i/n_i = \Delta n_e/n_e$ results in an estimated fractional error of $\pm 0.6\%$ on $T_{LTE,i}$.

The estimated errors on $T_{LTE,a}$ and $T_{LTE,i}$ are extremely low. If the LSP were known to be in complete Boltzmann equilibrium, these error estimates would be quite valuable. However, discussion in Chapter 4 pointed out that the neutral argon particles are less likely to be in Boltzmann equilibrium than the ions, and that there was as much as 4% discrepancy between neutral LTE temperatures from two different lines. Because of the importance of these LTE temperature error estimates in later calculations, $\Delta T_{LTE,a}$ will be taken as $\pm 3\%$, and $\Delta T_{LTE,i}$ as $\pm 1\%$. This changes the estimated error on n_a to $\pm 9\%$.

B.2.3. Kinetic Temperatures

Estimating the fractional errors for the kinetic temperatures T_e and T_g is more involved than the estimations above. The equations used are the gas equation of state for kinetic nonequilibrium (3.21), and the non-LTE ionization equation (3.22). The ionization equation can be rearranged to look like equation (B.2) for T_e , but then the right hand side of the equation for T_e fractional error contains a term involving the fractional error on T_e . Because of the implicit nature of this equation, an iterative approach must be taken.

The error on T_g is determined from the gas equation of state, applying equation (B.1) the expression is as follows:

$$(\Delta T_g)^2 = \left[\left(\frac{(T_e + T_g)}{(n_e + n_a)} \right)^2 (\Delta n_e)^2 + \left(\frac{-T_g}{(n_e + n_a)} \right)^2 (\Delta n_a)^2 + \left(\frac{-n_e}{(n_e + n_a)} \right)^2 (\Delta T_e)^2 \right] \quad (B.7)$$

The errors on n_e and n_a are known from above, but the presence of ΔT_e requires another equation so that a unique solution can be found. The ionization equation rearranged to resemble (B.1) is as follows:

$$\frac{1}{T_e} = \frac{-k_b}{E_{la}} \ln \left[\frac{n_e \left(1 + \frac{T_g}{T_e} \right) Z_{exa} \left(\frac{T_{exa}}{T_e} \right)}{2 \left(\frac{2\pi m_e k_b}{h^2} \right)^{3/2} n_a \left(\frac{T_g}{T_e} \right) T_e^{3/2} Z_{exi} \left(\frac{T_{exi}}{T_e} \right)} \right] \quad (B.8)$$

Using equation (B.1) the fractional error on T_e is expressed as:

$$\left(\frac{\Delta T_e}{T_e} \right)^2 = \left(\frac{1}{\ln(S)} \right)^2 \left[\left(1 + \frac{T_g}{T_e} \right)^2 (\Delta n_e/n_e)^2 + \left(\frac{T_g}{T_e} \right)^2 (\Delta n_a/n_a)^2 + \left(\frac{3}{2} \right)^2 (\Delta T_e/T_e)^2 + \left(\ln \left(\frac{n_e}{n_a} \right) \right)^2 (\Delta T_g/T_e)^2 + (\ln(Z_{exa}))^2 (\Delta T_{exa}/T_e)^2 + (\ln(Z_{exi}))^2 (\Delta T_{exi}/T_e)^2 \right] \quad (B.9)$$

where,

$$\ln(S) = \ln \left[\frac{n_e \left(1 + \frac{T_g}{T_e} \right) Z_{exa} \left(\frac{T_{exa}}{T_e} \right)}{2 \left(\frac{2\pi m_e k_b}{h^2} \right)^{3/2} n_a \left(\frac{T_g}{T_e} \right) T_e^{3/2} Z_{exi} \left(\frac{T_{exi}}{T_e} \right)} \right] \quad (B.10)$$

To begin the iteration ΔT_e must be initialized ($\Delta T_e = 0$ works). ΔT_g is then calculated from (B.7), which is then used in (B.9) to determine a new value for ΔT_e . The process is repeated until the fractional errors no longer change from one iteration to the next. Using values of $\Delta T_{exa} = \Delta T_{LTE,a}$, $\Delta T_{exi} = \Delta T_{LTE,i}$, Δn_e , and Δn_a from above, the estimated fractional errors on T_e and T_g are, $\pm 1\%$ and $\pm 10\%$ respectively.

C. EXCITATION ENERGY DENSITY

The density of energy contained in the electronic excitation of neutral argon is the sum over all energy levels of the product of level energy, E_m , and level population number density, n_m :

$$\text{Energy Density} = \sum_{m=1} E_m n_m \quad (\text{C.1})$$

Rearranging equation (3.26) to solve for level population:

$$n_m = \frac{n_a g_m}{Z_{\text{exa}}} \exp\left[\frac{-E_m}{k_b T_{\text{exa}}}\right] \quad (\text{C.2})$$

gives,

$$\sum_{m=1} E_m n_m = \frac{n_a}{Z_{\text{exa}}} \sum E_m g_m \exp\left[\frac{-E_m}{k_b T_{\text{exa}}}\right] \quad (\text{C.3})$$

Recalling equation (1.10) for the electronic excitation partition function, and taking the derivative with respect to excitation temperature of the natural logarithm of equation gives :

$$\frac{d}{dT_{\text{exa}}} [\ln(Z_{\text{exa}})] = \frac{1}{Z_{\text{exa}} k_b T_{\text{exa}}^2} \sum E_m g_m \exp\left[\frac{-E_m}{k_b T_{\text{exa}}}\right] \quad (\text{C.4})$$

Combining equations (C.3) and (C.4) the final result for electronic excitation energy density is:

$$\sum_{m=1} E_m n_m = n_a k_b T_{\text{exa}}^2 \frac{d}{dT_{\text{exa}}} [\ln(Z_{\text{exa}})] \quad (\text{C.5})$$

REFERENCES

Azer, M., personal communication, 1991.

Bender, T.D., M.S. Thesis, University of Illinois at Urbana-Champaign, August 1985.

Biberman, L. M., Vorob'ev, V. S., and Yakubov, I. T., Kinetics of Nonequilibrium Low-Temperature Plasmas, Consultants Bureau, New York, 1987.

Bober, L., Tankin, R. S., "Investigation of Equilibrium in an Argon Plasma," *Journal of Quantitative Spectroscopy and Radiative Transfer*, Vol. 10, p. 991, 1970.

Cambel, A.B., Duclos, D.P., and Anderson, T.P., Real Gases, Academic Press, 1962.

Caveny, L.H., Ed., Orbit-Raising and Maneuvering Propulsion: Research Status and Needs, AIAA Progress in Astronautics and Aeronautics, Vol. 89, 1984.

Chan, S.-K., Montaser, A., "Determination of Electron Number Density via Stark Broadening with an Improved Algorithm," *Spectrochimica Acta*, Vol. 44B, No. 2, pp. 175-184, 1989.

Chen, X., M.S. Thesis, University of Illinois at Urbana-Champaign, August, 1988.

Cho, K.Y., Ph.D. Thesis, Georgia Institute of Technology, 1988.

Cremers, C.J., and Birkebak, R.C., *Appl. Opt.*, Vol. 5, p. 1057, 1966.

Cremers, D. A., Archuleta, F. L., and Martinez, R. J., "Evaluation of the Continuous Optical Discharge for Spectrochemical Analysis," *Spectrochimica Acta*, Vol. 40B, No. 4, p. 665, 1985.

Drawin, H.W., *Z. Physik*, Vol. 228, p. 99, 1969.

Drellishak, K.S., Knopp, C.F., and Cambel, A.B., "Partition Functions and Thermodynamic Properties of Argon Plasma," AEDC-TDR-63-146, August 1963.

Eddy, T. L., and Sedghinasab, A., "The Type and Extent of Non-LTE in Argon Arcs at 0.1-10 Bar," *IEEE Transactions on Plasma Science*, Vol. 16, No. 4, p. 444, 1988.

Eddy, T. L., "Critical Review of Plasma Spectroscopic Diagnostics via MTE," *IEEE Transactions on Plasma Science*, Vol. PS-4, No. 2, p. 103, 1976.

Eddy, T. L., "Low Pressure Plasma Diagnostic Methods," AIAA Paper 89-2830, July 1989.

Eguiguren, J. V., M.S. Thesis, University of Illinois at Urbana-Champaign, 1989.

Farmer, A. J. D., Haddad, G. N., "Local Thermodynamic Equilibrium in Free-Burning Arcs in Argon," *Applied Physics Letters*, Vol. 45, No. 1, p. 24, 1984.

Freeman, M. P., "A Quantitative Examination of the LTE Condition in the Effluent of an Atmospheric Pressure Argon Plasma Jet," *Journal of Quantitative Spectroscopy and Radiative Transfer*, Vol. 8, p. 435, 1968.

Garcia, G., and Campos, J., *Journal of Quantitative Spectroscopy and Radiative Transfer*, Vol. 34, No. 1, p. 85, 1985.

Geltman, S., "Free-Free Radiation in Electron-Neutral Atom Collisions," *JQSRT*, Vol. 13, pp. 601-613, 1973.

Generalov, N. A., Zimakov, V. P., Kozlov, G. I., Masyukov, V. A., and Raizer, Y. P., "Experimental Investigation of a Continuous Optical Discharge," *Soviet Physics-JETP*, Vol. 34, p. 763, 1972.

Giannaris, R. J., and Incropera, F. P., "Nonequilibrium Effects in an Atmospheric Argon Arc Plasma," *Journal of Quantitative Spectroscopy and Radiative Transfer*, Vol. 11, p. 291, 1971.

Glumb, R. J. and Krier, H., "Concepts and Status of Laser-Supported Rocket Propulsion," *Journal of Spacecraft and Rockets*, Vol. 21, p. 70, 1984.

Glumb, R. J., and Krier, H., "Two-Dimensional Model of Laser-Sustained Plasmas in Axisymmetric Flowfields," *AIAA Journal*, Vol. 24, No. 8, p. 1331, 1986.

Glumb, R.J., and Krier, H., "Continuous-Wave (CW) Thermal Laser Rocket Propulsion: Designing an Operational Thruster," Final Technical Report, Contract NAS 3-25271, Combustion Sciences Inc., July 1988.

Glumb, R.J., Ph.D. Thesis, University of Illinois at Urbana-Champaign, June 1986.

Griem, H. R., Plasma Spectroscopy, McGraw-Hill, New York, 1964.

Incropera, F.P., and DeWitt, D.P., Fundamentals of Heat Transfer, John Wiley & Sons, Inc., 1981

Jeng, S.-M., and Keefer, D. R., "Theoretical Investigation of Laser-Sustained Argon Plasmas," *Journal of Applied Physics*, Vol. 60, No. 7, 1986.

Kantrowitz, A. R., "Propulsion to Orbit by Ground-Based Lasers," *Astronautics and Aeronautics*, Vol. 10, p. 74, 1972.

Kantrowitz, A. R., "The Relevance of Space," *Astronautics and Aeronautics*, Vol. 9, p. 34, 1971.

Keefer, D. R., Henriksen, B. B., Braerman, W. F., "Experimental Study of a Stationary Laser-Sustained Air Plasma," *Journal of Applied Physics*, Vol. 46, No. 3, p. 1080, 1975.

Keefer, D., Sedghinasab, A., Wright, N., and Zhang, Q., "Laser Propulsion Using Free-Electron Lasers," AIAA paper No. 90-2636, July 18-20, 1990.

Kline, S.J., and McClintock, F.A., "Describing Uncertainties in Single-Sample Experiments," *Mechanical Engineering*, p. 3, January 1953.

Kozlov, G.I., Kuznetsov, V.A., and Masyukov, V.A., "Radiative Losses by Argon Plasma and the Emissive Model of a Continuous Optical Discharge," *Soviet Physics JETP*, Vol. 39, pp. 463-468, September 1974.

Kruger, C.H., "Nonequilibrium in Confined-Arc Plasmas," *Physics of Fluids*, Vol. 13, No. 7, pp. 1737-1746, July 1970.

Langdon, A.B., "Nonlinear Inverse Bremsstrahlung and Heated-Electron Distributions," *Physical Review Letters*, Vol. 44, No. 9, pp. 575-579, March 1980.

Legner, H.H., and Douglas-Hamilton, D.H., "CW Laser Propulsion," *Journal of Energy*, Vol. 2, pp. 85-94, March 1978.

Lober, R., M.S. Thesis, University of Illinois at Urbana-Champaign, 1989.

McMillin, B.K., M.S. Thesis, University of Illinois at Urbana-Champaign, August 1987.

Mertogul, A. E., M.S. Thesis, University of Illinois at Urbana-Champaign, January 1989.

Mertogul, A. E., Ph.D. Thesis, University of Illinois at Urbana-Champaign, expected October 1992.

Mork, B.J., Scheeline, A., "Determination of Arbitrary Concomitant Absorption and Emission Distributions in Spark Discharges using the Abel Inversion," *Spectrochimica Acta*, Vol. 42B, No. 9, pp. 1063-1076, 1987.

Oettinger, P.E., and Bershader, D., "A Unified Treatment of the Relaxation Phenomenon in Radiating Argon Plasma Flows," *AIAA Journal*, Vol. 5, pp. 1625-1632, September 1967.

Olsen, H.N., *JQSRT*, Vol. 3, p. 59, 1963.

Patankar, S.V., Numerical Heat Transfer and Fluid Flow, Hemisphere Publishing Corporation, New York, 1980.

Potapov, A.V., "Chemical Equilibrium of Multitemperature Systems," *High Temperature*, Vol. 4, pp. 48-51, 1966.

Rachman, A., and Bassani, L., "Local Thermodynamic Equilibrium Conditions in Superhigh-Pressure Helium Plasmas Produced by Laser Action," *Physical Review Letters*, Vol. 23, No. 17, p. 954, 1969.

Rockstroh, T.J., Ph.D. Thesis, University of Illinois at Urbana-Champaign, October 1987.

Scheeline, A., and Walters, J.P., "Spatially Resolved Spectroscopy: Theory and Applications of the Abel Inversion," Contemporary Topics in Analytical and Clinical Chemistry, Vol. 4, pp. 295-372, Plenum Publishing Corporation, 1982.

Scheeline, A., personal communication, 1990.

Schwartz, S., M.S. Thesis, University of Illinois at Urbana-Champaign, May 1989.

Sedghinasab, A., Ph.D. Thesis, Georgia Institute of Technology, 1987.

Shkarofsky, I.P., Johnston, T.W., Bachynski, M.P., The Particle Kinetics of Plasmas, Addison-Wesley, 1969.

Smith, M.L., Keefer, D.R., and Sudharsanan, S.I., "Abel Inversion using Transform Techniques," *JQSRT*, Vol. 39, No. 5, pp. 367-373, 1988.

Sutton, G.P., Rocket Propulsion Elements, Fifth Edition, John Wiley & Sons, Inc., 1986.

Tonon, G., Schirman, D., Rabeau, M., "Electron and Ion Temperature Measurements of a Laser Created Plasma," 1971

Uhlenbusch, J.F., and Fischer, E., "Influence of Diffusion and Nonequilibrium Populations on Noble-Gas Plasmas in Electric Arcs," *Proceedings of the IEEE*, Vol. 59, No. 4, pp. 578-587, April 1971.

Venugopalan, M., Reactions Under Plasma Conditions. Vol. 1, Wiley-Interscience, 1973.

Vidal, C.R., Cooper, J., and Smith, E.W., "Hydrogen Stark-Broadening Tables," *The Astrophysical Journal Supplement Series No. 214*, Vol. 25, pp. 37-136, 1973.

Vorob'ev, V.S., and Khomkin, A. L., "Thresholds for the Appearance of Various States of a Nonequilibrium-Ionization Plasma Produced Near a Metal Surface by Laser Bombardment," *Soviet Technical Physics Letters*, Vol. 10, No. 8, p. 399, 1984.

Welle, R., Keefer, D., and Peters, C., "Laser-Sustained Plasmas in Forced Argon Convective Flow, Part I: Experimental Studies," *AIAA Journal*, Vol. 25, No. 8, p. 1093, 1987.

Wheeler, C.B., and Fielding, S.J., "Absorption of Infrared Radiation as a General Technique for Determination of Plasma Temperature," *Plasma Physics*, Vol. 12, pp. 551-564, 1970.

Wiese, W.L., Brault, J.W., Danzmann, K., Helbig, V., and Kock, M., "Unified Set of Atomic Transition Probabilities for Neutral Argon," *Physical Review A*, Vol. 39, No. 5, pp. 2461-2471, 1989.

Wiese, W.L., Smith, M.W., and Miles, B.M., "Atomic Transition Probabilities," *NSRDS-NBS 22*, 1969.

Zerkle, D.K., M.S. Thesis, University of Illinois at Urbana-Champaign, May 1988.